A DATABASE OF 2D ZEOLITE NANOSHEETS: DEVELOPMENT AND APPLICATIONS

A Dissertation
Presented to
The Academic Faculty

by

Omar Knio

In Partial Fulfillment
of the Requirements for the Degree
Doctor of Philosophy in the
School of Chemical & Biomolecular Engineering

Georgia Institute of Technology
May 2020

A DATABASE OF 2D ZEOLITE NANOSHEETS: DEVELOPMENT AND APPLICATIONS

Approved by:

Dr. David S. Sholl, Advisor
School of Chemical & Biomolecular Engineering
Georgia Institute of Technology

Dr. Christopher W. Jones
School of Chemical & Biomolecular Engineering
Georgia Institute of Technology

Dr. Sankar Nair, Co-advisor
School of Chemical & Biomolecular Engineering
Georgia Institute of Technology

Dr. Surya R. Kalidindi
School of Mechanical Engineering
Georgia Institute of Technology

Dr. Andrew J. Medford
School of Chemical & Biomolecular Engineering
Georgia Institute of Technology

Date Approved: April, 6, 2020

To my friends and family.

“Mathematics is the language with which God has written the universe.”

Galileo Galilei

ACKNOWLEDGEMENTS

I would like to thank my thesis advisor, Dr. David Sholl for his insight, guidance, and commitment to coherence. He has little tolerance for nonsense and leaves no stone unturned. I aspire to embody and continually practice his approach throughout my career.

My project would not be possible without Dr. Sankar Nair. His vision for 2D nanosheets was at the heart of my work. His suggestions laid the bases for the questions we answered and guided us through the many twists and turns.

I was fortunate to have Dr. Andrew Medford as a mentor at the beginning of my project. His practical advice regarding the programing language, python modules, and coding strategies hastened progress in my early stages as a PhD student.

I would like to thank my committee members, Dr. Christopher Jones and Surya Kalidindi for their insights. I am grateful for the NSF for its DMREF grant No. 1534179 and to Exxon Mobil for its support during my final semester. I would also like to acknowledge my experimental collaborators, Akshay Korde, Arvind Ganesan, Tom Wilhammar, and Jonas Hedlund, who have taken my research in unexpected and productive directions.

I grew as a person as a result of mentoring my undergraduate student, Adithya Krishnashand. I began to see projects from a supervisor's perspective and learned to trust, to teach, and to guide. It was inspiring to see great improvement in his scientific communications skills.

My time as a PhD student would not have been the same without my friends at Georgia Tech. Hanjun Fang and Salah Boulfelfel shared their wisdom with me on many occasions, advising me on what to do and what to avoid. The times I spent with John Findley, Anny Liu, Mayank Agrawal, and Wenqin You, Luc Le, Youn Ji Min, and Gabriela Saavedra were always fun. I will remember the laughs and tears we shared.

Finally I would like to give a shout out to everyone on the AIChEGs intramural Volleyball and Ultimate Frisbee teams. I always looked forward to our games and our (usually) victory in the graduate student league. A special thanks goes to Dylan Dautel and Alex Balzer who showed me some helpful techniques along the way.

TABLE OF CONTENTS

LIST OF TABLES

LIST OF FIGURES

SUMMARY

Distillation is a widespread but energy intensive method to separate chemical mixtures. Alternatives to distillation include membrane and adsorption based separations. Zeolites are used in such capacity because they are chemically stable and have pore sizes in the range of many common molecules. However, their use as membranes for high volume chemical feedstock remains elusive due in part to their low flux and high cost.

Though zeolites are generally formed as 3D crystals, new synthesis techniques have given access to 2D zeolite nanosheets with small diffusion path lengths and accelerated molecular diffusion. Since most previous research has focused on bulk zeolite crystals, there is little understanding of the surface adsorption and diffusion mechanisms likely involved at such length scales and their contributions to the permeability and selectivity of different species.

To enable the systematic examination of such surface properties, we constructed a database of more than 800,000 computation-ready 2D zeolite nanosheets from the full range of known zeolite structures in the IZA database of zeolite structure types. We then used molecular dynamics to quantify the effect of surface resistance of H_2, CH_4, CO_2, ethene, ethane, propene, and propane in a variety of nanosheets and at different temperature and pressure conditions. We found that in almost all instances, surface resistance is dominant in nanosheet diffusion.

CHAPTER 1. INTRODUCTION

1.1 2D Zeolite Nanosheets: Diffusion at the Nanoscale

Separation of multi-component mixtures in the chemical industry is an energy intensive process. A common form of separation is distillation, which uses phase transitions to obtain the species in difference phases. Distillation accounts for approximately 10-15% of global energy use.[1] Membrane separations can be as much as 90% more energy efficient than distillation since they use molecular properties such as size and kinetic behavior to perform the separation.[1] If applied to the United States alone, membrane separations could save 4 billion dollars and 100 million tons of CO_2 annually.[1] Promising materials in membrane research include Metal Organic Frameworks (MOFs), Carbon Molecular Sieves (CMS), and zeolites. Difficulties in transitioning from bench-scale to industrial scale processes include scale-up of expensive steps and materials degradation.

Zeolitic membranes are interesting because they are relatively stable and have pore diameters around the size of common industrial chemicals. However, due to high cost and low flux, their only industrial kinetically driven separation application is the dehydration of bioethanol.[2, 3] In a 2D nanosheet, diffusion through the sheet can happen rapidly due to a short path length normal to the lamellar surface of the crystal.[4] Therefore, the production of shorter nanosheets for separation has become a research target.[5] In catalysis experiments, 2D nanosheets have reduced coking by hastening the diffusion of byproducts out of the crystal and have increased reaction conversion.[4, 6]

Zeolites have traditionally been synthesized and conceived of as 3D crystals. However, that changed when it was discovered that MWW was found to form via two different paths, direct solvothermal synthesis and via 2D zeolite layer precursors (ZLP).[7] Since then, 12 other zeolite materials were discovered to have 2D forms.[7] So far, 3 synthetic routes for producing 2D zeolites are known: direct solvothermal synthesis, surfactant-templated synthesis, and 3D to 2D transformations.[7] In direct synthesis, a 2D layer is formed before the final reaction into a 3D crystal. In surfactant-templated synthesis, a polymer chain is added onto structure directing agent (SDA).[4] The polymer chain acts as a spacer that retards agglomeration normal to the plane of the zeolite.[4] In 3D to 2D transformations, a 3D crystal is treated with an acid solution untill the weakest T-O bonds hydrolyze.[8] Germanium is generally included at Si/Ge ratios of 4.3-6 because it produces strained bonds that facilitate structure disassembly.[8]

A main objective of 2D zeolite research has been the production of better catalysts. 2D nanosheets have an abundance of surface acid sites and increased mass transfer relative to the bulk crystal.[7] The disadvantage is an inability to carry out size-selective catalysis since screening at the pores plays a limited role.[7] A common post-synthesis step is pillaring of the 2D zeolite to form a hierarchical structure. Pillaring takes place when silica species present between layers separated by surfactant covalently bond to the top and bottom layers forming columns.[7] This creates mesoporous, stable structures that allow bulky molecules to access surface acid sites.[9] Adsorption of 2, 4-dimethylquinolinium on an MWW pillared structure showed that most of the protonic sites are accessible to bulky molecules in the pillared structure while only 15-20% are accessible in the bulk.[9]

For separations research, 2D zeolitic nanosheets alone cannot form a membrane since they would disintegrate under pressure.[3] Therefore, the zeolite portion of the membrane is typically grown on a porous support.[3] Since zeolite nucleation and growth in-situ is difficult to control, the zeolite media is formed via seeding and secondary growth. Zeolite nanosheets are first formed separately, then brought onto the support via dip or spin coating.[3] Hydrothermal secondary growth is necessary to close the gaps that exist after deposition since nanosheets do not have the necessary aspect ratio to guarantee good overlap. Traditionally hydrothermal growth has used a silica gel, but a gel-free method has recently been introduced to avoid the cost of gel; the support acts as a the silica source.[3]

Several separations of industrial importance include alkane/alkene and CO_2/H_2 separations. More than 200 million tonnes of ethene and propene are produced annually for the global plastics sector.[1] Cryogenic distillation, an energy intensive high pressure, low temperature phase-change separation is used to obtain the industrially required alkene purity, exceeding 99.9%. However, the distillation of propene and ethene alone uses about 0.3% of the world's annual energy production.[1]

The difficulty of alkane/alkene separation lies in their similarity. Membranes separate mixtures based on their adsorption properties, kinetic properties, or a combination of both. In selective adsorption, one molecule adsorbs onto the membrane at a much higher rate than another. In kinetic separation, one molecule diffuses through the membrane at a faster rate. However, both the kinetics and adsorption properties of alkanes and alkenes are similar, so their separation is challenging. Some membranes used to separate alkanes and alkenes incorporate silver atoms due to their ability to increase adsorption for olefins.[10, 11]

A question of interest is whether the surface of a zeolite can alter the kinetics and thermodynamics in favor of one molecule or another without the cost of silver.

H_2/CO_2 separation in the water gas shift reaction is responsible for 95% of American H_2 production, and the separation has recently become a syngas research objective since it can produce H_2 and capture CO_2 in one step.[12, 13] Syngas typically contains H_2, CO_2, CO, H_2O, and potentially traces of H_2S, so zeolites are particularly suited for the separation given their sulfur tolerance and hydrothermal stability.[14] The objective of work on this separation is developing membranes with high flux while maintaining the necessary selectivity.[14] One high performing membrane for H_2/CO_2 separation was made by depositing methyldiethoxysilane on the inner surface of MFI pores.[3, 14] This step avoided single file diffusion that could have stifled the separation, but the Chemical Vapor Separation (CVD) process used is expensive.[3] Significant cost reduction could be obtained using a zeolite layer with inherently selective pores.

Due to the aforementioned increased flux and possible decreased cost of zeolite nanosheets.[3, 4] their use as membranes could unlock opportunities unavailable to 3D crystals. However, zeolite nanosheet diffusion and selective separation properties have not been extensively studied. Of particular interest is the effect of the surface/adsorbate interactions, which is neglected in 3D crystals but may be significant in zeolite nanosheets.[15] Therefore, studying the relative contributions of the pores and surface to diffusion through a wide variety of zeolite nanosheets is an important task that could enable progression of the field. In this thesis, we describe the development of a database of 800,00 2D zeolite nanosheets with thermodynamically favorable surfaces. We then use molecular

dynamics to compare nanosheet and bulk diffusivities and show that, unlike in 3D crystals, surfaces dominate diffusion in nanosheets.

1.2 Computational Methods

1.2.1 Database Generation

The second chapter of this thesis deals with the generation of a database of atomically accurate 2D nanosheet structures. The slabs span a wide variety of experimentally relevant Miller indices and have surfaces that are thermodynamically favorable.[16] To derive a slab structure from a 3D zeolite, an algorithm must decide on termination points for a possible surface. An example of a simple surface formed by a plane is shown in **Figure 1.1**. The central challenge is that there are a near-infinite number of possible surface terminations, so one must decide on the properties of the surfaces most likely to be synthesized as well as an algorithm with which to obtain such surfaces.

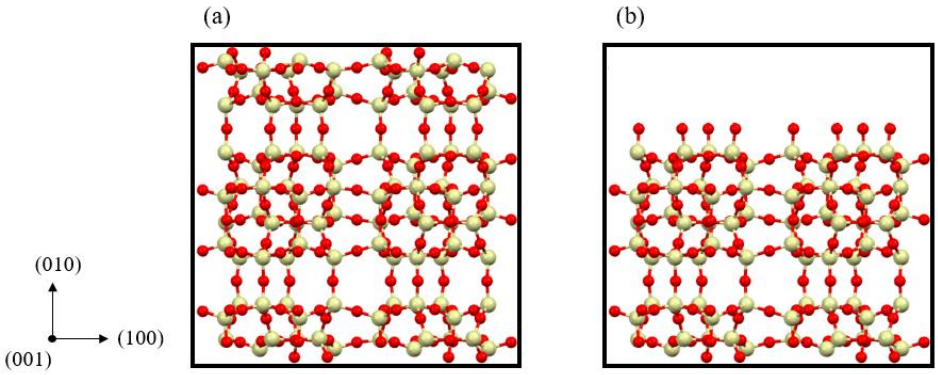

Figure 1.1. (a) A bulk MFI unit cell. (b) A surface formed by removing all atoms with a fractional b coordinate of 0.75 or larger.

Surfaces with the least number of broken bonds are typically expected to be the most thermodynamically favorable.[17] We adopted a heuristic approach where our algorithm generated many surfaces and selected those with the least number of broken

bonds. This approach defines a plane parallel to the surface then removed all Si atom above the plane. After plane removal, the algorithm carried out nine targeted removal cycles. In a targeted removal cycle, we first determined the coordination number of each Si, that is, how many Si are connected (through a bridging O) to the Si in question, and removed Si with a coordination number of 2 or less. Since the removal of a Si decreased the coordination number of a neighboring Si, there was a need for multiple cycles.

The algorithm was written using python and various plugin modules. The Atomic Simulation Environment[18] was used to read in crystallographic format files, and Pymatgen[19] was used to generate lattice reoriented unit cells to expose certain Miller indices. The Si counting required by the targeted removal cycles was computationally taxing, so Numpy[20] matrices were used since they were made for large scale arithmetic operations.

1.2.2 Molecular Dynamics

Molecular dynamics (MD) solves Newton's Equations of motion for a system to obtain macroscopic properties from microscopic interactions.[21] Such macroscopic properties include temperature, pressure, and free energy. The key to accurate results are properly defined force fields, or energy functions which are parametrized to calculate accurate molecular movement.[21]

MD is comprised of two basic steps: summing the forces on an atom based on its interaction with neighboring atoms, and moving the atom based on the net force acting on it. A Lennard-Jones potential is a standard method of defining interatomic energies between atoms that arise from Van der Waals interactions:

$$E_{Lennard-Jones}(r) = 4\varepsilon_{ij}\left[\left(\frac{\sigma_{ij}}{r}\right)^{12} - \left(\frac{\sigma_{ij}}{r}\right)^{6}\right] \quad (1.1)$$

where ε_{ij} describes the energy of the interaction, σ_{ij} is the distance at which attractive and repulsive forces are equal, r is the distance between both atoms, and the i and j subscripts denote the types of atoms involved in the interaction. The derivative of equation 1.1 gives the force on the atom:

$$F_{Lennard-Jones}(r) = -\frac{dE_{Lennard-Jones}(r)}{dx} = \frac{48\varepsilon_{ij}}{r}\left[\left(\frac{\sigma_{ij}}{r}\right)^{12} - \frac{1}{2}\left(\frac{\sigma_{ij}}{r}\right)^{6}\right] \quad (1.2)$$

where in this case $F_{Lennard-Jones}$ is the force along the x axis. The new position is given by:

$$a_i = \frac{F_{Lennard-Jones}(r)}{m} \quad (1.3)$$

$$x_{i+1} = x_i + v_i\Delta t + \frac{1}{2}a_i\Delta t^2 \quad (1.4)$$

$$v_{i+1} = v_i + \frac{1}{2}(a_i + a_{i+1})\Delta t \quad (1.5)$$

where a_i is the atom's acceleration, x_i is the atom's position, m is the mass of the atom, v_i is the velocity, and Δt is the time step (usually 1 fs), and the subscript i denotes the ith step. In addition to the Van der Waals interactions, electrostatic energies are commonly computed using the Coulomb potential:

$$E_{Coulombic} = \frac{Cq_iq_j}{\epsilon r} \quad (1.6)$$

where C is a universal constant, q is the charge on an atom, and ϵ is the dielectric constant. Due to the need to calculate forces between each atom and all of its neighboring atoms, the computational requirement to run an MD simulation, at least in the simplest implementations of this method, scales roughly with the square of the number of atoms in the unit cell. Therefore, unit cells must be large enough to accurately reflect the energetic environment and small enough to complete the simulation in a timely manner.

MD simulations in microporous materials can be either rigid or flexible. In a rigid simulation, only the adsorbates move. In a flexible simulation, both the adsorbates and the framework's atoms move. In the latter case the framework-framework interatomic interactions are calculated by Lennard-Jones potentials in addition to other terms, such as bond and angle terms meant to preserve average bond and angle geometries. For example:[22]

$$E_{bond} = A_1(r - r_0)^2 + A_2(r - r_0)^3 + A_3(r - r_0)^4 \tag{1.7}$$

$$E_{angle} = B_1(\theta - \theta_0)^2 + B_2(\theta - \theta_0)^3 + B_3(\theta - \theta_0)^4 \tag{1.8}$$

where E_{bond} is the bond energy, r is the distance between the bonded atoms, r_0 is the equilibrium bond distance between two atoms of a certain type, A_n are bond energy constants that weight each term, E_{angle} is the angle energy, θ is the angle between three atoms, θ_0 is the equilibrium angle between three atoms of a certain type, and B_n are angle energy constants. Some force fields use more complex bond and angle terms as well as four atom terms such as dihedrals and impropers for a more accurate description of framework flexibility.[23] Force fields are parameterized based on either first principles or

experimental data. The development of force fields is a non-trivial task,[24-26] and care must be taken to select the right force field for the system under consideration.

Most force fields are non-reactive, meaning they cannot describe bond breaking and bond forming events. If a bond or angle deviates too far from its equilibrium value, the force applied attempts to return the system to near equilibrium geometry. To remedy this drawback, reactive force fields such as the ReaxFF force field have been developed to study the kinetics and thermodynamics of bond breaking and forming events.[27] Its bond, angle, and other terms are more complex than those seen in non-reactive force fields and enable atoms to change their chemical environment by breaking bonds, forming bonds, and transitioning seamlessly between different phases of matter.[27] In addition, ReaxFF employs an algorithm, Qeq, to calculate new charges on an atoms as they change their electrostatic surroundings.[27, 28]

Another important choice when performing MD simulations is whether to use equilibrium molecular dynamics (EMD) or non-equilibrium molecular dynamics (NEMD). In EMD, the adsorbates are only acted upon by other adsorbate or framework atoms. In NEMD, another factor is introduced to drive flux in a certain direction. For example, an NEMD setup could apply a chemical potential in one direction to simulate the effect of a pressure gradient.[29] Other NEMD simulations divide the unit cell into boxes, then add atoms to some boxes and remove them from others to create a net flow between the controlled boxes.[15] Both NEMD and EMD simulations have their advantages, although EMD simulations are typically simpler to interpret..[30]

After analyzing previous studies, we chose to use flexible frameworks and EMD for our slab and bulk diffusion simulations.[15, 30, 31] Newsome and Sholl found that rigid frameworks gave inaccurate diffusivity results in slabs because they underestimated the adsorption rate.[15] They found that adsorption attempts failed because the structure could not absorb and dissipate the incoming kinetic energy, so molecules rebounded into the vacuum phase more often than would be expected given a more realistic surface.[15] In addition, Newsome and Sholl and Liu et al. compared EMD and NEMD simulations for measuring flux through nanoporous materials. They found that EMD gave close results to NEMD while demanding less computational resources.[30, 31]

1.2.3 Grand Canonical Monte Carlo

The loading, or amount of adsorbates per unit cell, has a great effect on the diffusivity in confined geometries. Generally, low loadings entail little adsorbate-adsorbate interaction and therefore higher self-diffusivities. At high loadings, adsorbates block each other's movement resulting in low self-diffusivities. In our simulations, we examine both high and low loadings. However, we need a method to initialize our simulation with the correct number of adsorbates given a certain temperature and pressure. The MD algorithm can move atoms, but it cannot create or delete atoms in a simulation. Therefore, we use Grand Canonical Monte Carlo (GCMC) simulations to initialize our MD simulations with the number of atoms commensurate with the required temperature and pressure.

GCMC is an algorithm that inserts, deletes, moves, rotates, and swaps molecules based on thermodynamic and probabilistic data.[32] Like MD, it calculates Van der Waals and electrostatic energies, but unlike MD, it does not move the molecules according to a

force vector. Instead, it attempts, an action, such as an insertion, deletion, rotation, or swap. It first calculates the energy of the molecule assuming the action is complete. If the energy is favorable, the action is accepted. If it is not favorable, a random probability is drawn and compared to a Boltzmann type energy distribution to determine acceptance. Using GCMC, we developed adsorption isotherms and obtained initial coordinates for adsorbates in our MD simulations.

1.2.4 Diffusivity Analysis

A diffusivity is a value that describes the speed at which molecules move through a medium. There are multiple diffusivity values, each describing a different aspect of mass transport.[33] The most basic is self-diffusivity, which describes the movement of a single molecule and is known to chemists as the Stokes-Einstein description of particle mobility.[34] For our purposes, we will use the corrected diffusivity, also known as the single component Maxwell-Stefan diffusivity, which describes the movement of the center of mass of a set of molecules and is used to calculate flux.[33, 35]

To analyze molecular diffusivities, MD is used to record a series of adsorbate positions at set intervals throughout the simulation. The positions are then analyzed using the Einstein relation:[31]

$$D_0 = \frac{N_{sys}}{2d} \lim_{t\to\infty} \frac{1}{t} \langle \left| z_{sys,com}(t) - z_{sys,com}(0) \right|^2 \rangle = \frac{N_{sys}}{2d} \lim_{t\to\infty} \frac{1}{t} \langle \left| \Delta z_{sys,com} \right|^2 \rangle \quad (1.9)$$

where D_0 is the corrected diffusivity, N_{sys} is the number of molecules in the system, $\Delta z_{sys,com}$ is the change in the center of mass of the system, and d is the dimensionality of the system.

This approach is not directly applicable to inhomogeneous systems such as zeolite nanosheets that include both gaseous and zeolite regions. **Figure 1.2** displays a bulk and nanosheet unit cell, both of which should be understood to have periodic boundary conditions in all directions. Using the traditional Einstein equation in this case would capture the contributions to the diffusivity of both regions, whereas only the contribution of the nanosheet is of interest. Since diffusion through vacuum is much faster than diffusion through zeolite, the Einstein relation would overestimate the diffusivity in a slab unit cell.

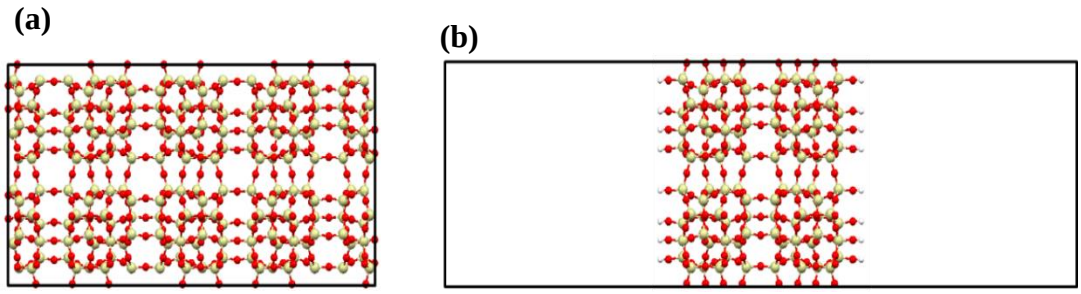

Figure 1.2 (a) A bulk 1×2×1 and (b) a slab 1×1×1 MFI unit cell oriented parallel to the (010) direction. In each case, the system boundaries represent periodic boundary conditions.

Liu et al. solved this problem by defining the effective diffusivity as[31]:

$$D_{eff} = \left\{ \frac{N_{slab}}{\left(\frac{N_{gas}\rho_{slab}A_{slab}}{N_{sys}\ \rho_{gas}A_{gas}} + \frac{N_{slab}}{N_{sys}} \right)^2} \right\} \lim_{t\to\infty} \frac{1}{t} \left\langle \left| z_{sys,com(t)} - z_{sys,com}(0) \right|^2 \right\rangle \qquad (1.10)$$

where N and ρ are the time-averaged number of atoms and density in either region, and A is the cross-sectional area of the unit cell normal to the diffusion pathway.[31] Once the effective diffusivity has been determined by equation 1.10, the flux through a slab is given by:

$$j_{slab} = \frac{\rho_{slab}(f) D_{eff}(f)}{L_{slab} f} (f_1 - f_2) \quad (1.11)$$

where j_{slab} is the flux through the slab, L_{slab} is the thickness of the slab, f_1 and f_2 are the fugacities on the feed and permeate side of the slab, and f is the average of both fugacities. Eqn. 1.11 is only accurate when f_1 and f_2 are similar.[31] It is important to note that this approach captures the effects of interfacial resistances to mass transfer (also known as surface barriers) if they exist and that the effective diffusivities used in this approach are valid only for the specific slab thickness for which they are measured.

1.3 Dissertation Scope

The topics described in this thesis advance the understanding of zeolite surface favorability and surface diffusion properties. We first generate a database of atomically accurate 2D zeolite nanosheets with a large set of frameworks and orientations. We then investigate the effect of surfaces on the diffusion process.

Chapter 2 describes the generation of an 800,000 structure database ideal for zeolite surface property analysis. We created surfaces using an algorithm that minimized the number of broken bonds then compared our slabs and predicted crystal shapes to experimentally refined nanosheet structures and crystal morphologies.

Chapter 3 was motivated by a lack of knowledge regarding the extent to which surfaces effect diffusion in zeolite nanosheets. We use molecular dynamics to compare diffusion in nanosheets to diffusion in bulk zeolites. We investigate different molecules, temperatures, loadings, nanosheet heights, and zeolite frameworks to develop a comprehensive understanding of the variance in the magnitude of surface resistance.

Chapter 4 uses a set of 2D nanosheets from the database to investigate the utility of models of zeolite nanotubes, structures for which no experimental equivalents exist in literature. We describe a method of curling zeolite nanosheets into nanotubes then compare simulated XRD patterns of Nanotubes and bulk zeolites.

Chapter 5 is motivated by a desire to hasten research into zeolite dealumination, a process that is damages a zeolite's catalytic properties. We compare the results of ReaxFF, a computationally inexpensive reactive molecular dynamics method, to DFT, the traditional ab initio method used to investigate such mechanisms.

1.4 References

1. Sholl, D.S. and R.P. Lively, *Seven chemical separations to change the world.* Nature, 2016. **532**(7600): p. 435.

2. Feng, C., K. Khulbe, T. Matsuura, R. Farnood, and A. Ismail, *Recent progress in zeolite/zeotype membranes.* Journal of Membrane Science and Research, 2015. **1**(2): p. 49-72.

3. Rangnekar, N., N. Mittal, B. Elyassi, J. Caro, and M. Tsapatsis, *Zeolite membranes–a review and comparison with MOFs.* Chemical Society Reviews, 2015. **44**(20): p. 7128-7154.

4. Choi, M., K. Na, J. Kim, Y. Sakamoto, O. Terasaki, and R. Ryoo, *Stable single-unit-cell nanosheets of zeolite MFI as active and long-lived catalysts.* Nature, 2009. **461**(7261): p. 246-249.

5. Rangnekar, N., M. Shete, K.V. Agrawal, B. Topuz, P. Kumar, Q. Guo, I. Ismail, A. Alyoubi, S. Basahel, and K. Narasimharao, *2D zeolite coatings: Langmuir–Schaefer deposition of 3 nm thick MFI zeolite nanosheets.* Angewandte Chemie International Edition, 2015. **54**(22): p. 6571-6575.

6. Luo, H.Y., V.K. Michaelis, S. Hodges, R.G. Griffin, and Y. Román-Leshkov, *One-pot synthesis of MWW zeolite nanosheets using a rationally designed organic structure-directing agent.* Chemical science, 2015. **6**(11): p. 6320-6324.

7. Roth, W.J., P. Nachtigall, R.E. Morris, and J. Cejka, *Two-dimensional zeolites: current status and perspectives.* Chemical reviews, 2014. **114**(9): p. 4807-4837.

8. Eliášová, P., M. Opanasenko, P.S. Wheatley, M. Shamzhy, M. Mazur, P. Nachtigall, W.J. Roth, R.E. Morris, and J. Čejka, *The ADOR mechanism for the synthesis of new zeolites.* Chemical Society Reviews, 2015. **44**(20): p. 7177-7206.

9. Laforge, S., P. Ayrault, D. Martin, and M. Guisnet, *Acidic and catalytic properties of MCM-22 and MCM-36 zeolites synthesized from the same precursors.* Applied Catalysis A: General, 2005. **279**(1): p. 79-88.

10. Aguado, S., G.r. Bergeret, C. Daniel, and D. Farrusseng, *Absolute molecular sieve separation of ethylene/ethane mixtures with silver zeolite A.* Journal of the American Chemical Society, 2012. **134**(36): p. 14635-14637.

11. Sakai, M., Y. Sasaki, T. Tomono, M. Seshimo, and M. Matsukata, *Olefin selective Ag-exchanged X-type zeolite membrane for propylene/propane and ethylene/ethane separation.* ACS Applied Materials & Interfaces, 2019. **11**(4): p. 4145-4151.

12. First, E.L., C.E. Gounaris, and C.A. Floudas, *Predictive framework for shape-selective separations in three-dimensional zeolites and metal–organic frameworks.* Langmuir, 2013. **29**(18): p. 5599-5608.

13. Lai, Z., G. Bonilla, I. Diaz, J.G. Nery, K. Sujaoti, M.A. Amat, E. Kokkoli, O. Terasaki, R.W. Thompson, and M. Tsapatsis, *Microstructural optimization of a zeolite membrane for organic vapor separation.* Science, 2003. **300**(5618): p. 456-460.

14. Tang, Z., J. Dong, and T.M. Nenoff, *Internal surface modification of MFI-type zeolite membranes for high selectivity and high flux for hydrogen.* Langmuir, 2009. **25**(9): p. 4848-4852.

15. Newsome, D.A. and D.S. Sholl, *Predictive assessment of surface resistances in zeolite membranes using atomically detailed models.* The Journal of Physical Chemistry B, 2005. **109**(15): p. 7237-7244.

16. Knio, O., A.J. Medford, S. Nair, and D.S. Sholl, *Database of Computation-Ready 2D Zeolitic Slabs.* Chemistry of Materials, 2018. **31**(2): p. 353-364.

17. Witman, M., S. Ling, P. Boyd, S. Barthel, M. Haranczyk, B. Slater, and B. Smit, *Cutting Materials in Half: A Graph Theory Approach for Generating Crystal Surfaces and Its Prediction of 2D Zeolites.* ACS Central Science, 2018.

18. Larsen, A.H., J.J. Mortensen, J. Blomqvist, I.E. Castelli, R. Christensen, M. Dułak, J. Friis, M.N. Groves, B. Hammer, and C. Hargus, *The atomic simulation environment—a Python library for working with atoms.* Journal of Physics: Condensed Matter, 2017. **29**(27): p. 273002.

19. Ong, S.P., W.D. Richards, A. Jain, G. Hautier, M. Kocher, S. Cholia, D. Gunter, V.L. Chevrier, K.A. Persson, and G. Ceder, *Python Materials Genomics (pymatgen): A robust, open-source python library for materials analysis.* Computational Materials Science, 2013. **68**: p. 314-319.

20. Walt, S.v.d., S.C. Colbert, and G. Varoquaux, *The NumPy array: a structure for efficient numerical computation.* Computing in Science & Engineering, 2011. **13**(2): p. 22-30.

21. van Gunsteren, W.F. and H.J. Berendsen, *Computer simulation of molecular dynamics: Methodology, applications, and perspectives in chemistry.* Angewandte Chemie International Edition in English, 1990. **29**(9): p. 992-1023.

22. Sun, H., *COMPASS: an ab initio force-field optimized for condensed-phase applications overview with details on alkane and benzene compounds.* The Journal of Physical Chemistry B, 1998. **102**(38): p. 7338-7364.

23. Hill, J.-R. and J. Sauer, *Molecular mechanics potential for silica and zeolite catalysts based on ab initio calculations. 2. Aluminosilicates.* The Journal of Physical Chemistry, 1995. **99**(23): p. 9536-9550.

24. Boulfelfel, S.E., P.I. Ravikovitch, L. Koziol, and D.S. Sholl, *Improved Hill–Sauer force field for accurate description of pores in 8-ring zeolites.* The Journal of Physical Chemistry C, 2016. **120**(26): p. 14140-14148.

25. Fang, H., P. Kamakoti, J. Zang, S. Cundy, C. Paur, P.I. Ravikovitch, and D.S. Sholl, *Prediction of CO_2 adsorption properties in zeolites using force fields derived from periodic dispersion-corrected DFT calculations.* The Journal of Physical Chemistry C, 2012. **116**(19): p. 10692-10701.

26. Fang, H., P. Kamakoti, P.I. Ravikovitch, M. Aronson, C. Paur, and D.S. Sholl, *First principles derived, transferable force fields for CO_2 adsorption in Na-exchanged cationic zeolites.* Physical Chemistry Chemical Physics, 2013. **15**(31): p. 12882-12894.

27. Senftle, T.P., S. Hong, M.M. Islam, S.B. Kylasa, Y. Zheng, Y.K. Shin, C. Junkermeier, R. Engel-Herbert, M.J. Janik, and H.M. Aktulga, *The ReaxFF reactive force-field: development, applications and future directions.* npj Computational Materials, 2016. **2**: p. 15011.

28. Verstraelen, T., S. Vandenbrande, and P.W. Ayers, *Direct computation of parameters for accurate polarizable force fields.* The Journal of chemical physics, 2014. **141**(19): p. 194114.

29. MacElroy, J., *Nonequilibrium molecular dynamics simulation of diffusion and flow in thin microporous membranes.* The Journal of chemical physics, 1994. **101**(6): p. 5274-5280.

30. Newsome, D.A. and D.S. Sholl, *Atomically detailed simulations of surface resistances to transport of CH_4, CF_4, and C_2H_6 through silicalite membranes.* Microporous and Mesoporous Materials, 2008. **107**(3): p. 286-295.

31. Liu, L., D. Nicholson, and S.K. Bhatia, *Interfacial resistance and length-dependent transport diffusivities in carbon nanotubes.* The Journal of Physical Chemistry C, 2016. **120**(46): p. 26363-26373.

32. Frenkel, D. and B. Smit, *Understanding molecular simulation: From algorithms to applications*. 2002, Elsevier (formerly published by Academic Press). p. 1-638.

33. Sholl, D.S., *Understanding macroscopic diffusion of adsorbed molecules in crystalline nanoporous materials via atomistic simulations.* Accounts of chemical research, 2006. **39**(6): p. 403-411.

34. Miller, C.C., *The Stokes-Einstein law for diffusion in solution.* Proceedings of the Royal Society of London. Series A, Containing Papers of a Mathematical and Physical Character, 1924. **106**(740): p. 724-749.

35. Krishna, R., J. Van Baten, E. Garcia-Perez, and S. Calero, *Incorporating the Loading Dependence of the Maxwell− Stefan Diffusivity in the Modeling of CH_4 and CO_2 Permeation Across Zeolite Membranes.* Industrial & engineering chemistry research, 2007. **46**(10): p. 2974-2986.

CHAPTER 2. A DATABASE OF COMPUTATION-READY 2D ZEOLITIC SLABS*

2.1 Introduction

Nanoporous materials such as zeolites are of great interest as adsorbents, catalysts, and membranes in a number of chemical production applications. For example, membrane separations can be up to 90% more energy efficient than distillation.[1] However, zeolitic membranes have generally faced difficulties in scale-up of expensive steps and materials degradation[2], and their current industrial application is focused upon dehydration of organic-water mixtures.[3, 4] New synthesis techniques have led to the synthesis of 2D zeolite nanosheets wherein crystallization is restricted to two dimensions and the third is only a few unit cells in thickness.[5-7] This confers a number of attractive properties such as lower diffusion resistance (especially for large molecules), very high surface areas, and direct surface access to shape/size-selective catalytic sites that would otherwise be embedded inside a 3D zeolite crystal. Although it is known that diffusion is enhanced in nanosheets relative to bulk materials, the dominant surface diffusion and blockage mechanisms and their magnitude with respect to bulk diffusion, remain largely unknown.[8-13]

---

*Contents of this chapter have been reproduced from the previously published article
Omar Knio, Andrew J. Medford, Sankar Nair, David S. Sholl, ″Database of Computation-Ready 2D Zeolitic Slabs″, Chemistry of Materials, 31.2 (2019) 353-364.

It has been suggested that surface diffusion through nanosheets can be retarded by repeated cycles of entry and exit into the silica layers.[13] Other proposed mechanisms for diffusion in zeolitic nanosheets involve pore blockage by adsorption of water on silanol groups, pore narrowing, and high rates of desorption from the surface.[11, 14] Separate studies have reported enhanced water permeability as a result of increasing zeolite surface hydrophilicity.[8, 15]

A significant challenge to systematically examining these issues is that very limited structural information is available on 2D zeolitic nanosheets. Zeolite databases with bulk (3D) material structures have been generated by a variety of methods. The International Zeolite Association (IZA) database contains more than 200 experimentally known zeolites.[16, 17] To expand upon the properties of synthesized zeolites, several computational groups have created databases of hypothetical zeolite frameworks.[18] Foster and Treacy developed the symmetry constrained intersite bond searching (SCIBS) method and obtained a database of over 2 million structures.[19, 20] Their database contained 97 IZA frameworks, and two predicted 18-membered ring pore frameworks were later synthesized as ITQ-33 and ITQ-44.[18, 21, 22] Friedrichs et al. systematically enumerated the structural possibilities of networks of 4-connected atoms and matched predicted tilings to known IZA structures.[23] Yu and Xu developed hypothetical structures by placing atoms around forbidden zones to achieve the desired porous pattern.[18] Pophale, Cheeseman, and Deem developed a database of hypothetical zeolites using a Monte Carlo search for zeolite like materials.[24] About 15% of the structures had energy densities within the range occupied by known zeolites.[24]

As mentioned earlier, the above databases listed only describe bulk (3D) zeolite materials. To accelerate the development of 2D zeolitic nanosheets, it would be useful to have access to a wide range of 2D zeolite structures. To that end, Jamali et al. developed a database of 27 zeolite nanosheets and screened the structures for potential use in water desalination.[25] Their work identified four promising nanosheets based on their pore limiting diameter and channel density properties.[25] Witman et al. recently systematically enumerated minimum bond cut surface terminations and developed a descriptor based on the favorability of the two most favorable Miller indices to determine the potential of synthesizing a nanosheet from a particular zeolite framework .[26] Their results provided structures for 3,682 surfaces representing 91% of the bulk structure types in the IZA database. In this chapter, we describe a different approach that leads to a set of 804,842 structures that greatly exceed in their quantity, span of heights, and surface diversity the nanosheets of any previous work.[25, 26] Our database includes the different surfaces/nanosheets that result from multiple possible terminations of a zeolite surface at a given Miller plane, and includes nanosheet slabs of arbitrary thickness along all crystallographic planes for which the absolute value of each Miller index is < 3. We have generated an average of 705 different surface terminations for each of about 92% of the bulk structures in the IZA database. As an initial application for our collection of structures, we discuss the equilibrium Wulff shapes predicted for 86% of the IZA structures.

2.2 Methods

2.2.1 Zeolite Surface Generation

Throughout this chapter, we consider zeolitic surfaces of siliceous materials that can be defined as Miller index surfaces of known bulk zeolite structures. It is not obvious *a priori* which Miller indices are most relevant for a given bulk structure. One way to get insight into this issue is to list the Miller indices of surfaces that have been observed experimentally on various zeolite crystals. A partial list is given in **Table A.1** (Appendix), which includes examples such as the {211} surface of ANA and the {-202} surface of LAU.[27] This list indicates that a range of Miller indices must be considered in any effort to define surface structures for a diverse collection of zeolites. We define the Maximum Miller index (MMI) as the maximum of the absolute values of each index in the set *{hkl}*. The results in **Table A.1** show that 97% of the observed Miller indices have an MMI < 3. In addition, the number of unique Miller index surfaces that must be considered increases rapidly as MMI is increased. For example, MFI has 19 unique Miller index surfaces with MMI = 2 and 49 unique surfaces with MMI = 3. Moreover, the number and complexity of candidate structures that must be considered for each Miller index typically increases as MMI increases. We therefore used an MMI of 2 in our calculations, and we set out to examine every Miller index surface satisfying this restriction for each bulk structure. We applied our methods to 217 of the 221 tetrahedrally coordinated (non-interrupted) framework materials as defined by the IZA database; four were excluded due to memory requirements.[16] The IZA database includes an additional 14 structures that are not fully tetrahedrally coordinated and denoted with a "-" sign before the framework (for example, structure type "-CLO").[16] These structures were excluded from our analysis.

A goal of this chapter is to generate structures with the atomic accuracy necessary for geometric calculations and diffusion property analysis.[10, 28-31] With this in mind, we note that the atomic coordinates from the IZA database are only estimates of a pure silica unit cell.[16, 17] To refine the IZA bulk structures, each bulk unit cell was relaxed with the ReaxFF force field using the LAMMPS Molecular Dynamics package.[32, 33] This force field was chosen because it allows for the effective relaxation of complex surface terminations and is parameterized to accurately account for bond breaking and formation events necessary for surface energy calculations.[32, 34] Each cell was relaxed for 40 loops of conjugate gradient descent energy minimization with an energy tolerance of 10^{-8} and a force tolerance of 10^{-10} kcal/mole-Å. The effect of relaxation on several cells is shown in **Table A.2**. All calculations generating surfaces started with bulk unit cells that had been optimized as just described. Generation of surfaces with arbitrary Miller indices was then accomplished with the Pymatgen software package.[35] Pymatgen was first used to reduce the full set of {*hkl*} Miller indices to a minimal set of symmetry-equivalent (*hkl*) Miller indices using the space group symmetry of the bulk material.[35] For each (*hkl*) index of this kind, a Lattice Reoriented Unit Cell (LRUC) was then generated such that the original Miller index of interest is oriented along the *c* axis of the LRUC.[35] In principle, any termination of a material perpendicular to the *c* axis of an LRUC defines an (*hkl*) surface of the material. However, termination of zeolite surfaces requires breaking of chemical bonds, so appropriate choices must be made regarding the location of these terminations to generate chemically meaningful surfaces. The general principle adopted is that surfaces should be terminated to minimize the number of broken bonds relative to other possible

terminations.[26] In all cases we assume that broken bonds are -OH terminated in the final slab.[36]

Surfaces were generated from LRUCs in two phases: primary surface generation and targeted removal. In primary surface generation, a plane parallel to the reoriented surface is placed at a Si atom, and all Si atoms above this plane are removed. **Figure 2.1(a)** shows one of the many possible examples of a primary surface for the (110) LRUC of MFI. This process was repeated for every Si with unique coordinates along the *c* axis in the LRUC. For the (110) direction in MFI, this process generates 96 different primary surface terminations.

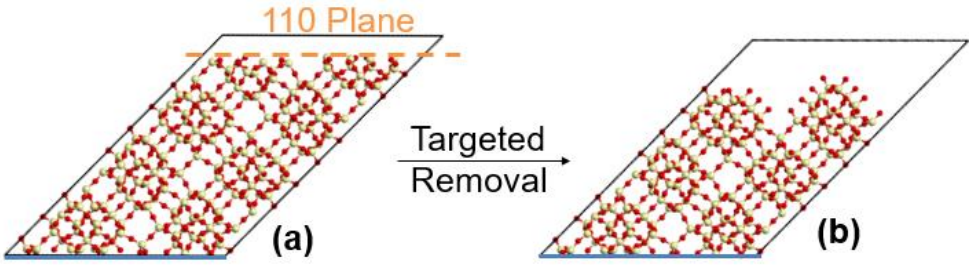

Figure 2.1. (a) A primary surface of the MFI (110) LRUC. (b) A surface obtained after several targeted corrections with only Q^3 Si on the surface. The blue line at the bottom of the LRUC represents a boundary with the bulk structure.

Each round of targeted removal proceeds in three steps. In step 1, the number of bonds connecting to each Si on the surface is counted, and the Si is labeled as Q^n, where n is the number of Si connected to the labeled Si via an O atom. In step 2, all Q^2, Q^1, and Q^0 Si are removed from a candidate surface structure with the aim of finding a surface structure containing only Q^3 Si. An all Q^3 surface was chosen as a target because Q^3 atoms have the least number of broken bonds and would therefore be expected to minimize the number of broken bonds on the surface. The removal of Q^2 Si breaks two bonds, and gets rid of two broken bonds, so its effect on the total number of broken bonds on a surface is

neutral. The removal of a Q^1 atom breaks one bond and removes three broken bonds. Therefore, in step 3, all Q^1 and Q^0 Si are removed to increase the number and diversity of surfaces that fall within the minimum bond broken tolerance. At the completion of step 3, the surface is saved as a potential surface and sent to another round of targeted removal. The removal of $Q^{<3}$ Si can sometimes convert a Q^3 Si to $Q^{<3}$ Si, so the procedure is repeated 9 times for each primary surface, generating a total of 10 surfaces. The process terminates once an all Q^3 surface is found but was not continued past 9 iterations. **Figure 2.1(b)** shows an example of an MFI (110) surface generated in this way. On MFI (110), the 96 primary surfaces resulted in 193 corrected surfaces (not 960 since many were identical), and 55% of primary surfaces terminated in an all Q^3 surface after an average of 3.6 removal steps. An analysis in the Appendix shows that 9 iterations were sufficient to find at least 1 all Q^3 surface for each MFI Miller index examined.

Our algorithm finds the minimum number of broken bonds by heuristically relying on the number of surfaces generated. A comparison of our method to that of Witman et al. shows that our method succeeds in finding the minimum number of broken bonds in almost all instances.[26] Specifically, out of the 108 Miller indices used to create the 8 Wulff constructions in **Figures 2.9** and **2.10**, only one Miller index, MER (212), did not possess the minimum number of broken bonds. For this specific surface, our algorithm found 22 broken bonds to be the minimum while Witman et al. found 20 broken bonds to be the minimum.[26] We view a success rate of finding the minimum bond count of more than 99% to be adequate for the creation of our database.

Figure 2.2 illustrates the formation of a surface that can terminate the upper part of a slab. In a nanosheet, the lower part of a slab will also require a surface termination, so

primary surfaces are generated in an identical manner with atoms being removed below the plane instead of above. Targeted removal is then used to refine the surface in the same way described previously. The end result is a set of lower surfaces that can terminate the bottom end of a slab. For MFI (110), the 96 primary surfaces produced 180 such corrected surfaces.

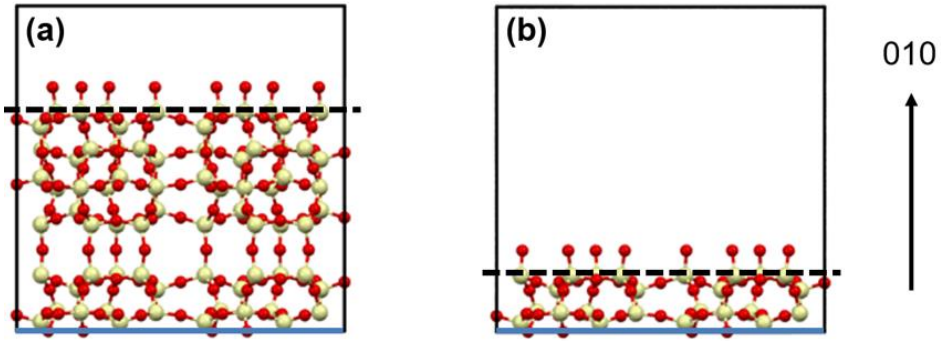

Figure 2.2. Two MFI (010) surface cells showing surfaces from the same surface symmetry family at fractional coordinates of (a) 0.17 and (b) 0.67 along the *b* axis. The dashed line represents the average surface Si positions and the blue line represents the boundary with the bulk structure.

After surface generation, surfaces were analyzed to determine their total broken bond count. For each Miller index of a specific bulk structure, the number of broken bonds on all surfaces was counted and the minimum noted. Only surfaces within 130% of the minimum number of broken bonds for each Miller index were retained for further use. The tolerance of 130% was chosen because the surfaces with the lowest broken bond count are not always those with the lowest surface energy (**Figure A.1**). For MFI (110), broken bond screening retained 57 upper surfaces and 48 lower surfaces. Among the set of surfaces just described, the surface Si (Q^3 or Q^m Si) on some surfaces exhibited symmetry relationships to the surface Si on other surfaces. This is not surprising given the symmetry operations that define the atomic coordinates in zeolite unit cells. For example, in the MFI unit cell, the Si atoms at fractional coordinates of 0.67 along the *b* axis are related to the Si atoms at

0.17 along the *b* axis by a glide plane (**Figure A.2**). Upon the formation of MFI (010) surfaces, two surfaces appear related by this symmetry. Identifying symmetry-related surfaces has several advantages. Most obviously, the total number of distinct surfaces can be reduced. A more subtle advantage is that slabs can be generated with symmetry-related top and bottom surfaces, which simplifies the interpretation of surface energies. We return to this point later. A radial distribution function (RDF) was used to develop a fingerprint for each upper and lower surface (**Figure A.3**). Surfaces with the same fingerprint were grouped into a surface symmetry family. For MFI (110), the result was 28 lower surface families with an average of 1.7 members, and 37 upper surface families with an average of 1.5 members. In addition, 28 of the upper surface symmetry families were matched with each of the lower surface symmetry families. Grouping by surface symmetry family allowed generation of unique slabs with identical upper and lower surfaces.

2.2.2 Slab Generation

The methods above generated zeolitic surfaces, but additional operations are needed to form 2D nanosheets. Specifically, an "upper" and "lower" surface must be combined with the appropriate connecting structure to generate a complete 2D sheet, or slab. This process varies depending on the slab height and is illustrated schematically in **Figure 2.3**. For a one-unit-cell slab, the upper and lower surface cells are combined such that any atom missing in either surface cell is also missing in the final slab, as shown in **Figure 2.3(a)**. For a two-unit-cell slab, the upper and lower surface cells are joined together as shown in **Figure 2.3(b)**. Slabs of height $n > 2$ unit cells are assembled by adding n-2 bulk LRUCs between the upper and lower surfaces; **Figure 2.3(c)** shows an example of adding 1 LRUC to form a 3 unit cell slab. Because all the structures used in these operations

were derived from optimized bulk unit cell structures, no artificial stresses due to structural mismatches occur at boundaries inside the nanosheets. After the formation of each slab, H atoms were added 0.9 Å above the surface O to form chemically stable surface terminations as shown in **Figure 2.3(d,e)**.[37]

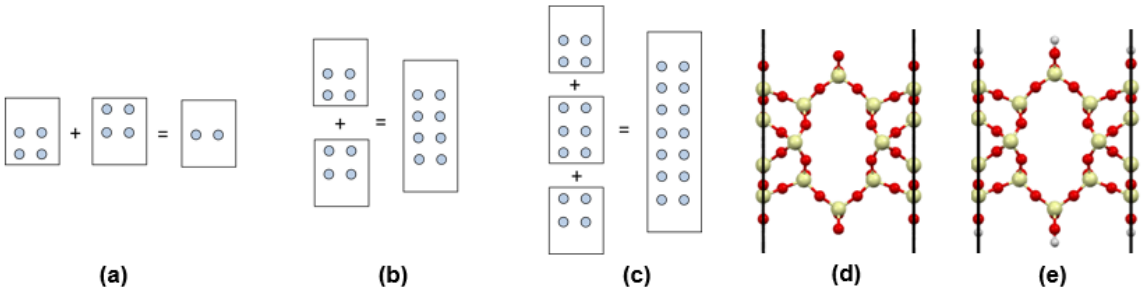

Figure 2.3. (a) A one unit cell slab formed from an LRUC by the elimination of atoms that are not present in either the upper or lower unit cell. (b) A two unit cell slab formed by the combination of an upper and a lower unit cell. (c) A three unit cell slab formed by the combination of an upper unit cell, an LRUC bulk, and a lower unit cell. (d) A one unit cell EZT (001) slab after formation from an upper and a lower surface. (e) The EZT (001) slab after capping the unbonded O with H to form silanol groups.

The goal of the database is to facilitate simulations with both thin and thick structures. Structures with thicknesses in the nm range, such as nanosheets synthesized with modified structure-directing agents,[5] are easier to directly simulate than larger, micron sized structures, such as 3D crystal cross-sections. In addition to defining the thickness of a zeolitic slab in a simulation, a choice must be made in such simulations between using a flexible or rigid framework. Using a flexible framework uses more computational resources, but in cases where adsorbates are similar in size to the zeolite's pores, flexibility may be crucial in quantitatively predicting molecular diffusivities.[38, 39] These observations suggest it would be helpful to have the option of using rigid frameworks to simulate thicker slabs but that this option would be less necessary in thinner nanosheets. Motivated by this reasoning, two distinct workflows were employed to create two separate databases. The methods described in section 2 generated a comprehensive set of surface terminations, with

surfaces related by symmetry operations identified as symmetry families. Starting with each surface symmetry family, the first workflow created a database of nanosheets with a set height and unrelaxed surfaces, while the second workflow created a database of slabs with arbitrary heights and relaxed surfaces as shown in **Figure 2.4**.

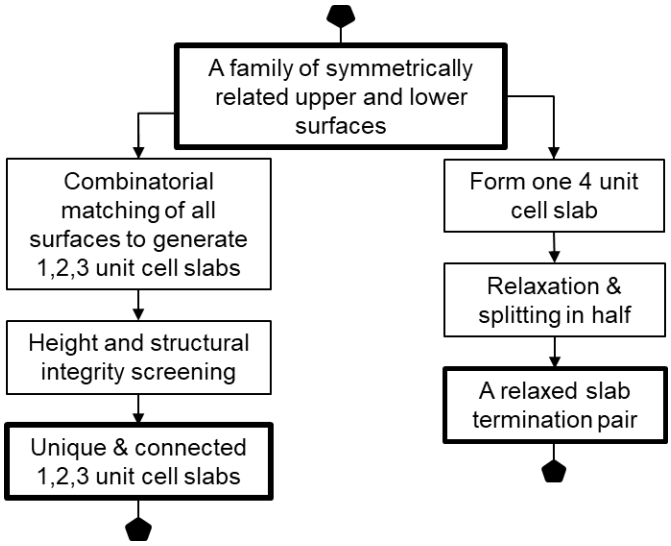

Figure 2.4. Schematic illustration of methods used to generate a database of thin zeolitic slabs of specified thicknesses (left) and nanosheets that can be used to generate slabs of arbitrary thicknesses (right).

In the first workflow, slabs were formed separately as 1, 2, and 3 unit cell structures as shown in **Figure 2.3**. For each slab thickness, an initial set of slabs was formed by a combinatorial matching of all upper surfaces with all lower surfaces from the same surface symmetry family. The initial set of slabs was reduced so each slab was unique as illustrated in **Figure 2.5**. In **Figure 2.5(b)**, the slabs u(1/4)-l(3/4) and u(3/4)-l(1/4) are unique while u(3/4)-l(3/4) and u(1/4)-l(1/4) are identical, so only one of the latter two slabs is retained in the database. Some slabs with very small heights were excluded from the database because they were composed of disconnected clusters of atoms. An example is shown in **Figure A.4**. This workflow produced a database of unique slabs with unrelaxed surfaces that had heights of 1, 2, and 3 unit cells.

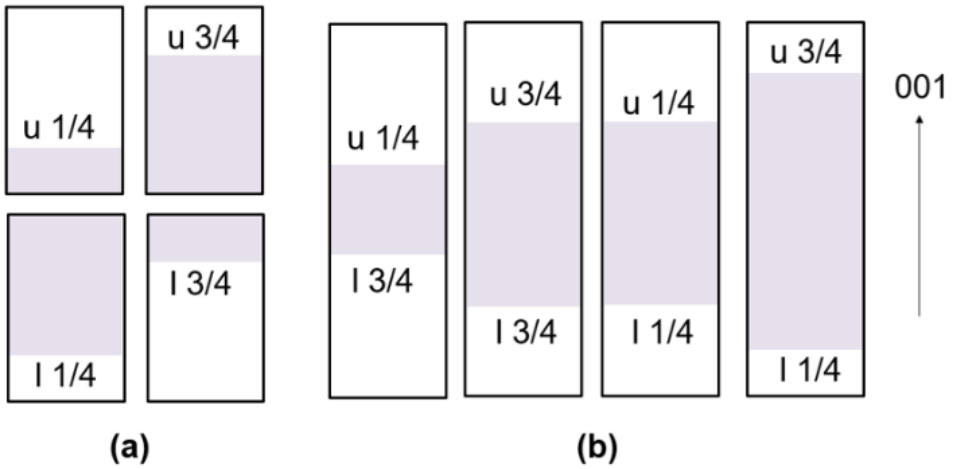

Figure 2.5. (a) A set of upper and lower surfaces belonging to the same surface symmetry family. Upper surfaces are denoted by a "u(x)", and lower surfaces are denoted by an "l(x)" where x is the fractional coordinate of surface on the c axis of the unit cell. (b) A family of two unit cell slabs formed from the surfaces. Note that there are only three unique slabs because the middle two are identical in height and surface.

The second workflow created slab terminations with relaxed surfaces that can be assembled into a slab of any height. This occurred in three phases: assembly, relaxation, and disassembly, as illustrated in **Figure 2.6**. During assembly, the upper and lower surfaces are combined with 2 or more LRUCs to form a slab with 4 or more unit cells as shown in **Figure 2.6(b)**. The outer layers of the slab (**Figure A.5**) were then relaxed with LAMMPS using the ReaxFF force field with one loop of conjugate gradient descent energy minimization with an energy tolerance of 10^{-8}, a force tolerance of 10^{-10} kcal/mole-Å, and fixed cell parameters.[32, 33] We attempted to use simulated annealing before conjugate gradient descent to better explore energy space, but that strategy was discarded because in some instances it caused the breakup of the structure at the surface (**Figure A.6**). During relaxation with the ReaxFF force field, about 1.4% of surfaces incurred reactions that separated the H from the silanol group or the OH group from the Si. Such surfaces were discarded so that all generated surfaces could be described by force fields that assume

tetrahedrally coordinated Si atoms terminated with complete silanol groups.[40-42] An additional 1.9% were rejected due to memory requirements or similar computational errors. After relaxation, the slab was split into a top and bottom slab termination pair as shown in **Figure 2.6(c)**. The two sections can be added to LRUCs to form a slab of any height. The relaxed surfaces often display hydrogen bonding between the H of one silanol group and the O of a neighboring silanol group,[43] so they are representative of real surfaces which are known to exhibit such bonding.[44] An example is shown in **Figures 2.6(d,e)**.

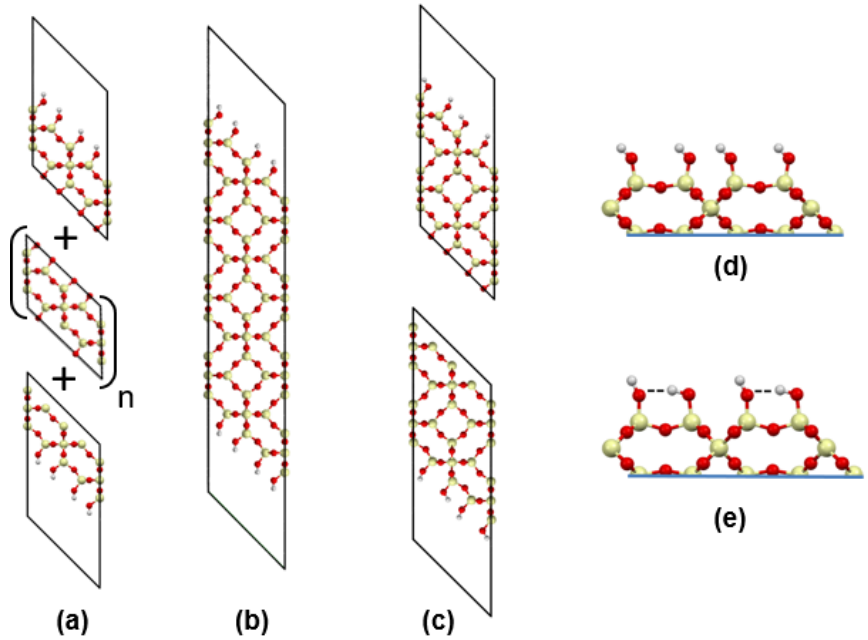

Figure 2.6. (a) The upper and lower surface unit cells of an SOD (110) symmetry family are combined with *n* LRUCs to form a slab with an identical top and bottom surface. (b) The resulting slab is relaxed with molecular dynamics and split into the (c) top and bottom slab termination pairs. (d) The surface of SOD (110) before relaxation shows the H atoms in their initial position. (e) After relaxation, H bonds (dashed lines) are observed between the H of one silanol group and the O of another silanol group. The blue line at the bottom of (d) and (e) represents a boundary with the bulk structure.

The final slab database contains 3,694 LRUCs, 152,992 slab termination pairs, and 651,850 slabs. Directions to download a zipped file containing all structures and other

documentation are found at https://pubs.acs.org/doi/10.1021/acs.chemmater.8b03290.[45] **Figure 2.7** illustrates the types of structures in the database for each Miller index. **Figure 2.7(a)** shows a CAS (001) slab termination pair along with the CAS (001) LRUC. The pair of upper and lower surfaces have been relaxed as described above and can be stacked around any number of LRUCs to make a slab with any height of interest. This approach is well suited for simulations on large structures where framework flexibility is neglected. **Figure 2.7(b)** shows CAS (001) slabs of varying heights. These slabs do not have relaxed surfaces and are intended for simulations in which framework flexibility would be included. They are meant to resemble the nanosheets obtained experimentally using modified structure-directing agents.[5]

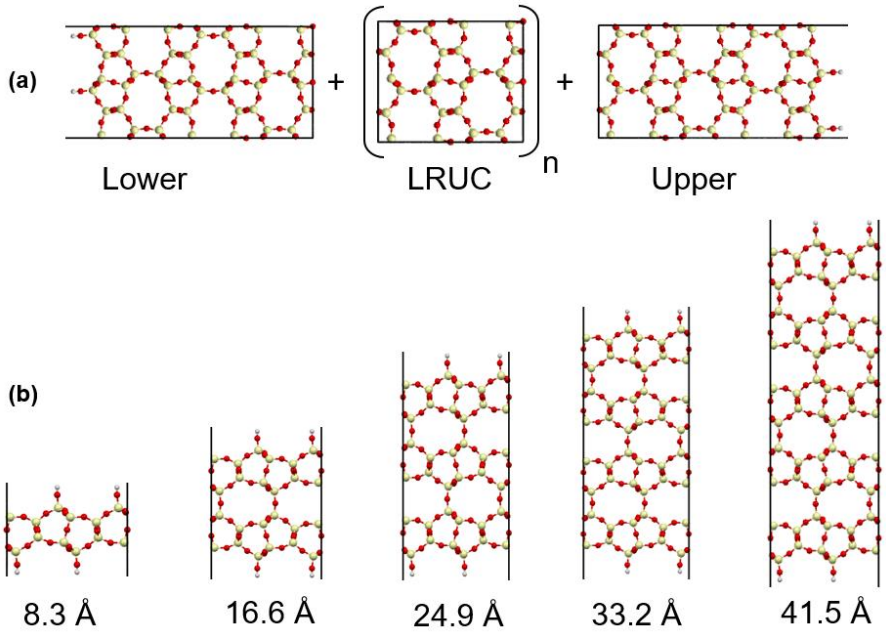

Figure 2.7. (a) A slab termination pair with a relaxed surface and the LRUC for CAS (001). (b) CAS (001) Slabs with set height and unrelaxed surfaces.

Figure 2.8 compares known nanosheets from previous experimental reports and their slab counterparts from the database. The experimental structures were obtained from

Rietveld-type refinements of XRD patterns, usually of zeolite layer precursors.[46-56] Two exceptions to this were IPC-1 and MFI, for which no refined structures could be found. The IPC-1 structure displayed was derived from a comparison of XRD pattern peaks before and after calcination.[57, 58] For MFI, an SEM image was used. [5]

The refined precursor structures usually contained structure directing agent cations which were edited out of the images in **Figure 2.8** for clarity. The slabs were chosen by visually comparing slabs in the database to cross-sectional images of the refined structures. The close agreement between the experimental data and the slabs is an indication that the procedures we used yield physically meaningful results. Though the resemblance was close overall, some nanosheets seemed to deviate more from their slab counterpart than others. Most notably, PKU-22 appears less atomically dense in the center of the structure. Experimentally, PKU-22 contains F- anions (cyan) bonded to Ge T-sites,[46] so this is likely why it looks slightly dissimilar from the all-silica nanosheet in our database. For MFI, it is notable that the thickness of the silica section of the SEM image (2 nm) and the database slab with the lowest number of broken bonds on the surface (2.2 nm) were roughly equivalent.[5] The difference in heights could be due the difficulty of identifying the exact termination point of the MFI silica layer in the SEM image.

The only other extensive 2D zeolite database to our knowledge is that of Witman et al.[26] That database only includes 3,682 slabs, all with surfaces that minimize the number of broken bonds and are more than 30 Å thick.[26] For example, the Witman et al. CAS (001) slab is slightly taller than the 41.5 Å slab in **Figure 2.7(b)** and far thicker than the CAS nanosheet in **Figure 2.8**. A key advantage of the present database is that it has structures

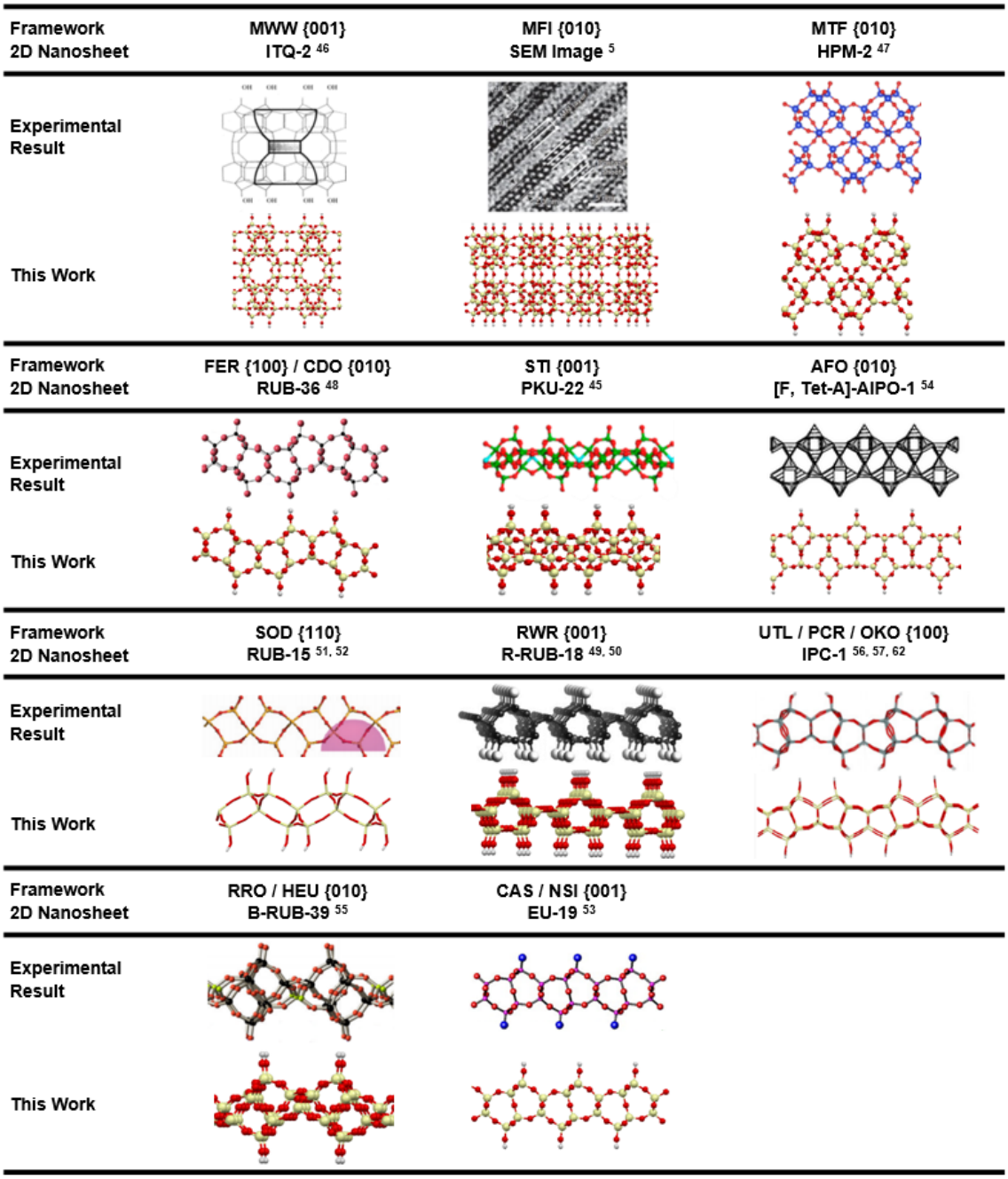

Figure 2.8. A comparison of experimentally obtained nanosheets with their database counterparts. The MFI SEM image was adapted with permission from Choi et al. (2009). Copyright 2009 Nature Springer.[5] R-RUB-18 was adapted with permission from Marler et al. (2005). Copyright 2005 Elsevier.[50] IPC-1 was adapted with permission from Grajciar et al. (2013). Copyright 2013 Elsevier.[56] EU-19 was adapted with permission from Marler et al. (2006). Copyright 2006 Elsevier.[53] B-RUB-39 was adapted with permission from Grünewald-Lüke et al. (2012). Copyright 2012 Elsevier.[55] [F, Tet-A]-AlPO-1 was adapted with permission from Wheatley and Morris (2006). Copyright 2006 Royal Society of Chemistry.[54]

representative of nanosheets of variable height. In addition, Witman et al. limited their attention to only those surfaces with the minimum number of broken bonds, hindering the ability to consider the effects of different surfaces with the same Miller index. As noted in **Figure A.1**, the surface with the minimum number of broken bonds does not always result in the surface with the lowest surface energy. We note, however, that the graph theory method of Witman et al. could readily be augmented to produce surfaces with a higher broken bond tolerance.[26]

2.3 Wulff Constructions

2.3.1 Crystal Habit Prediction Method

One immediate use of our database is to predict the equilibrium crystal habit of zeolite crystals. Here we do this using the Wulff construction, which minimizes the surface energy of a crystal.[59] Crystal habit can of course be influenced by the kinetics of crystal growth, but modeling of this situation must incorporate details of nucleation and growth that are beyond the scope of our work. While work by Anderson et al. has shown that simulation of kinetically-controlled zeolite crystal growth is possible,[60] it is not feasible to apply these methods to a broad range of materials and growth conditions. We therefore focus here on using the Wulff construction to provide the first comprehensive description of equilibrium zeolite crystal habits.

The surface energy of an -OH terminated zeolite surface is a measure of the thermodynamic favorability of the bulk relative to the surface and is defined as:[61]

$$\gamma_{Reaxff} = \frac{1}{2A}(E_{slab} - r * E_{bulk} - n * \mu_{water}) \quad (2.1)$$

where γ is the surface energy, A is the surface area, E_{slab} is the minimized energy of the nanosheet, r the number of Si atoms in the slab divided by the number of Si atoms in the bulk, E_{bulk} is the minimized energy of the bulk, n is the number of water molecules added to terminate the structure, and μ_{water} is the chemical potential of liquid water. We used the chemical potential of water at 0 K, found by subtracting the condensation energy at 100 ˚C (373.15 K) from the minimized energy of a gaseous water molecule.[62] Estimating the chemical potential by simulating bulk liquid water using ReaxFF gave a very similar value. Minimized energies for each surface were obtained from the relaxed slab prior to splitting slabs into top and bottom terminations. Because we defined slabs in which the upper and lower surfaces were related by symmetry, the surface energy can be unambiguously assigned to each surface, unlike the situation that arises when the top and bottom of a slab are not identical. The minimized energy for gaseous water was obtained from relaxation of a single water molecule in a large computational volume with ReaxFF in LAMMPS.[32, 33] It is important to note that the use of a force field such as ReaxFF that allows for bond formation and breaking is critical to computing the surface energy of these surfaces. Simpler force fields such as the Hill-Sauer force field allow the simulation of -OH terminated zeolites,[41] but cannot be used to self-consistently compare the relative energy required to hydrate a variety of surfaces.

Since the number of broken bonds has a large impact on surface energy, surface energy can also be estimated by dividing the number of broken bonds by the surface area:[26]

$$\gamma_{estimate} = \frac{N_{Broken\ Bonds}}{2A} \tag{2.2}$$

The Pymatgen software package was used to generate the Wulff constructions for each material.[35] It took as input a list of Miller indices and their respective surface energies for all Miller indices with MMI < 3. Two sets of Wulff constructions were generated, one using γ_{Reaxff} and one using $\gamma_{estimate}$. For both cases, the surface energy used to represent a Miller index was the minimum surface energy calculated amongst all surfaces on that Miller index. The resulting Wulff shapes for each zeolite are available for download using the link in shown on the page https://pubs.acs.org/doi/10.1021/acs.chemmater.8b03290.[45] Further information about these shapes is given in the Appendix.

2.3.2 Crystal Habit Analysis

Several of the Wulff constructions obtained from our calculations are compared to SEM images of zeolite crystals from previous reports in **Figures 2.9** and **2.10**. The zeolites shown in these figures exhibited a range of crystal habits. For each framework, an SEM image of a single crystal, a Wulff shape based on $\gamma_{estimate}$, and a Wulff shape based on γ_{Reaxff} are shown respectively. Each Wulff shape also has a legend which contains the surface area percentage occupied by each Miller index. The results were sorted between **Figures 2.9** and **2.10** depending on the level of resemblance between the experimentally observed crystal and the predicted Wulff shapes. If the Miller indices that are dominant on the experimentally reported crystal are also dominant on one of the two Wulff constructions, the framework is displayed in **Figure 2.9**. If Miller indices dominant on the experimentally reported crystal are not dominant on either Wulff construction, the framework is displayed in **Figure 2.10**. We reiterate that the Wulff constructions included all Miller index surfaces with MMI < 3. Frequently, only a subset of the surfaces considered

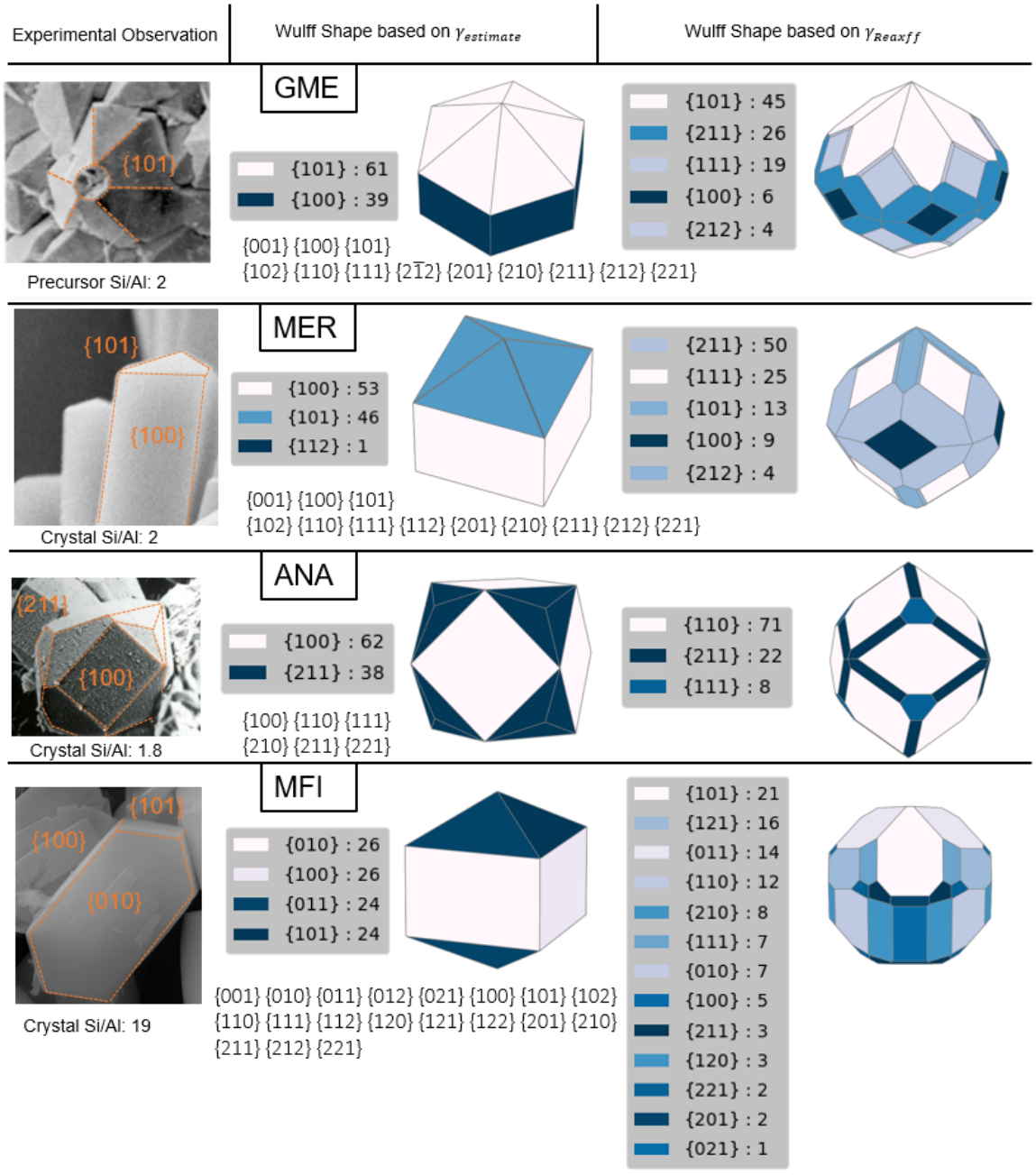

Figure 2.9. For each framework, an SEM image (left), a $\gamma_{estimate}$ Wulff shape (center), and a γ_{Reaxff} Wulff shape (right) are shown. The Wulff shape legends show the surface area (%) occupied by each Miller index. The Miller indices used to generate both Wulff constructions are listed below the Wulff shapes. GME was adapted with permission from Ghobarkar et al. (2001). Copyright 2001 John Wiley and Sons. [63] MER was adapted with permission from Jin et al. (2014). Copyright 2014 Elsevier. [64] ANA was adapted with permission from Ghobarkar et al. (1999). Copyright 1999 Elsevier. [65] MFI was adapted from Qin et al. Copyright 2013 American Chemical Society. [66]

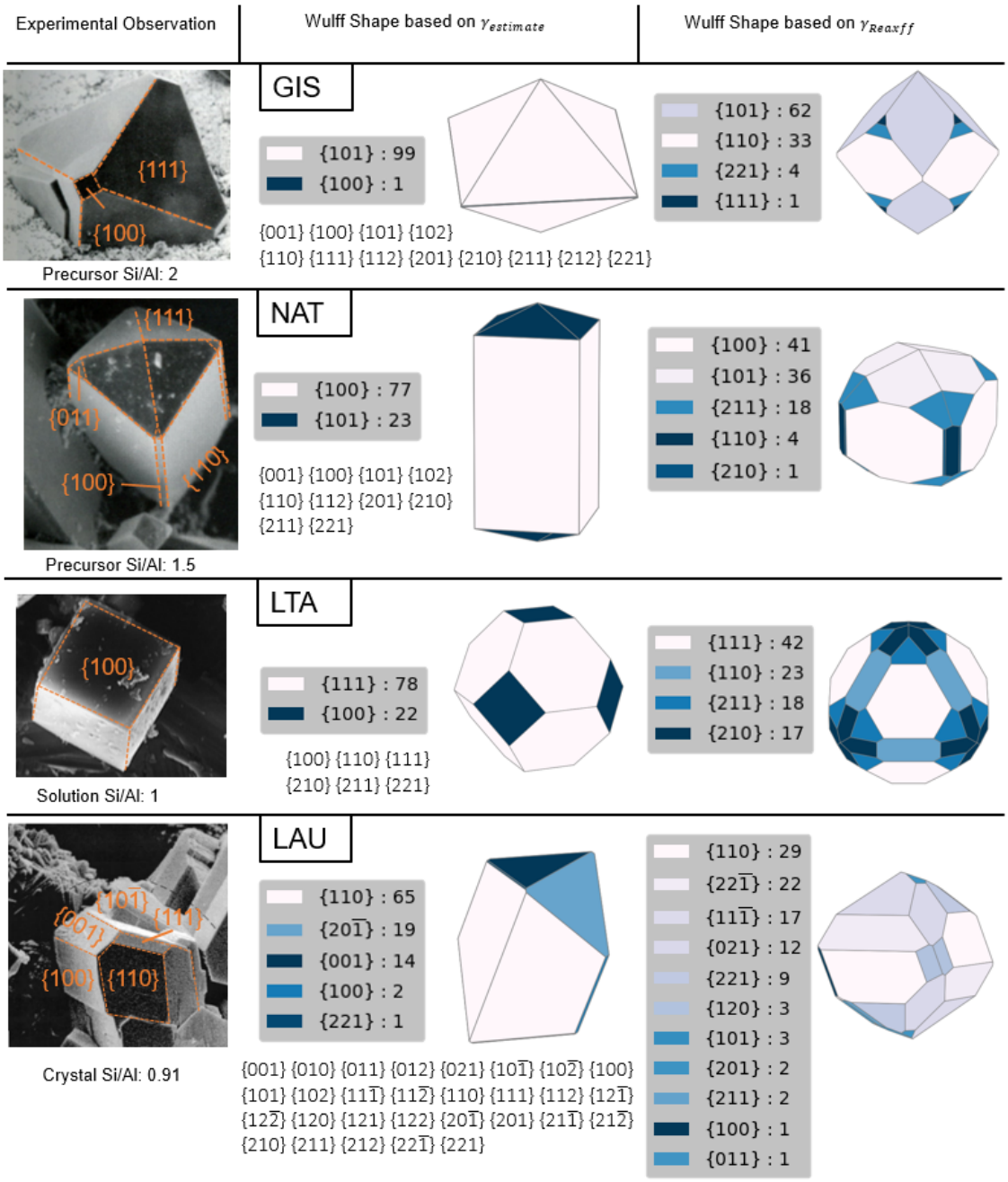

Figure 2.10. For each framework, an SEM image (left), a $\gamma_{estimate}$ Wulff shape (center), and a γ_{Reaxff} Wulff shape (right) are shown. The Wulff shape legends show the surface area (%) occupied by each Miller index. The Miller indices used to generate both Wulff constructions are listed below the Wulff shapes. GIS was adapted with permission from Ghobarkar et al. (1999). Copyright 1999 Elsevier.[67] NAT was adapted with permission from Ghobarkar et al. (2003). Copyright 2003 Springer Nature.[68] LTA was adapted with permission from Basaldella et al. (1998). Copyright 1998 Elsevier.[69] LAU was adapted with permission from Ghobarkar et al. (1998). Copyright 1998 Elsevier.[70]

are predicted to actually be expressed on the crystal habit. For example, our calculations for ANA included the {100}, {110}, {111}, {210}, {211} and {221} surfaces, but only the {100} and {211} surfaces appear on the Wulff shape generated using $\gamma_{estimate}$. Similarly, the Wulff construction for NAT includes the {001}, {100}, {101}, {102}, {110}, {112}, {201}, {210}, {211} and {221} surfaces, but only the {100} and {101} surfaces appear on the Wulff shape from $\gamma_{estimate}$.

One observation from **Figures 2.9** and **2.10** is that the Wulff shapes based on $\gamma_{estimate}$ resembled the SEM images more than Wulff shapes based on γ_{Reaxff}. In **Figure 2.9**, the GME, MER, ANA, and MFI Wulff shapes based on $\gamma_{estimate}$ are similar, although not identical to the experimental images. In **Figure 2.10**, the GIS and NAT Wulff shapes based on $\gamma_{estimate}$ show resemblance to the experimentally reported crystals while those of LTA and ABW do not, so it may seem at first glance that GIS and NAT should be in **Figure 2.9**. Closer inspection of GIS shows that while the {111} surface is dominant on the experimentally reported crystal, the {101} surface is dominant on the Wulff shape. A similar scenario is observed in NAT, where the {110} and {111} surfaces dominate the observed crystal while the {100} and {101} Miller index groups dominate the Wulff shape. Finally, as noted earlier, our algorithm did not find the surface with the absolute minimum number of cut bonds for MER {212}. When we rebuilt the Wulff construction based on $\gamma_{estimate}$ using 20 bonds broken for the {212} Miller index (the correct number of minimum bonds as identified by Witman et. al.[26]), instead of 22 bonds broken, we obtained the same Wulff shape shown in **Figure 2.9**; the {212} surface did not appear.

A second observation from **Figures 2.9 and 2.10** is that the experimental crystals and Wulff shapes based on $\gamma_{estimate}$ are dominated by lower Miller indices (ex. {100},

{101}) while those based on γ_{Reaxff} exhibit many high Miller index surfaces (ex. {212}, {210}). We believe this to be because our surfaces are relaxed in vacuum rather than in water. Experimentally, surface silanol groups form hydrogen bonds with water.[44] Since this cannot occur in our vacuum simulations, surface silanol groups form hydrogen bonds with themselves as shown in **Figure 2.6(d)**. Therefore, the surfaces that form more hydrogen bonds are likely to obtain lower surface energies. Incidentally, the LRUC of high Miller index surfaces are often non-orthogonal, so H atoms (which are located vertically above the O in orthogonal unit cells as seen in **Figure 2.3(e)**) are located diagonally above the O in non-orthogonal unit cells as seen in **Figure 2.6(d)**. The location of H atoms in high Miller index unit cells facilitates the formation of hydrogen bonds and therefore lowers the surface energy of the high Miller index surfaces without the corresponding decrease in surface energy that would have occurred in lower Miller index unit cells due to interactions with water.

The subtleties associated with comparing our Wulff shapes with experimental results are highlighted by previous work by Gren et al., who simulated siliceous and aluminosilicate LTA surfaces.[62] They found that the presence of Al stabilizes the {100} surface relative to the {111} surface, and that this trend is further exacerbated by the presence of liquid water. The resulting pure silica crystal was rounded while their Si/Al=1 crystal was cubic.[62] Therefore, their predicted Si/Al=1 crystal morphology resembles that of most experimental crystals.[69, 71-74] Although the surface energies of our siliceous slabs give different relative surface energies than those obtained by Gren et al. for aluminosilicates, the structure of the low energy surfaces found by Gren et al. and the surfaces from our calculations are very similar (see **Figure A.7**). The experimental data for

the materials shown in **Figures 2.9** and **2.10** are all aluminosilicates, but those in **Figure 2.9** generally have a higher Si:Al ratio than those in **Figure 2.10**. The Si:Al ratios refer to either the precursor, solution, or crystal Si:Al ratios. The precursor Si:Al ratio refers to the composition of glass which was melted and quenched with water during hydrothermal synthesis to form the final crystal.[63] The LAU crystal's 0.9 Si:Al ratio is likely less than one solely due to the elemental analysis' accuracy of 10%.[70] Since our database only contains materials that are pure silica,, it is not surprising that the zeolites with higher Si:Al ratio bear more resemblance to the known structures.

It is interesting to examine the ability of the calculated surface energies from our database to predict the specific surfaces that appear on the experimentally known nanosheets shown in **Figure 2.8**. For each of the 16 experimentally reported nanosheets, the surface of the framework with the lowest $\gamma_{estimate}$ and γ_{Reaxff} was chosen from the set of all surfaces belonging to that framework as the prediction from our database for the surface that would be observed as a nanosheet. For 13 of the 16 frameworks, the surface defined by both $\gamma_{estimate}$ and γ_{Reaxff} was the same as the experimentally reported material. For 2 of the 13 frameworks, namely UTL and OKO, there were two surfaces (identical in both frameworks because they are formed from the same zeolite layer precursor)[75] with equal $\gamma_{estimate}$values. In these cases, γ_{Reaxff} gives slightly different surface energies and the prediction based on the lowest of these energies is the same as the experimentally reported surface. For the remaining 3 frameworks, MFI, SOD, and RWR, the surface indicated by $\gamma_{estimate}$ differed from that using γ_{Reaxff}. For MFI, the surface indicated by $\gamma_{estimate}$ correctly matches the (010) orientation seen experimentally (noting that the exact termination has not been determined experimentally to date).[5] However, the

MFI surface indicated by γ_{Reaxff} displayed a {101} Miller index. For RWR, the surface indicated by $\gamma_{estimate}$ was seen on the experimentally observed nanosheet while the surface indicated by γ_{Reaxff} was not. SOD is the only structure for which the surface indicated by $\gamma_{estimate}$, a {100} surface, was not seen experimentally, although the {110} surface observed on the nanosheet was indicated by γ_{Reaxff}. The above discussion shows that the surface with the lowest $\gamma_{estimate}$ and γ_{Reaxff} is most likely to be observed experimentally in zeolitic nanosheets. Although this was not the case with the MFI {101} and SOD {100} surfaces predicted by γ_{Reaxff} and $\gamma_{estimate}$ respectively, those surfaces are observed on their framework's bulk crystal habit.[76, 77] The identification of the experimental nanosheet surfaces in most instances by $\gamma_{estimate}$ concurs with Witman's results which assume that the surface with the lowest $\gamma_{estimate}$will be seen on the nanosheet.[26] We combine this information, along with the finding that the γ_{Reaxff} can break a $\gamma_{estimate}$ tie to produce a shortlist (also included in the database) of the 217 most likely zeolite surfaces to be synthesized as a nanosheet.

2.4 Conclusion

We have created a very large database of 2D zeolite nanosheets which can form the basis for systematic studies of the functional properties (e.g., diffusion, adsorption, catalytic) of this rapidly emerging class of nanoporous materials. We first formed surfaces using an algorithm that iteratively removed undercoordinated atoms to find terminations with a low number of broken bonds. The selected surfaces were screened for symmetry and uniqueness and then combined to form slabs. The database currently contains 651,850 2D zeolitic slabs and 152,992 slab termination pairs. The slabs have set thicknesses (1–15

nm) and contain nanosheets with the same thicknesses as those found experimentally. The slab termination pairs can form structures with thicknesses greater than those spanned by the slabs. Our database can therefore be used to study nanosheet properties as a function of thickness and surface structure, a feature that is unique to the current work. We used surface energies obtained using the ReaxFF force field and surface energies obtained from broken bond densities to predict the crystal morphology of zeolite crystals and the surfaces observed on nanosheets. The broken bond density predicted more accurate crystal structures while both metrics were equally favorable at predicting which surfaces are present on a nanosheet.

It is important to note that our 2D zeolite structures are pure silica materials and that our calculated surface energies do not include the solvent effects that are certain to be present during zeolite synthesis. As discussed above, examples are known in which variations in the Si:Al ratio and/or inclusion of solvent effects can alter the relative surface energy ordering of surfaces on zeolites. Despite the complications associated with these effects, we were able to narrow the list of surfaces to those most likely to be synthesizable. We hope that this subset can be used to identify synthesized slabs in a high throughput way, such as the matching of theoretical to experimental XRD patterns. Alternatively, we foresee its use in the screening of structure directing agents to identify those best suited to form a particular slab. Finally, our database of atomically detailed structures will be valuable for molecular simulations of zeolitic nanosheets that aim to understand how the performance of these materials differs from bulk materials.

2.5 References

1. Sholl, D.S. and R.P. Lively, *Seven chemical separations to change the world.* Nature, 2016. **532**(7600): p. 435.

2. Walton, K.S. and D.S. Sholl, *Research Challenges in Avoiding "Showstoppers" in Developing Materials for Large-Scale Energy Applications.* Joule, 2017. **1**(2): p. 208-211.

3. Feng, C., K. Khulbe, T. Matsuura, R. Farnood, and A. Ismail, *Recent progress in zeolite/zeotype membranes.* Journal of Membrane Science and Research, 2015. **1**(2): p. 49-72.

4. Rangnekar, N., N. Mittal, B. Elyassi, J. Caro, and M. Tsapatsis, *Zeolite membranes–a review and comparison with MOFs.* Chemical Society Reviews, 2015. **44**(20): p. 7128-7154.

5. Choi, M., K. Na, J. Kim, Y. Sakamoto, O. Terasaki, and R. Ryoo, *Stable single-unit-cell nanosheets of zeolite MFI as active and long-lived catalysts.* Nature, 2009. **461**(7261): p. 246-249.

6. Luo, H.Y., V.K. Michaelis, S. Hodges, R.G. Griffin, and Y. Román-Leshkov, *One-pot synthesis of MWW zeolite nanosheets using a rationally designed organic structure-directing agent.* Chemical science, 2015. **6**(11): p. 6320-6324.

7. Rangnekar, N., M. Shete, K.V. Agrawal, B. Topuz, P. Kumar, Q. Guo, I. Ismail, A. Alyoubi, S. Basahel, and K. Narasimharao, *2D zeolite coatings: Langmuir–Schaefer deposition of 3 nm thick MFI zeolite nanosheets.* Angewandte Chemie International Edition, 2015. **54**(22): p. 6571-6575.

8. Fasano, M., T. Humplik, A. Bevilacqua, M. Tsapatsis, E. Chiavazzo, E.N. Wang, and P. Asinari, *Interplay between hydrophilicity and surface barriers on water transport in zeolite membranes.* Nature Communications, 2016. **7**: p. 12762.

9. Newsome, D.A. and D.S. Sholl, *Predictive assessment of surface resistances in zeolite membranes using atomically detailed models.* The Journal of Physical Chemistry B, 2005. **109**(15): p. 7237-7244.

10. Newsome, D.A. and D.S. Sholl, *Atomically detailed simulations of surface resistances to transport of CH_4, CF_4, and C_2H_6 through silicalite membranes.* Microporous and Mesoporous Materials, 2008. **107**(3): p. 286-295.

11. Teixeira, A.R., C.-C. Chang, T. Coogan, R. Kendall, W. Fan, and P.J. Dauenhauer, *Dominance of surface barriers in molecular transport through silicalite-1.* The Journal of Physical Chemistry C, 2013. **117**(48): p. 25545-25555.

12. Teixeira, A.R., X. Qi, W.C. Conner, T. Mountziaris, W. Fan, and P.J. Dauenhauer, *2D surface structures in small zeolite MFI crystals.* Chemistry of Materials, 2015. **27**(13): p. 4650-4660.

13. Vattipalli, V., X. Qi, P.J. Dauenhauer, and W. Fan, *Long walks in hierarchical porous materials due to combined surface and configurational diffusion.* Chemistry of Materials, 2016. **28**(21): p. 7852-7863.

14. Tzoulaki, D., W. Schmidt, U. Wilczok, and J. Kärger, *Formation of surface barriers on silicalite-1 crystal fragments by residual water vapour as probed with isobutane by interference microscopy.* Microporous and Mesoporous Materials, 2008. **110**(1): p. 72-76.

15. Li, L., N. Liu, B. McPherson, and R. Lee, *Enhanced water permeation of reverse osmosis through MFI-type zeolite membranes with high aluminum contents.* Industrial & engineering chemistry research, 2007. **46**(5): p. 1584-1589.

16. Baerlocher, C. and L. McCusker, *IZA database of zeolite structures*. 2007.

17. Baerlocher, C., A. Hepp, and W.M. Meier, *DLS-76: A Program for the Simulation of Crystal Structures by Geometric Refinement*. revised ed. 1978: Institute of crystallography and petrography - ETH.

18. Wang, Z., J. Yu, and R. Xu, *Needs and trends in rational synthesis of zeolitic materials.* Chemical Society Reviews, 2012. **41**(5): p. 1729-1741.

19. Treacy, M., S. Rao, and I. Rivin, *A combinatorial method for generating new zeolite frameworks.* R. von Ballmoos, JB Higgins, MMJ Treacy (Eds.), 1992: p. 381-388.

20. Treacy, M., I. Rivin, E. Balkovsky, K. Randall, and M. Foster, *Enumeration of periodic tetrahedral frameworks. II. Polynodal graphs.* Microporous and Mesoporous Materials, 2004. **74**(1): p. 121-132.

21. Corma, A., M.J. Díaz-Cabañas, J.L. Jordá, C. Martínez, and M. Moliner, *High-throughput synthesis and catalytic properties of a molecular sieve with 18-and 10-member rings.* Nature, 2006. **443**(7113): p. 842-845.

22. Jiang, J., J.L. Jorda, M.J. Diaz-Cabanas, J. Yu, and A. Corma, *The Synthesis of an Extra-Large-Pore Zeolite with Double Three-Ring Building Units and a Low Framework Density.* Angewandte Chemie International Edition, 2010. **49**(29): p. 4986-4988.

23. Friedrichs, O.D., A.W. Dress, D.H. Huson, J. Klinowski, and A.L. Mackay, *Systematic enumeration of crystalline networks.* Nature, 1999. **400**(6745): p. 644-647.

24. Pophale, R., P.A. Cheeseman, and M.W. Deem, *A database of new zeolite-like materials.* Physical Chemistry Chemical Physics, 2011. **13**(27): p. 12407-12412.

25. Jamali, S.H., T.J. Vlugt, and L.-C. Lin, *Atomistic understanding of zeolite nanosheets for water desalination.* The Journal of Physical Chemistry C, 2017. **121**(21): p. 11273-11280.

26. Witman, M., S. Ling, P. Boyd, S. Barthel, M. Haranczyk, B. Slater, and B. Smit, *Cutting Materials in Half: A Graph Theory Approach for Generating Crystal Surfaces and Its Prediction of 2D Zeolites.* ACS Central Science, 2018.

27. Habib Ghobarkar, O.S., Yvan Massiani, Philippe Knauth, *The reconstruction of natural zeolites*. 2003: Kluwer Academic Publishers. 146.

28. Gounaris, C.E., C.A. Floudas, and J. Wei, *Rational design of shape selective separation and catalysis—I: Concepts and analysis.* Chemical engineering science, 2006. **61**(24): p. 7933-7948.

29. Gounaris, C.E., J. Wei, and C.A. Floudas, *Rational design of shape selective separation and catalysis—II: Mathematical model and computational studies.* Chemical engineering science, 2006. **61**(24): p. 7949-7962.

30. Haldoupis, E., S. Nair, and D.S. Sholl, *Efficient calculation of diffusion limitations in metal organic framework materials: a tool for identifying materials for kinetic separations.* Journal of the American Chemical Society, 2010. **132**(21): p. 7528-7539.

31. Haldoupis, E., S. Nair, and D.S. Sholl, *Finding MOFs for highly selective CO_2/N_2 adsorption using materials screening based on efficient assignment of atomic point charges.* Journal of the American Chemical Society, 2012. **134**(9): p. 4313-4323.

32. Fogarty, J.C., H.M. Aktulga, A.Y. Grama, A.C. Van Duin, and S.A. Pandit, *A reactive molecular dynamics simulation of the silica-water interface.* The Journal of chemical physics, 2010. **132**(17): p. 174704.

33. Brown, W.M., P. Wang, S.J. Plimpton, and A.N. Tharrington, *Implementing molecular dynamics on hybrid high performance computers–short range forces.* Computer Physics Communications, 2011. **182**(4): p. 898-911.

34. Senftle, T.P., S. Hong, M.M. Islam, S.B. Kylasa, Y. Zheng, Y.K. Shin, C. Junkermeier, R. Engel-Herbert, M.J. Janik, and H.M. Aktulga, *The ReaxFF reactive force-field: development, applications and future directions.* npj Computational Materials, 2016. **2**: p. 15011.

35. Tran, R., Z. Xu, B. Radhakrishnan, D. Winston, W. Sun, K.A. Persson, and S.P. Ong, *Surface energies of elemental crystals.* Scientific Data, 2016. **3**: p. 160080.

36. Lunevich, L., P. Sanciolo, A. Smallridge, and S. Gray, *Silica scale formation and effect of sodium and aluminium ions-29 Si NMR study.* Environmental Science: Water Research & Technology, 2016. **2**(1): p. 174-185.

37. Slater, B., J. Titiloye, F. Higgins, and S. Parker, *Atomistic simulation of zeolite surfaces.* Current Opinion in Solid State and Materials Science, 2001. **5**(5): p. 417-424.

38. Verploegh, R.J., S. Nair, and D.S. Sholl, *Temperature and loading-dependent diffusion of light hydrocarbons in ZIF-8 as predicted through fully flexible molecular simulations.* Journal of the American Chemical Society, 2015. **137**(50): p. 15760-15771.

39. Krishna, R. and J.M. Van Baten, *A molecular dynamics investigation of the diffusion characteristics of cavity-type zeolites with 8-ring windows.* Microporous and Mesoporous Materials, 2011. **137**(1): p. 83-91.

40. de Leeuw, N.H., F.M. Higgins, and S.C. Parker, *Modeling the surface structure and stability of α-quartz.* The Journal of Physical Chemistry B, 1999. **103**(8): p. 1270-1277.

41. Hill, J.R. and J. Sauer, *Molecular mechanics potential for silica and zeolite catalysts based on ab initio calculations. 1. Dense and microporous silica.* The Journal of Physical Chemistry, 1994. **98**(4): p. 1238-1244.

42. Sanders, M., M. Leslie, and C. Catlow, *Interatomic potentials for SiO_2.* Journal of the Chemical Society, Chemical Communications, 1984(19): p. 1271-1273.

43. Zang, J., S. Chempath, S. Konduri, S. Nair, and D.S. Sholl, *Flexibility of ordered surface hydroxyls influences the adsorption of molecules in single-walled aluminosilicate nanotubes.* The Journal of Physical Chemistry Letters, 2010. **1**(8): p. 1235-1240.

44. Chuang, I.-S. and G.E. Maciel, *Probing hydrogen bonding and the local environment of silanols on silica surfaces via nuclear spin cross polarization dynamics.* Journal of the American Chemical Society, 1996. **118**(2): p. 401-406.

45. Knio, O., A.J. Medford, S. Nair, and D.S. Sholl, *Database of Computation-Ready 2D Zeolitic Slabs.* Chemistry of Materials, 2018. **31**(2): p. 353-364.

46. Chen, Y., S. Huang, X. Wang, L. Zhang, N. Wu, F. Liao, and Y. Wang, *Synthesis and Characterization of a Layered Silicogermanate PKU-22 and Its Topotactic Condensation to a Three-Dimensional STI-type Zeolite.* Crystal Growth & Design, 2017. **17**(10): p. 5465-5473.

47. Narkhede, V.V. and H. Gies, *Crystal structure of MCM-22 (MWW) and its delaminated zeolite ITQ-2 from high-resolution powder X-ray diffraction data: an analysis using Rietveld technique and atomic pair distribution function.* Chemistry of Materials, 2009. **21**(18): p. 4339-4346.

48. Rojas, A. and M.A. Camblor, *HPM-2, the layered precursor to zeolite MTF.* Chemistry of Materials, 2014. **26**(2): p. 1161-1169.

49. Gies, H., U. Müller, B. Yilmaz, M. Feyen, T. Tatsumi, H. Imai, H. Zhang, B. Xie, F.-S. Xiao, and X. Bao, *Interlayer expansion of the hydrous layer silicate RUB-36 to a functionalized, microporous framework silicate: crystal structure analysis and physical and chemical characterization.* Chemistry of Materials, 2012. **24**(8): p. 1536-1545.

50. Vortmann, S., J. Rius, S. Siegmann, and H. Gies, *Ab initio structure solution from X-ray powder data at moderate resolution: crystal structure of a microporous layer silicate.* The Journal of Physical Chemistry B, 1997. **101**(8): p. 1292-1297.

51. Marler, B., N. Ströter, and H. Gies, *The structure of the new pure silica zeolite RUB-24, $Si_{32}O_{64}$, obtained by topotactic condensation of the intercalated layer silicate RUB-18.* Microporous and mesoporous materials, 2005. **83**(1): p. 201-211.

52. Moteki, T., W. Chaikittisilp, Y. Sakamoto, A. Shimojima, and T. Okubo, *Role of acidic pretreatment of layered silicate RUB-15 in Its topotactic conversion into pure silica sodalite.* Chemistry of Materials, 2011. **23**(15): p. 3564-3570.

53. Oberhagemann, U., P. Bayat, B. Marler, H. Gies, and J. Rius, *A Layer Silicate: Synthesis and Structure of the Zeolite Precursor RUB-15—$[N(CH_3)_4]_8[Si_{24}O_{52}(OH)_4]\cdot 20\ H_2O$.* Angewandte Chemie International Edition in English, 1996. **35**(23-24): p. 2869-2872.

54. Marler, B., M. Camblor, and H. Gies, *The disordered structure of silica zeolite EU-20b, obtained by topotactic condensation of the piperazinium containing layer silicate EU-19.* Microporous and mesoporous materials, 2006. **90**(1): p. 87-101.

55. Wheatley, P.S. and R.E. Morris, *Calcination of a layered aluminofluorophosphate precursor to form the zeolitic AFO framework.* Journal of Materials Chemistry, 2006. **16**(11): p. 1035-1037.

56. Grünewald-Lüke, A., H. Gies, U. Müller, B. Yilmaz, H. Imai, T. Tatsumi, B. Xie, F.-S. Xiao, X. Bao, and W. Zhang, *Layered precursors for new zeolitic materials: Synthesis and characterization of B-RUB-39 and its condensation product B-RUB-41.* Microporous and Mesoporous Materials, 2012. **147**(1): p. 102-109.

57. Grajciar, L., O. Bludský, W.J. Roth, and P. Nachtigall, *Theoretical investigation of layered zeolite frameworks: Interaction between IPC-1P layers derived from zeolite UTL.* Catalysis today, 2013. **204**: p. 15-21.

58. Roth, W.J., O.V. Shvets, M. Shamzhy, P. Chlubná, M. Kubů, P. Nachtigall, and J.i. Čejka, *Postsynthesis transformation of three-dimensional framework into a lamellar zeolite with modifiable architecture.* Journal of the American Chemical Society, 2011. **133**(16): p. 6130-6133.

59. Ringe, E., R. Van Duyne, and L. Marks, *Wulff construction for alloy nanoparticles.* Nano Letters, 2011. **11**(8): p. 3399-3403.

60. Anderson, M.W., J.T. Gebbie-Rayet, A.R. Hill, N. Farida, M.P. Attfield, P. Cubillas, V.A. Blatov, D.M. Proserpio, D. Akporiaye, and B. Arstad, *Predicting crystal growth via a unified kinetic three-dimensional partition model.* Nature, 2017. **544**(7651): p. 456.

61. De Leeuw, N., S. Parker, C. Catlow, and G. Price, *Modelling the effect of water on the surface structure and stability of forsterite.* Physics and Chemistry of Minerals, 2000. **27**(5): p. 332-341.

62. Gren, W., S.C. Parker, B. Slater, and D.W. Lewis, *Structure of zeolite A (LTA) surfaces and the zeolite A/water interface.* The Journal of Physical Chemistry C, 2010. **114**(21): p. 9739-9747.

63. Ghobarkar, H., O. Schäf, and P. Knauth, *Zeolite Synthesis by the High-Pressure Hydrothermal Method: Synthesis of Natural 6-Ring Zeolites with Different Void Systems.* Angewandte Chemie International Edition, 2001. **40**(20): p. 3831-3833.

64. Jin, N., C. Meng, and J. Hou, *Preparation and characterization of merlinoite for potassium extraction from seawater.* Journal of Industrial and Engineering Chemistry, 2014. **20**(4): p. 1227-1230.

65. Ghobarkar, H. and O. Schäf, *Effect of temperature on hydrothermal synthesis of analcime and viséite.* Materials Science and Engineering: B, 1999. **60**(3): p. 163-167.

66. Qin, Z., L. Lakiss, J.-P. Gilson, K. Thomas, J.-M. Goupil, C. Fernandez, and V. Valtchev, *Chemical equilibrium controlled etching of MFI-Type zeolite and its influence on zeolite structure, acidity, and catalytic activity.* Chemistry of Materials, 2013. **25**(14): p. 2759-2766.

67. Ghobarkar, H. and O. Schäf, *Synthesis of gismondine-type zeolites by the hydrothermal method.* Materials research bulletin, 1999. **34**(4): p. 517-525.

68. Ghobarkar, H., O. Schäf, Y. Massiani, and P. Knauth, *The Zeolite Minerals*, in *The Reconstruction of Natural Zeolites*. 2003, Springer US: Boston, MA. p. 42-124.

69. Basaldella, E.I. and J. Tara, *Modification of crystallite morphology during synthesis of LTA zeolite using triethanolamine as additive.* Materials Letters, 1998. **34**(3-6): p. 119-123.

70. Ghobarkar, H. and O. Schäf, *Hydrothermal synthesis of laumontite, a zeolite.* Microporous and mesoporous materials, 1998. **23**(1-2): p. 55-60.

71. Bouizi, Y., J.-L. Paillaud, L. Simon, and V. Valtchev, *Seeded synthesis of very high silica zeolite A.* Chemistry of materials, 2007. **19**(4): p. 652-654.

72. Cubillas, P., J.T. Gebbie, S.M. Stevens, N. Blake, A. Umemura, O. Terasaki, and M.W. Anderson, *Atomic Force Microscopy and High Resolution Scanning*

Electron Microscopy Investigation of Zeolite A Crystal Growth. Part 2: In Presence of Organic Additives. The Journal of Physical Chemistry C, 2014. **118**(40): p. 23092-23099.

73. Kosanović, C., T.A. Jelić, J. Bronić, D. Kralj, and B. Subotić, *Chemically controlled particulate properties of zeolites: Towards the face-less particles of zeolite A. Part 1. Influence of the batch molar ratio $[SiO_2/Al_2O_3]_b$ on the size and shape of zeolite A crystals.* Microporous and mesoporous materials, 2011. **137**(1-3): p. 72-82.

74. Sathupunya, M., E. Gulari, and S. Wongkasemjit, *Na-A (LTA) zeolite synthesis directly from alumatrane and silatrane by sol-gel microwave techniques.* Journal of the European Ceramic Society, 2003. **23**(8): p. 1293-1303.

75. Roth, W.J., P. Nachtigall, R.E. Morris, and J. Cejka, *Two-dimensional zeolites: current status and perspectives.* Chemical reviews, 2014. **114**(9): p. 4807-4837.

76. Zeng, G., C. Chen, D. Li, B. Hou, and Y. Sun, *Exposure of (001) planes and (011) planes in MFI zeolite.* CrystEngComm, 2013. **15**(18): p. 3521-3524.

77. Holden, M.A., P. Cubillas, M.P. Attfield, J.T. Gebbie, and M.W. Anderson, *Growth mechanism of microporous zincophosphate sodalite revealed by in situ atomic force microscopy.* Journal of the American Chemical Society, 2012. **134**(31): p. 13066-13073.

CHAPTER 3. MOLECULAR DYNAMICS INVESTIGATION OF SURFACE RESISTANCES IN ZEOLITE NANOSHEETS*

3.1 Introduction

Mass transfer in zeolites is critical to their performance in catalysis, adsorption, ion-exchange, sensing, and membrane applications.[1] A long standing goal in fabrication of zeolite membranes has been to develop ever-thinner zeolite layers to increase the flux through these membranes.[2] Zeolite membranes that are 500 nm to 3 μm thick can be synthesized by secondary growth on seed crystals.[3, 4] In contrast, several techniques have recently been developed to synthesize zeolite nanosheets that are roughly a unit cell thick.[5] Choi et al. synthesized 2 nm thick MFI zeolite nanosheets using a long-chain structure directing agent (SDA) and found that it exhibited faster catalysis due to rapid diffusion into and out of the sheet.[6] Other 2D synthesis strategies include assembly–disassembly–organisation–reassembly (ADOR)[7] and post-synthesis modification.[5, 8, 9] Significant efforts have been made to synthesize zeolite nanosheets to increase the catalytic activity for molecules whose diffusion into bulk crystals is strongly hindered.[10-17] Zeolite nanosheets have also been used in membranes with varying degrees of structural modification. Jeon et al. used 5 nm thick MFI nanosheets as seed layers for secondary growth resulting in an interconnected zeolite layer, giving p/o-xylene separation factors as large as 2,500.[18] Cao et al. formed a multilayer ZSM-5 hierarchical structure by vapor phase growth of stacked

---

*Contents of this chapter have been submitted for publication as
Knio, O., H. Fang, S.E. Boulfelfel, S. Nair, and D. S. Sholl, ″Molecular Dynamics Investigation of Surface Resistances in Zeolite Nanosheets ″ to The Journal of Physical Chemistry C

nanosheets preloaded with dilute SDAs, achieving promising results for water desalination.[19] Jeong et al. made mixed matrix membranes consisting of 5-10 nm thick AlPO flakes as the selective phase in a polyamide matrix, greatly increasing the CO_2/CH_4 selectivity relative to the polymer alone.[20] The aforementioned membranes require connecting the nanosheets either through silica growth or by a polymer support, but these modifications increase cost. Zhang et al. synthesized a membrane by vacuum suction of MFI nanosheets but did not perform any further chemical or physical alterations.[21] This resulted in a layered, non-hierarchical structure. The membrane achieved a far lower butane isomer selectivity than well intergrown membranes, but it hints that simple fabrication methods could potentially be developed.[21]

Although molecular diffusion in zeolites has been extensively studied, less is known about the surface resistances associated with movement of an adsorbate from a fluid phase into a zeolite or the reverse process.[22-28] A variety of experiments have indicated that surface resistances can be important for zeolite crystals. Wloch studied the effect of a crust layer on n-hexane diffusion through 40 μm ZSM-5 zeolite crystals at 298 K and 0.01 bar.[29] Etching the surface with hydrofluoric acid was found to increase molecular diffusion by two orders of magnitude. Wloch attributed the formation of a jagged surface crust layer to rapid cooling of the crystal post-synthesis.[29] Gueudre et al. determined that surface resistance accounted for 60% of the total diffusion resistance for cyclohexane at 398 K in 2 μm silicalite-1 crystals, an outcome that did not change after surface etching.[30] Teixeira et al. used zero length chromatography and discrete space simulations and concluded that more than 99.9% of surface pores on a sample of MFI crystals were closed to benzene permeation.[26] Saint Remi et al. showed that surface resistance in the same batch of SAPO-

34 crystals with a size range of 40-50 μm can vary by two orders of magnitude.[31] They attributed surface resistance to water degradation at the surface because water is known to reduce SAPO-34 porosity and nearly eliminates adsorption.[31] Briend et al. attributed this structural degradation to water attacking Si-O-Al sites.[32] Kalanzopoulos et al. tested the effect of grafting four moieties on 20 μm MFI crystals.[33] They measured the contact angle with water to determine the hydrophobicity and diffusivity of hydrogen at 77 K. They found that the unaltered surface had the lowest diffusivity and attributed the decrease in diffusivity to water crystallizing at the terminal –OH groups.[33] The more hydrophobic moieties led to faster gas diffusivities.[33] Related results have also been reported by Hibbe et al. and Karger et al. in metal-organic framework crystals. Their IR spectroscopy imaging of hydrocarbon diffusion in Zn(tbip) crystals showed concentration gradients during desorption associated with strong surface resistances to molecular transport.[34, 35]

A challenge with interpreting experimental observations of surface resistances is that they cannot unambiguously distinguish between resistances associated with material imperfections such as blocked pores and surface "crusts" and the resistances that arise solely from the existence of an interface between the crystal and the surrounding fluid phase. Molecular simulations have been used to quantify the latter class of surface resistances because in these simulations the atomic-scale structure of the crystal and its surface can be precisely controlled. Dual control volume grand canonical molecular dynamics (DCV-GCMD)[23, 36] and equilibrium molecular dynamics (EMD) have both been used to quantify surface resistances to molecular diffusion through nanoporous materials. Arya et al. used DCV-GCMC to determine surface barriers of various molecules in $AlPO_4$-5. They found that exit effects were more important than entrance effects and that surface

resistance became larger as the adsorbate to pore diameter approaches unity.[36] Ahunbay and Richardson used DCV-GCMD to simulate diffusion through a 48 nm MFI layer and found that higher pressure and smaller molecules result in lower surface resistance. They extrapolated their results and calculated that the surface resistance contribution to total diffusion resistance in a 1μm membrane is 17% for CH_4 and 2% for Ar.[37]

DCV-GCMD is a computationally expensive process, so Newsome and Sholl introduced an alternative called the local equilibrium flux method (LEFM).[23, 24] It uses equilibrium molecular dynamics and measures the flux through a plane placed at the surface.[23, 24] LEFM simulations are considerably faster than DCV-GCMD and are accurate enough to calculate order of magnitude estimates of surface resistance.[23] Newsome and Sholl also highlighted how care must be taken in thermalizing MD simulations involving surface resistances, particularly in simulations that approximate the adsorbing solid as rigid for computational convenience and speed.

Thompho et al. simulated the adsorption of CH_4 into silicate-1 to study the effect of including surface silanol groups in the model.[38] They started with an empty 3.8 nm MFI empty cell surrounded by a gas phase and used a flexible framework MD simulation at 300 K to measure the rate of adsorption into the zeolite. They found that the inclusion of silanol groups increased the rate of CH_4 adsorption.[38] Jee, McGaughey, and Sholl added a dense layer of silica on silicalite and investigated its effect on the surface resistance and ideal selectivity of H_2 and CH_4.[39] The dense layers were roughly 1 nm thick and varied in their free volume from 1% to 4% for CH_4 and 5% to 11% for H_2.[39] For a 10 nm slab the ratio of surface resistance to internal resistance was ~1 for H_2 and 110 for CH_4, while for 1000 nm slabs that surface resistances were negligible.[39]

Combariza and Sastre investigated the effect of CH_4 concentration in the gas phase on the adsorption rate into a rigid 4.4 nm Si-LTA slab at 300 K and concluded that the surface has negligible effect on adsorption and an almost total blockage of pores would be necessary to affect the overall adsorption rate.[40] Zimmerman et al. used dynamically corrected transition state theory to investigate the effect of surface barriers on hydrocarbon diffusion in siliceous zeolite AFI membranes.[41] They defined an effective self-diffusivity, $D_{s,eff}$, as the self-diffusivity that includes surface barriers and compared it to the standard self-diffusivity, D_s, of the bulk material. In a 5 nm thick AFI membrane, D_s of methane at 200 K was 10 times larger than $D_{s,eff}$.[41] This ratio decreases to 4.5 for a 20 nm membrane and became ~1 for a 1000 nm membrane. Zimmerman et al. defined the membrane critical thickness as the thickness for which $D_s/D_{s,eff} \sim 4$. At low pressures, higher molecular weight adsorbates like hexane and pentane had critical thicknesses around 60 nm while methane and ethane had critical thicknesses around 20 nm. At high pressures, the critical thickness for each species decreases to less than 10 nm.

Dutta and Bhatia investigated CO_2, H_2, and CH_4 diffusion in rigid 3-14 nm MFI, SAS, and PON slabs.[1, 42] They separated surface resistance into an internal zeolite slab resistance and an external fluid phase resistance.[1] They found that external resistance is an order of magnitude less than internal resistance and could be neglected.[1] Similar to Zimmerman et al., they defined the critical thickness as the slab thickness for which the surface resistance to methane diffusion is 25% of the total diffusion resistance. They found that the critical thicknesses for diffusion of methane in SAS, MFI, and PON were 14 nm, 65 nm, and 95 nm, respectively. Their analysis of H_2/CH_4 selectivity showed that larger

slabs were selective to methane owing to its higher solubility in the zeolite while smaller slabs (< 4 nm) were selective to H_2 due to its smaller kinetic diameter and faster diffusivity.

The simulation results reviewed above suggest that significant surface resistances to molecular diffusion can arise in nanometer-scale zeolite slabs even when the surfaces of these slabs are free from dramatic surface coatings or deformation. Given the growth of interest in synthesizing zeolites of this type, there is considerable value in quantitatively understanding the magnitude of these surface resistances. The surface resistance of any thin zeolite will of course be dependent on the details of the material's surface structure. In Chapter 2, we developed a systematic series of models of zeolite surfaces and thin zeolite slabs that aims to construct well-defined models with realistic surface terminations.[43] These models provide a useful basis for making a comparison between the surface resistances associated with several distinct zeolite frameworks.

In this Chapter, we use detailed molecular simulations to assess the surface resistances for seven molecules (H_2, CH_4, CO_2, C_2H_4, C_2H_6, C_3H_6, and C_3H_8) in silica zeolite slabs of ~2 nm thickness for 6 zeolites: MFI, AFI, AEL, ATO, LTA, and CHA. We chose the first four zeolites because they have been synthesized as nanosheets and have permeable pores normal to the slab.[6, 44] Since the first four zeolites have channel-like pores, we included LTA and CHA to compare to structures with cage-like pores. We examined adsorbates of varying sizes under different temperature and pressure conditions to obtain a range of surface resistance values. We then compared ideal selectivities in slab and bulk structures to determine the effect that surface resistance has on molecular transport relevant to separations.

3.2 Methods

3.2.1 Force Field

We used equilibrium Molecular Dynamics (EMD) in the LAMMPS software package to simulate diffusion of small molecules in fully flexible pure silica zeolites.[45] Realistic models of zeolite nanosheets were taken from Chapter 2, which made extensive comparisons between these models and experimental structural information.[43] These models have hydroxyl terminated surfaces and were constructed to minimize the number of broken bonds made when creating a surface.[43, 46] We compared diffusion through nanosheets to diffusion through the bulk material to calculate the surface resistance.

We used the Hill-Sauer force field with the angle modifications of Boulfelfel et al. to simulate zeolite framework flexibility.[47, 48] This force field simulates the interaction of atoms in the zeolite framework with Coulombic interactions, a 9-6 Lennard-Jones potential, as well as bond, angle, dihedral, improper, and other terms.[48] Boulfelfel et al. changed the Si-O-Si and O-Si-O angle terms to improve the force field description of zeolite pore sizes.[47] More details summarizing their findings are given in Appendix **B.1**. To model the terminal OH groups, we used the original Hill Sauer silanol parameters.[48]

All of the adsorbate-zeolite Lennard-Jones parameters we used in this study were obtained from previously published works except those for CO_2 and H_2, which we reparametrized to be consistent with the Hill-Sauer charges.[49-52] Hill and Sauer reduced the charges in their FF by roughly half of their ab initio values.[53] Using adsorbate-zeolite FFs that were based on charges similar to the latter charges would likely lead to inaccuracies. We used the methods described by Fang et al. to parametrize the Lennard-Jones parameters

such that the sum of the Coulombic and Van der Waals energy calculated using the partial charges in the Hill-Sauer force field was consistent with the energy calculated using the quantum chemistry methods.[54] Further details are provided in the Appendix. We explicitly parametrized the Lennard-Jones terms for CO_2 and H_2 interactions with Si, bulk O (O_{SiOSi}), and silanol H (H_{OH}). We did not parametrize the silanol oxygen O_{SiOH} and instead assumed that its Lennard-Jones parameters would be the same as those of the bulk O (O_{SiOSi}).

We described CO_2 using the EPM2 model, which assumes a partial point charge and Lennard-Jones interaction centered at each atom.[55] We used the Darkrim and Levesque model for H_2, which assumes a partial point charge centered on each atom and a partial charge and Lennard-Jones interaction at the center of the molecule.[56] We simulated the H_2 center in LAMMPS as an atom of zero mass. The adsorbate (CO_2, H_2) self-interaction parameters from their original papers and the adsorbate-zeolite interaction parameters parametrized in this study are listed in Appendix **Table B.2**.

We used TraPPE and TraPPE-zeo Lennard-Jones parameters for hydrocarbon-hydrocarbon and hydrocarbon-zeolite interactions. We simulated ethane, ethene, propane, and propene self-interactions using the united atom TraPPE parameters with the CH, CH_2, and CH_3 groups shown in Appendix **Table B.3**.[50, 51] For zeolite-hydrocarbon interactions, we applied Lorentz-Berthelot mixing rules to the hydrocarbon TraPPE and TraPPE-zeo parameters in **Table B.3**.[49-51] The TraPPE-zeo force field has parameters for bulk framework oxygen atoms (O_{SiOSi}), but not for silanol oxygen (O_{SiOH}).[49] We used the same Lennard-Jones parameters for both oxygen types and did not include silanol hydrogen-hydrocarbon interactions in our simulations.[49] We note that the Lennard-Jones parameters for Si, O_{SiOSi}, O_{SiOH} in **Table B.3** were used only to calculate zeolite-hydrocarbon Lennard-

Jones parameters, not to calculate zeolite-zeolite Lennard-Jones parameters. The original Hill Sauer 9-6 Lennard-Jones potential was used for the latter interactions.[48]

We simulated hydrocarbon flexibility using the parameters from Jakobtorweihen et al. and Calero et al.[57, 58] The TraPPE hydrocarbon force field allows for angle bending but not for bond stretching.[50, 51] We incorporated bond flexibility because LAMMPS cannot readily simulate flexible angles without flexible bonds.[45] Further details are given in Appendix **B.3**.

For CH_4, we used the united atom Lennard-Jones parameters calculated by Fang et al. for zeolite-adsorbate interactions and TraPPE parameters for adsorbate-adsorbate interactions as shown in Appendix **Table B.5**.[50, 52] We chose the Fang et al. model because it was explicitly parametrized for zeolite diffusion.[52] Fang et al. used the TraPPE model for CH_4 self-interactions, so we did so as well.[52] Fang et al. did not include silanol groups in their CH_4 model.[52] Therefore, we assumed that bulk oxygen and silanol oxygen could share the same Lennard-Jones parameters, and we did not simulate silanol hydrogens.

3.2.2 Structures

We used zeolite slab models from Chapter 2, where we systematically generated an all silica database of zeolite nanosheets, including models for all examples of experimentally synthesized zeolite nanosheets.[43] In this chapter we considered the 14 known nanosheets then eliminated those that did not have an 8 member ring (MR) or larger pore normal to the plane of the nanosheet, that is MWW (ITQ-2)[59], MTF (HPM2)[60], FER (RUB-36)[61], STI (PKU-22)[62], AFO ([F, Tet-A]-AlPO-1)[63], SOD (RUB-15)[64], RWR (R-RUB-18)[65], UTL (IPC-1)[66], RRO (B-RUB-39)[67], CAS (EU-19)[68]. This approach resulted

in 4 structures: MFI (010), AEL (100), AFI (001), and ATO (001), none of which have specific nanosheet names.[6, 44] AFI and ATO nanosheets have only been reported as AlPO structures, but the all silica counterparts were used in this study.[44]

Since these four slabs have channel-like pores, we included LTA (100) and CHA (101) nanosheets to compare to the results to structures with cage-like pores. We chose the LTA and CHA Miller indices that occupied the largest surface area on experimentally reported crystals.[69, 70] Most of our simulations used slabs of height ~2 nm because that corresponds to the smallest known height for the four known nanosheets.[6, 44] An example of one of these structures is shown in **Figure 3.1**. We also studied the properties of MFI as a function of thickness, so MFI slabs of various heights were used. The unit cell lengths were adjusted so that the vacuum spacing between each periodic image of the slab was 4 nm. Bulk unit cells were expanded normal to the nanosheet Miller index while the LTA and CHA nanosheets were expanded in the planar direction to obtain for accurate diffusivity values.

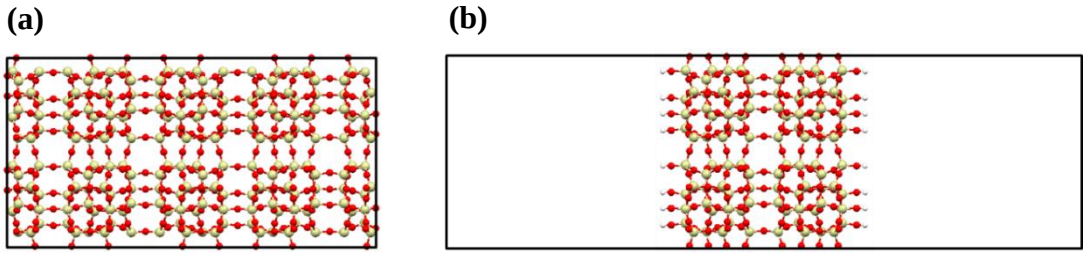

Figure 3.1. (a) A bulk 1×2×1 and (b) a slab 1×1×1 MFI unit cell oriented parallel to the (010) direction. In each case, the system boundaries represent periodic boundary conditions.

All bulk and slab cells were relaxed in LAMMPS using the FFs defined above with conjugate gradient descent energy minimization.[45, 47, 48, 71] In the bulk materials all cell parameters were allowed to change. In the slab, the normal axis was fixed, but the cell

parameters in the in plane direction were allowed to change (were not fixed to the relaxed bulk values). No constraints were imposed on atom positions.

3.2.3 Molecular Dynamics

Simulations were performed with periodic boundary conditions in all directions. Bulk unit cells were simulated in the NVT ensemble with a chain of 6 Nosé-Hoover thermostats. For slab simulations, we used an NVT ensemble in the interior of the slab and an NVE ensemble on the slab edges. We found that this setup allowed us to account for heat lost during desorption as explained further in Appendix **B.4**. We used the particle-particle particle-mesh (PPPM) strategy of Hockney and Eastwood to calculate Coulombic interactions.[72] All time steps were 1 fs and the cutoff for Coulombic and Lennard-Jones interactions was 11 Å. Each EMD simulation was run for 50 ns and 20 independent simulations were performed at each condition. We used Grand Canonical Monte Carlo (GCMC) with the RASPA software package to initialize our Hill-Sauer relaxed unit cells with the loading corresponding to the temperature and pressure conditions of the simulation and to obtain the heat of adsorption, Q_{ads}, at those conditions.[73]

Coordinates were recorded every 10 ps. To obtain well converged results, we divided each trajectory into non-overlapping 1 ns intervals.[74] Our error bars represent the standard error in the mean given by

$$\sigma_M = \frac{\sigma}{\sqrt{N}} \tag{3.1}$$

where σ is the sample standard deviation, and N is the sample size. The sample comprises of all 1 ns intervals from the 20 simulations An example of convergence with mean square displacements is shown in Appendix **B.5**.

3.2.4 Trajectory Analysis

To characterize surface resistances with EMD we used methods due to Liu et al.[75] In an isotropic nanoporous material the corrected diffusivity of adsorbed molecules is[76]

$$D_0 = \frac{N}{2d} \lim_{t\to\infty} \frac{1}{t} \langle |r_{com}(t) - r_{com}(0)|^2 \rangle \tag{3.2}$$

where N is the number of adsorbates, d is the dimensionality, and r_{com} is the center of mass of the adsorbed molecules. This equation can also be applied to a simulation volume containing a slab of finite thickness as in **Figure 3.1(b)**. Below we assume that the slab is oriented so its normal points along the *z* direction, giving

$$D_z = \frac{N}{2} \lim_{t\to\infty} \frac{1}{t} \langle \left|\Delta z_{sys,com}\right|^2 \rangle \tag{3.3}$$

where $\Delta z_{sys,com}$ refers to the change in center of mass along the z axis. Applying this equation to a simulation volume containing a gas phase and a zeolite phase will of course give different results than for a simulation of a bulk zeolite. The method of Liu et al. separates the contributions due to adsorbed molecules and the surrounding bulk phase as explained in Appendix **B.6**. For our geometry, their method gives

$$D_{z,zeo} = \frac{N_{sys}^2}{2N_{zeo}\left(\frac{L_{gas}}{L_{zeo}}+1\right)} \lim_{t\to\infty} \frac{1}{t} \langle \left|\Delta z_{sys,com}\right|^2 \rangle \tag{3.4}$$

where $D_{z,zeo}$ is the diffusivity through the zeolite portion of the unit cell, N_{sys} is the total number of molecules in the system, N_{zeo} is the average number of molecules in the zeolite throughout the duration of the simulation, L_{gas} is the length of the gas portion of the unit cell, L_{zeo} is the height of the zeolite nanosheet, and $\Delta z_{sys,com}$ is the change in the center of mass of all adsorbates in the simulation. N_{zeo} is obtained from a histogram of adsorbate densities

$$N_{zeo} = \frac{C_{zeo}}{C_{total}} N_{sys} \tag{3.5}$$

where C_{zeo} is the total count of adsorbate molecules observed in the zeolite, and C_{total} is the total count of adsorbate molecules observed in the system. Both counts are summations based on coordinate information from each simulation run. Liu et al. compared the flux calculated with the diffusivity from equation 3.4 with the flux obtained from NEMD simulations for carbon nanotubes and found that NEMD gave slightly higher fluxes due to temperature gradients caused by adsorption and desorption.[75]

We are interested in comparing the surface resistance to the bulk resistance to obtain the surface resistance in terms of an equivalent thickness of the bulk material. To do this, we write resistance to diffusion as a series of resistances[1]

$$R_{total} = R_{bulk} + R_{surf} \tag{3.6}$$

The flux through a slab in the presence of a pressure gradient can be written as

$$j = \frac{\rho(f) D_0(f) \Delta f}{Lf} \tag{3.7}$$

where j is the flux, f is the average fugacity in the slab, $\rho(f)$ is the adsorbate density, $D_0(f)$ is the corrected diffusivity, Δf is the fugacity gradient across the slab and L is the thickness of the slab. Equation 3.6 holds when Δf is small, in which case $\rho(f)$ and $D_0(f)$ remain approximately constant across the slab.[75] The diffusion resistance is defined as[75]

$$R = \frac{\Delta f}{j} = \frac{Lf}{\rho(f)D_0(f)} \tag{3.8}$$

Equation 3.7 can be substituted for each term in equation 3.5 to obtain

$$\frac{Lf}{\rho_{slab}D_{0,slab}} = \frac{Lf}{\rho_{slab}D_{0,bulk}} + \frac{H_{surf\_equiv}f}{\rho_{slab}D_{0,bulk}} \tag{3.9}$$

This gives

$$H_{surf\_equiv} = L\left(\frac{D_{0,bulk}}{D_{0,slab}} - 1\right) \tag{3.10}$$

where H_{surf_equiv} is the equivalent height of the bulk slab that provides a diffusion resistance equivalent to the surface resistance.

3.3 Results and Discussion

3.3.1 Surface Resistance in MFI Nanosheets

We first investigated diffusion in the MFI (010) nanosheet shown in **Figure 3.1** at various conditions. This slab has a thickness of 2.2 nm and its surface is normal to the *b* axis, both characteristics of the nanosheet synthesized by Choi et al. in 2009.[6] The MFI (010) surface termination we chose is predicted to have the minimum number of cut bonds using both the graph theory approach of Witman et al. and the repetitive sampling approach

of Knio et al.[43, 46] For each molecule, simulations were performed at a pressure corresponding to a loading of 1 molecule/unit cell in the bulk zeolite and at a "high loading" condition similar to the molecule's saturation loading. The specific pressures and bulk loadings for these conditions are listed in **Table B.8**. Our results in **Figure 3.2** show that there is a large range of surface resistances at low loading, from 1600 nm for propane at 250 K to <5 nm for H_2 at all temperatures. At low loading, the surface resistance increases strongly as the temperature is reduced; for propane the surface resistance increases by ~2 orders of magnitude as the temperature decreases from 500 K to 250 K. The surface resistances are considerably smaller at high loadings than at low loadings.

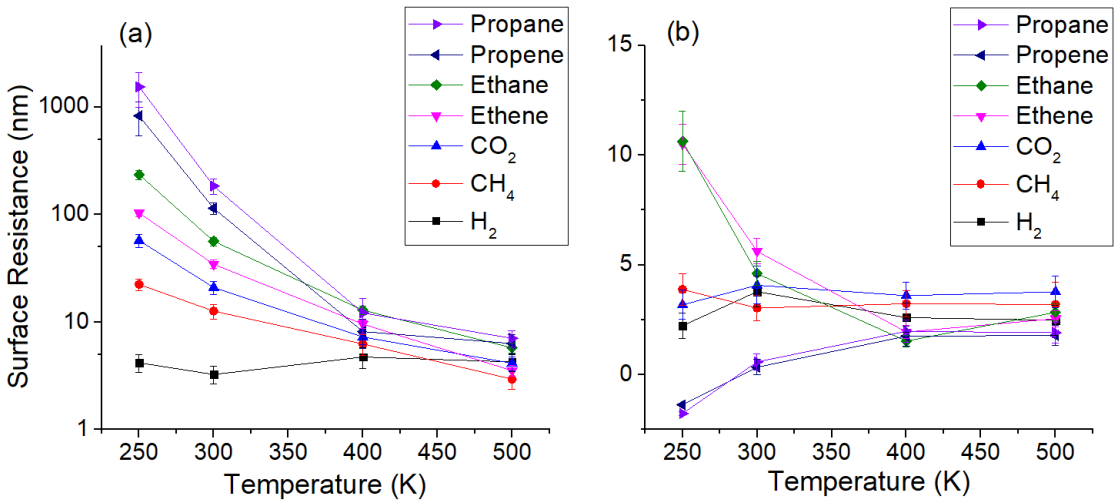

Figure 3.2. Surface resistance in a 2 nm MFI (010) slab at (a) low loading conditions and (b) high loading conditions.

Previous studies of surface resistance in crystals and nanosheets deemed surface resistance to be critical when it is responsible for 25% or more of the total diffusion resistance through the structure.[1, 41] For the 2 nm MFI nanosheet in **Figure 3.1**, this threshold corresponds to a surface resistance of 0.67 nm. **Figure 3.2** shows that in almost all instances, the surface resistance is not only critical but is the dominant source of

diffusion resistance. At 250 K and low loading conditions, surface resistance for diffusion through a 2 nm MFI nanosheet is responsible for > 90% of the total diffusion resistance in CH_4 and > 99% of the total diffusion resistance for propane. These examples indicate that surface resistances may be of great importance in understanding the properties of emerging ultra-thin zeolite membranes or similar applications of zeolite nanosheets.

Figure 3.2(b) shows that propane has a negative surface resistance at 250 K. This unusual result arises from a lower propane density in the slab compared to the bulk zeolite. The slab:bulk adsorbate density ratio for this specific example is 77%, as shown in Appendix **B.7**. This situation occurs because a fraction of the zeolite slab very near the surface is less favorable for adsorption than the equivalent sites in the bulk zeolite. As a general rule, lower adsorbate density in the zeolite phase results in lower zeolite phase resistance because there is less impedance to the movement of neighboring molecules.[77] The negative surface resistance arises because the total resistance in the slab (i.e. the sum of zeolite and surface resistances) is less than the resistance in a bulk of equal height due to lower adsorbate density and zeolite resistance.

In light of the observation that lower propane density in the slab gives negative surface resistance, we asked if this holds for other molecules. In Appendix **Figure B.13**, we find that the density of CO_2 in the slab is 97% of the density of CO_2 in the bulk, meaning that the zeolite portion of the slab resistance is essentially equal to the bulk zeolite resistance for CO_2. The difference between propane and CO_2 appears to be due to the molecular sizes. A propane molecule nearly fills the MFI channel, so it is less likely to adsorb on the surface where the disappearance of the half the channel wall leaves it exposed to vacuum on one side. Since CO_2 is smaller, its adsorption is likely dependent on smaller

regions of the zeolite channel. The reduced total resistance observed for propane at low temperature in **Figure 3.2(b)** appears to be an exception rather than the usual situation; in every other case we examined for this 2 nm MFI slab the surface resistance was positive and often large.

Figure 3.2 shows that larger molecules typically have larger surface resistances. This observation can be correlated with the heat of adsorption, Q_{ads}, of the molecules in the bulk zeolite, as shown in **Figure 3.3**. The strong increase in surface resistance with the Q_{ads} is reasonable because desorption of molecules from the nanosheet is expected to be a key contributor to surface resistance.[78] For a better understanding of surface resistance, we compared the activation energy of $1/R_{surf}$ to the Q_{ads}. After defining an effective activation energy for $1/R_{surf}$ for each molecule, we found that this activation energy is uniformly ~8 kJ/mol smaller than the heat of adsorption (see **Figure B.14**).

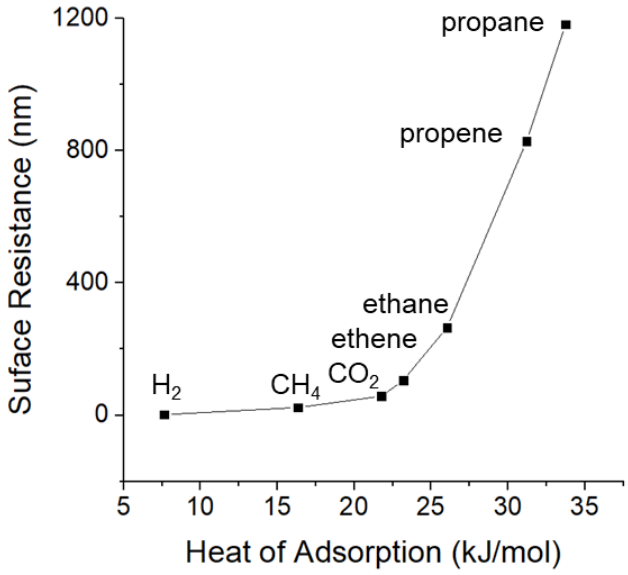

Figure 3.3. The surface resistance from a 2 nm MFI (010) nanosheet at 250 K and 1 molec/uc graphed against the Q_{ads} at 250 K and 1 molec/uc.

Figure 3.2 showed that surface resistance was high at low loading and but much smaller at near-saturation loadings. The trend of decreased surface resistance with increased loading was also observed by Ahunbay et al. and Arya et al., who attributed this phenomena to the presence of a fugacity gradient that descends in the direction of the vacuum.[36, 37] In our simulations we observe that higher pressures result in adsorption layers a few Å in thickness (Appendix **B.6**) at the zeolite surface, suggesting that molecules at high pressure can leave the nanosheet environment from a point in the adsorption layer farther away from the surface where the attractive interaction of the zeolite is diminished.

3.3.2 Ideal Selectivity in MFI

To test the effect of surface resistance on ideal selectivity, we calculated the ideal selectivity of ethene/ethane and propene/propane separation in bulk MFI and 2 nm MFI (010) slabs using equation 3.7. For the high loading examples, the same loading was used for each species as shown in **Table B.8**. The ideal selectivity results are shown in **Figure 3.4**. When the surface resistance is low, the slab and bulk ideal selectivities are of course approximately the same. At conditions where the surface resistances are significant, however, we find that the slabs exhibited higher ideal selectivity than the bulk zeolite. Because the low loading surface resistances of the two C_2 species are more dissimilar than the low loading surface resistances of the two C_3 species, the increase in the ideal selectivity at low temperature is slightly more pronounced for the slab for the former molecular pair. It is interesting to note that surface resistance increases the ideal selectivity for each molecular mixture we considered for this specific nanosheet (see **Figure B.18**).

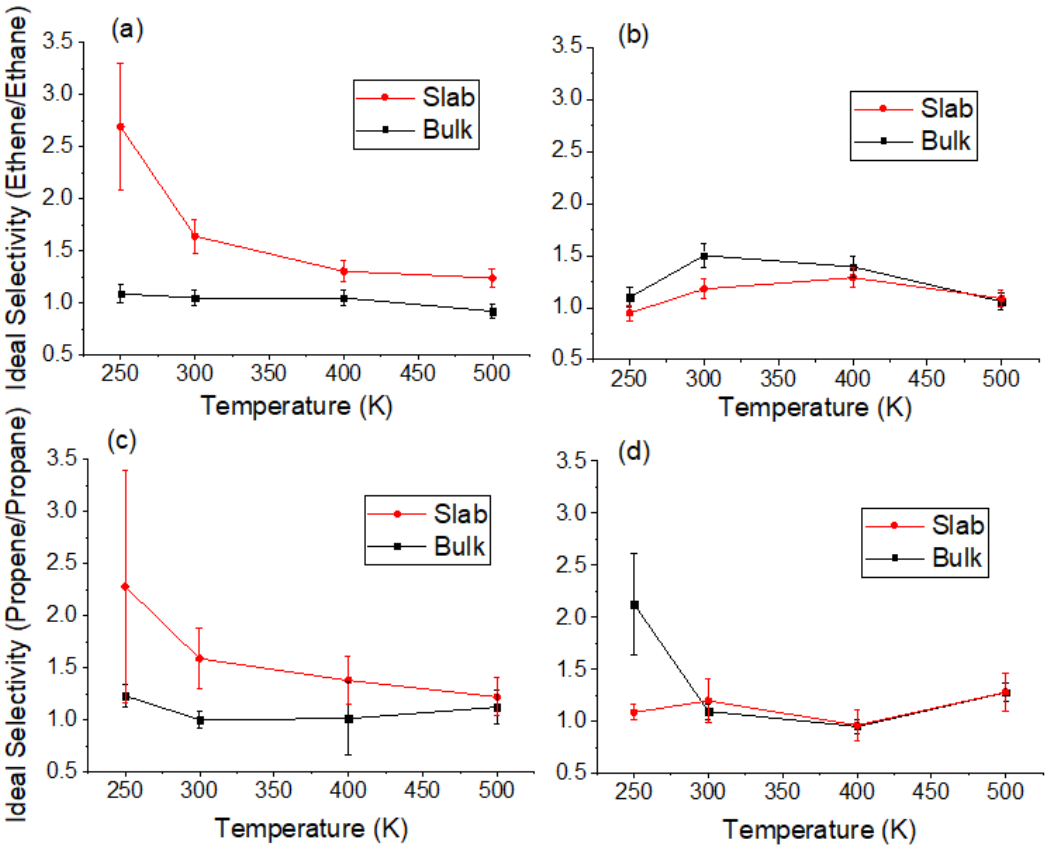

Figure 3.4. Data from bulk MFI and a 2 nm MFI (010) slab. (a) Ethene/ethane ideal selectivity at 1 molec/uc. (b) Ethene/ethane ideal selectivity at high loading. (c) Propene/propane ideal selectivity at 1 molec/uc. (d) Propene/propane ideal selectivity at high loading.

The ideal selectivity for H_2/CO_2 and CH_4/CO_2 are shown in **Figure 3.5**. Because the high loading conditions we considered above for these molecules are from different pressures, we only calculated the ideal selectivity at low loading conditions. However, even the low loading scenario is also not as straightforward to analyze as it is for alkanes/alkanes. The gas pressure that gives a loading of 1 molec/uc for CO_2 will not result in loading of 1 molec/uc for CH_4 or H_2. For all the data in **Figure 3.5** we performed simulations at the pressure that gives a loading of 1 molec/uc of CO_2 in bulk MFI.

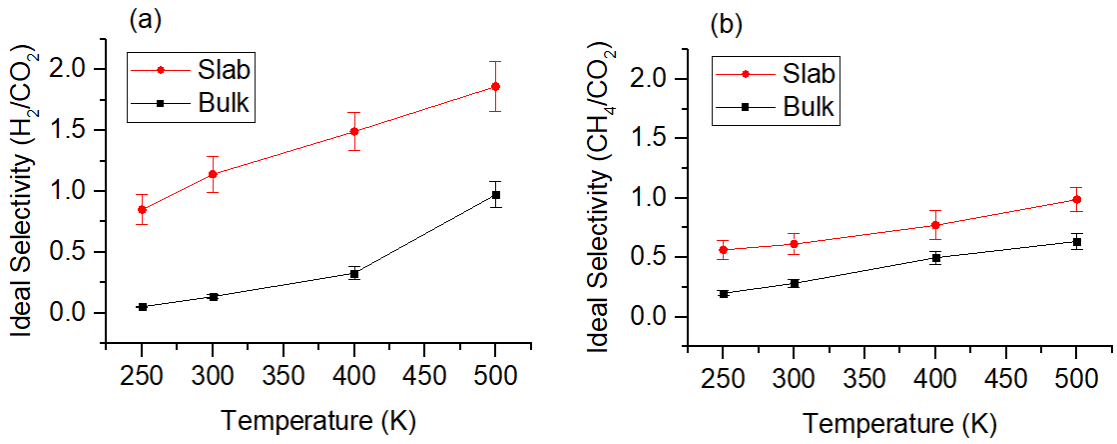

Figure 3.5. Data from bulk MFI and a 2 nm MFI (010) slab. (a) H_2/CO_2 ideal selectivity at low loading. (b) CH_4/CO_2 ideal selectivity at low loading.

At the same pressure and temperature conditions, CO_2, H_2, and CH_4 have different loadings. Since CH_4 has a surface resistance roughly equivalent to CO_2, both the slab and bulk favor CO_2. Therefore, the CH_4/CO_2 separation is thermodynamically driven. However, H_2 has a much lower surface resistance than CO_2, so, the slab favors H_2 while the bulk favors CO_2. Therefore, the H_2/CO_2 slab separation is kinetically driven. Our predicted slab ideal selectivity in favor of H_2 indicates that the usual selectivity in favor of CO_2 in bulk H_2/CO_2 separations observed experimentally[79] will likely not hold in the nanosheet due to the transition to a kinetically dominant separation regime. Dutta and Bhatia observed the same phenomena in their simulations of CH_4/H_2 ideal selectivity in the SAS zeolite.[1]

3.3.3 Surface Resistance as Function of Slab Height

The specific thickness of the MFI (010) slab in **Figure 3.1** was chosen because it matches with an experimentally synthesized material. It is, however, interesting to understand how the surface resistance of slabs of this kind varies as the nanosheet thickness

varies. To this end, we performed simulations of H_2, CH_4, and CO_2 in MFI (010) slabs varying in thickness from 1 to 14 nm at a range of temperature and pressure conditions. These three molecules were chosen because their relatively fast diffusion in the small pore zeolites we consider below meant that we could perform similar calculations for the full range of materials of interest. Our results for MFI (010) are summarized in **Figure 3.6**. In almost all cases, the surface resistance in a 1 nm slab is equivalent to that encountered in a 14 nm slab within the uncertainties in our data. However, at 300 K and 2 bar, the surface resistance of CO_2 increases from 1 nm to 4 nm and levels off for thicker slabs.

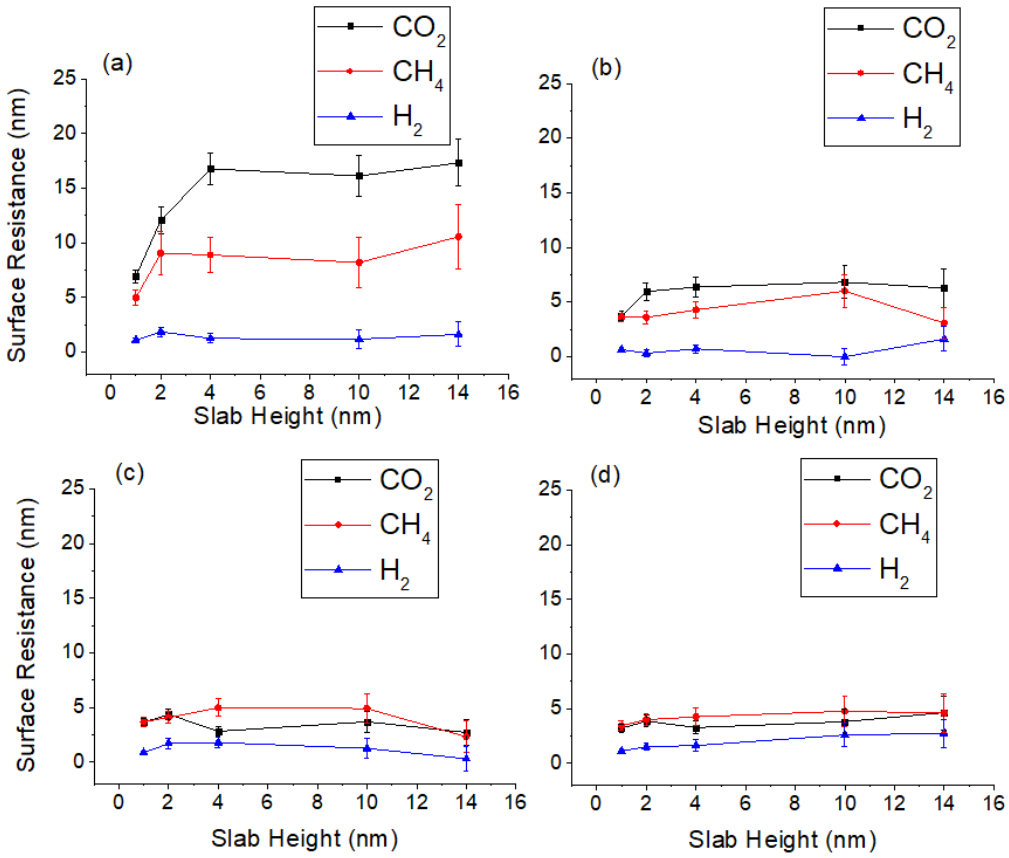

Figure 3.6. Surface resistance plotted against MFI (010) slab heights at (a) 2 bar and 300 K (b) 2 bar and 400 K, (c) 20 bar and 300 K, and (d) 20 bar and 400 K.

Most of the examples in **Figure 3.6** are situations where the surface resistance is at worst a moderate correction to the resistance associated diffusion through the bulk portion of the slab. We showed above, however, that using larger molecules and low temperatures can give very large surface resistances for a 2 nm MFI (010) slab. To understand if this situation changes the way the surface resistance varies with slab thickness, we collected the data in **Figure 3.7** for H_2, CH_4, CO_2, ethane, and propane in 2 nm and 10 nm MFI (010) slabs at 1 molec/uc and 250 K. This data**,** combined with the information in **Figure 3.6**, indicates that the surface resistances vary weakly with slab thickness for slabs thicker than 2 nm. This suggests that the surface resistance for each diffusing species of interest can be determined for zeolite slabs with a large range of thicknesses from a single calculation with a zeolitic nanosheet. This outcome is useful because the computational cost of measuring surface resistances increases significantly as the volume of the slab that must be simulated increases.

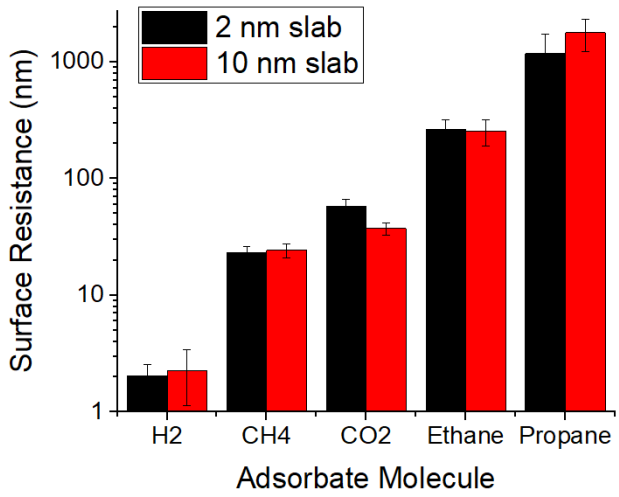

Figure 3.7. The surface resistance of five adsorbates at 250 K and 1 molec/uc in an MFI (010) 2 nm slab and 10 nm slab.

3.3.4 Nanosheets from Different Frameworks

The data above exclusively examined nanosheets of the MFI framework, so we expanded our study to include nanosheets from the LTA, CHA, AFI, AEL, and ATO frameworks. More specifically, we simulated LTA (100) 2.3 nm, CHA (101) 1.8 nm, AFI (001) 2.1 nm, AEL (001) 2.1 nm, and ATO (001) 2.2 nm slabs. In each case, the nanosheet was chosen by first identifying which surface from the chosen Miller index had the lowest broken bond density using the documentation provided in the database of Knio et al.,[43] then finding the slab with a height closest to 2 nm. The surface resistances for the diffusion of CO_2, CH_4, and H_2 at 250 K and 1 molec/uc in each of these zeolite nanosheets are shown in **Figure 3.8(a)**. The surface resistance for all three molecules generally increases in the following order: LTA, CHA, AFI, MFI, AEL, and ATO.

We expect that the slab diffusivity, D_{slab}, will depend on the rate of diffusion through the bulk zeolite, D_{bulk}, and the heat of adsorption, Q_{ads}, calculated at 250 K and 1 molec/uc. To test this hypothesis, we fit a polynomial to estimate D_{slab} based on D_{bulk} and Q_{ads} for all six frameworks using Matlab's nonlinear regression model:[80]

$$D_{bulk} \times x_1 + Q_{ads} \times x_2 + x_3 = D_{slab,NLR} \approx D_{slab,MD} \tag{3.11}$$

where x_1, x_2, and x_3 are fitted scalar parameters, $D_{slab,NLR}$ is the slab diffusivity predicted by nonlinear regression, and $D_{slab,MD}$ is the slab diffusivity from the molecular dynamics simulations. The fitted parameters are shown in Appendix **Table B.10** and plots of $D_{slab,NLR}$ and $D_{slab,MD}$ against D_{bulk} and Q_{ads} are shown in Appendix **Figure B.19**. **Figure 3.8** shows parity plots comparing $D_{slab,,NLR}$ to $D_{slab,MD}$.

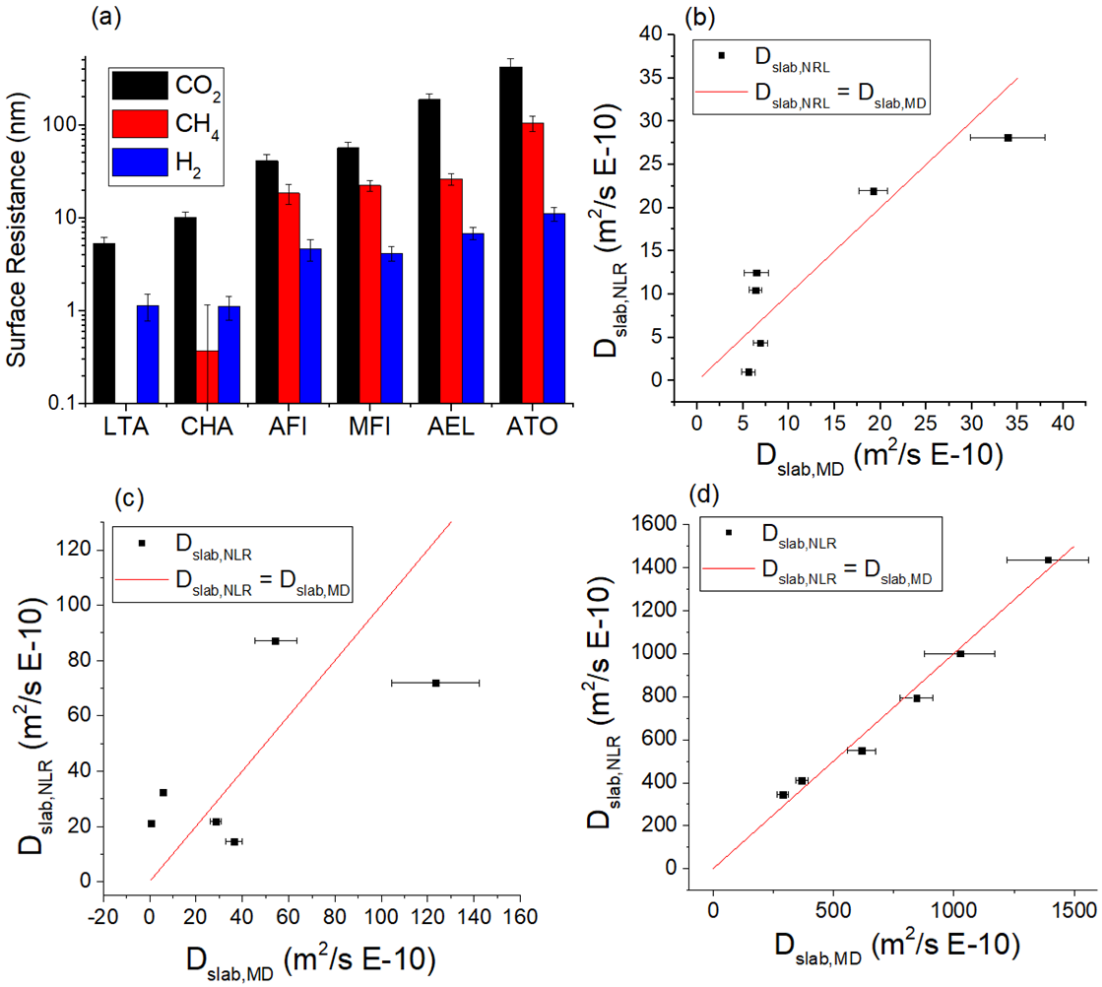

Figure 3.8. (a) Surface resistance at 250 K and 1 molec/uc for CO_2, CH_4, and H_2 in 2 nm slabs of various frameworks. The LTA CH_4 surface resistance was effectively 0 nm (-0.3 nm with a 0.3 nm uncertainty). The $D_{slab,NLR}$ estimates for (b) CO_2, (c) CH_4, and (d) H_2.

The $D_{slab,NLR}$ predictions in order of best fit are H_2 (R^2 = 0.98), CO_2 (R^2 = 0.81), and CH_4 (R^2 = 0.46). The H_2 $D_{slab,MD}$ values show a strong trend against the H_2 D_{bulk} values (**Figure S.19**), and the CO_2 $D_{slab,MD}$ show a fairly strong trend against Q_{ads} (**Figure S.19**). In the case of CH_4, its 8 MR $D_{slab,MD}$ values trend with D_{bulk} while its 10 MR $D_{slab,MD}$ values trend with Q_{ads}, so the CH_4 fit was less accurate. The trends show that for a species with a high Q_{ads} like CO_2, higher framework Q_{ads} leads to lower D_{slab}, and for species with low Q_{ads} like H_2, higher framework D_{bulk} leads to higher D_{slab}.

We calculated the ideal selectivity for the bulk and slab structures for the six framework nanosheets following the same method we used for MFI above. We ran all simulations at the pressure and temperature conditions (1,689 Pa at 250 K) that resulted in a loading of 1 molec/uc of CO_2 for bulk MFI. We then used the Matlab nonlinear regression algorithm[80] to estimate the ideal selectivity in a slab based on the ideal selectivity in the bulk and the heat of adsorption of both species.

$$IS_{bulk} \times x_1 + Q_{ads,CO2} \times x_2 + Q_{ads,CH4/H2} \times x_3 = IS_{slab,NLR} \approx IS_{slab,MD} \quad (3.12)$$

where $IS_{slab,NLR}$ is the ideal selectivity in the slab from nonlinear regression, and $IS_{slab,MD}$ is the ideal selectivity in the slab from molecular dynamics. The fitted parameters are shown in **Table B.11**, and plots of $IS_{slab,MD}$ and $IS_{slab,NLR}$ against IS_{bulk} are shown in Appendix **Figure B.20**. **Figure 3.9** shows a parity plot of $IS_{slab,NLR}$ against $IS_{slab,MD}$.

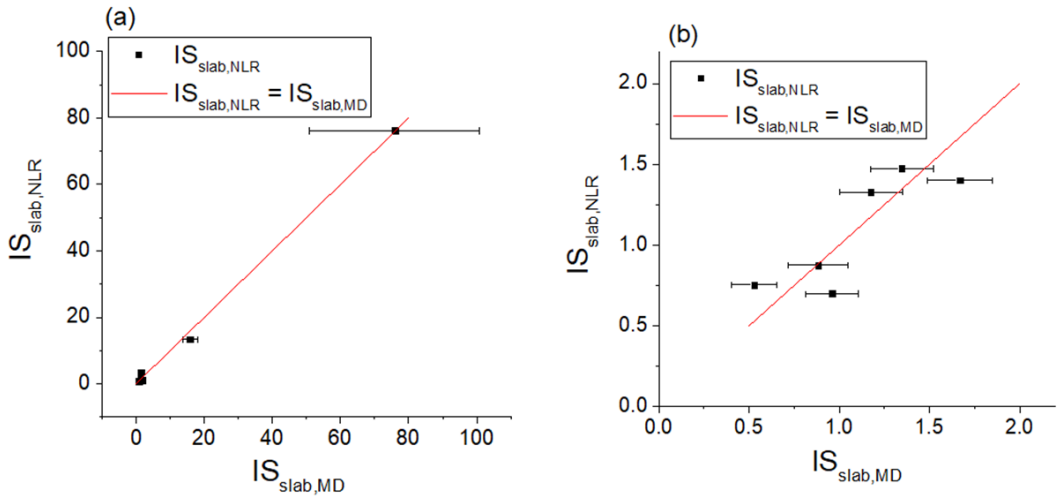

Figure 3.9. Ideal selectivity from the simulations and the regression estimate at 250 K and 1,689 Pa for (a) CO_2/CH_4, and (b) CO_2/H_2.

The $IS_{slab,NLR}$ prediction for CO_2/H_2 is reasonable (R^2 of 0.707). $IS_{slab,MD}$ shows a clear negative trend against IS_{bulk} in **Figure B.20**. A larger IS_{bulk} indicates higher CO_2

loading, and since loading correlates with Q_{ads}, and Q_{ads} correlates with surface resistance, a bulk with a higher IS_{bulk} in favor of CO_2 will have a slab with a higher IS_{slab} in favor of H_2. For CO_2/CH_4, the R^2 is 0.997. Although there are six data points in **Figure 3.9(a)**, the fitting considers three effective data points, with the four 10 MR structures forming the equivalent of a single point at ~(0,0). Since CH_4 is very slow to diffuse in 8 MR zeolites, the CO_2/CH_4 ideal selectivity in both the slab and the bulk 8MR structures are primarily a function of the respective species' bulk diffusivities.

Slab diffusivity in frameworks depends on both the bulk diffusivity and the heat of adsorption. As with different molecules, frameworks with higher heat of adsorption show slower slab diffusion. Overall, the bulk ideal selectivities are higher than the slab ideal selectivities for CO_2/CH_4 and CO_2/H_2 because of the difference in bulk loading between both species. In the bulk, there is a thermodynamic (loading) preference for the species with the highest Q_{ads}, but in the slab, this advantage is counteracted by a kinetic (diffusion) preference for the species with the lowest Q_{ads}.

Our analysis has focused on isolated nanosheets surrounded by vacuum. In reality, zeolite nanosheets used in membranes have a specific stacking architecture such as a compact laminate,[21] hierarchical nanosheets separated by columns,[28, 81] or nanosheets separated by crystals.[19] It would be useful to study these structures since the size of the vacuum spacing in between nanosheets is likely to have an effect on the surface resistance. If the spacing is too small, then hopping from one nanosheet to the next would require only a small activation energy barrier and surface resistance will be reduced. We predict that maximum surface resistance would require a spacing equal to or larger than the adsorption layers that form at the surface. In addition to the nanosheet spacing, the spacing of the

columns that separate the nanosheets could affect surface resistance. Adsorbates near columns could travel to the opposing nanosheet on a column rather than through the vacuum. Therefore, columns that are too close could form a series of bridges that bypass surface-to-surface hopping and decrease the surface resistance of the structure.

We have only studied all silica structures. Many zeolites, however, include Al atoms and various cations. Species with strong charges, such as Ca^{2+}, show preferential bonding to olefin double bonds in 3D zeolites.[82] It seems likely that including such species in zeolite nanosheets would give olefins higher surface resistance than that present in all silica nanosheets because of the higher heats of adsorption in cationic materials. The distribution of charges is also likely to affect the surface resistance. We expect structures with charges on the surface to show a greater surface resistance than structures with charges in the interior. Findley et al. explored methods for assessing Al ordering[83] in bulk zeolites. It would be interesting in the future to extend this to the pure silica nanosheets in the database of Knio et al.[43].

3.4 Conclusion

In this paper we characterized the effect of the surface resistances on diffusion in zeolite nanosheets. We used equilibrium Molecular Dynamics to study the diffusion of H_2, CH_4, CO_2, ethene, ethane, propene, and propane in bulk and slab zeolite structures at various temperatures and loadings. We found that high temperatures and loadings resulted in moderate surface resistance while low temperatures and loadings resulted in high surface resistance. In almost all instances, the surface resistance dominated the total resistance to mass transfer through zeolite nanosheets that were a few nm thick. The surface resistance

of zeolite slabs was found to be roughly independent of the slab thickness. This observation is useful because it implies that accurate information about the total resistance to mass transfer through zeolite nanosheets of a wide range of thicknesses can be obtained from simulations of a single nanosheet and the corresponding bulk zeolite.

The main factor that determined the magnitude of surface resistance was the heat of adsorption of the diffusing molecule. Among the molecules we considered, propane had the highest surface resistance measured as well as the highest heat of adsorption. Hydrogen had the lowest surface resistance and the lowest heat of adsorption. We found that the effective activation energy for surface resistance was consistently about 8 kJ/mol less than the heat of adsorption. Comparisons of diffusion in different frameworks revealed that for molecules with higher heats of adsorption like CO_2, frameworks with higher heats of adsorption in the bulk displayed lower diffusion in the slab. For molecules with low heats of adsorption like H_2, slab diffusivity was mainly a function of bulk diffusivity.

All the nanosheets we analyzed were pure silica structures considered as isolated structures. It would be useful in the future to analyze nanosheet architectures that more accurately mimic materials that are of interest as hierarchical catalysts or supported membranes. It would also be useful to extend our work to cationic aluminosilicate zeolite nanosheets, since the synthesis methods that are known for making zeolite nanosheets are in some cases limited to particular Si:Al ratios.

3.5 References

1. Dutta, R.C. and S.K. Bhatia, *Interfacial barriers to gas transport in zeolites: distinguishing internal and external resistances.* Physical Chemistry Chemical Physics, 2018. **20**(41): p. 26386-26395.

2. Rangnekar, N., N. Mittal, B. Elyassi, J. Caro, and M. Tsapatsis, *Zeolite membranes–a review and comparison with MOFs.* Chemical Society Reviews, 2015. **44**(20): p. 7128-7154.

3. Hedlund, J., J. Sterte, M. Anthonis, A.-J. Bons, B. Carstensen, N. Corcoran, D. Cox, H. Deckman, W. De Gijnst, and P.-P. de Moor, *High-flux MFI membranes.* Microporous and Mesoporous Materials, 2002. **52**(3): p. 179-189.

4. Yang, S., Y.H. Kwon, D.Y. Koh, B. Min, Y. Liu, and S. Nair, *Highly Selective SSZ-13 Zeolite Hollow Fiber Membranes by Ultraviolet Activation at Near-Ambient Temperature.* ChemNanoMat, 2019. **5**(1): p. 61-67.

5. Přech, J., P. Pizarro, D. Serrano, and J. Čejka, *From 3D to 2D zeolite catalytic materials.* Chemical Society Reviews, 2018. **47**(22): p. 8263-8306.

6. Choi, M., K. Na, J. Kim, Y. Sakamoto, O. Terasaki, and R. Ryoo, *Stable single-unit-cell nanosheets of zeolite MFI as active and long-lived catalysts.* Nature, 2009. **461**(7261): p. 246-249.

7. Eliášová, P., M. Opanasenko, P.S. Wheatley, M. Shamzhy, M. Mazur, P. Nachtigall, W.J. Roth, R.E. Morris, and J. Čejka, *The ADOR mechanism for the synthesis of new zeolites.* Chemical Society Reviews, 2015. **44**(20): p. 7177-7206.

8. Varoon, K., X. Zhang, B. Elyassi, D.D. Brewer, M. Gettel, S. Kumar, J.A. Lee, S. Maheshwari, A. Mittal, and C.-Y. Sung, *Dispersible exfoliated zeolite nanosheets and their application as a selective membrane.* Science, 2011. **334**(6052): p. 72-75.

9. Díaz, U. and A. Corma, *Layered zeolitic materials: an approach to designing versatile functional solids.* Dalton Transactions, 2014. **43**(27): p. 10292-10316.

10. Opanasenko, M.V., W.J. Roth, and J. Čejka, *Two-dimensional zeolites in catalysis: current status and perspectives.* Catalysis Science & Technology, 2016. **6**(8): p. 2467-2484.

11. Corma, A., V. Fornes, S. Pergher, T.L. Maesen, and J. Buglass, *Delaminated zeolite precursors as selective acidic catalysts.* Nature, 1998. **396**(6709): p. 353.

12. Corma, A., V. Fornes, J. Martınez-Triguero, and S. Pergher, *Delaminated zeolites: Combining the benefits of zeolites and mesoporous materials for catalytic uses.* Journal of Catalysis, 1999. **186**(1): p. 57-63.

13. Gil, B., W. Makowski, B. Marszalek, W.J. Roth, M. Kubu, J. Čejka, and Z. Olejniczak, *High acidity unilamellar zeolite MCM-56 and its pillared and delaminated derivatives.* Dalton Transactions, 2014. **43**(27): p. 10501-10511.

14. Corma, A., U. Diaz, M.E. Domine, and V. Fornés, *New aluminosilicate and titanosilicate delaminated materials active for acid catalysis, and oxidation reactions using H_2O_2.* Journal of the American Chemical Society, 2000. **122**(12): p. 2804-2809.

15. Yang, B., J.-g. Jiang, H. Xu, P. Ji, and P. Wu, *Sub-zeolite of FER topology derived from an interlayer modification of PLS-3 lamellar precursor.* Microporous and Mesoporous Materials, 2015. **203**: p. 54-62.

16. Chica, A., U. Diaz, V. Fornes, and A. Corma, *Changing the hydroisomerization to hydrocracking ratio of long chain alkanes by varying the level of delamination in zeolitic (ITQ-6) materials.* Catalysis today, 2009. **147**(3-4): p. 179-185.

17. Zhu, X., L. Wu, P.C. Magusin, B. Mezari, and E.J. Hensen, *On the synthesis of highly acidic nanolayered ZSM-5.* Journal of catalysis, 2015. **327**: p. 10-21.

18. Jeon, M.Y., D. Kim, P. Kumar, P.S. Lee, N. Rangnekar, P. Bai, M. Shete, B. Elyassi, H.S. Lee, and K. Narasimharao, *Ultra-selective high-flux membranes from directly synthesized zeolite nanosheets.* Nature, 2017. **543**(7647): p. 690.

19. Cao, Z., S. Zeng, Z. Xu, A. Arvanitis, S. Yang, X. Gu, and J. Dong, *Ultrathin ZSM-5 zeolite nanosheet laminated membrane for high-flux desalination of concentrated brines.* Science advances, 2018. **4**(11): p. eaau8634.

20. Jeong, H.-K., W. Krych, H. Ramanan, S. Nair, E. Marand, and M. Tsapatsis, *Fabrication of polymer/selective-flake nanocomposite membranes and their use in gas separation.* Chemistry of Materials, 2004. **16**(20): p. 3838-3845.

21. Zhang, H., Q. Xiao, X. Guo, N. Li, P. Kumar, N. Rangnekar, M.Y. Jeon, S. Al-Thabaiti, K. Narasimharao, and S.N. Basahel, *Open-Pore Two-Dimensional MFI Zeolite Nanosheets for the Fabrication of Hydrocarbon-Isomer-Selective Membranes on Porous Polymer Supports.* Angewandte Chemie International Edition, 2016. **55**(25): p. 7184-7187.

22. Fasano, M., T. Humplik, A. Bevilacqua, M. Tsapatsis, E. Chiavazzo, E.N. Wang, and P. Asinari, *Interplay between hydrophilicity and surface barriers on water transport in zeolite membranes.* Nature Communications, 2016. **7**: p. 12762.

23. Newsome, D.A. and D.S. Sholl, *Predictive assessment of surface resistances in zeolite membranes using atomically detailed models.* The Journal of Physical Chemistry B, 2005. **109**(15): p. 7237-7244.

24. Newsome, D.A. and D.S. Sholl, *Atomically detailed simulations of surface resistances to transport of CH_4, CF_4, and C_2H_6 through silicalite membranes.* Microporous and Mesoporous Materials, 2008. **107**(3): p. 286-295.

25. Teixeira, A.R., C.-C. Chang, T. Coogan, R. Kendall, W. Fan, and P.J. Dauenhauer, *Dominance of surface barriers in molecular transport through silicalite-1.* The Journal of Physical Chemistry C, 2013. **117**(48): p. 25545-25555.

26. Teixeira, A.R., X. Qi, W.C. Conner, T. Mountziaris, W. Fan, and P.J. Dauenhauer, *2D surface structures in small zeolite MFI crystals.* Chemistry of Materials, 2015. **27**(13): p. 4650-4660.

27. Tzoulaki, D., W. Schmidt, U. Wilczok, and J. Kärger, *Formation of surface barriers on silicalite-1 crystal fragments by residual water vapour as probed with isobutane by interference microscopy.* Microporous and Mesoporous Materials, 2008. **110**(1): p. 72-76.

28. Vattipalli, V., X. Qi, P.J. Dauenhauer, and W. Fan, *Long walks in hierarchical porous materials due to combined surface and configurational diffusion.* Chemistry of Materials, 2016. **28**(21): p. 7852-7863.

29. Wloch, J., *Effect of surface etching of ZSM-5 zeolite crystals on the rate of n-hexane sorption.* Microporous and mesoporous materials, 2003. **62**(1-2): p. 81-86.

30. Gueudré, L., E. Jolimaître, N. Bats, and W. Dong, *Diffusion in zeolites: is surface resistance a critical parameter?* Adsorption, 2010. **16**(1-2): p. 17-27.

31. Saint Remi, J.C., A. Lauerer, C. Chmelik, I. Vandendael, H. Terryn, G.V. Baron, J.F. Denayer, and J. Kärger, *The role of crystal diversity in understanding mass transfer in nanoporous materials.* Nature materials, 2016. **15**(4): p. 401.

32. Briend, M., R. Vomscheid, M. Peltre, P. Man, and D. Barthomeuf, *Influence of the Choice of the Template on the Short-and Long-Term Stability of SAPO-34 Zeolite.* The Journal of Physical Chemistry, 1995. **99**(20): p. 8270-8276.

33. Kalantzopoulos, G., A. Policicchio, E. Maccallini, I. Krkljus, F. Ciuchi, M. Hirscher, R. Agostino, and G. Golemme, *Resistance to the transport of H_2 through the external surface of as-made and modified silicalite-1 (MFI).* Microporous and Mesoporous Materials, 2016. **220**: p. 290-297.

34. Hibbe, F., C. Chmelik, L. Heinke, S. Pramanik, J. Li, D.M. Ruthven, D. Tzoulaki, and J.r. Kärger, *The nature of surface barriers on nanoporous solids explored by microimaging of transient guest distributions.* Journal of the American Chemical Society, 2011. **133**(9): p. 2804-2807.

35. Kärger, J., *In-depth study of surface resistances in nanoporous materials by microscopic diffusion measurement.* Microporous and Mesoporous Materials, 2014. **189**: p. 126-135.

36. Arya, G., E.J. Maginn, and H.-C. Chang, *Effect of the surface energy barrier on sorbate diffusion in AlPO4-5.* The Journal of Physical Chemistry B, 2001. **105**(14): p. 2725-2735.

37. Ahunbay, M.G., J.R. Elliott, and O. Talu, *Surface resistance to permeation through the silicalite single crystal membrane: Variation with permeant.* The Journal of Physical Chemistry B, 2004. **108**(23): p. 7801-7808.

38. Thompho, S., R. Chanajaree, T. Remsungnen, S. Hannongbua, P.A. Bopp, and S. Fritzsche, *The Permeation of Methane Molecules through Silicalite-1 Surfaces.* The Journal of Physical Chemistry A, 2009. **113**(10): p. 2004-2014.

39. Eun Jee, S., A.J. McGaughey, and D.S. Sholl, *Molecular simulations of hydrogen and methane permeation through pore mouth modified zeolite membranes.* Molecular Simulation, 2009. **35**(1-2): p. 70-78.

40. Combariza, A.F. and G. Sastre, *Influence of zeolite surface in the sorption of methane from molecular dynamics.* The Journal of Physical Chemistry C, 2011. **115**(28): p. 13751-13758.

41. Zimmermann, N.E., S.P. Balaji, and F.J. Keil, *Surface barriers of hydrocarbon transport triggered by ideal zeolite structures.* The Journal of Physical Chemistry C, 2012. **116**(5): p. 3677-3683.

42. Dutta, R.C. and S.K. Bhatia, *Interfacial barriers to gas transport: probing solid-gas interfaces at the atomistic level.* Molecular Simulation, 2019. **45**(14-15): p. 1148-1162.

43. Knio, O., A.J. Medford, S. Nair, and D.S. Sholl, *Database of Computation-Ready 2D Zeolitic Slabs.* Chemistry of Materials, 2018. **31**(2): p. 353-364.

44. Seo, Y., S. Lee, C. Jo, and R. Ryoo, *Microporous aluminophosphate nanosheets and their nanomorphic zeolite analogues tailored by hierarchical structure-directing amines.* Journal of the American Chemical Society, 2013. **135**(24): p. 8806-8809.

45. Plimpton, S., P. Crozier, and A. Thompson, *LAMMPS-large-scale atomic/molecular massively parallel simulator.* Sandia National Laboratories, 2007. **18**.

46. Witman, M., S. Ling, P. Boyd, S. Barthel, M. Haranczyk, B. Slater, and B. Smit, *Cutting Materials in Half: A Graph Theory Approach for Generating Crystal Surfaces and Its Prediction of 2D Zeolites.* ACS Central Science, 2018.

47. Boulfelfel, S.E., P.I. Ravikovitch, L. Koziol, and D.S. Sholl, *Improved Hill–Sauer force field for accurate description of pores in 8-ring zeolites.* The Journal of Physical Chemistry C, 2016. **120**(26): p. 14140-14148.

48. Hill, J.-R. and J. Sauer, *Molecular mechanics potential for silica and zeolite catalysts based on ab initio calculations. 2. Aluminosilicates.* The Journal of Physical Chemistry, 1995. **99**(23): p. 9536-9550.

49. Bai, P., M. Tsapatsis, and J.I. Siepmann, *TraPPE-zeo: Transferable potentials for phase equilibria force field for all-silica zeolites.* The Journal of Physical Chemistry C, 2013. **117**(46): p. 24375-24387.

50. Martin, M.G. and J.I. Siepmann, *Transferable potentials for phase equilibria. 1. United-atom description of n-alkanes.* The Journal of Physical Chemistry B, 1998. **102**(14): p. 2569-2577.

51. Wick, C.D., M.G. Martin, and J.I. Siepmann, *Transferable potentials for phase equilibria. 4. United-atom description of linear and branched alkenes and alkylbenzenes.* The Journal of Physical Chemistry B, 2000. **104**(33): p. 8008-8016.

52. Fang, H., R. Awati, S.E. Boulfelfel, P.I. Ravikovitch, and D.S. Sholl, *First-principles-derived force fields for CH_4 adsorption and diffusion in siliceous zeolites.* The Journal of Physical Chemistry C, 2018. **122**(24): p. 12880-12891.

53. Hill, J.R. and J. Sauer, *Molecular mechanics potential for silica and zeolite catalysts based on ab initio calculations. 1. Dense and microporous silica.* The Journal of Physical Chemistry, 1994. **98**(4): p. 1238-1244.

54. Fang, H., P. Kamakoti, P.I. Ravikovitch, M. Aronson, C. Paur, and D.S. Sholl, *First principles derived, transferable force fields for CO_2 adsorption in Na-exchanged cationic zeolites.* Physical Chemistry Chemical Physics, 2013. **15**(31): p. 12882-12894.

55. Harris, J.G. and K.H. Yung, *Carbon dioxide's liquid-vapor coexistence curve and critical properties as predicted by a simple molecular model.* The Journal of Physical Chemistry, 1995. **99**(31): p. 12021-12024.

56. Darkrim, F. and D. Levesque, *Monte Carlo simulations of hydrogen adsorption in single-walled carbon nanotubes.* The Journal of chemical physics, 1998. **109**(12): p. 4981-4984.

57. Calero, S., D. Dubbeldam, R. Krishna, B. Smit, T.J. Vlugt, J.F. Denayer, J.A. Martens, and T.L. Maesen, *Understanding the role of sodium during adsorption: A force field for alkanes in sodium-exchanged faujasites.* Journal of the American Chemical Society, 2004. **126**(36): p. 11377-11386.

58. Jakobtorweihen*, S., N. Hansen, and F.J. Keil, *Molecular simulation of alkene adsorption in zeolites.* Molecular Physics, 2005. **103**(4): p. 471-489.

59. Narkhede, V.V. and H. Gies, *Crystal structure of MCM-22 (MWW) and its delaminated zeolite ITQ-2 from high-resolution powder X-ray diffraction data: an*

analysis using Rietveld technique and atomic pair distribution function. Chemistry of Materials, 2009. **21**(18): p. 4339-4346.

60. Rojas, A. and M.A. Camblor, *HPM-2, the layered precursor to zeolite MTF*. Chemistry of Materials, 2014. **26**(2): p. 1161-1169.

61. Zhao, Z., W. Zhang, P. Ren, X. Han, U. Müller, B. Yilmaz, M. Feyen, H. Gies, F.-S. Xiao, and D. De Vos, *Insights into the topotactic conversion process from layered silicate RUB-36 to FER-type zeolite by layer reassembly.* Chemistry of Materials, 2013. **25**(6): p. 840-847.

62. Chen, Y., S. Huang, X. Wang, L. Zhang, N. Wu, F. Liao, and Y. Wang, *Synthesis and Characterization of a Layered Silicogermanate PKU-22 and Its Topotactic Condensation to a Three-Dimensional STI-type Zeolite.* Crystal Growth & Design, 2017. **17**(10): p. 5465-5473.

63. Wheatley, P.S. and R.E. Morris, *Calcination of a layered aluminofluorophosphate precursor to form the zeolitic AFO framework.* Journal of Materials Chemistry, 2006. **16**(11): p. 1035-1037.

64. Moteki, T., W. Chaikittisilp, Y. Sakamoto, A. Shimojima, and T. Okubo, *Role of acidic pretreatment of layered silicate RUB-15 in Its topotactic conversion into pure silica sodalite.* Chemistry of Materials, 2011. **23**(15): p. 3564-3570.

65. Marler, B., N. Ströter, and H. Gies, *The structure of the new pure silica zeolite RUB-24, $Si_{32}O_{64}$, obtained by topotactic condensation of the intercalated layer silicate RUB-18.* Microporous and mesoporous materials, 2005. **83**(1): p. 201-211.

66. Grajciar, L., O. Bludský, W.J. Roth, and P. Nachtigall, *Theoretical investigation of layered zeolite frameworks: Interaction between IPC-1P layers derived from zeolite UTL.* Catalysis today, 2013. **204**: p. 15-21.

67. Grünewald-Lüke, A., H. Gies, U. Müller, B. Yilmaz, H. Imai, T. Tatsumi, B. Xie, F.-S. Xiao, X. Bao, and W. Zhang, *Layered precursors for new zeolitic materials: Synthesis and characterization of B-RUB-39 and its condensation product B-RUB-41.* Microporous and Mesoporous Materials, 2012. **147**(1): p. 102-109.

68. Marler, B., M. Camblor, and H. Gies, *The disordered structure of silica zeolite EU-20b, obtained by topotactic condensation of the piperazinium containing layer silicate EU-19.* Microporous and mesoporous materials, 2006. **90**(1): p. 87-101.

69. Basaldella, E.I. and J. Tara, *Modification of crystallite morphology during synthesis of LTA zeolite using triethanolamine as additive.* Materials Letters, 1998. **34**(3-6): p. 119-123.

70. Kim, E., W. Cai, H. Baik, and J. Choi, *Uniform Si-CHA Zeolite Layers Formed by a Selective Sonication-Assisted Deposition Method.* Angewandte Chemie International Edition, 2013. **52**(20): p. 5280-5284.

71. Brown, W.M., P. Wang, S.J. Plimpton, and A.N. Tharrington, *Implementing molecular dynamics on hybrid high performance computers–short range forces.* Computer Physics Communications, 2011. **182**(4): p. 898-911.

72. Hockney, R.W. and J.W. Eastwood, *Computer simulation using particles*. 1988: crc Press.

73. Dubbeldam, D., S. Calero, D.E. Ellis, and R.Q. Snurr, *RASPA: molecular simulation software for adsorption and diffusion in flexible nanoporous materials.* Molecular Simulation, 2016. **42**(2): p. 81-101.

74. Pranami, G. and M.H. Lamm, *Estimating error in diffusion coefficients derived from molecular dynamics simulations.* Journal of chemical theory and computation, 2015. **11**(10): p. 4586-4592.

75. Liu, L., D. Nicholson, and S.K. Bhatia, *Interfacial resistance and length-dependent transport diffusivities in carbon nanotubes.* The Journal of Physical Chemistry C, 2016. **120**(46): p. 26363-26373.

76. Sholl, D.S., *Understanding macroscopic diffusion of adsorbed molecules in crystalline nanoporous materials via atomistic simulations.* Accounts of chemical research, 2006. **39**(6): p. 403-411.

77. Krishna, R. and J.M. Van Baten, *A molecular dynamics investigation of the diffusion characteristics of cavity-type zeolites with 8-ring windows.* Microporous and Mesoporous Materials, 2011. **137**(1): p. 83-91.

78. Ling, C. and D.S. Sholl, *Using first-principles calculations to predict surface resistances to H_2 transport through metal alloy membranes.* Journal of Membrane Science, 2007. **303**(1-2): p. 162-172.

79. Wirawan, S.K., D. Creaser, J. Lindmark, J. Hedlund, I.M. Bendiyasa, and W.B. Sediawan, *H_2/CO_2 permeation through a silicalite-1 composite membrane.* Journal of membrane science, 2011. **375**(1-2): p. 313-322.

80. *MATLAB*. R2016b (9.1.0.441655), The MathWorks Inc.: Natick, Massachusetts.

81. Shen, X., W. Mao, Y. Ma, D. Xu, P. Wu, O. Terasaki, L. Han, and S. Che, *A hierarchical MFI zeolite with a two-dimensional square mesostructure.* Angewandte Chemie, 2018. **130**(3): p. 732-736.

82. Luna-Triguero, A., A. Sławek, R. Sánchez-de-Armas, J.J. Gutiérrez-Sevillano, C.O. Ania, J.B. Parra, J.M. Vicent-Luna, and S. Calero, *π-Complexation for olefin/paraffin separation using aluminosilicates.* Chemical Engineering Journal, 2020. **380**: p. 122482.

83. Findley, J.M., P.I. Ravikovitch, and D.S. Sholl, *The effect of aluminum short-range ordering on carbon dioxide adsorption in zeolites.* The Journal of Physical Chemistry C, 2018. **122**(23): p. 12332-12340.

CHAPTER 4. ATOMISTIC MODELING OF ZEOLITIC NANOTUBES

4.1 Introduction

Single walled nanotubes (SWNT) are nanoscale building blocks with highly desirable electrical, thermal, and mechanical properties. Carbon nanotubes are the most famous member of this family and have been investigated for a variety of applications including biosensors, biomedical devices, transistors, supercapacitor electrodes, strengthening reinforcement agents, and battery anodes.[1-6]

One drawback facing carbon nanotubes is the inability to readily functionalize the inner surface for a particular application.[7] The addition of moieties requires converting carbon atoms in SWNTs from sp^2 to sp^3 hybridization. This is a difficult conversion, and is only possible on the outer surface under harsh conditions.[7] However, the concave nature of the inner surface renders this conversion thermodynamically unfavorable, so the inner surface is considered unreactive except under certain extreme conditions.[7-9]

Synthetic metal oxide nanotubes, such as aluminosilicate and aluminogermanate have proven easier to functionalize.[7, 10-13] Single walled aluminosilicate nanotubes consist of a an aluminum (III) hydroxide outer wall and a silanol inner wall, with a total wall thickness of 0.7 nm.[7] Johnson and Pinnavaia functionalized aluminosilicate nanotubes with (γ-aminopropyl)triethoxysilane while Kang et al. applied acetyl chloride, methyltrimethoxysilane, and trichlorosilane.[14, 15]

If zeolitic nanotubes could be created they would be another possible nanoscale building block. The existence of zeolite nanosheets motivates the possibility of creating zeolitic nanotubes. Zeolite nanosheets exhibit fast catalysis due to the short distance normal to the height of the sheet.[16] However, the synthesis of hierarchical mesoporous zeolite nanosheet architectures, such as pillared structures and multilamellar stacks is difficult due to the tendency to undergo partial condensation after calcination.[16-22] Zeolite nanotubes, should they be synthesized, could open interesting routes to mesoporous zeolite structures with applications that could extend beyond separations and catalysis. The modeling methods developed earlier in this thesis to describe zeolite nanosheets make it possible to consider possible structures of zeolitic nanotubes. In this chapter we describe a method to generate atomically accurate zeolite nanotube models using the nanosheets described in Chapter 2. We then produce XRD patterns for these model structures to aid in structure identification if experiments are performed aiming to synthesize these materials.

4.2 Methods

We developed an algorithm that expands a nanosheet and curls it to obtain a nanotube. A brief overview of the process is shown in **Figure 4.1**, where we started with a 2 nm MFI (010) slab from the database in Chapter 2, expanded it ten times along the (001) axis, then curled it into the final structure shown in Figure **4.1(d)**. For each nanosheet, two different nanotubes can be made depending on which of the two axes in the plane of the nanotube was expanded prior to curling.

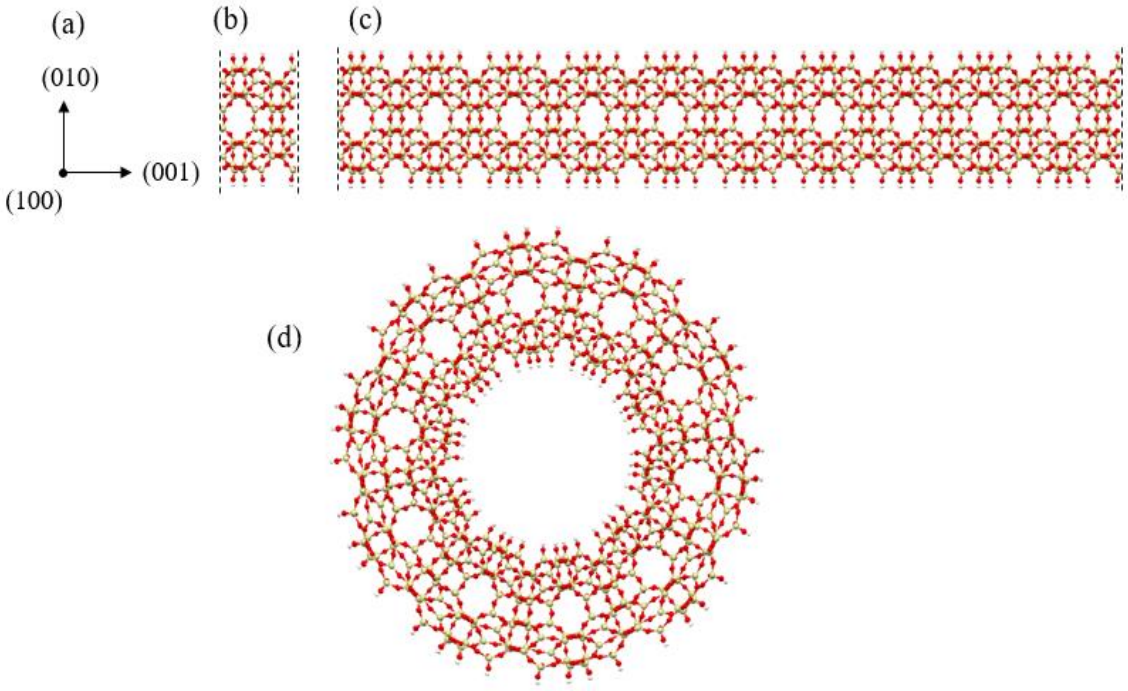

Figure 4.1. (a) A Miller index coordinate axis with (100) pointing into the plane of the page. The coordinate axis describes the orientations of the structures in (b) and (c). (b) An MFI (010) slab with a height of 2 nm. (c) An MFI (010) slab expanded ten times in the (001) direction. (d) An MFI (010) zeolite nanotube with the b axis in the radial direction, the c axis in the azimuthal direction, and the a axis in the axial direction.

To curl a nanosheet, our algorithm requires three items as input: the axis along which the nanotube is expanded, the number of unit cells included in the circumference of the nanotube, and the inner radius of the nanotube, R_{inner}.

The curling step is complicated because it generates a new x' and y' coordinate for each atom. The z' coordinate is equal to the coordinate on the axis normal to the plane of the nanosheet. The algorithm first measures three distances needed to curl: $L_{supercell}$, the length of the expanded unit cell, $L_{vertical}$, the distance between the atom in question and the plane intersecting the bottom-most atom in the structure, and $L_{horizontal}$, the distance

between the atom in question and the vertical wall of the original unit cell. The dimensions are illustrated in **Figure 4.2**. It then calculates θ such that:

$$\theta = \frac{L_{horizontal}}{L_{supercell}} \times 360° \tag{4.1}$$

and a radius:

$$R_{atom} = R_{inner} + L_{vertical} \tag{4.2}$$

where R_{atom} is the distance between the center and the atom's new position. Finally, x' and y' are calculated:

$$x' = R_{atom} \times \cos\theta, \; y' = R_{atom} \times \sin\theta \tag{4.3}$$

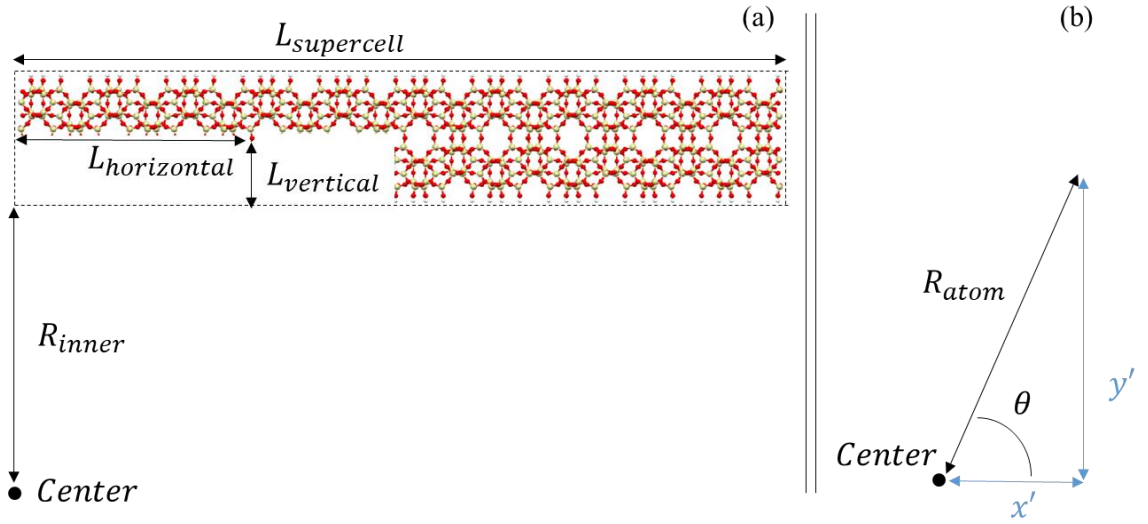

Figure 4.2. (a) The four distances needed in order to transform an atomic coordinate from an expanded slab to a nanotube. A rectangular section of the expanded slab is removed from the image for a better view of the distance labels. (b) The x' and y' coordinates shown in relation to R_{atom} and θ.

4.3 Results and Discussion

We first made two different nanotubes made from the same 2 nm MFI (010) slab starting structure as shown in **Figure 4.3**. For the nanotube in **Figure 4.3 (a)**, Nanotube-1 (NT-1), the slab was expanded ten times in the (100) direction while for NT-2, the slab was expanded 10 times in the (001) direction. However, they both have a 2.8 nm inner diameter by design and a 7.2 nm outer diameter due to the height of the nanosheet. The structures shown in **Figure 4.3** did not involve any relaxation of any atoms in the nanotubes; they are purely geometrical constructions from the initial coordinates in the underlying nanosheet.

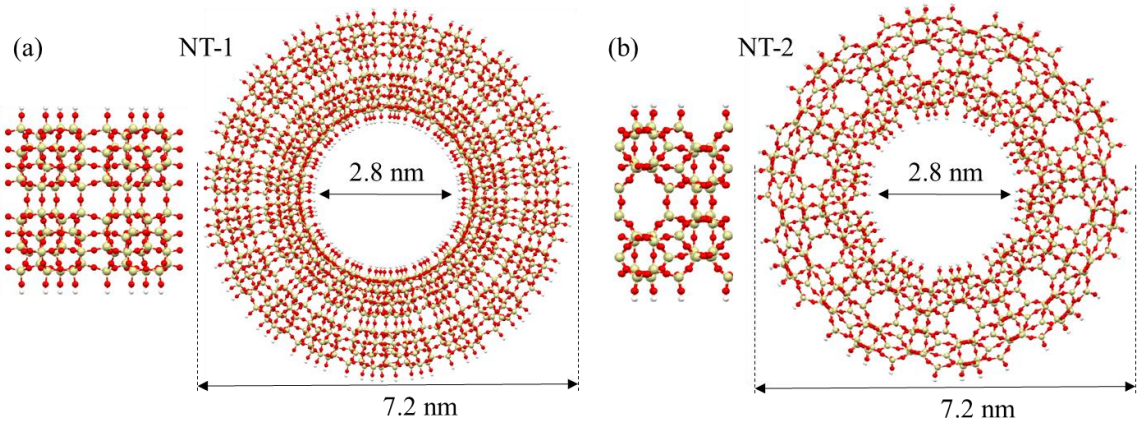

Figure 4.3. (a) A 2 nm MFI (010) slab and its nanotube with the b axis in the radial direction, the a axis in the azimuthal direction, and the c axis in the axial direction. (b) The 2 nm MFI (010) slab and its nanotube with the b axis in the radial direction, the c axis in the azimuthal direction, and the a axis in the axial direction.

A single nanosheet can generate a wide variety of nanotubes based on the input parameters, so it is useful to employ a descriptor to define the nanotube. NT-1 can be referred to as MFI–(2.2, 20.2, 2.8, b, a, c), where 2.2, 20.2, and 2.8 nm refer to the height of the nanosheet, the length of the expanded sheet prior to curling, and the inner diameter of the nanotube. The axes b, a, and c refer to the axis normal to the plane of the nanosheet

(radial direction of nanotube), the axis along which the nanosheet is expanded (azimuthal direction of nanotube), and the axis along the axial direction of the nanotube. Similarly, NT-2 can be defined as MFI–(2.2, 13.3, 2.8, b, c, a). Our descriptor assumes expanding and curling along the original unit cell axes. To describe extension and curling along axes with a larger Miller index, a more complex descriptor may be necessary. We further note that in this chapter, all nanosheets used are from the database described in Chapter 2, and the nanosheet chosen had a surface with the least number of broken bonds from among the set of nanosheets with the same framework and Miller index.

The nanotubes in **Figure 4.3** have strained bond lengths. Bonds on the outer surface are larger than bonds on the inner surface because the algorithm expanded the distance between atoms to fill the outer circumference and contracted them to fill the inner circumference. The average Si-O bond length in an MFI unit cell relaxed by ReaxFF[23] is 1.56 Å. However, the Si-O bond length of the innermost NT-1 bond is ~0.86 Å and the outermost bond length of the NT-2 bond is 2.3 Å, as shown in **Table 4.1**.

Table 4.1 – Nanotube Si-O Bond Lengths (2 nm Thick Wall)

Nanotube	Inner Bond (Å)	Outer Bond (Å)
NT-1	0.86	1.63
NT-2	1.30	2.30

Since the amount of expanding and contracting needed to fit the circumferences is proportional to the height of the slab, we used a thinner nanosheet to obtain better Si-O bond lengths. The nanotubes NT-3 and NT-4 are made from the 1 nm MFI (010) nanosheet shown in **Figure 4.4(a)** expanded in the (100) direction six times, curled, and then then relaxed with the ReaxFF force field.[23] However, NT-3 was given a slightly larger initial

inner diameter (4.2 nm) than NT-4 (3.0 nm), so NT-3's outer bonds broke during relaxation. The nanotubes prior to relaxation are shown in **Figure 4.4(b)** and **4.4(d)** and the post relaxation structures are shown in **Figure 4.4(c)** and **4.4(e)**. The inner diameters of both nanotubes are smaller post relaxation. NT-3 and NT-4 are described respectively as MFI–(1.2, 12.1, 3.1, b, a, c) and MFI–(1.2, 12.1, 2.6, b, a, c).

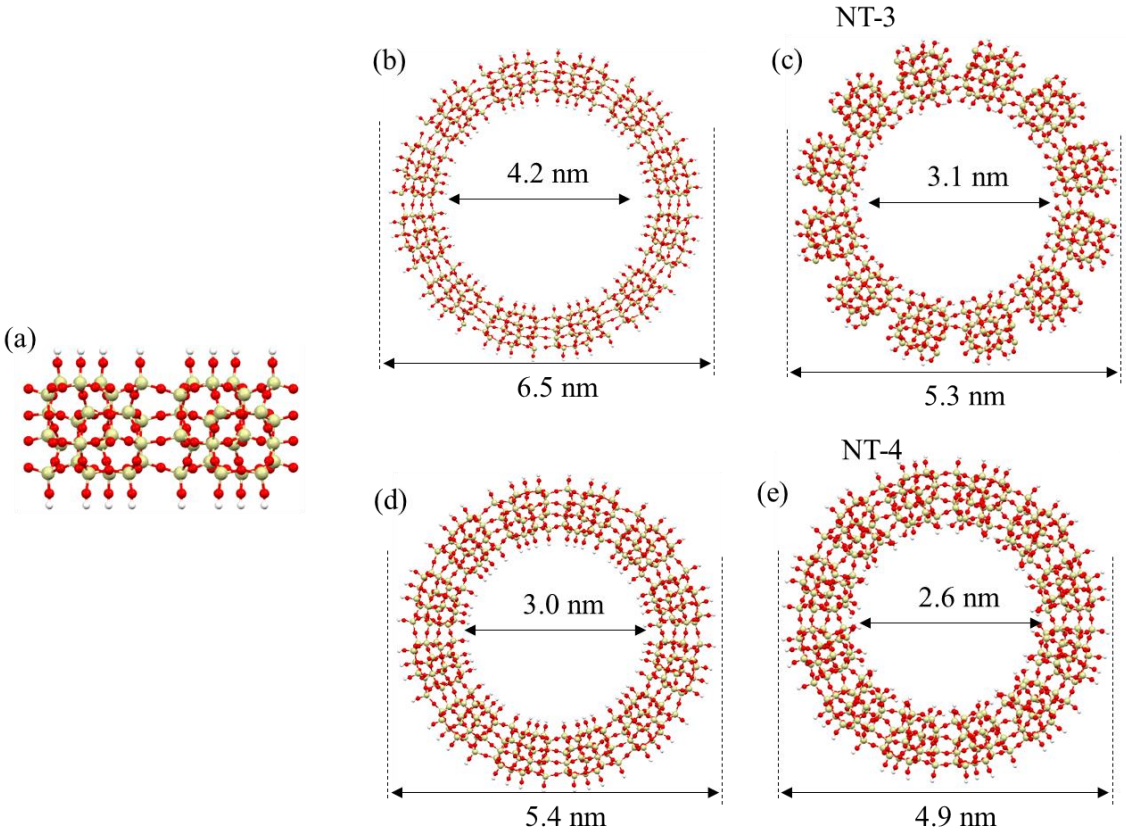

Figure 4.4. (a) The 1 nm MFI (010) slab used as the basis for the four nanotubes. (b) A nanotube before relaxation, MFI–(1.2, 121, 4.2, b, a, c), and (c) the nanotube after relaxation, MFI–(1.2, 121, 3.1, b, a, c), labeled as NT-3. The nanotube shown in (d) is generated using the same conditions as (b) but its inner diameter is smaller. Its structure after relaxation is shown in (e) and labeled as NT-4.

The Si-O bond lengths for NT-3 and NT-4 are shown in **Table 4.2** Overall, they are closer to the bulk MFI bond length of 1.55 Å. This shows that a thinner slab wall is likely more favorable than a thicker one. Since ReaxFF allows for bond breaking,[23] some NT-3 Si atoms were left without O bridges to neighboring Si. In solution, water molecules or silica fragments could bond to such sites leading to deviations from the pristine MFI framework.

Table 4.2 – Nanotube Si-O Bond Lengths (1 nm Thick Wall)

Nanotube	Inner Bond (Å)	Outer Bond (Å)
NT-3	1.56	1.55
NT-4	1.56	1.59

The nanotube models could be useful in identifying an experimental nanotube structure using simulated diffraction patterns. In **Figure 4.5**, we compare the simulated XRD patterns from bulk MFI to the simulated XRD patterns of NT-3 and NT-4. The nanotube unit cells have 5 nm of vacuum between the outer nanotube edge and each of the four cell walls as shown in Appendix **Figure C.1**. Bulk MFI has two intense peaks at 2θ = 8.0° and 8.9° and a less intense peak from 2θ = 23.0° to 25.0°. In the nanotubes, the less intense peak disappears and a new intense peak is formed at 2θ = 5°. The low angle peak is replaced by a less intense, broad peak, in both nanotubes, but NT-3 has a more intense replacement peak than NT-4.

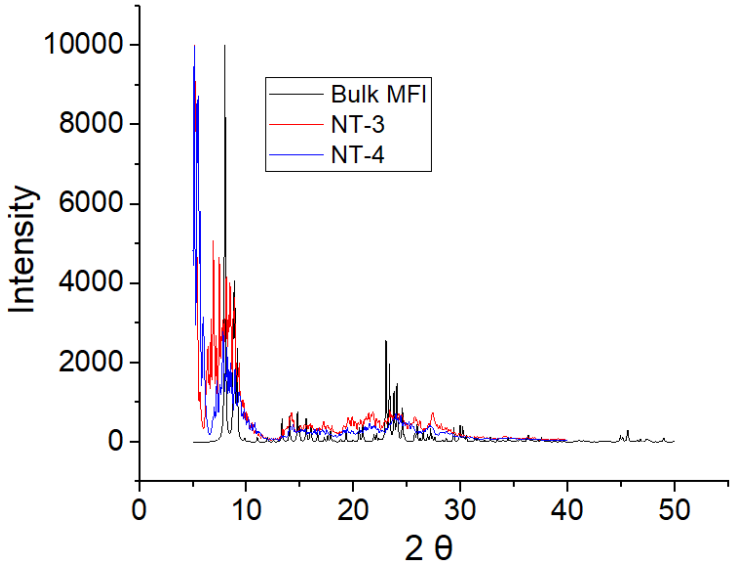

Figure 4.5. XRD patterns for bulk MFI, NT-3, and NT-4.

The differences between the bulk MFI spectrum and the nanotube spectra indicate that knowledge of the bulk zeolite framework spectra is likely insufficient to readily characterize a nanotube from that framework. Therefore, because our method can generate structures for specific candidate nanotubes our models could be useful for generating simulated XRD patterns to compare to experimentally obtained XRD results. Since our models are continuous unit cells, they may also be used to generate IR and ED patterns for further comparisons.

Our methods are generalizable to any 2D slab structure. Using several slabs from the database described in Chapter 2, we have generated structures from different frameworks as shown in Appendix C. In principle this effort could be extended to the full range of zeolite nanosheets examined in earlier chapters, but because of the paucity of experimental data it is likely that the first applications of these methods will be to help understand specific targeted structures in experiments.

4.4 Conclusion

Zeolite nanotubes, if they could be produced, may be useful as nanoscale building blocks. In this chapter, we developed an algorithm that curls nanosheets into nanotubes using trigonometric calculations. Simulated nanotube XRD patterns differed from simulated bulk XRD patterns of the same zeolite topology, so knowledge of bulk XRD patterns will likely not be enough to identify nanotube XRD patterns. Therefore, we believe our method of nanotube curling could be useful in identifying possible experimentally synthesized structures.

4.5 References

1. Alim, S., J. Vejayan, M.M. Yusoff, and A. Kafi, *Recent uses of carbon nanotubes & gold nanoparticles in electrochemistry with application in biosensing: a review.* Biosensors and Bioelectronics, 2018. **121**: p. 125-136.

2. White, A.A., S.M. Best, and I.A. Kinloch, *Hydroxyapatite–carbon nanotube composites for biomedical applications: a review.* International Journal of Applied Ceramic Technology, 2007. **4**(1): p. 1-13.

3. Che, Y., H. Chen, H. Gui, J. Liu, B. Liu, and C. Zhou, *Review of carbon nanotube nanoelectronics and macroelectronics.* Semiconductor Science and Technology, 2014. **29**(7): p. 073001.

4. Fisher, R.A., M.R. Watt, and W.J. Ready, *Functionalized carbon nanotube supercapacitor electrodes: a review on pseudocapacitive materials.* ECS Journal of Solid State Science and Technology, 2013. **2**(10): p. M3170.

5. Liu, Y. and S. Kumar, *Polymer/carbon nanotube nano composite fibers–a review.* ACS applied materials & interfaces, 2014. **6**(9): p. 6069-6087.

6. De las Casas, C. and W. Li, *A review of application of carbon nanotubes for lithium ion battery anode material.* Journal of Power Sources, 2012. **208**: p. 74-85.

7. Kang, D.-Y., N.A. Brunelli, G.I. Yucelen, A. Venkatasubramanian, J. Zang, J. Leisen, P.J. Hesketh, C.W. Jones, and S. Nair, *Direct synthesis of single-walled aminoaluminosilicate nanotubes with enhanced molecular adsorption selectivity.* Nature communications, 2014. **5**(1): p. 1-9.

8. Chamberlain, T.W., J.C. Meyer, J. Biskupek, J. Leschner, A. Santana, N.A. Besley, E. Bichoutskaia, U. Kaiser, and A.N. Khlobystov, *Reactions of the inner surface of carbon nanotubes and nanoprotrusion processes imaged at the atomic scale.* Nature chemistry, 2011. **3**(9): p. 732.

9. Giambastiani, G., S. Cicchi, A. Giannasi, L. Luconi, A. Rossin, F. Mercuri, C. Bianchini, A. Brandi, M. Melucci, and G. Ghini, *Functionalization of multiwalled carbon nanotubes with cyclic nitrones for materials and composites: addressing the role of CNT sidewall defects.* Chemistry of Materials, 2011. **23**(7): p. 1923-1938.

10. Kang, D.-Y., J. Zang, E.R. Wright, A.L. McCanna, C.W. Jones, and S. Nair, *Dehydration, dehydroxylation, and rehydroxylation of single-walled aluminosilicate nanotubes.* Acs Nano, 2010. **4**(8): p. 4897-4907.

11. Zanzottera, C., A.l. Vicente, E. Celasco, C. Fernandez, E. Garrone, and B. Bonelli, *Physico-chemical properties of imogolite nanotubes functionalized on both*

external and internal surfaces. The Journal of Physical Chemistry C, 2012. **116**(13): p. 7499-7506.

12. da Silva, M.C., E.C. dos Santos, M.P. Lourenço, M.P. Gouvea, and H.A. Duarte, *Structural, electronic, and mechanical properties of inner surface modified imogolite nanotubes.* Frontiers in Materials, 2015. **2**: p. 16.

13. Paineau, E., *Imogolite nanotubes: a flexible nanoplatform with multipurpose applications.* Applied Sciences, 2018. **8**(10): p. 1921.

14. Johnson, L.M. and T.J. Pinnavaia, *Hydrolysis of (γ.-aminopropyl) triethoxysilane-silylated imogolite and formation of a silylated tubular silicate-layered silicate nanocomposite.* Langmuir, 1991. **7**(11): p. 2636-2641.

15. Kang, D.-Y., J. Zang, C.W. Jones, and S. Nair, *Single-walled aluminosilicate nanotubes with organic-modified interiors.* The Journal of Physical Chemistry C, 2011. **115**(15): p. 7676-7685.

16. Choi, M., K. Na, J. Kim, Y. Sakamoto, O. Terasaki, and R. Ryoo, *Stable single-unit-cell nanosheets of zeolite MFI as active and long-lived catalysts.* Nature, 2009. **461**(7261): p. 246-249.

17. Xu, D., Y. Ma, Z. Jing, L. Han, B. Singh, J. Feng, X. Shen, F. Cao, P. Oleynikov, and H. Sun, *π–π interaction of aromatic groups in amphiphilic molecules directing for single-crystalline mesostructured zeolite nanosheets.* Nature Communications, 2014. **5**: p. 4262.

18. Zhang, Y., Y. Ma, and S. Che, *Synthesis of lamellar mesostructured ZSM-48 nanosheets.* Chemistry of Materials, 2018. **30**(6): p. 1839-1843.

19. Seo, Y., S. Lee, C. Jo, and R. Ryoo, *Microporous aluminophosphate nanosheets and their nanomorphic zeolite analogues tailored by hierarchical structure-directing amines.* Journal of the American Chemical Society, 2013. **135**(24): p. 8806-8809.

20. Zhang, X., D. Liu, D. Xu, S. Asahina, K.A. Cychosz, K.V. Agrawal, Y. Al Wahedi, A. Bhan, S. Al Hashimi, and O. Terasaki, *Synthesis of self-pillared zeolite nanosheets by repetitive branching.* Science, 2012. **336**(6089): p. 1684-1687.

21. Na, K., C. Jo, J. Kim, K. Cho, J. Jung, Y. Seo, R.J. Messinger, B.F. Chmelka, and R. Ryoo, *Directing zeolite structures into hierarchically nanoporous architectures.* Science, 2011. **333**(6040): p. 328-332.

22. Shen, X., W. Mao, Y. Ma, D. Xu, P. Wu, O. Terasaki, L. Han, and S. Che, *A hierarchical MFI zeolite with a two-dimensional square mesostructure.* Angewandte Chemie, 2018. **130**(3): p. 732-736.

23. Senftle, T.P., S. Hong, M.M. Islam, S.B. Kylasa, Y. Zheng, Y.K. Shin, C. Junkermeier, R. Engel-Herbert, M.J. Janik, and H.M. Aktulga, *The ReaxFF reactive force-field: development, applications and future directions.* npj Computational Materials, 2016. **2**: p. 15011.

CHAPTER 5. TESTING THE FEASIBILITY OF QUANTITATIVELY MODELING ZEOLITE DEALUMINATION WITH THE REAXFF FORCE FIELD

5.1 Introduction

Zeolites are widely used as catalysts in industry.[1] They are used extensively for oil refining, petrochemistry, and the production of specialty chemicals. Their success as catalysts is due to their high surface area and adsorption capacity as well as the ability to control the hydrophilicity of their channels and the strength and concentration of their acid sites.[1] In addition, the ~200 known zeolite frameworks have a wide range of pore characteristics, which provide shape selectivity for the reactant, product, or transition state that can be used to direct catalytic activity towards the desired product and away from undesired side reactions.[1]

A pure silica zeolite has an elemental composition of SiO_2. Most industrial zeolites replace some Si atoms with Al, turning Si-O-Si sequences into Si-OX-Al sequences, where the Al has a net negative charge that is offset by a positively charged species X near the bridging O. Here, X can be an H atom or a cation such as Li, K, Na, or Ca. These Si-OX-Al sites are acidic and are considered the active catalytic sites in zeolites, so their chemical integrity is necessary to maintain catalytic activity.[2]

Unfortunately, water is known to attack Al sites and, through a series of reactions, remove aluminum atoms from zeolites.[3] A detailed mechanistic explanation for dealumination is unfortunately not yet available.[3] Swang et al. studied dealumination with

DFT and proposed a disilanol intermediate with a high activation energy.[4, 5] Silaghi et al. identified a more favorable pathway involving nondissociative water adsorption on Al using DFT.[6, 7] Nielsen et al. found that the Al-O hydrolysis energy barrier is decreased when more water molecules are in the system.[8] Sun et al. found that cationic zeolites have higher energy barriers than protonic zeolites because the Al-O bonds do not break concurrently with the dissociation of water.[3]

The drawback to the DFT based methods used in previous studies is their computational burden. In addition, most of the DFT studies mentioned use one or two water molecules.[3-8] In reality, tens of water molecules could be present in a zeolite's pores and these clusters could greatly change the reaction dynamics.[2] Joshi et al. used ReaxFF[2], a reactive molecular dynamics force field that can simulate reactions orders of magnitude faster than DFT to investigate proton hopping in zeolite channels. They found that the larger the number of water molecules in a cluster, the lower the activation barrier to proton hopping since more water molecules could now share the charge burden.[2]

The use of the ReaxFF force field for the study of zeolite dealumination would be ideal due to its speed, but the accuracy of ReaxFF for such calculations in unknown. There is no body of evidence suggesting that ReaxFF can calculate dealumination activation energies, Gibbs free energies, or heats of reaction comparable to DFT results. In this chapter, we compare the heats of reaction found by ReaxFF to the heats of reaction found recently by Sun et al. using DFT for zeolite dealumination.[3]

5.2 Methods

Sun et al. studied twenty two reaction pathways for H-LTA, Na-LTA, K-LTA, and Ca-LTA Al-O hydrolysis reactions using plane wave DFT calculations with the PBEsol + D3 functional.[3] They used the nudged elastic band method to find transition states, then calculated the activation energy and Gibbs free energy. They also found the final state energy, from which a ΔH_{rxn} could be obtained.[3]

To evaluate the ReaxFF force field, we chose to compare against the Sun et al.[3] values for ΔH_{rxn} since ΔH_{rxn} allows a quantitative comparison of the different computational methods with relatively simple calculations. We used the Joshi et al. ReaxFF force field version since a subset of its parameters pertaining to the Al-O bond were refitted to better describe aluminosilicate geometries.[2]

Sun et al. relaxed their unit cells to obtain geometries that minimized the strain on the atoms as calculated by DFT forces.[3] However, the bond lengths and angles that minimize strain using one DFT or MD treatment usually differ slightly from their ideal equivalents using a different treatment. Therefore, we relaxed the initial state and final state unit cells (formerly relaxed with DFT) from each reaction mechanism using LAMMPS geometry optimization with the ReaxFF force field. For each structure, we ran the optimization cycle 20 times with an energy tolerance of 1E-8.

5.3 Results and Discussion

We first examine the effect of relaxation on a structure using the Sun et al. HLTA-H_2O-path3-IS unit cell[3] as an example. The name indicates that the structure is an LTA unit cell with a H atom rather than a cation on the bridging oxygen, has only one water in

the vicinity of the Al atom, and describes the geometry of the initial state of the third possible dealumination path proposed and examined.[3] In **Table 5.1**, we compare the unit cell parameters of HLTA-H_2O-path3-IS cell prior to our relaxation (i.e. the structure as relaxed by Sun et al.) and after relaxation (using LAMMPS and ReaxFF). We find that ReaxFF preferred a slightly smaller unit cell with angles that are closer to 90° by a fraction of a degree.

Table 5.1 - Cell Parameter Comparison

Method	a (Å)	b (Å)	c (Å)	alpha (°)	Beta (°)	gamma (°)
Sun et al. (DFT Relaxed)[3]	11.95	11.98	11.84	89.7	89.9	89.5
This work (ReaxFF Relaxed)	11.91	11.91	11.73	90	90	89.47

For a better understanding of the origin of the difference in unit cell parameters, we can examine individual bonds and angles from the unit cell before and after relaxation with the ReaxFF force field. In **Figure 5.1**, we show a section of the unit cell featuring an Al atom, a nearby H_2O molecule, a bridging OH group, and an Si-O-Si-O connection to the rest of the structure. All other atoms in the unit cell have been removed for clarity. Select interatomic distances and angles are labeled and numbered.

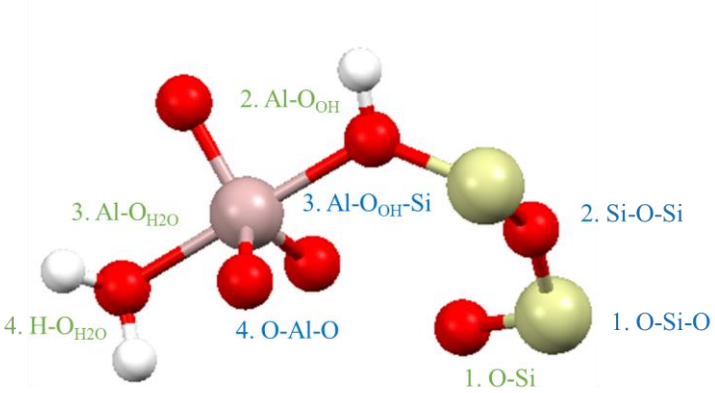

Figure 5.1. A portion of an LTA unit cell with select bonds and angles labeled in green and blue respectively. The atoms are colored as follows, H: white, O: red, Al: pink, Si: beige.

The bond and angle measurements for the atoms shown in **Figure 5.1** are displayed in **Tables 5.2** and **5.3**. **Table 5.2** shows that ReaxFF predicts shorter bonds for O-Si, but larger bonds around Al and between the water molecule's O and H atoms. **Table 5.3** shows that angles involving Si and O differ by up to 6° from their DFT counterparts, whereas angles involving Al differ up to 16° from their DFT counterpart. Although The Joshi et al. version of the ReaxFF force field was parametrized to obtain more accurate bonds and angles involving Al,[2] the pure silica geometries still bear a closer resemblance to the DFT description. These comparisons show that a ReaxFF relaxation was carried out successfully and the resulting structure was optimized to a different geometry.

Table 5.2 – Bond Distance Comparison

Method	1 O-Si (Å)	2 Al-O_{OH} (Å)	3 Al-O_{H2O} (Å)	4 H-O_{H2O} (Å)
Sun et al. (DFT Relaxed)[3]	1.62	2.035	2.059	0.985
This work (ReaxFF Relaxed)	1.575	2.166	2.079	1.023

Table 5.3 – Angle Comparison

Method	1 O-Si-O (°)	2 Si-O-Si (°)	3 Al-O_{OH}-Si (°)	4 O-Al-O (°)
Sun et al. (DFT Relaxed)[3]	112.32	155.22	128.08	116.34
This work (ReaxFF Relaxed)	106.29	154.94	144.50	102.15

Figure 5.2 compares the ΔH_{rxn} using three different methods. The DFT ΔH_{rxn} is obtained directly from the Sun et al. data,[3] so it compares the energies of the initial state unit cell as relaxed by DFT and the final state unit cell as relaxed by DFT. Therefore, it uses DFT relaxed geometries and DFT potentials. The ReaxFF Relaxed ΔH_{rxn} uses ReaxFF relaxed geometries and ReaxFF potentials. The ReaxFF t_0 data uses DFT relaxed geometries with a ReaxFF potential. The values for the latter data set were gathered at the 0^{th} time step of the relaxation, i.e. before the geometry was changed by ReaxFF. The ReaxFF Relaxed data has a lower ΔH_{rxn} than the ReaxFF t_0 data. However, neither data set matches the DFT data in any quantitative way.

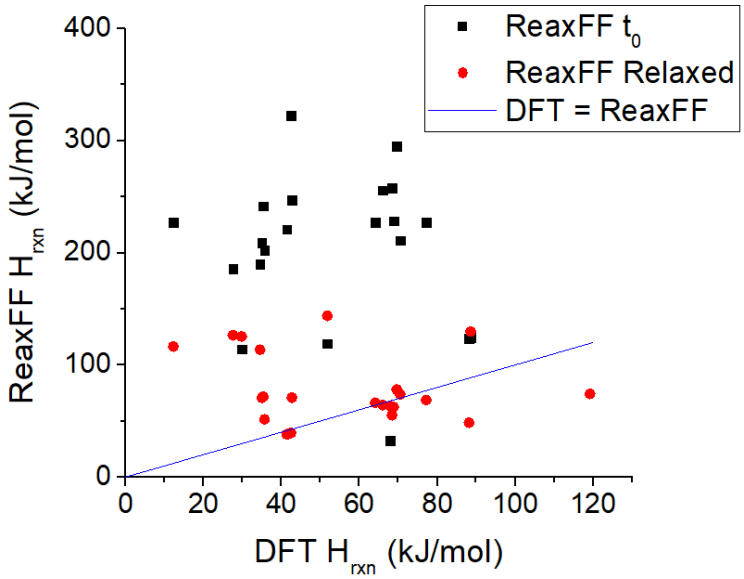

Figure 5.2. A parity plot of DFT ΔH_{rxn} and ReaxFF ΔH_{rxn} obtained at the DFT configurations of Sun et al. and upon completion of the relaxation algorithm with ReaxFF.

To investigate further why the ReaxFF Relaxed dataset in **Figure 5.2** did not match the DFT dataset, we considered a simpler situation consisting of a unit cell with a methane and a silanol molecule with the formula $O(SiO_3H_3)_2$. We placed the two molecules at various distances apart and calculated the interaction energies:

$$E_{interaction} = E_{silanol,methane} - (E_{silanol} + E_{methane}) \qquad (5.1)$$

where $E_{silanol,methane}$ is the energy of the unit cell with silanol and methane, $E_{silanol}$ is the energy of the silanol molecule in isolation, and $E_{methane}$ is the energy of the methane molecule in isolation. The methane and silanol molecule geometries were obtained from Fang et al. who relaxed them using the DFT/CC (Coupled Cluster) method.[9, 10] We calculated the interaction energies using the DFT/CC relaxed geometries with the ReaxFF potential, so we again term these energies ReaxFF t_0 in **Figure 5.3**, which compares the

interaction energy from this work to the interaction energy calculated by Fang et al. with DFT/CC.[9]

In both this work and that of Fang et al, the geometries of both molecules were kept rigid while calculating the energy in isolation and in the combined unit cell.[9] Therefore, the internal energy of the molecules is expected to cancel out and leave only the interaction energy. We expect the interaction energy to converge to 0 as the C-O distance approaches infinity. This trend is observed in the DFT/CC data from Fang et al., but the ReaxFF energies in **Figure 5.3**, converge to approximately -13 kJ/mol for large separations.

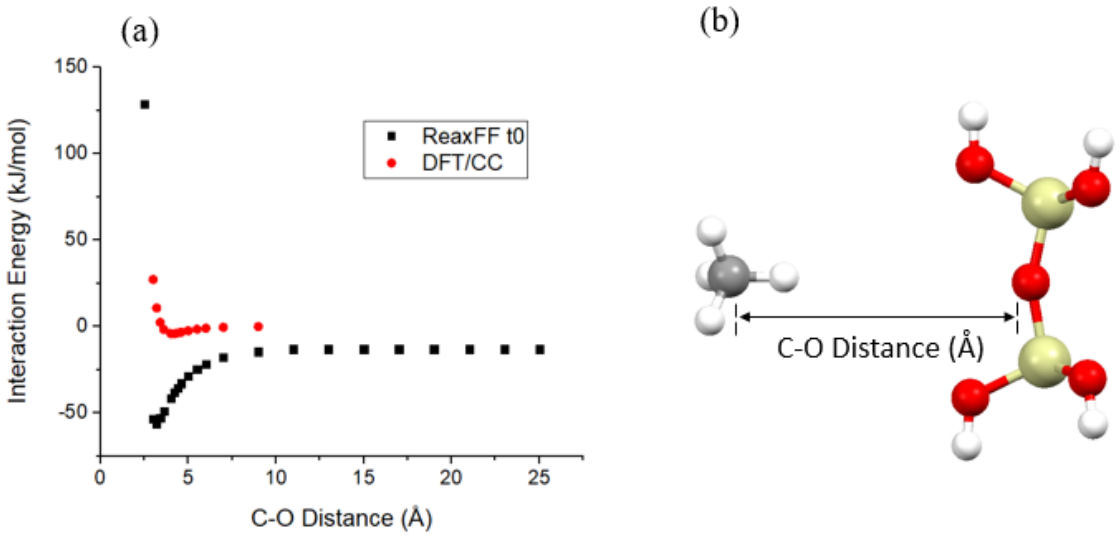

Figure 5.3. (a) The interaction energy calculated using DFT by Fang et al.[9] and calculated using ReaxFF in the current work. (b) The methane and silanol molecules considered.

The origin of the unphysical behavior by ReaxFF in **Figure 5.3** can be understood by examining the charge on each molecule. A key feature of ReaxFF is that is dynamically assigns point charges to each depending on their local environment. At the large

separations shown in **Figure 5.3**, the methane molecule had a charge of 0.13e while the silanol cluster had a charge of -0.13e, a clearly unphysical result. It is important to note that when ReaxFF is applied to a large simulation volume that contains only a single CH_4 molecule or silanol cluster, the net charge on each set of atoms is zero, as physically expected.

We performed a final set of simulations with a single Na and Cl atom together in a unit cell. They were placed at separate distances, and the charge (positive on the Na and negative on the Cl) was calculated with ReaxFF. The results are shown in **Figure 5.4**. The partial charge decreases until it levels off to ±0.46e at 10 Å. Again, this is an unphysical result and confirms that ReaxFF cannot adequately handle long-distance charge transfer.

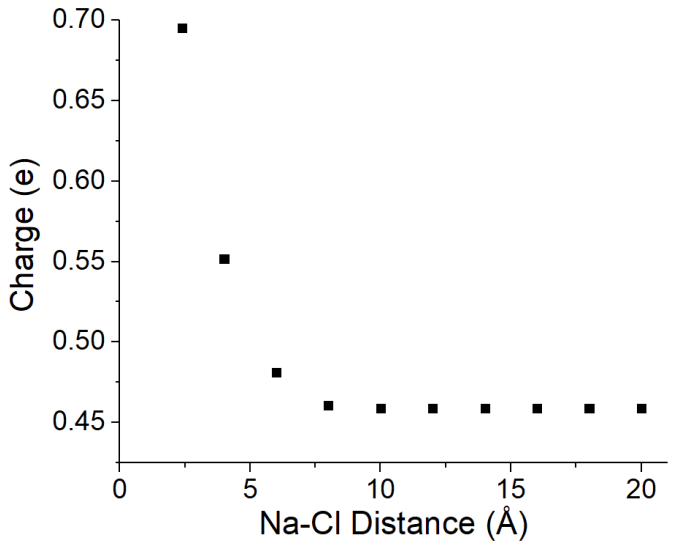

Figure 5.4. The net charge on the Na and Cl atom at various distances as computed with ReaxFF.

The Qeq algorithm used to equilibrate charges for ReaxFF attempts to minimize the Gibbs free energy of electron transfer.[11, 12] In other words, it assumes that all atoms in the system have interacted sufficiently to share electrons.[12] In reality, charge transfer is a function of the distance between atoms as well as the propensity of electron

transfer.[11, 13] Verstraelen, Vandenbrande, and Ayers have made progress in developing potentials to fully incorporate distance in charge distribution algorithms.[13, 14] However, the problem is non-trivial since the potentials needed are complex and cannot fit easily into a molecular dynamics framework. This remains an ongoing topic of research.[13, 14] Since dealumination requires accurate charge transfer between water clusters and the framework, ReaxFF cannot be used to study the topic.

We note that the ReaxFF force field was used in several places in preceding chapters to relax zeolitic nanostructures. The structures that were used in those instances were all continuous zeolites or, in Chapter 2, an H_2O molecule in isolation. It therefore seems likely that ReaxFF is far more reliable in giving physically plausible structures in those instances than in the dealumination examples examined above.

5.4 Conclusion

We have described tests of the ReaxFF force field for describing dealumination by water in zeolites by comparing results from force field calculations with previous DFT calculations. Unfortunately, our results indicate that ReaxFF cannot be used to study zeolite dealumination quantitatively. The inaccuracy of ReaxFF in this case is rooted in unphysical charge partitioning that can occur between chemically distinct species, which leads to unphysical charges that give unreliable dealumination energies.

5.5 References

1. Corma, A., *From microporous to mesoporous molecular sieve materials and their use in catalysis.* Chemical reviews, 1997. **97**(6): p. 2373-2420.

2. Joshi, K.L., G. Psofogiannakis, A.C. Van Duin, and S. Raman, *Reactive molecular simulations of protonation of water clusters and depletion of acidity in H-ZSM-5 zeolite.* Physical Chemistry Chemical Physics, 2014. **16**(34): p. 18433-18441.

3. Sun, J., H. Fang, P.I. Ravikovitch, and D.S. Sholl, *Understanding Dealumination Mechanisms in Protonic and Cationic Zeolites.* The Journal of Physical Chemistry C, 2019.

4. Fjermestad, T., S. Svelle, and O. Swang, *Mechanistic Comparison of the Dealumination in SSZ-13 and the Desilication in SAPO-34.* The Journal of Physical Chemistry C, 2013. **117**(26): p. 13442-13451.

5. Malola, S., S. Svelle, F.L. Bleken, and O. Swang, *Detailed reaction paths for zeolite dealumination and desilication from density functional calculations.* Angewandte Chemie International Edition, 2012. **51**(3): p. 652-655.

6. Silaghi, M.-C., C. Chizallet, E. Petracovschi, T. Kerber, J. Sauer, and P. Raybaud, *Regioselectivity of Al–O bond hydrolysis during zeolites dealumination unified by brønsted–evans–polanyi relationship.* ACS Catalysis, 2015. **5**(1): p. 11-15.

7. Silaghi, M.-C., C. Chizallet, J. Sauer, and P. Raybaud, *Dealumination mechanisms of zeolites and extra-framework aluminum confinement.* Journal of Catalysis, 2016. **339**: p. 242-255.

8. Nielsen, M., R.Y. Brogaard, H. Falsig, P. Beato, O. Swang, and S. Svelle, *Kinetics of zeolite dealumination: insights from H-SSZ-13.* ACS Catalysis, 2015. **5**(12): p. 7131-7139.

9. Fang, H., R. Awati, S.E. Boulfelfel, P.I. Ravikovitch, and D.S. Sholl, *First-principles-derived force fields for CH_4 adsorption and diffusion in siliceous zeolites.* The Journal of Physical Chemistry C, 2018. **122**(24): p. 12880-12891.

10. Bludský, O., M. Rubeš, P. Soldán, and P. Nachtigall, *Investigation of the benzene-dimer potential energy surface: DFT/CCSD (T) correction scheme.* The Journal of chemical physics, 2008. **128**(11): p. 114102.

11. Senftle, T.P., S. Hong, M.M. Islam, S.B. Kylasa, Y. Zheng, Y.K. Shin, C. Junkermeier, R. Engel-Herbert, M.J. Janik, and H.M. Aktulga, *The ReaxFF reactive force-field: development, applications and future directions.* npj Computational Materials, 2016. **2**: p. 15011.

12. Verstraelen, T., P. Bultinck, V. Van Speybroeck, P. Ayers, D. Van Neck, and M. Waroquier, *The significance of parameters in charge equilibration models.* Journal of chemical theory and computation, 2011. **7**(6): p. 1750-1764.

13. Verstraelen, T., S. Vandenbrande, and P.W. Ayers, *Direct computation of parameters for accurate polarizable force fields.* The Journal of chemical physics, 2014. **141**(19): p. 194114.

14. Verstraelen, T., P. Ayers, V. Van Speybroeck, and M. Waroquier, *ACKS2: Atom-condensed Kohn-Sham DFT approximated to second order*. The Journal of chemical physics, 2013. **138**(7): p. 074108.

CHAPTER 6. CONCLUSION

6.1 Thesis Impact

Separating chemical mixtures with thermal distillation uses a significant portion of the world's energy. Replacing distillation columns with membranes could reduce the energy dedicated to chemical separation and lead to reductions in greenhouse gas emissions. Zeolites are widely studied for use as membranes due to their chemical stability and pore sizes in the range of many common industrial chemicals. Zeolite membranes consist of an active layer of μm sized zeolite crystals above a stronger, pressure bearing substrate. An increase in flux is required for commercial viability so research groups have focused on developing ever thinner zeolite membranes. A recent development is the ability to synthesize zeolite nanosheets, which are 2D materials with thicknesses of around 2 nm. These materials have exhibited faster diffusion than 3D zeolites, so they have generated much interest in their properties.

Zeolite diffusion studies usually focus on diffusion through the crystal phase and neglect the effect of the surface on movement into or out of the crystal. Since most studies examine μm sized crystals, the effect of the surface is assumed to be negligible. However, in a nanosheet with a height of 2 nm, the surface resistance could play a larger role in diffusion.

Molecular simulations require atomically accurate models of zeolite nanosheets to probe surface properties, but prior to this work, there was no computation ready database of slabs that resembled experimental nanosheets. Therefore, in Chapter 2 we developed a database of 800,000 zeolite slab structures. We used a python code to develop surfaces by

minimizing the number of bonds broken while severing the bulk unit cell. The slabs consist of structures with a set height that can be used directly and others with an arbitrary height that require assembly prior to use. The latter type consists of slab surfaces that can terminate any number of bulk unit cells to form a slab with a predetermined height. To test the accuracy of our methods, we compared our slabs to synthesized nanosheets and found that our database contains a representation of every known zeolite nanosheet. We were also able to predict crystal morphologies for structures with high Si/Al ratios. The result is a database with realistic 2D nanosheets that can be used for investigations of zeolite surface properties.

In Chapter 3 we asked if surfaces can significantly affect diffusion though a nanosheet. We investigated seven different molecules, a range of temperatures, high and low loadings, a range of nanosheet heights, and nanosheets from various frameworks. We used molecular dynamics to compare diffusion in bulk and slab structures and calculated a surface resistance, which describes the extent to which the surface slows diffusion. We found that in almost all the conditions we studied, the surface exhibited more resistance than the zeolite phase.

Molecules with higher heats of adsorption have higher surface resistance because they are more attracted to the framework and are therefore slower to desorb. Low temperature exhibits high surface resistance because it decreases the energy available for desorption. High loadings decrease surface resistance because they allow molecules to desorb from an adsorption layer at a distance farther from the zeolite surface. Nanosheets as large as 10 nm in height were found to exhibit roughly the same magnitude of surface resistance as nanosheets 2 nm in height. Nanosheets from frameworks with high heats of

adsorption exhibited higher surface resistance than those from frameworks with low heats of adsorption. Overall, we conclude that surface resistance is an activated process with energy needed to overcome the desorption step.

The dominance of surface resistance in nanosheets effects their ideal selectivity. In the bulk phase, zeolites are widely known to favor CO_2 over H_2 due to higher CO_2 loading. However, we found that slabs favor H_2 because CO_2 has a higher heat of adsorption and therefore higher surface resistance. Our pure silica bulk MFI simulations show little ideal selectivity for C_2 and C_3 olefin/paraffin species. However, we found that paraffins have slightly higher heats of adsorption and surface resistances than olefins, so the nanosheet ideal selectivity favored olefins. Therefore, surface resistances can be harnessed to improve a membrane's separation ability.

There exists no published literature on the existence of zeolite nanotubes, but they could be prove adaptable molecular building blocks should they be synthesized. In Chapter 4, we used slabs from our database to make zeolite nanotube models. We describe an algorithm that expands a nanosheet and curls it into a nanotube using trigonometric operations. We compared simulated bulk XRD patterns to simulated nanotube XRD patterns from the same framework and found that they were different, so knowledge of bulk characterizations is insufficient to identify and prove the synthesis of a nanotube. Therefore, our nanotubes could provide simulated nanotube characterization patterns to match against experimental data.

Dealumination is the process by which water molecules gradually remove Al atoms from zeolite frameworks leading to a reduction in the zeolite's catalytic ability. In Chapter

5, we attempted to study zeolite dealumination using the ReaxFF force field. We compare our data to that generated using DFT methods and found that ReaxFF gives unrealistic results. We traced this back to the ReaxFF charge partitioning function's inability to fully take distance into account when assigning charges. Since dealumination simulations would include water clusters unbound to the framework, the inability to assign the system correct charges render's ReaxFF's results meaningless.

6.1 Suggested Future Work

Our 2D slab database can be used to study a wide variety nanosheet properties. Since synthesis strategies for new nanosheets remain elusive, one could obtain a better understanding of zeolite synthesis thermodynamics by examining the affinity of structure directing agents to the zeolite pores. To study catalytic properties, our pure silica structures can be augmented with Al and cations to give realistic representations of acid sites. The aluminosilicate slabs can then be used in DFT calculations to better understand surface reactions mechanisms. Finally, our database could aid in the characterization of new nanosheets and their derivative structures such as zeolite nanotubes.

The nanosheets we used to study surface resistance were pure silica slabs suspended in vacuum. It would be useful to investigate realistic structures such as hierarchical zeolites to test the effects of nanosheet spacing and column density. The vacuum layer around nanosheets is responsible for the surface resistance, so diminishing it by columns or excessively close nanosheets could decrease the surface resistance. Finally, the addition of cations to our structures could increase their ideal selectivities, especially for olefin/paraffin separations.

APPENDIX A. SUPPORTING INFORMATION FOR CHAPTER 2

A.1 Explanatory Tables

Table A.1 - Miller Indices Observed on Experimentally Reported Crystal Habits

Framework	Miller Indices
EDI [1]	{111}, {110}, {001}
MER [1]	{111}, {110}
MAZ [1]	{100}, {102}
PHI [1]	{110}, {010}, {001}
GIS [1]	{101}, {100}
ABW [1]	{130}, {111}, {110}, {101}, {010}
SOD [2]	{100}
ANA [1]	{211}, {100}
LTA [3]	{110}, {100}
LAU [1]	{-201}, {110}, {100}, {001}
THO [1]	{010}, {110}, {100}, {001}
NAT [1]	{111}, {110}, {100}
MFI [4]	{101}, {100}, {010}

Table A.1 was used to choose the Maximum Absolute Miller index (MMI) for the database. It was compiled by noting the Miller indices identified on the crystal surfaces of various zeolites (observed in SEM images) [1-4]. Of the 36 Miller indices shown, 32 (89%) Miller indices had an MMI =1, 3 (8%) Miller indices had an MMI=2, and 1 (3%) Miller index had an MMI=3. The scarcity of Miller indices with MMI=3 indicated that generating surfaces with an MMI > 2 would likely not be fruitful.

Table A.2 - A Comparison of Relaxed and Unrelaxed Unit Cells

		Cell Dimensions (Å)			Cell Angles (°)			Cell Volume (Å^3)
Framework	Status	a	b	c	α	β	γ	
AEL	IZA	8.31	18.73	13.39	90	90	90	2085
AEL	Relaxed	8.32	18.26	13.46	90	90	90	2044
AFO	IZA	9.76	25.61	8.33	90	90	90	2083
AFO	Relaxed	9.71	25.26	8.31	90	90	90	2038
FER	IZA	19.02	14.30	7.54	90	90	90	2051
FER	Relaxed	18.57	14.04	7.42	90	90	90	1935
HEU	IZA	17.52	17.64	7.40	90	116	90	2055
HEU	Relaxed	17.62	17.46	7.37	90	116	90	2036
LTA	IZA	11.92	11.92	11.92	90	90	90	1693
LTA	Relaxed	11.82	11.82	11.82	90	90	90	1650
MFI	IZA	20.09	19.74	13.14	90	90	90	5211
MFI	Relaxed	20.16	19.86	13.29	90	90	90	5324
MTF	IZA	9.63	30.39	7.25	90	90	90	2122
MTF	Relaxed	9.50	30.65	7.29	90	90	90	2124
MWW	IZA	14.39	14.39	25.20	90	90	120	4519
MWW	Relaxed	14.30	14.31	24.75	90	90	120	4385
NSI	IZA	14.13	5.25	8.93	90	105	90	639
NSI	Relaxed	13.92	5.05	8.65	90	105	90	587
RWR	IZA	7.81	7.81	27.35	90	90	90	1667
RWR	Relaxed	7.68	7.68	27.30	90	90	90	1610
SOD	IZA	8.97	8.97	8.97	90	90	90	721
SOD	Relaxed	8.74	8.74	8.74	90	90	90	667
STI	IZA	13.50	17.80	17.94	90	90	90	4313
STI	Relaxed	13.73	17.34	17.73	90	90	90	4221
UTL	IZA	29.00	13.97	12.45	90	105	90	4872
UTL	Relaxed	29.55	13.88	12.44	90	105	90	4931

Table A.2 shows that cell volume and dimensions are smaller in the cells relaxed with the ReaxFF force field relative to unrelaxed cells from the IZA database [5]. The angles remain identical. The frameworks were chosen to represent those in **Figure 8** as well as two commonly used frameworks, LTA and AEL [6-9].

Table A.3 - Statistics on MFI Primary Surface Terminations

LRUC (Miller Index)	Average Removal Steps	Terminating Surfaces (%)	Primary Surfaces
001	2.9	100	96
010	1.2	100	87
011	4.3	100	96
012	5.9	76	192
021	6.3	90	192
100	1.4	100	93
101	3.1	74	96
102	3.4	99	192
110	3.6	55	96
111	7.7	30	96
112	7.8	26	192
120	5.0	75	192
121	7.2	43	192
122	8.2	16	192
201	4.3	94	192
210	4.3	87	188
211	7.3	33	291
212	8.6	21	192
221	8.6	9	192
All (Weighted Average)	4.8	60	3059

The step responsible for the generation of most surfaces is targeted removal, which attempts to converge upon all Q^3 surface (hereby termed terminating surface) for each primary surface. It is therefore of interest to obtain a measure of the "effectiveness" of this algorithm at reaching its objective. A study conducted on all examined Miller indices of MFI divided "effectiveness" into two criteria: the percentage of primary surfaces for which a terminating surface was found, and the average number of targeted removal steps needed to reach a terminating surface. The results of the two criteria are shown in the middle two columns in **Table A.3**. The first column is the Miller index of the LRUC, and the last column is the number of primary surfaces in that LRUC. Overall, at least one terminating

surface was found for each LRUC, and 60% of the surfaces terminated with an average of 4.8 steps. Since the algorithm allowed for 9 steps, we assume it was robust enough to capture most surfaces of interest.

A.2 Naming Surfaces

Slabs are named based on their upper and lower primary surfaces and number of removal steps needed to converge upon their upper and lower applied surfaces (surfaces obtained after Q^m removal). Usually, identical applied surfaces are obtained by a different number of removal steps from different primary surfaces. Therefore, the primary surface that gave rise to the applied surface using the least number of removal steps is used to name the surface.

For example, the slab "zz_EMTff-[1,0,2]-L-0.0949825_3-U-0.903703_3-ss-39.6736472808" is an EMT framework slab from an LRUC with a (1,0,2) Miller index that has a lower applied surface that was obtained after 3 targeted corrections (indicated by '_3') from the lower primary surface formed by eliminating all Si underneath the Si at z = 0.0949825 (fractional coordinate at c axis). While another primary surface may have led to this applied surface, 3 was the minimum number of removal steps needed.

The upper applied surface was obtained after 3 targeted corrections (indicated by '_3') from the upper primary surface formed by eliminating all Si above the Si at z = 0.0903703 (fractional coordinate at c axis). The 'ss' indicates that the upper and lower surfaces come from the same surface symmetry family. The final number, 39.6736472808, is the height from the topmost Si to the bottommost Si in Å.

A.3 Broken Bond Tolerance

The surface generation step produces many surfaces, of which only few will likely ever be synthesized. The objective of the elimination step is to reduce the size of the database while keeping the most promising surfaces. Surface energies (as discussed in Chapter 2) are a measure of the energetic favorability of the bulk relative to the surface, so they can be used as a measure of "promise". However, surface energies are not known *a priori* because they must be calculated after slab generation. Therefore, the broken bond count, which can be easily obtained *in situ*, was used as an estimate of surface energy.

A question of interest is then how to establish broken bond tolerance used to screen the surfaces at each Miller index. A tolerance of 100% means that only surfaces with the minimum number of broken bonds (BB_{min}) are generated. A tolerance of 130%, the final value we settled on, means that surfaces within 130% of BB_{min} can be produced. To allow surface with more than BB_{min}, there must be evidence to prove that the surface with BB_{min} is not necessary the surface with the minimum surface energy (SE_{min}). **Figure A.1** is generated from all 152,992 surfaces for which BB_{min} and SE_{min} for the group of surfaces in each Miller index were recorded during the relaxation of the slab termination pairs. It shows that in 56% of Miller indices, the SE_{min} came from a surface with BB_{min}, and in 100% of Miller indices (by definition only) the SE_{min} came from a surface with a 130% tolerance of BB_{min}. Therefore, about 44% of Miller indices had an SE_{min} from a surface that did not have BB_{min}, so surfaces with more than BB_{min} of broken bonds are not necessarily unattainable from a thermodynamic point of view.

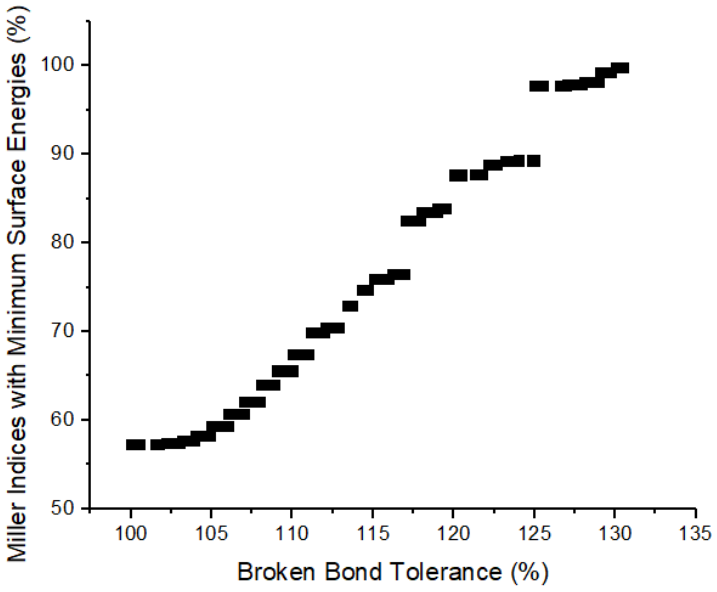

Figure A.1. The % of Miller indices for which the surface with the minimum surface energy can be found within a specified broken bond tolerance.

A.4 Cell Symmetry

The original (unrelaxed) MFI unit cell has two rows (**Figure A.2**) of Si atoms that are related to each other by a glide plane shift. The fractional coordinates are displayed in **Table A.4**. There are more symmetry relationships throughout the cell because the atom coordinates are generated by applying symmetry operations to an original asymmetric set of Si and O [10].

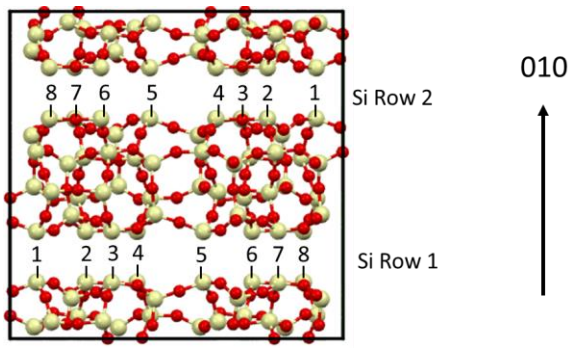

Figure A.2. Two rows of Si that are symmetrically related in the MFI unit cell.

Table A.4 - Fractional Coordinates in the Unrelaxed MFI Unit Cell

	Si Row 1			Si Row 2		
Si	x	y	z	-x	y + 0.5	-z
1	0.0805	0.1726	0.1805	0.9195	0.6726	0.8195
2	0.2267	0.1722	0.5402	0.7733	0.6722	0.4598
3	0.3053	0.1712	0.2092	0.6947	0.6712	0.7908
4	0.3815	0.1721	0.5183	0.6185	0.6721	0.4817
5	0.5805	0.1762	0.3195	0.4195	0.6726	0.6805
6	0.7267	0.1722	0.9598	0.2733	0.6722	0.0402
7	0.8053	0.1712	0.2908	0.1947	0.6712	0.7092
8	0.8815	0.1721	0.9817	0.1185	0.6721	0.0183

A.5 Radial Distribution Function (RDF)

An RDF is computed to sort surfaces related by symmetry operations into distinct families. The first step, obtaining the Si atoms with at least one broken bond, is illustrated in **Figure A.3(a,b)**. The final RDF fingerprint is a histogram of interatomic distances with a bin-size of 0.5 Å and a cutoff of 8 Å. Each bin of the RDF contains the number of interatomic distances that fall within its boundaries. The RDF in **Table A.5** is determined from the interatomic distances in **Figure A.3(c)**. For example, the 3 - 3.5 Å bin has a count of "2" because a pair of atoms is 3.1 Å apart, and a histogram will record that distance twice. Surfaces are grouped into the same surface symmetry family if every bin of the RDF is identical.

Table A.5 – RDF for Figure A.3(c)

RDF Bins (Å)	0 - 0.5	0.5 - 1	1 - 1.5	1.5 - 2	2 - 2.5	2.5 - 3	3 - 3.5	3.5 - 4
	4 - 4.5	4.5 - 5	5 - 5.5	5.5 - 6	6 - 6.5	6.5 - 7	7 - 7.5	7.5 - 8
RDF Fingerprint	0	0	0	0	0	0	2	0
	0	0	0	2	0	0	0	0

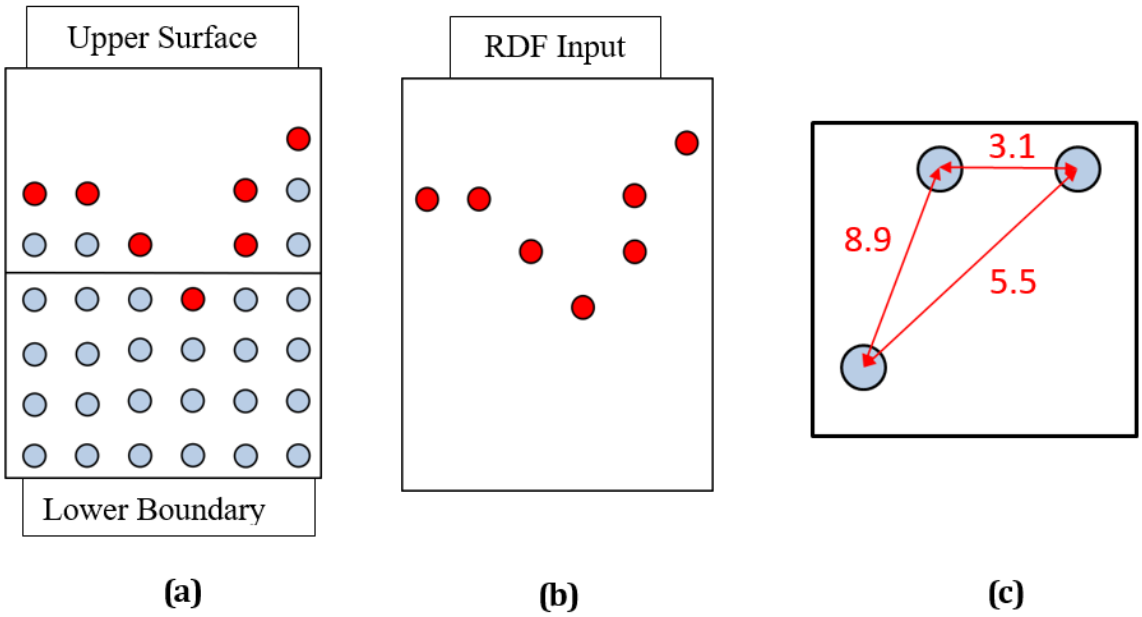

Figure A.3. (a) The upper surface cell after many targeted removals is shown with tetrahedrally coordinated Si in blue and Si with broken bonds in red. (b) Only atoms with at least 1 broken bond are used as input to the RDF to give the surface fingerprint. (c) A simple example of the interatomic distances used to generate the RDF.

A.6 Discontinuity

Figure 3 illustrates the formation of slabs of varying thickness from upper and lower surfaces. However, during slab generation, when upper and lower surfaces were very close, the resulting structure was a series of disconnected silica islands and not a nanosheet, as shown in **Figure A.4(a,b)**. This phenomena was not limited to one unit cell thick slabs. It was therefore of interest to check for discontinuities during slab formation to ensure that all slabs in the database were continuous. A simple algorithm was used to check if, starting from any atom A, any atom B could be reached by jumping from one neighboring Si to the other. First, each slab was expanded in the lamellar direction to form a 2*2*1 supercell as shown in **Figure A.4(c)**. Then, an atom was (effectively randomly) chosen and its nearest

neighbors (< 3.4 Å) were added to a list of connected atoms. Then, the neighbors' neighbors were added, and so forth. The adding algorithm ceased once all the atoms it could reach were already in the connected atoms list. Finally, the size of the list was compared to the number of Si in the 2*2*1 supercell to see if all had been added. The expansion at the beginning was to ensure the ability to detect structures that were connected within a unit cell but not connected to neighboring unit cells.

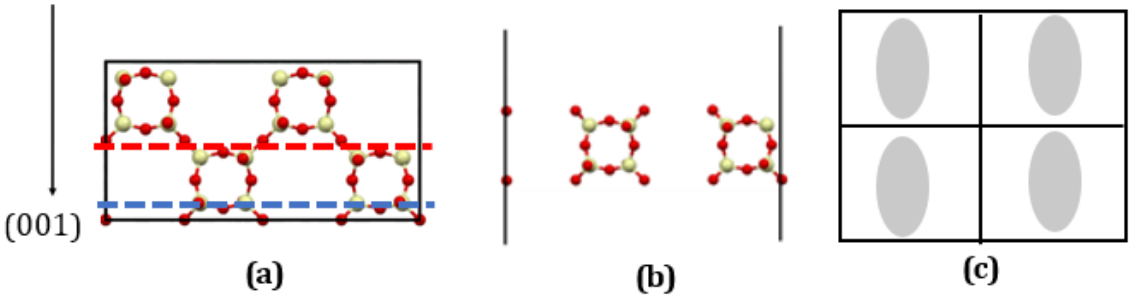

Figure A.4. (a) An APD unit cell with dashed lines representing an upper (red) and lower (blue) surface from the same surface symmetry family. (b) The one unit cell thick slab formed from the surfaces in (a) is discontinuous. (c) A 2*2*1 supercell used to test for discontinuity. Each square represents a unit cell, and the grey areas represent silica regions. The silica regions are continuous onto themselves but are not bonded to neighboring silica regions. Legend: The arrow is normal to the (001) surface in (a) and (b). In (c), the surface normal is into the plane of the page.

A.7 Assembly Step of Slab Termination Pair

A question of interest during the formation of the slabs was how many LRUCs to add. Since the Si-Si maximum bond distance used was 3.4 Å, an attachment zone was defined 3.4 Å above and below the combination/splitting boundary (dotted line in **Figure A.5(b)**). In this zone, all atoms were rigid to allow for assembly and disassembly without structural mismatches. The region 5 Å beneath the two H atoms nearest to the center on each end

was declared the mobile zone and would subsequently be relaxed. If upon the initial combination of a slab, the mobile zone intruded into the attachment zone, extra LRUCs was added to each side (top and bottom) until there was no overlap between the attachment and mobile zones. Only then did relaxation commence.

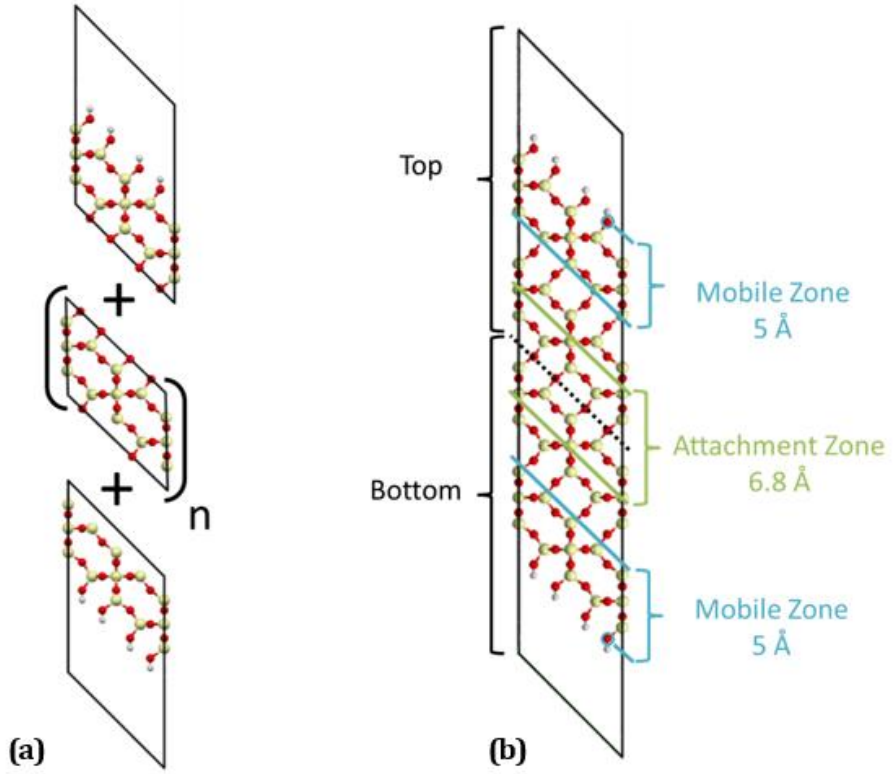

Figure A.5. (a) Upper and lower surface unit cells are combined with a number of LRUCs (b) The newly formed slab will be relaxed then split into a new pair of upper and lower surfaces across the boundary between the LRUCs from which it was formed (dotted line).

A.8 Simulated Annealing

Though the surfaces were relaxed with conjugate gradient descent, the relaxation method did not converge up on the lowest known local energy minima in all instances. An initial relaxation method explored energy space with a simplified simulated annealing

procedure prior to conjugate gradient descent. This single-step annealing method cooled the silanol groups from 300 K to 1 K within 10 ps. Although simulated annealing reached lower local minima in some instances as shown in **Figure A.6**, it was abandoned because it also caused the abstraction of H from silanol groups and/or the abstraction of OH groups from Si atoms and subsequently higher surface energies in other instances.

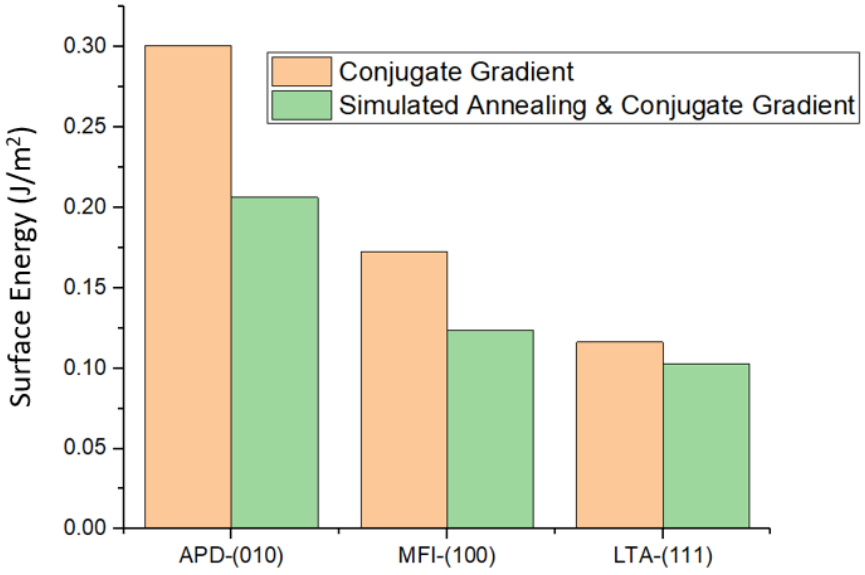

Figure A.6. Relaxation that included simulated annealing found lower local energy minima than conjugate gradient alone.

A.9 LTA Surface Comparison

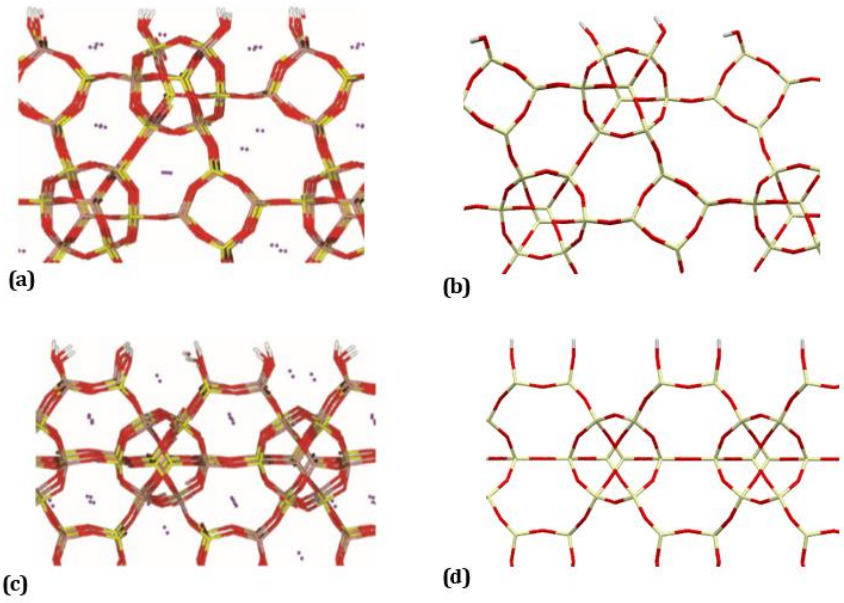

Figure A.7. (a) The {111} LTA surface which gave the lowest energy in the simulations of Gren et al.[11] is represented in the current database (b). (c) The {100} LTA surface which gave the lowest energy in the simulations of Gren et al.[11] is represented in the current database (d).

A.10 Software

The software packages used to conduct the research in this chapter are as follows:

- Pymatgen 4.4.0 was used to make LRUCs and Wulff Constructions [12].
- Atomic Simulation Environment (ASE) 3.11.10 was used to read in and manipulate unit cells [13].
- LAMMPS 11/17/2016 was used for structure and surface relaxation [14].
- Conda Version 4.3.21 was used to simplify the creation of a python environment for visualizing the Wulff constructions.

A.11 References

1. Habib Ghobarkar, O.S., Yvan Massiani, Philippe Knauth, *The reconstruction of natural zeolites*. 2003: Kluwer Academic Publishers. 146.

2. Holden, M.A., P. Cubillas, M.P. Attfield, J.T. Gebbie, and M.W. Anderson, *Growth mechanism of microporous zincophosphate sodalite revealed by in situ atomic force microscopy.* Journal of the American Chemical Society, 2012. **134**(31): p. 13066-13073.

3. Basaldella, E.I. and J. Tara, *Modification of crystallite morphology during synthesis of LTA zeolite using triethanolamine as additive.* Materials Letters, 1998. **34**(3-6): p. 119-123.

4. Qin, Z., L. Lakiss, J.-P. Gilson, K. Thomas, J.-M. Goupil, C. Fernandez, and V. Valtchev, *Chemical equilibrium controlled etching of MFI-Type zeolite and its influence on zeolite structure, acidity, and catalytic activity.* Chemistry of Materials, 2013. **25**(14): p. 2759-2766.

5. Baerlocher, C. and L. McCusker, *IZA database of zeolite structures*. 2007.

6. Alfaro, S., C. Rodriguez, M. Valenzuela, and P. Bosch, *Aging time effect on the synthesis of small crystal LTA zeolites in the absence of organic template.* Materials Letters, 2007. **61**(23-24): p. 4655-4658.

7. Li, Y., J. Liu, and W. Yang, *Formation mechanism of microwave synthesized LTA zeolite membranes.* Journal of membrane science, 2006. **281**(1-2): p. 646-657.

8. Morris, R.E., *Ionic liquids and microwaves—making zeolites for emerging applications.* Angewandte Chemie International Edition, 2008. **47**(3): p. 442-444.

9. Zhai, J., H. Lee, I. Li, S. Ruan, and Z. Tang, *Synthesis and characterization of iodine molecular wires in channels of zeolite AEL single crystals.* Nanotechnology, 2008. **19**(17): p. 175604.

10. Macrae, C.F., P.R. Edgington, P. McCabe, E. Pidcock, G.P. Shields, R. Taylor, M. Towler, and J.v.d. Streek, *Mercury: visualization and analysis of crystal structures.* Journal of Applied Crystallography, 2006. **39**(3): p. 453-457.

11. Gren, W., S.C. Parker, B. Slater, and D.W. Lewis, *Structure of zeolite A (LTA) surfaces and the zeolite A/water interface.* The Journal of Physical Chemistry C, 2010. **114**(21): p. 9739-9747.

12. Tran, R., Z. Xu, B. Radhakrishnan, D. Winston, W. Sun, K.A. Persson, and S.P. Ong, *Surface energies of elemental crystals.* Scientific data, 2016. **3**: p. 160080.

13. Larsen, A.H., J.J. Mortensen, J. Blomqvist, I.E. Castelli, R. Christensen, M. Dułak, J. Friis, M.N. Groves, B. Hammer, and C. Hargus, *The atomic simulation environment—a Python library for working with atoms.* Journal of Physics: Condensed Matter, 2017. **29**(27): p. 273002.

14. Brown, W.M., P. Wang, S.J. Plimpton, and A.N. Tharrington, *Implementing molecular dynamics on hybrid high performance computers–short range forces.* Computer Physics Communications, 2011. **182**(4): p. 898-911.

APPENDIX B. SUPPORTING INFORMATION FOR CHAPTER 3

B.1 Hill Sauer Implementation

Boulfelfel et al. modified the Hill Sauer force field for a better description of zeolite pore dimensions.[1] They changed the equilibrium angle of the Si-O-Si and O-Si-O terms while keeping all other parameters constant.[1] The Hill-Sauer FF uses LAMMPS' Class 2 angle terms with the format

$$E = K_2(\theta - \theta_0)^2 + K_3(\theta - \theta_0)^3 + K_4(\theta - \theta_0)^4 + M\left(r_{ij} - r_1\right)\left(r_{jk} - r_2\right) + N_1\left(r_{ij} - r_1\right)(\theta - \theta_0) + N_2\left(r_{jk} - r_2\right)(\theta - \theta_0) \quad \text{(B.1)}$$

where i-j-k refer to the order of the three atoms, *K*, *M*, and *N* are energy scalars, θ_0 is the equilibrium angle, θ is the angle between the three atoms, r_1 and r_2 are the equilibrium bond distances between atoms i-j and j-k respectively, r_{ij} and r_{jk} are the bond distances between atoms i-j and j-k respectively.[2] Boulfelfel et al. only changed the θ_0 terms for both angles and kept all other distance and scalar terms at their original values.[1] The Boulfelfel et al. terms used in this study and the original terms are shown in **Table B.1** for comparison.

Table B.1 – Equilibrium Angle Comparisons

	Si-O-Si	O-Si-O
θ_0 – Original Hill-Sauer[3]	173.7651	112.0200
θ_0 – Boulfefel et al.[4]	150.0	113.0

There are other parameters in the Hill-Sauer force field that use the Si-O-Si and O-Si-O θ_0 such as dihedral and improper terms. However, Boulfelfel et al. kept the original Hill-Sauer θ_0 for the angle component of these terms, so we followed their example in our work as well.[3]

B.2 DFT-derived Force Field Parametrization for CO_2 and H_2

Fang et al. developed a first-principles-based force field for CO_2 in siliceous zeolites that showed good transferability across different zeolite topologies.[5] This approach used the fully periodic framework to represent the adsorbent structure and relies on electronic structure calculations for hundreds or thousands of adsorption configurations randomly scattered throughout the framework. This approach was later extended to develop parameters for CH_4 in siliceous zeolites that can accurately predict both adsorption and diffusion properties.[6] In those studies, the charges for CH_4 and zeolite atoms were obtained from the density derived electrostatic and chemical (DDEC) method while the charges for CO_2 were obtained from the EPM2 model.[7-10] In this chapter, we developed first-principles-based force fields for CO_2 and H_2 in bulk and nanosheet siliceous zeolites that use atomic charges from the Hill Sauer force field, since these charges are quite different than DDEC charges.[11, 12] We used the EPM2 model for $CO_2 \ldots CO_2$ interactions; this model correctly captures the phase behavior of pure CO_2.[10] $H_2 \ldots H_2$ interactions were treated as a three-point model used previously by Yang et al.[13]

B.2.1 Generating Training Sets for Force Field Fitting

The first step in force field fitting is the generation of a training set of atomic coordinates that adequately samples the potential energy surface. We generated one training set to describe adsorbate interactions with the bulk zeolite (Si, O_{SiOSi}) using biased molecular dynamics (MD) and another training set to describe adsorbate interactions with the hydrogen of silanol groups (H_{OH}) using Grand Canonical Monte Carlo (GCMC). The biased MD method is useful for deriving a force field that is accurate for both adsorption

and diffusion properties because it generates adsorbate configurations in both pore and cage regions.[6]

We generated bulk zeolite adsorbate coordinates using half the cage volume of Zeolite A (LTA) as shown in **Figure B.1**. We divided this volume into six bins with equal width (1 Å) parallel to the 8-ring plane. In each bin we performed a biased NVT molecular dynamics (MD) simulation for 200 ps after an equilibration period of 100 ps. Each simulation had one adsorbate and used a time step of 1 fs. Configurations were collected every 0.5 ps for a total of 2400 (400 from each bin). We used biased molecular dynamics to ensure that adsorbates remain inside their cage so that our configuration sample is representative. An unconstrained adsorbate will likely oversample the cage and undersample the transition state region. We confined each adsorbate near to its bin-defining plane with a harmonic spring constant of 15 kcal/mol using the COLVARS package[14] from LAMMPS[15]. In all biased MD simulations, the adsorbent atoms were fixed and only the adsorbate was allowed to move. The force field we used for the initial simulation was derived from Grimme's empirical dispersion expression in the DFT-D2 method,

$$C_6^{ij} = 4\varepsilon_{ij}\sigma_{ij}^6 \;\; and \; C_{12}^{ij} = \frac{\left(R_0^i + R_0^j\right)^6}{2} C_6^{ij} = 4\varepsilon_{ij}\sigma_{ij}^{12} \tag{B.2}$$

where R_0^i and R_0^j are the Van der Waals radii of each atom.[16] Grimme's work lists parameters for C_6 and R_0 for elements from H to Xe.[16] The C_6^{ij} term is defined as

$$C_6^{ij} = \sqrt{C_6^i C_6^j} \tag{B.3}$$

where the superscripts refer to the element described by C_6.[16] Solving equation B.1 gives ε_{ij} and σ_{ij}. The ε_{ij} and σ_{ij} terms are used to calculate the van der Waals energy in our MD simulations using the 12-6 form of the Lennard-Jones equation

$$E_{vdW} = E_{Lennard-Jones} = 4\varepsilon_{ij}\left[\left(\frac{\sigma_{ij}}{r}\right)^{12} - \left(\frac{\sigma_{ij}}{r}\right)^{6}\right] \quad \text{(B.4)}$$

where r is the distance between both atoms.

(a) (b)

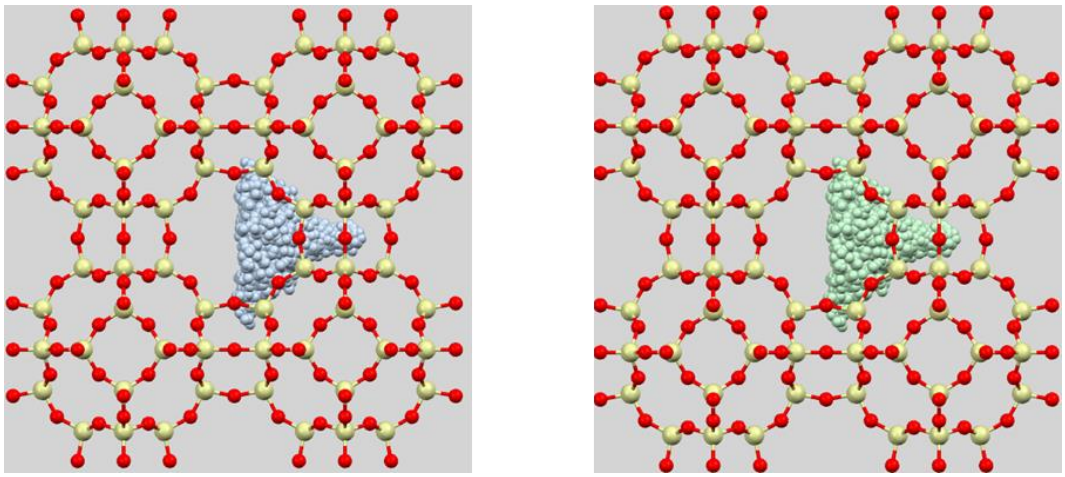

Figure B.1. Illustration of the training sets used to fit force field parameters for (a) CO_2–framework and (b) H_2–framework interactions based on a bulk siliceous zeolite, Si-LTA. O, Si, CO_2 and, H_2 atoms are depicted as red, beige, blue and green respectively.

To make training sets for CO_2 and H_2 interactions with the hydrogen of the surface hydroxyl group (H_{OH}) on zeolite surfaces, we generated initial configurations using NVT Monte Carlo (N = 1, T = 300 K) on 9 Å CHA (101) nanosheets. We used the force field parameters derived from the bulk zeolites to define interactions with the Si, O_{SiOSi}, and O_{SiOH} atoms. The van der Waals (vdW) parameters for the oxygen atom of the hydroxyl group were assumed to be equivalent to those for framework oxygen atoms. The initial H_{OH} parameters were obtained from Grimme's empirical dispersion expression in the DFT-D2 method.[16] Based on the simulation snapshots, 800 configurations were randomly chosen as shown in **Figure B.2**.

(a) (b)

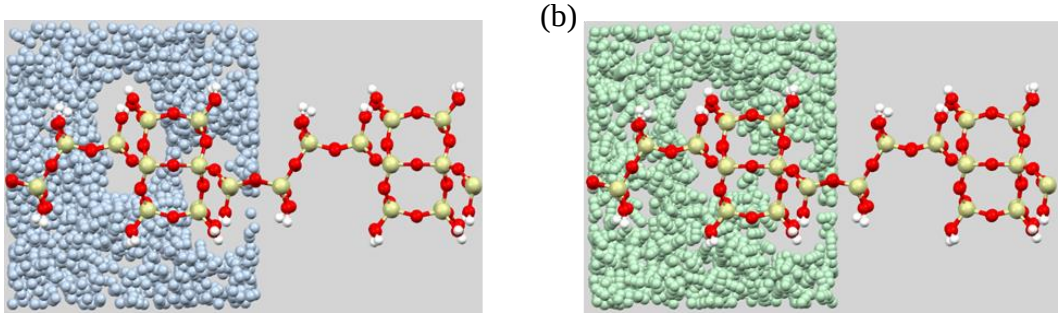

Figure B.2: Illustration of the training sets used to fit force field parameters for (a) CO_2–hydroxyl and (b) H_2–hydroxyl interactions based on a two-dimensional chabazite nanosheet. O, Si, H, CO_2 and, H_2 atoms are depicted as red, beige, white, blue and green respectively.

B.2.2 Adsorbate Zeolite Interactions

After the training sets above were generated, our next step was to compute PBE DFT adsorbate–adsorbent interaction energies defined as:

$$E_{interaction}^{DFT} = E_{adsorbate,zeolite} - (E_{adsorbate} - E_{zeolite}) \qquad \text{(B.5)}$$

For each configuration, the total energy of the system (adsorbate + adsorbent) was calculated, then the energies of the empty adsorbent and isolated adsorbate were subtracted to obtain the corresponding interaction energy. All DFT single-point calculations were performed using VASP package[17-20] version 5.4.4 in combination with projector augmented wave (PAW) pseudopotentials.[21, 22] A plane-wave basis set energy cut-off equal to 520 eV was used. Gaussian electronic smearing with width equal to 0.2 eV was applied. A Blocked Davidson electronic minimization algorithm was used to calculate the electronic ground state, with convergence stopping criterion set to 10^{-4} eV. It has been shown that dispersion corrections are important for accurately describing interactions between adsorbate molecules and zeolites, and the DFT/CC (density functional theory/coupled cluster) method performs well for these system,[5, 23] so the CC corrections

that were developed previously for adsorption of CO_2 and H_2 in zeolites were added to the PBE interaction energies.[24, 25]

The electrostatic part of the interaction energy was independently computed for each configuration using Ewald summation. After computing $E_{interaction}^{DFT/CC}$ and $E_{Coulomb}^{FF}$, the fitting itself involved least-squares regression to determine new values for C_6^{ij} and C_{12}^{ij} in equation B.5.

$$E_{vdW}(R_{ij}) = E_{Lennard-Jones}(R_{ij}) = \frac{C_{12}^{ij}}{R_{ij}^{12}} - \frac{C_6^{ij}}{R_{ij}^6} \quad \text{(B.6)}$$

To calculate bulk parameters, we fitted equation B.5 to 2400 configurations then used the bulk parameters in the next iteration of the biased NVT MD simulations. This procedure was performed for 3-6 iterations until the fitted force field parameters were converged (the changes of parameters are within ±3%). For nanosheets, we were unable to obtain complete convergence of the potential parameters (i.e. all parameter value's $\Delta < 3\%$) after six iterations, so we chose to use the configurations from last three iterations to finalize force field parameters. The resulting force field (denoted CCFF) parameters for CO_2 and H_2 in bulk siliceous zeolites and zeolite nanosheets are summarized in **Table B.2**.

Table B.2: CO_2 and H_2 Self Interaction and Zeolite Interaction Parameters

Self Interaction	Reference	ϵ/k_B (K)	σ (Å)	Charge (e)
C_{CO2}	[10]	28.129	2.757	0.6512
O_{CO2}	[10]	80.507	3.033	-0.3256
H_{H2}	[26]	NA	NA	0.468
c_{H2}	[26]	36.7	2.96	-0.936
C=O bond 1.149 (Å) [10]		H-H bond 0.74 (Å) [26]		
Hill-Sauer Charge				
Si	[3]			0.5236
Oz (O_{SiOSi})	[3]			-0.2618
Oz (O_{SiOH})	[3]			-0.195
H (H_{OH})	[3]			0.0641
CO_2 Cross Species				
C_{CO2} – Oz	This work	28.610	3.016	
O_{CO2} – Oz	This work	35.549	3.140	
C_{CO2} – Si	This work	60.747	3.560	
O_{CO2} – Si	This work	47.494	3.436	
C_{CO2} – Hz	This work	50.515	2.424	
O_{CO2} – Hz	This work	42.073	2.316	
H_2 Cross Species				
c_{H2} – Oz	This work	31.726	2.971	
c_{H2} – Si	This work	47.376	3.446	
c_{H2} – Hz	This work	19.213	2.348	
H_{H2} – All atoms		NA	NA	

B.2.3 Force Field Analysis

In the FF fitting, the residual standard deviation (RSD) is minimized,

$$RSD = \sqrt{\frac{\sum_k^n \left(E_{FF}^k - E_{DFT/CC}^k\right)^2}{n-2}} \tag{B.7}$$

where E_{FF}^k is the interaction energy calculated at the FF level for CH_4 configuration k, $E_{DFT/CC}^k$ is the interaction energy calculated at the DFT/CC level, and n is the number of

configurations for our FF fitting dataset. The mean deviation (MD) is also calculated after the parameterization,

$$MD = \frac{\sum_k^n \left(E_{FF}^k - E_{DFT/CC}^k\right)}{n} \quad \text{(B.8)}$$

The RSD and MD can give an overall evaluation of the performance of the fitted FF in reproducing the ab initio data.

A comparison of the interaction energies predicted with CCFF and the corresponding energies at the DFT/CC level for CO_2 and H_2 in bulk Si-LTA and nanosheet CHA is shown in **Figures B.3** and **B.4**. For CO_2 in Si-LTA, the DFT/CC calculations of the last iteration span a range of adsorption energies, from -31 to 2 kJ/mol. The CCFF underestimates the most energetically favorable configurations by about 8 kJ/mol, and overestimates the least stable configurations by 11 kJ/mol. This imperfect fit is also observed as high RSD and MD values of 2.8 and -0.3 kJ/mol, respectively. A similar trend is seen with CO_2 in nanosheet CHA.

For H_2 in Si-LTA and OH-CHA-2D, the fitting results are better than those from CO_2. The CCFF reproduces the DFT/CC interaction energies for both energetically favorable and unfavorable configurations, with and RSD and MD 0.4 and 0.04 kJ/mol for H_2 in Si-LTA, and 0.7 and 0.02 kJ/mol for H_2 in OH-CHA-2D.

In Fang et al.'s previous work, we obtained a better fit for CO_2 interactions with Si-CHA where the fitted force field describes both favorable and unfavorable configurations reasonably well.[5, 23] This is probably due to the smaller charges of the Hill-Sauer force field, which has weaker Coulomb interactions that cannot be fully compensated by vdW interactions via force field fitting.

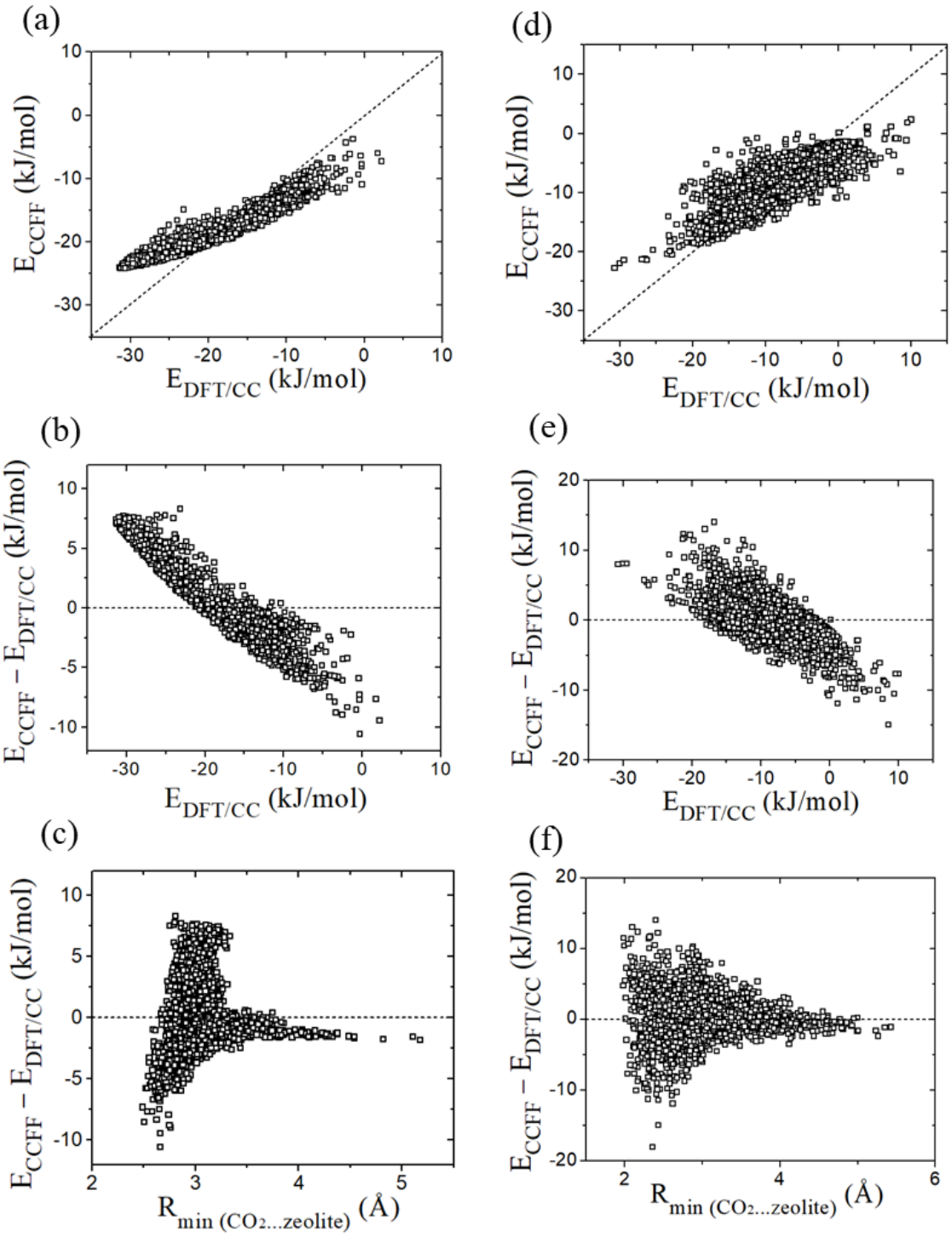

Figure B.3: Force field fitting results for CO_2 in (a–c) Si-LTA and (d–f) OH-CHA-2D: (a, d) Comparison of the interaction energies of CO_2 in zeolite for CCFF and DFT/CC, (b, e) the difference in interaction energies ($E_{CCFF} - E_{DFT/CC}$) as a function $E_{DFT/CC}$, and (c, f) $E_{CCFF} - E_{DFT/CC}$ as a function of the nearest interatomic distance between the atoms of CO_2 and zeolite. A total of 2400 CO_2 configurations are included for both bulk Si-LTA and nanosheet Si-CHA.

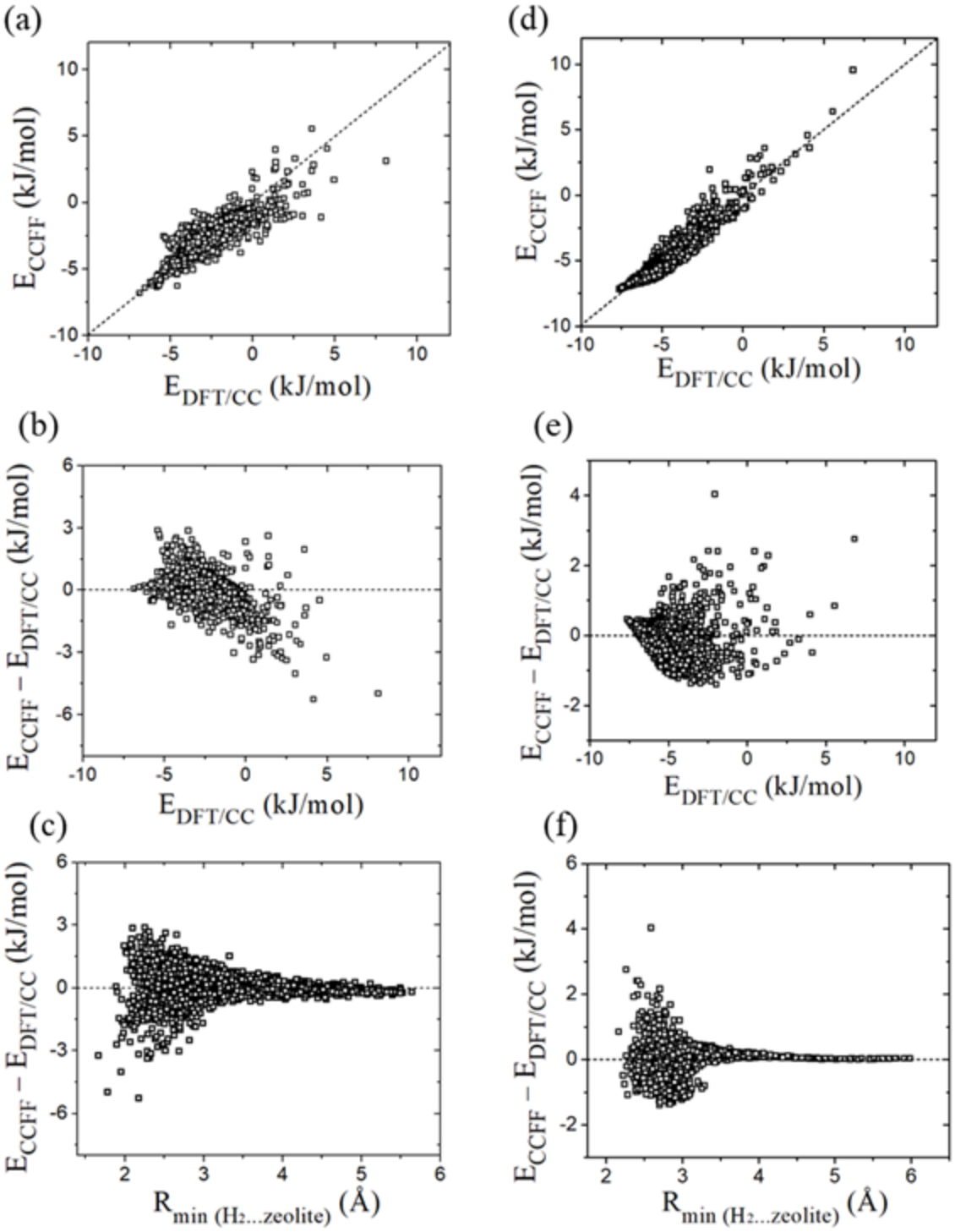

Figure B.4: Force field fitting results for H_2 in (a–c) Si-LTA and (d–f) OH-CHA-2D: (a, d) Comparison of the interaction energies of H_2 in zeolite for CCFF and DFT/CC, (b, e) the difference in interaction energies ($E_{CCFF} - E_{DFT/CC}$) as a function $E_{DFT/CC}$, and (c, f) $E_{CCFF} - E_{DFT/CC}$ as a function of the nearest interatomic distance between the atoms of H_2 and zeolite. A total of 2400 H_2 configurations are included for both bulk Si-LTA and nanosheet Si-CHA.

B.2.4 Force Field Validation

We validated the CCFF listed above by comparing the simulated adsorption isotherms and heats of adsorption for CO_2 in siliceous chabazite (Si-CHA) with available experimental data. The validation results are shown in **Figures B.5**. CCFF predicts adsorption isotherms well for CO_2 in Si-CHA at 301 and 323 K compared to experimental data from Fang et al. and Pham et al.[5, 27] The heats of adsorption predicted using CCFF agree reasonably well with the calorimetric data from Fang et al.[5] and the results from Pham et al. that were obtained from the isotherm data using the Clausius-Clapeyron equation.[27] The deviation is about 2–3 kJ/mol at all loadings. We note that it is not possible to validate our FF against equilibrium adsorption data for zeolitic nanosheets because no experimental data of this kind is available.

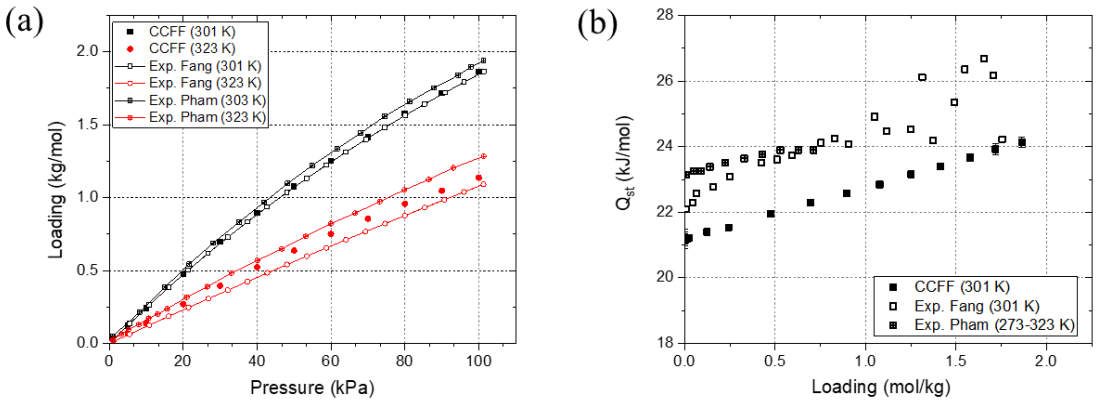

Figure B.5: Comparison of simulated and experimental (a) adsorption isotherms and (b) isosteric heats of adsorption for CO_2 in bulk Si-CHA. The experimental data are from Fang et al. and Pham et al.[5, 27]

B.3 Hydrocarbon Lennard-Jones Parameters

The hydrocarbon Lennard-Jones parameters for ethane, ethene, propane, and propene obtained from the TraPPE force field, and the zeolite Lennard-Jones parameters obtained from the TraPPE-zeo force field are listed in **Table B.3**.[28-30]

Table B.3 – Hydrocarbon Lennard-Jones Parameters

Self Interaction	Reference	ϵ/k_B (K)	σ (Å)	Charge (e)
CH_{3_sp3}	[29]	98.0	3.75	0
CH_{2_sp3}	[29]	46.0	3.95	0
CH_{2_sp2}	[30]	85.0	3.675	0
$CH_{\_sp2}$	[30]	47.0	3.73	0
Si	[28, 31]	22	2.3	0.5236
Oz (O_{SiOSi})	[28, 31]	53	3.3	-0.2618
Oz (O_{SiOH})	[31]	53	3.3	-0.195
Hz	[31]	NA	NA	0.0641

We simulated hydrocarbons as flexible molecules using the parameters given by Granato et al.[32] The parameters in **Table B.4** refer to the following bond and angle potentials

$$u_{bond} = \frac{k_1}{2}(r - r_0) \qquad u_{angle} = \frac{k_2}{2}(\cos\theta - \cos\theta_0) \tag{B.9}$$

where u_{bond} is the bond energy, k_1 is an energy scalar, r is the distance between both atoms, r_0 is the equilibrium bond distance, u_{angle} is the angle bending energy, k_2 is an energy scalar, θ is the angle formed by three atoms, and θ_0 is the equilibrium angle.

Table B.4 – Hydrocarbon Flexibility Parameters[32]

	Single Bond		Double Bond		Angle	
	r_0 (Å)	k_1/k_B (K/Å^2)	r_0 (Å)	k_1/k_B (K/Å^2)	θ_0 (°)	k_2/k_B (K)
Ethane	1.54	96,500	NA	NA	NA	NA
Ethene	NA	NA	1.33	96,500	NA	NA
Propane	1.54	96,500	NA	NA	114	62,500
Propene	1.54	96,500	1.33	96,500	119.7	70,400

The CH_4 self-interaction parameters from the TraPPE force field and the CH4 zeolite interactions from the work of Fang et al. are listed in **Table B.5**.[29, 33]

Table B.5 – CH_4 Lennard-Jones Parameters

Self Interaction	Reference	ϵ/k_B (K)	σ (Å)	Charge (e)
CH_4	[29]	147.9	3.73	0
CH_4 Cross Species				
CH_4 – Oz	[33]	109.156	3.3815	
CH_4 – Si	[33]	0	0	
CH_4 – Hz		NA	NA	

B.4 Slab Thermalization

Several NEMD studies have shown that it is critical to model the adsorption and desorption step in simulations of porous nanosheets accurately. Newsome and Sholl showed that a rigid zeolite framework increases surface resistance by repelling attempts at adsorption.[34] Liu, Nicholson, and Bhatia showed that a temperature gradient develops due to the exothermic/endothermic heats of adsorption/desorption at opposite ends of the nanotube.[35] As a result of the temperature gradient, their NEMD simulations resulted in slightly higher flux compared to the EMD case.[35]

In our simulations, we wanted to allow for local cooling and heating upon desorption and adsorption, so we modeled the edges of our zeolite nanosheets using an NVE thermostat. The interior of the nanosheet was modeled using an NVT thermostat to prevent energy drift. **Figure B.6** shows an example of a 14 nm MFI (010) nanosheet with a 4 nm NVT thermostat in the interior and a 5 nm NVE thermostat at each end.

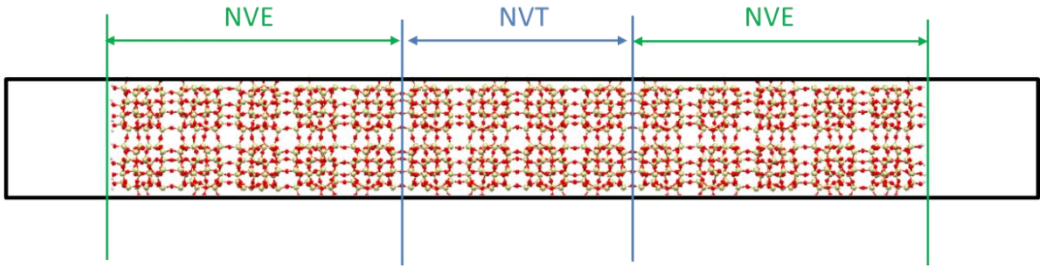

Figure B.6. An MFI (010) 14 nm slab with a 4 nm NVT thermostat in the center and an NVE thermostat at each end.

We conducted several simulations to find an appropriate thickness of the NVT region. Ideally the region should be thick enough to maintain constant temperature, but no thicker, lest the thermostat interfere with adsorption and desorption kinetics. For each simulation, any zeolite atom not in the NVT region was included in the NVE regions. We ran EMD simulations of CO_2 in a 14 nm MFI (010) slab at 2 bar and 300 K with a 1 fs time step for 1 ns. Our data was saved every 100 ps and we averaged over 15 independent simulations. To measure desorption, we counted the number of molecules that crossed the cell boundary. We defined a desorption constant equal to

$$k_{des} = \frac{j}{AC} \tag{B.10}$$

where j is the flux out of the slab, A is the surface area of the slab, and C is the concentration of adsorbate in the slab.[36]

Figure B.7(a) shows the effect of the NVT region thickness on k_{des}, which increases from 0.2 to 0.5 nm, remains roughly constant from 0.5 to 8 nm, and increases thereafter. The initial increase can be explained by **Figure B.7(b)** which shows that a 0.2 nm NVT thermostat region is unable to maintain constant temperature. The increase in k_{des} from 8 nm onwards is due to the NVT thermostat's interference with the desorption process, where it likely replenishes the kinetic energy at the surface faster than it would be replenished via heat flux. We found that 0.5 nm was the thinnest NVT region that maintained a constant temperature, so a 0.5 nm NVT region was used in all slab simulations. We chose the thinnest region possible to ensure the ability to effectively simulate very thin slabs.

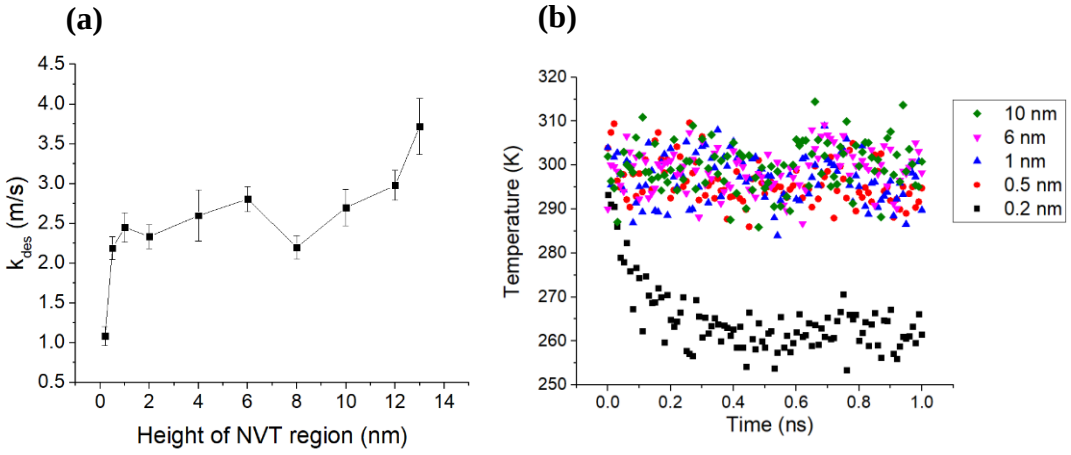

Figure B.7. Simulations of CO_2 in a 14 nm MFI slab at 2 bar and 300 K. (a) k_{des} increases with the thickness of the NVT region. (b) The system temperature holds steady for NVT regions at least 0.5 nm thick, but not for the 0.2 nm region. The legend lists the thickness of each NVT region tested.

B.5 Convergence

To calculate accurate diffusivities, it is standard practice to simulate a trajectory that is long enough to capture the characteristic diffusion length, the distance from one transition state to another. In LTA, for example, this is defined as the distance between the centers of two neighboring cages (1.2 nm).[33] Therefore, an LTA diffusion run that results in mean squared displacement (MSD) larger than 1.44 nm^2 implies than on average each molecule has hopped to a neighboring cage and overcome the energy barrier to diffusion at least once.

In slab unit cells, we assume that diffusion is encumbered by resistance inside the zeolite as well as desorption from the surface. Therefore, we defined the characteristic diffusion length as the total length of the unit cell as that would entail movement from the center of one slab to the center of its nearest image. **Figure B.8(a)** displays an MSD plot averaged over 20 runs of ethene diffusion through a 2 nm MFI (010) unit cell at 250 K and 1 molec/uc. Since the squared length of the unit cell is 36 nm^2, and the MSD at 50 ns is 1,648 nm^2, each adsorbate on average jumped to a neighboring slab 45 times.

Although we use the MSD to tell if a run was sufficiently long, we use the center of mass squared displacement (CoM SD) to obtain a diffusivity. The CoM SD for the ethene diffusion simulations is shown in **Figure B.8(b)**. The plot is not entirely linear, so a diffusivity derived from the slope will have a high standard deviation. Therefore, we break up the trajectories into non-overlapping time blocks, calculate the diffusivity using the slope of each block, and measure the standard error in the mean of the set of diffusivity

values.[37] The average diffusivities and errors for the data in **Figure B.8** is shown in **Table B.6**, which shows that the error decreases as the time block size decreases.

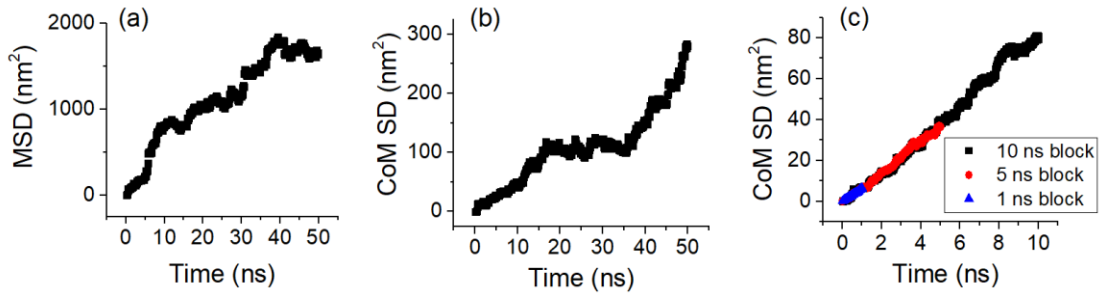

Figure B.8. Trajectories for diffusion of ethene through 2 nm MFI at 250 K and 1 molec/uc displaying (a) the MSD of the total run, (b) the CoM SD for the total run, and (c) the CoM SD for time blocks of different size.

Table B.6 – Diffusivity and Standard Error of Mean for Ethene in a 2nm MFI Slab

Time block (ns)	**50**	**10**	**5**	**1**
$D_{z,zeo}$ (m^2/s E-10)	2.5	3.9	3.7	3.7
s_m (m^2/s E-10)	1.8	1.1	0.9	0.7

In order to use the diffusivity from the 1 ns time block, it is best to ensure that it is statistically equivalent to output from larger time blocks. **Table B.6** shows that the diffusivity of the 1 ns time block is within the margin of error of the larger time blocks.[37] In addition, **Figure B.8(c)** shows that the slopes for various time blocks are overlapping. This data allows us to conclude that the 1 ns time block is sampling the same phenomena as larger time blocks.

There are some scenarios in which the diffusion mechanism observed at 1 ns is different than that observed at larger time intervals. **Figure B.9** shows trajectories for propane diffusion through a 10 nm MFI (010) slab at 250 K and 1 molec/uc. The CoM SD of different time blocks in **Figure B.9(c)** do not share the same slope. In this instance the

1 ns time block is capturing only diffusion through the slab, whereas the 5 ns and 10 ns time blocks capture both diffusion through the slab and desorption onto a neighboring slab. In such scenarios, we used data from the full 50 ns trajectory.

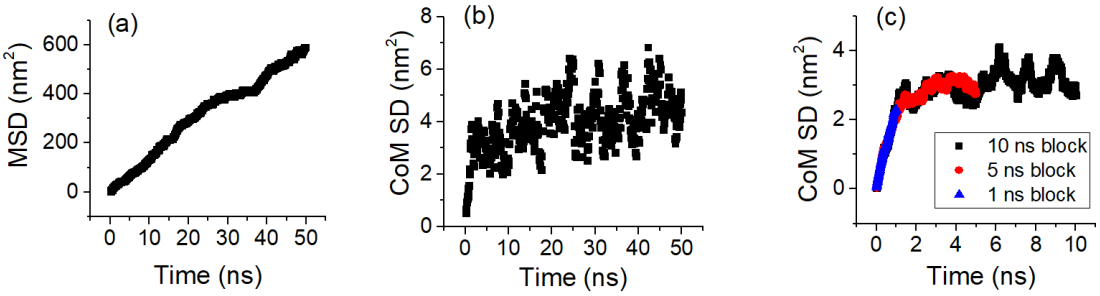

Figure B.9. Trajectories for diffusion of propane through 10 nm MFI at 250 K and 1 molec/uc displaying (a) the MSD of the total run, (b) the CoM SD for the total run, and (c) the CoM SD for time blocks of different size.

B.6 Defining the Zeolite/Gas Interface

In the main text of Chapter 3, we describe using equation 3.4 to calculate an effective corrected diffusivity ($D_{z,zeo}$) across the zeolite nanosheet. Here, we describe how we define the boundary between the nanosheet and the gas layer. The adsorption profile for CO_2 in MFI at high loading in **Figure B.10(a)** shows that molecules form adsorption layers at both ends of the nanosheet. This external layering does not occur in all cases, as seen in the case of propane at low temperature and low loading in **Figure B.10(b)**.

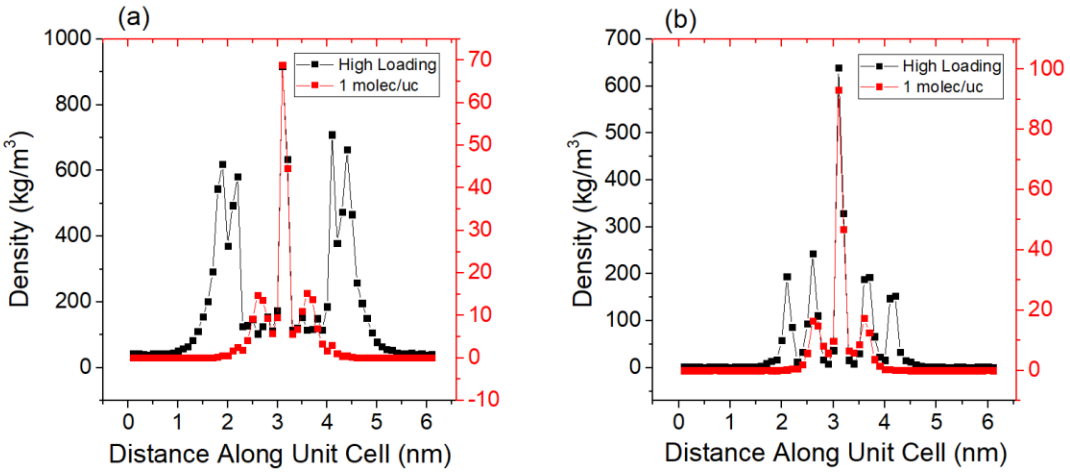

Figure B.10. Density profiles in a 2.2 nm MFI (010) slab at 250 K for (a) CO_2 and (b) propane. The unit cell is superimposed near the center of each graph.

To test whether the $D_{z,zeo}$ should be measured across a region that includes these adsorption layers, we calculated $D_{z,zeo}$ for CO_2 diffusion through a 2 nm MFI (010) unit cell using four different adsorption layer correction (L_{cor}) estimates. This correction was applied (shown in red) to equation 3.4 of the main text such that

$$D_{z,zeo} = \frac{N_{sys}^2}{2N_{zeo+cor}\left(\frac{L_{gas}-L_{cor}}{L_{zeo}+L_{Lcor}}+1\right)} \lim_{t\to\infty} \frac{1}{t} \left\langle \left|\Delta z_{sys,com}\right|^2 \right\rangle \tag{3.4}$$

$N_{zeo+cor}$ is the sum of the molecules of gas in the zeolite proper (silanol H on one end to silanol H on the opposite end) and the molecules inside the adsorption layers of length L_{cor} at each end.

Dutta and Bhatia tested two different values of L_{cor} (0 nm and total gas phase length) to distinguish internal and external resistance.[38] The equations they used to calculate diffusivity tracked a molecule's trajectory through a predetermined section of the nanosheet unit cell, as determined by L_{cor}.[38] If the section ended at the surface of the

zeolite, the resistance the molecule encountered was due to the zeolite media and desorption. If the section encompassed the entire unit cell, then the molecule also encountered resistance from adsorption and gas phase movement.[38] Since our method to calculate surface resistance is functionally equivalent to theirs,[35, 38] we used different values of L_{cor} to quantify the magnitude of different resistances.

Our objective was to calculate the surface resistance due to adsorption and desorption. Since these events take place within the adsorption layers, the most accurate L_{cor} is one which captures the length of the adsorption layer(s) but no more. **Figure B.11** shows the surface resistances obtained for CO_2 diffusion through a 2 nm MFI unit cell using various L_{cor}. The "Tailored Manually" L_{cor} was obtained by visually estimating the size of the adsorption layer from adsorption profiles for each temperature and pressure condition and are listed in **Table B.7**. We view this result as the correct value of L_{cor}, but it is impractical to estimate the value by hand for each simulation. Our aim below, therefore, is to establish an algorithmic approach to this issue.

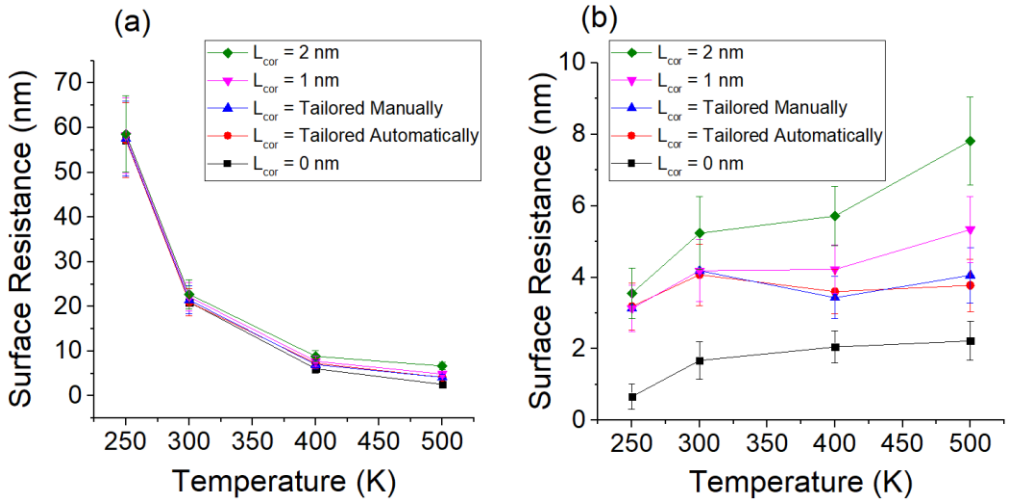

Figure B.11. A comparison of CO_2 surface resistance calculated using $D_{0,eff}$ measured across the length of the zeolite (without correction) or length of the zeolite and the adsorption layer (with correction) simulated at a loading of (a) 1 molec/uc and (b) high loading.

Table B.7 – Tailored L_{cor} for CO_2 in a 2 nm MFI Slab

Temperature	250 K	300 K	400 K	500 K
1 molec/uc L_{cor} (nm)	0.1	0.2	0.4	0.6
High Loading L_{cor} (nm)	1	1	0.5	0.5

Since the largest adsorption layers were ~1 nm in length, we first employed an L_{cor} of length 1 nm. We also tested L_{cor} with lengths 0 nm and 2 nm. **Figure B.11** shows that the L_{cor} value does not have a great effect on surface resistance when temperature and pressure are low, but it does have a greater effect when temperature and pressure are high. At high temperature and pressure, molecules spend a larger portion of time outside the nanosheet than they do at lower temperature and pressure, so larger L_{cor} measure larger gas phase resistances. Dutta and Bhatia found that gas phase resistance (adsorption and gas movement) only amounted to a maximum of 25% of total resistance.[38] We examined a wider range of conditions and found that adsorption and gas phase resistance can account for up to 70% of the total surface resistance.

Motivated by the results above we developed a simple algorithm to automatically determine L_{cor}. With this approach L_{cor} is defined to be the largest distance from the nanosheet surface at which the average density of the adsorbate is 10% larger than the average gas phase density. Comparisons between the automatically tailored approach and the manually tailored approach in **Figure B.11** show similar results, so we used this algorithm in all calculations reported in Chapter 3.

B.7 Adsorbate Density in Nanosheets

Figure B.12 shows the propane density in an MFI (010) slab and an MFI (010) bulk structure. The average density in the bulk is 152 kg/m^3 while the average density in the slab is 118 kg/m^3, so the slab has 77% of the bulk density. The density profile in the bulk shows a repeat pattern of a large peak followed by two smaller peaks, with the large peaks occurring at the center of the MFI a and b channel intersections. The center of the MFI slab has such a channel intersection with an accompanying large peak. Though the surface surface on each side has half the volume of the full intersection, it has less than half of the full intersection density.

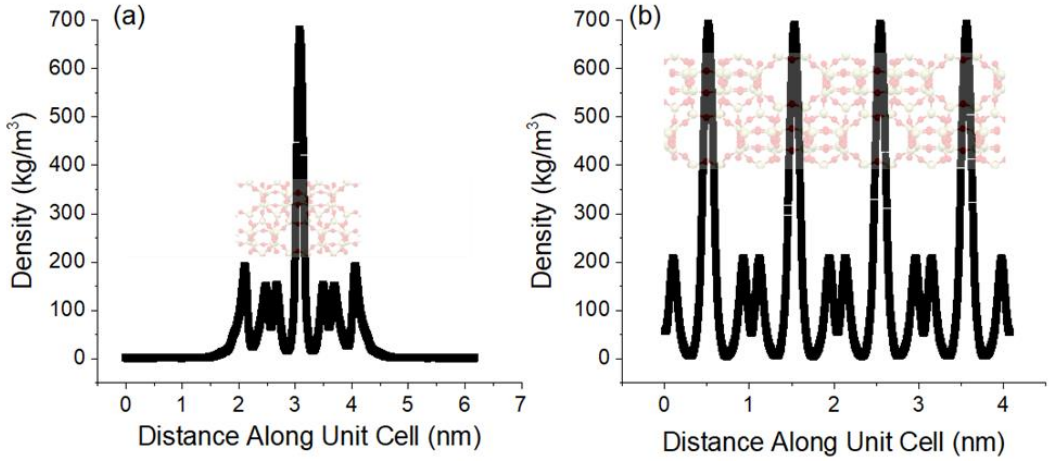

Figure B.12. The density profile of propane post equilibration at 0.5 bar and 250 K in an MFI (010) (a) 2 nm slab and (b) 4 nm bulk unit cell.

Figure B.13 shows the CO_2 density in an MFI (010) slab and an MFI (010) bulk structure. The average density in the bulk is 277 kg/m^3 while the average density in the slab is 269 kg/m^3, so the slab has 97% of the bulk density.

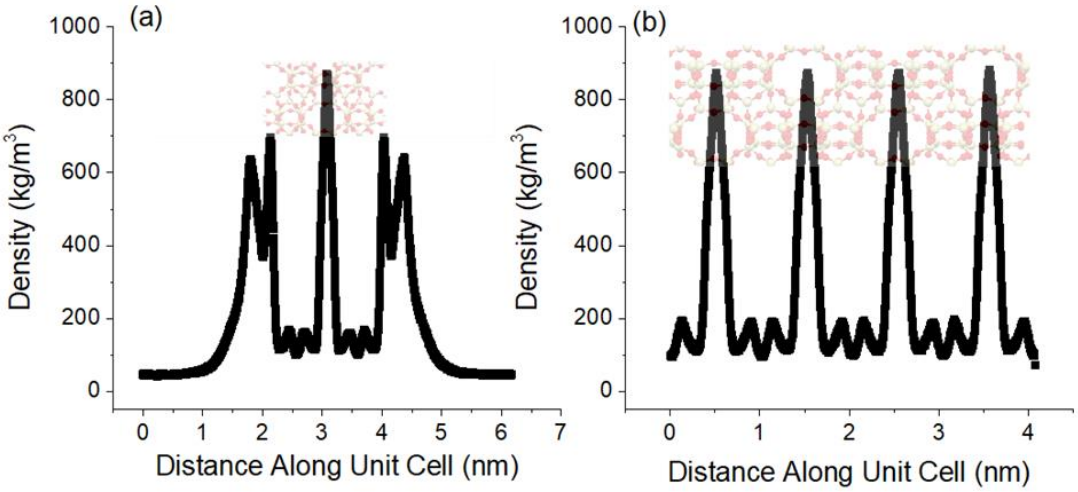

Figure B.13. The density profile of CO2 post equilibration at 15 bar and 250 K in an MFI (010) (a) 2 nm slab and (b) 4 nm bulk unit cell.

B.8 Activation Energy

Figure B.14 shows an Arrhenius plot used to find the effective activation energies associated with the surface resistance in an MFI (010) nanosheet for the seven molecules we studied. For this analysis we set R_{surf} equal to the surface resistance as defined in equation 3.6 rather than the surface resistance equivalent height as defined in equation 3.10 (and used in throughout Chapter 3) to avoid including information from $D_{0,bulk}$ included in the latter term. Although some curvature can be seen in the data for propane and propene, the effective activation energies were obtained simply by linear fits to each data set in **Figure B.14(a)**.

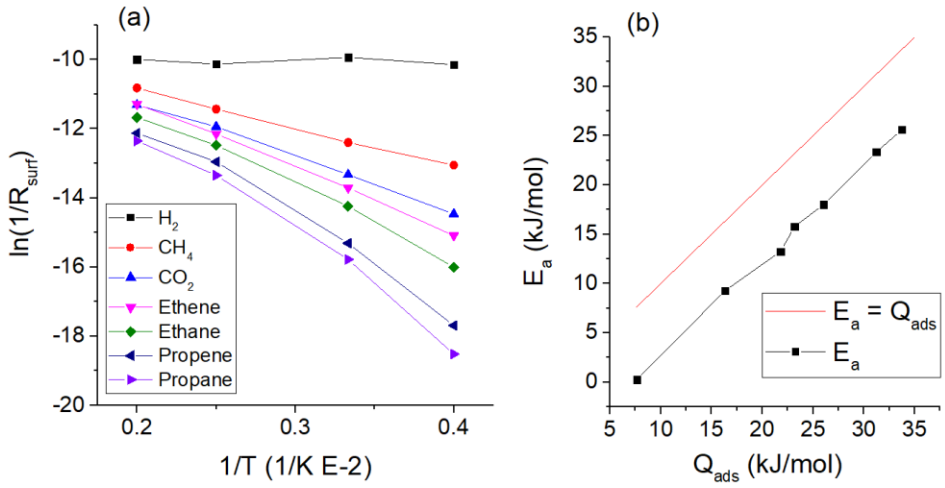

Figure B.14. (a) Arrhenius plots based on the surface resistance in 2 nm MFI (010) slabs at a loading of 1 molec/uc. (b) The E_a graphed against the Q_{ads} for all seven molecules.

B.9 High Loading

The MFI surface resistances displayed in **Figure 2** of the main text were calculated at a high and low loading scenario. For low loading, we used one molecule in the slab unit cell, and two molecules in the MFI 1×2×1 supercell. For high loading, we used the loadings shown in **Table B.8**. Some of the loadings in the bulk unit cell portion of the table have a ½ molecule because the GCMC simulation sometimes populates the 1×2×1 supercell with an odd number of molecules but the numbers in **Table B.8** were divided in half to correspond to one unit cell. The slab is equivalent to one unit cell of MFI so the simulation loadings are reported as is.

Table B.8 – High Loading at each Temperature

	Slab MFI (010) Loading (molec/uc)						
Temperature (K)	H_2	CH_4	CO_2	ethane	ethene	propane	propene
250	28	31	47	19	18	11	11
300	22	22	36	25	23	12	12
400	15	12	18	17	17	21	20
500	12	8	11	11	10	12	12
	Bulk MFI (010) loading (molec/uc)						
250	10	16.5	22	16	16	12	12
300	6.5	13	19	15	15	11.5	11.5
400	3.5	6.5	12	11	10.5	10.5	10.5
500	2	3	6	5.5	6	7	7.5

To determine the saturation loadings, we developed the isotherms shown in **Figures B.15**, **B.16**, and **B.17**.

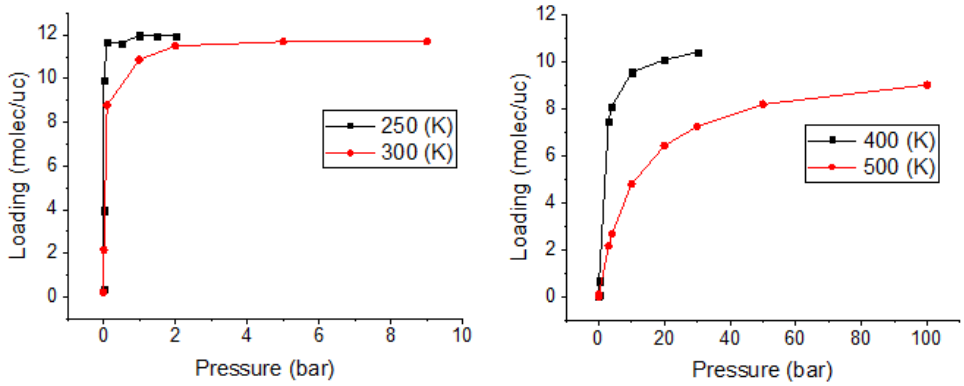

Figure B.15. Propane isotherms in bulk MFI.

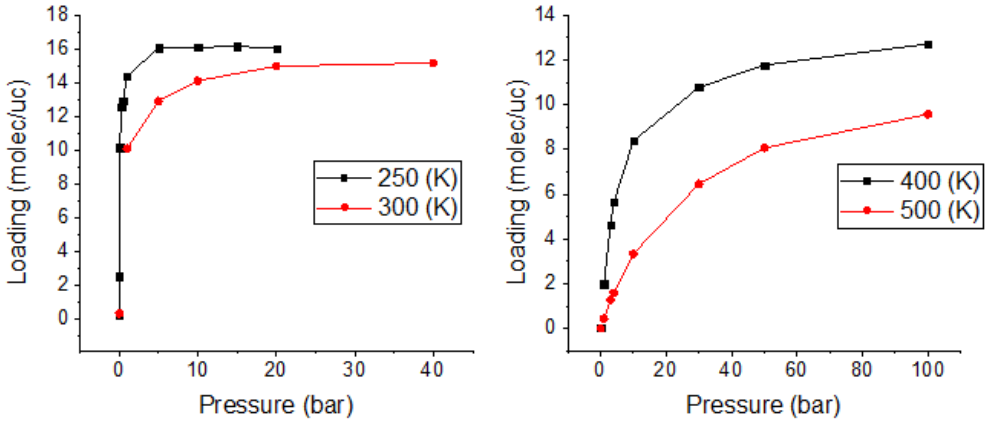

Figure B.16. Ethane isotherms in bulk MFI.

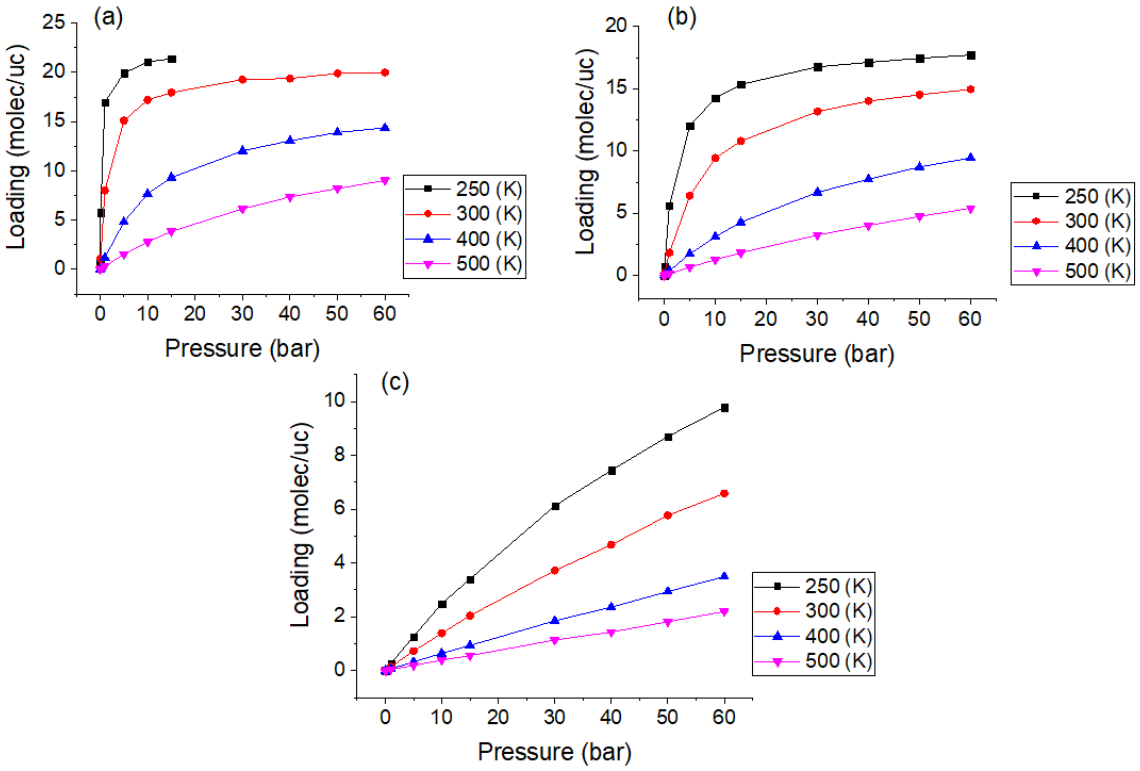

Figure B.17. (a) CO_2, (b) CH_4, and (c) H_2 isotherms in bulk MFI.

We determined the saturation pressure by visually observing were the curve became approximately horizontal. The saturation pressures are shown in **Table B.9**. Though they were taken from the bulk isotherm, we used the same pressure to load both the bulk and slab unit cells. For species whose isotherm does not follow the standard shape, such as H_2, we simply chose a high pressure from within the examined pressure range. Additionally, the saturation pressure from the ethane isotherm was used for ethene and the saturation pressure from the propane isotherm was used for propene.

Table B.9 – Saturation Pressures

	Pressure (bar)						
Temperature (K)	H_2	CH_4	CO_2	ethane	ethene	propane	propene
250	60	30	15	1	1	0.5	0.5
300	60	30	30	20	20	3	3
400	60	30	30	30	30	30	30
500	60	30	30	30	30	30	30

B.10 Ideal Selectivities

The ideal selectivities for H_2/CO_2, CH_4/CO_2, ethene/ethane, and propene/propane for MFI are shown in **Figure B.18**. For each case, the slab ideal selectivity is higher that the bulk ideal selectivity due to surface resistance having a larger effect on the molecule with the larger heat of adsorption.

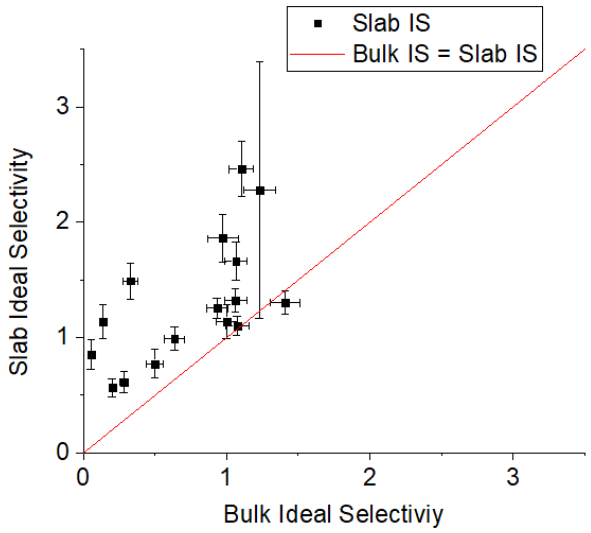

Figure B.18. The slab ideal selectivity and bulk ideal selectivity for H_2/CO_2, CH_4/CO_2, ethene/ethane, and propene/propane in bulk MFI and a 2 nm MFI (010) slab at 1 molec/uc and 250, 300, 400, and 500 K.

B.11 $D_{slab,NLR}$ Prediction for Six Frameworks

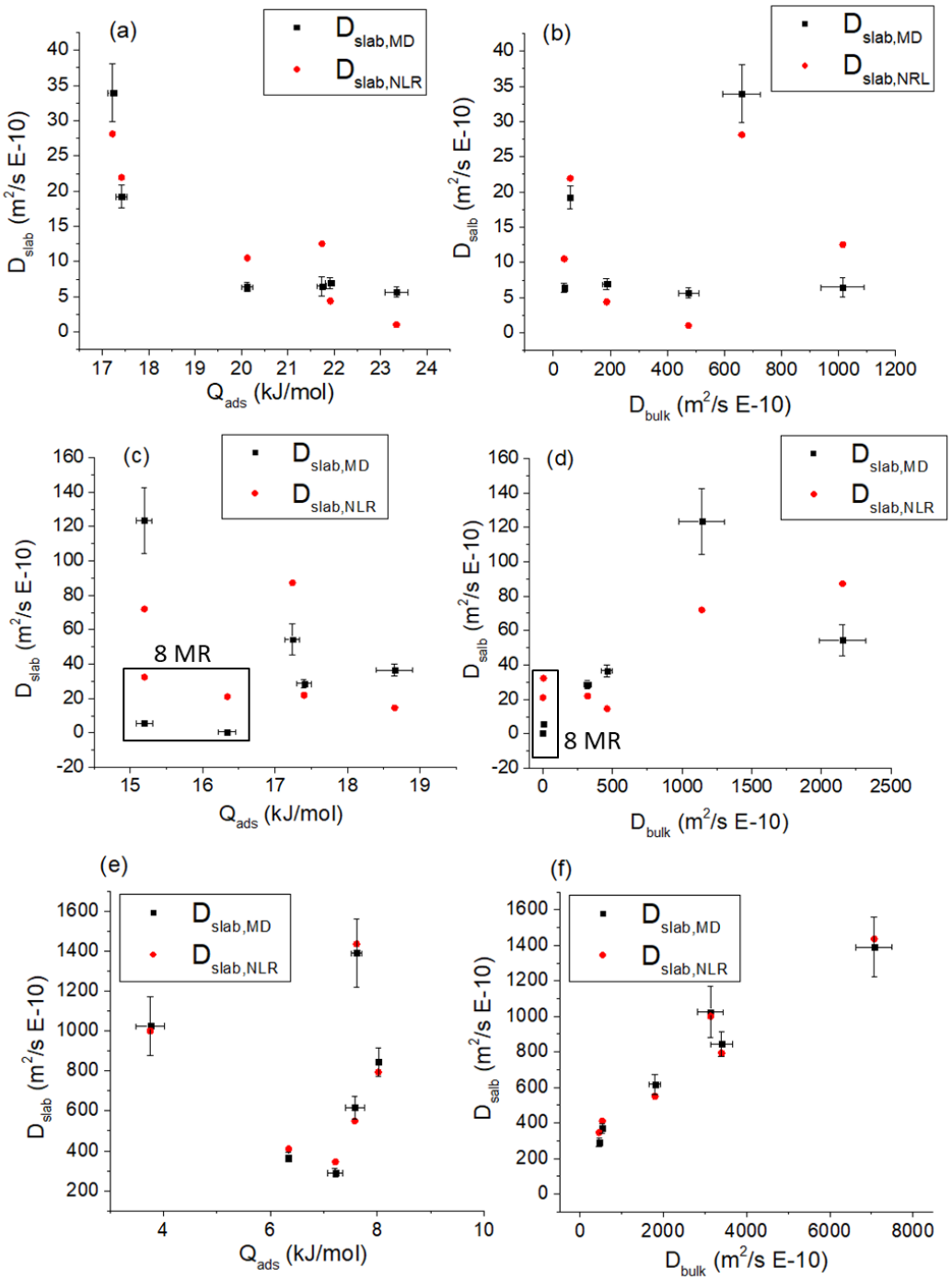

Figure B.19. The $D_{slab,MD}$ at 250 K and 1,689 Pa and the $D_{slab,NLR}$ graphed against Q_{ads} in (a) CO_2, (c) CH_4, and (e) H_2; graphed against D_{bulk} in (b) CO_2, (d) CH_4, and (f) H_2. The 8MR data is boxed in the CH_4 graphs in (c) and (d).

Table B.10 – Best Fit For D_{slab} Estimate

	x_1 Unitless	x_2 (m^2/s E-10)/(kJ/mol)	x_3 m^2/s E-10	R^2 Fit
CO_2	0.001787	-0.83051	18.746	0.813
CH_4	0.034845	-9.7439	180.24	0.462
H_2	0.1685	-58.956	694.07	0.983

The IS_{bulk} and IS_{slab} results **in Figure B.20** show that for CO_2/CH_4, the IS_{slab} increases with IS_{bulk} while the opposite is true for CO_2/H_2. For CO_2/H_2 separation in the slab, surface resistance reduces CO_2 diffusion and gives a preference to H_2. For CO_2/CH_4 separation in the 10 MR zeolite slabs, there is no clear trend against the bulk diffusivity. This lack of trend is likely because CH_4 also has a surface resistance so it does not have quite the kinetic advantage in slab diffusion that H_2 has.

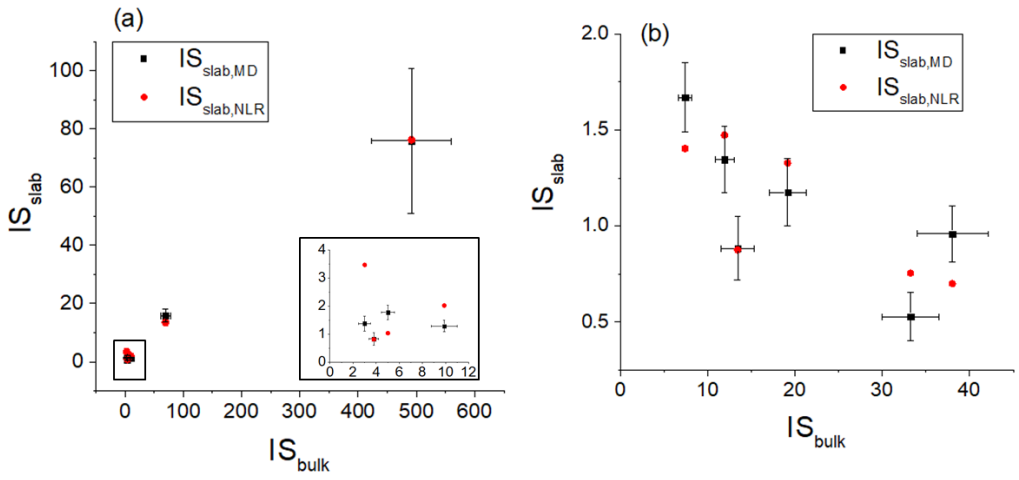

Figure B.20. Ideal selectivity of slab and bulk structures at 250 K and 1,689 Pa for (a) CO_2/CH_4 with an inset expanding the 10 MR zeolites, and (b) CO_2/H_2.

Table B.11 – Best Fit for IS_{slab} Estimate

Slab Ideal Selectivity	x_1	x_2	x_3	R^2
	Unitless	1/(kJ/mol)	1/(kJ/mol)	
CO_2/CH_4	0.1532	-1.4462	1.8367	0.997
CO_2/H_2	-0.040186	0.059104	0.10573	0.707

B.12 Raw Data and Graph Data

Tables B.12.1 to **B.12.9** display the raw diffusivity data from our calculations. They are not graphed in the main body of this chapter but form the foundation for the graphs therein. The loading in nanosheets is the average number of adsorbates in the zeolite phase throughout the simulation. **Tables B.12.9** to **B.12.30** are the numerical data directly displayed in the main text graphs and are labeled as such.

Table B.12.1 – H_2 Diffusion at High and Low Loadings

	Bulk MFI (010)			2 nm MFI (010) Slab		
Temperature	Loading	$D_{z,zeo}$	s_m	Loading	$D_{z,zeo}$	s_m
K	molec/uc	m^2/s E-10	m^2/s E-10	molec/uc	m^2/s E-10	m^2/s E-10
250	2.00	1796	136	8.54	1022	80
300	2.00	2055	154	5.79	1283	100
400	2.00	1971	265	3.11	1999	211
500	2.00	3381	277	2.14	2216	206
250	20.00	1333	138	0.37	926	87
300	13.00	2131	186	0.30	1288	105
400	7.00	2691	251	0.22	1676	121
500	4.00	2800	316	0.18	2213	195

Table B.12.2 – CH_4 Diffusion at High and Low Loadings

	Bulk MFI (010)			2 nm MFI (010) Slab		
Temperature	Loading	$D_{z,zeo}$	s_m	Loading	$D_{z,zeo}$	s_m
K	molec/uc	m^2/s E-10	m^2/s E-10	molec/uc	m^2/s E-10	m^2/s E-10
250	2.00	321	25	0.95	28	2
300	2.00	349	27	0.86	55	6
400	2.00	552	42	0.69	156	22
500	2.00	647	52	0.55	276	21
250	33.00	292	22	22.21	115	10
300	26.00	317	23	15.36	137	11
400	13.00	559	39	7.44	226	20
500	6.00	720	57	4.24	273	47

Table B.12.3 – CO_2 Diffusion at High and Low Loadings

	Bulk MFI (010)			2 nm MFI (010) Slab		
Temperature	Loading	$D_{z,zeo}$	s_m	Loading	$D_{z,zeo}$	s_m
K	molec/uc	m^2/s E-10	m^2/s E-10	molec/uc	m^2/s E-10	m^2/s E-10
250	2.00	188	15	0.99	7	1
300	2.00	225	18	0.96	20	2
400	2.00	339	29	0.84	80	6
500	2.00	434	32	0.69	155	10
250	44.00	85	7	39.75	38	3
300	38.00	160	13	27.67	61	7
400	24.00	286	22	12.80	111	8
500	12.00	421	29	6.87	147	15

Table B.12.4 – Ethene Diffusion at High and Low Loadings

	Bulk MFI (010)			2 nm MFI (010) Slab		
Temperature	Loading	$D_{z,zeo}$	s_m	Loading	$D_{z,zeo}$	s_m
K	molec/uc	m^2/s E-10	m^2/s E-10	molec/uc	m^2/s E-10	m^2/s E-10
250	2	179	9	0.99	4	0
300	2	247	12	0.97	14	1
400	2	357	18	0.85	68	4
500	2	391	22	0.67	155	7
250	32	238	12	16.34	42	2
300	30	259	14	17.75	78	4
400	22	204	11	11.48	112	6
500	13	326	17	6.02	151	8

Table B.12.5 – Ethane Diffusion at High and Low Loadings

	Bulk MFI (010)			2 nm MFI (010) Slab		
Temperature	Loading	$D_{z,zeo}$	s_m	Loading	$D_{z,zeo}$	s_m
K	molec/uc	m^2/s E-10	m^2/s E-10	molec/uc	m^2/s E-10	m^2/s E-10
250	2	163	10	1.00	1	0
300	2	232	12	0.98	9	1
400	2	336	17	0.88	50	3
500	2	418	23	0.71	115	6
250	32	210	14	17.30	37	3
300	30	170	9	19.11	60	4
400	22	138	7	11.71	84	5
500	13	281	15	6.74	122	6

Table B.12.6 – Propene Diffusion at High and Low Loadings

	Bulk MFI (010)			2 nm MFI (010) Slab		
Temperature	Loading	$D_{z,zeo}$	s_m	Loading	$D_{z,zeo}$	s_m
K	molec/uc	m^2/s E-10	m^2/s E-10	molec/uc	m^2/s E-10	m^2/s E-10
250	2	106	6	1.00	0.3	0.1
300	2	159	8	0.99	3.0	0.3
400	2	132	27	0.94	26.6	3.4
500	2	259	28	0.78	69.3	7.8
250	24	3	0	10.79	8.0	0.4
300	23	26	3	11.13	21.2	2.7
400	21	62	8	13.41	44.9	4.5
500	15	161	17	7.51	95.0	9.6

Table B.12.7 – Propane Diffusion at High and Low Loadings

	Bulk MFI (010)			2 nm MFI (010) Slab		
Temperature (K)	Loading molec/uc	$D_{z,zeo}$ m^2/s E-10	s_m m^2/s E-10	Loading molec/uc	$D_{z,zeo}$ m^2/s E-10	s_m m^2/s E-10
250	2	86	6	1.00	0.2	0.1
300	2	159	9	1.00	1.9	0.3
400	2	130	37	0.95	19.1	2.1
500	2	230	21	0.79	55.6	5.4
250	24	1	0	10.81	7.4	0.4
300	23	23	2	11.15	17.7	2.2
400	21	71	8	13.85	45.2	5.1
500	14	143	15	7.50	74.3	7.7

Table B.12.8 – Diffusion in a 14 nm MFI (010) Slab at 250 K and 1 molec/uc

Adsorbate	Loading molec/uc	$D_{z,zeo}$ m^2/s E-10	s_m m^2/s E-10
H_2	3.86	1470	72
CH_4	4.96	96	5
CO_2	4.99	41	2
Ethane	5.00	6	1
Propane	5.00	0.5	0.1

Table B.12.9 – Surface Resistance in 2 nm MFI at 1 molec/uc (Figure 3.2(a))

	Surface Resistance (nm)						
Temperature (K)	H_2	CH_4	CO_2	Ethene	Ethane	Propene	Propane
250	4.2	22.4	57.3	103.4	235.2	827.3	1537.1
300	3.3	12.6	20.9	34.5	56.3	114.4	183.7
400	4.7	6.3	7.3	9.6	12.9	8.2	12.1
500	4.3	2.9	4.1	3.5	5.7	6.3	7.1
	Surface Resistance Error (nm)						
250	0.8	2.8	8.4	7.7	23.6	286.7	551.1
300	0.6	2.0	3.0	3.0	5.1	14.2	29.4
400	1.1	1.4	1.1	0.9	1.1	2.5	4.4
500	0.8	0.6	0.6	0.4	0.6	1.3	1.2

Table B.12.10 – Surface Resistance in 2 nm MFI at High Loading (Figure 3.2(b))

	Surface Resistance (nm)						
Temperature (K)	H_2	CH_4	CO_2	Ethene	Ethane	Propene	Propane
250	0.7	3.4	2.7	10.2	10.3	-1.4	-1.8
300	1.4	2.9	3.5	5.1	4.0	0.5	0.7
400	0.8	3.2	3.4	1.8	1.4	0.9	1.2
500	0.6	3.6	4.1	2.6	2.8	1.5	2.0
	Surface Resistance Error (nm)						
250	0.4	0.6	0.6	0.9	1.3	0.1	0.1
300	0.4	0.6	0.8	0.5	0.5	0.4	0.5
400	0.4	0.6	0.6	0.3	0.3	0.5	0.5
500	0.4	1.1	0.8	0.4	0.4	0.5	0.6

Table B.12.11 – Surface Resistance vs. Heat of Adsorption (Figure 3.3)

			Surface Resistance (nm)				
Temperature (K)	H_2	CH_4	CO_2	Ethene	Ethane	Propene	Propane
250	0.7	3.4	2.7	10.2	10.3	-1.4	-1.8
			Surface Resistance Error (nm)				
250	0.4	0.6	0.6	0.9	1.3	0.1	0.1
			Q_{ads} (kJ/mol)				
	7.6	16.3	21.8	23.2	26.0	31.2	33.7

Table B.12.12 – C_2 Ideal Selectivity in MFI (010) at 1 molec/uc (Figure 3.4(a))

	Ethane/Ethene - Bulk		Ethane/Ethene - Slab	
Temperature (K)	IS	Error	IS	Error
250	1.1	0.1	2.7	0.6
300	1.1	0.1	1.6	0.2
400	1.0	0.1	1.3	0.1
500	0.9	0.1	1.2	0.1

Table B.12.13 – C_2 Ideal Selectivity in MFI (010) at High Loading (Figure 3.4(b))

	Ethane/Ethene - Bulk		Ethane/Ethene - Slab	
Temperature (K)	IS	Error	IS	Error
250	1.1	0.1	0.9	0.1
300	1.5	0.1	1.2	0.1
400	1.4	0.1	1.3	0.1
500	1.1	0.1	1.1	0.1

Table B.12.14 – C_3 Ideal Selectivity in MFI (010) at 1 molec/uc (Figure 3.4(c))

	Propane/Propene - Bulk		Propene/Propane - Slab	
Temperature (K)	IS	Error	IS	Error
250	1.2	0.1	2.3	1.1
300	1.0	0.1	1.6	0.3
400	1.0	0.4	1.4	0.2
500	1.1	0.2	1.2	0.2

Table B.12.15 – C_3 Ideal Selectivity in MFI (010) at High Loading (Figure 3.4(d))

	Propane/Propene - Bulk		Propene/Propane - Slab	
Temperature (K)	IS	Error	IS	Error
250	2.1	0.5	1.1	0.1
300	1.1	0.1	1.2	0.2
400	0.9	0.1	1.0	0.1
500	1.3	0.1	1.3	0.2

Table B.12.16 – H_2/CO_2 Ideal Selectivity in MFI (010) at 1 molec/uc (Figure 3.5(a))

	H_2/CO_2 - Bulk		H_2/CO_2 - Slab	
Temperature (K)	IS	Error	IS	Error
250	0.052	0.006	0.851	0.126
300	0.138	0.015	1.140	0.149
400	0.330	0.052	1.492	0.156
500	0.974	0.108	1.861	0.206

Table B.12.17 – CH_4/CO_2 Ideal Selectivity in MFI (010) at High Loading (Figure 3.5(b))

	CH_4/CO_2 - Bulk		CH_4/CO_2 - Slab	
Temperature (K)	IS	Error	IS	Error
250	2.1	0.5	1.1	0.1
300	1.1	0.1	1.2	0.2
400	0.9	0.1	1.0	0.1
500	1.3	0.1	1.3	0.2

Table B.12.18 – Surface Resistance at 2 bar 300 K (Figure 3.6(a))

	Surface Resistance (nm)		
Slab Height (nm)	H_2	CH_4	CO_2
1	1.1	5.0	6.9
2	1.9	9.1	12.1
4	1.3	8.9	16.8
10	1.2	8.2	16.1
14	1.6	10.6	17.3
	Surface Resistance Error (nm)		
1	0.2	0.7	0.6
2	0.4	2.0	1.3
4	0.4	1.6	1.4
10	0.8	2.3	1.8
14	1.1	2.9	2.1

Table B.12.19 – Surface Resistance at 2 bar 400 K (Figure 3.6(b))

	Surface Resistance (nm)		
Slab Height (nm)	H_2	CH_4	CO_2
1	0.6	3.6	3.7
2	0.3	3.6	6.0
4	0.7	4.3	6.3
10	0.0	6.0	6.8
14	1.6	3.1	6.3
	Surface Resistance Error (nm)		
1	0.2	0.4	0.4
2	0.3	0.6	0.8
4	0.3	0.8	0.9
10	0.7	1.5	1.5
14	1.1	1.5	1.8

Table B.12.20 – Surface Resistance at 20 bar 300 K (Figure 3.6(c))

	Surface Resistance (nm)		
Slab Height (nm)	H_2	CH_4	CO_2
1	0.9	3.7	3.6
2	1.7	4.1	4.4
4	1.8	5.0	2.8
10	1.3	4.9	3.7
14	0.3	2.3	2.7
	Surface Resistance Error (nm)		
1	0.2	0.4	0.3
2	0.5	0.6	0.5
4	0.5	0.8	0.5
10	0.9	1.4	0.9
14	1.1	1.5	1.1

Table B.12.21 – Surface Resistance at 20 bar 400 K (Figure 3.6(d))

	Surface Resistance (nm)		
Slab Height (nm)	H_2	CH_4	CO_2
1	1.1	3.5	3.2
2	1.5	4.0	3.9
4	1.6	4.3	3.3
10	2.6	4.8	3.8
14	2.7	4.6	4.6
	Surface Resistance Error (nm)		
1	0.2	0.4	0.4
2	0.3	0.6	0.5
4	0.5	0.8	0.6
10	1.1	1.4	1.1
14	1.3	1.7	1.6

Table B.12.22 – Surface Resistance vs. Height in MFI Slabs (Figure 3.7 of Main Text)

	Surface Resistance (nm)				
Slab Height (nm)	H_2	CH_4	CO_2	Ethane	Propane
2	2	23	58	265	1181
10	2	24	37	256	1780
	Surface Resistance Error (nm)				
2	1	3	8	56	554
10	1	3	5	65	549

Table B.12.23 – Surface Resistance in Different Frameworks (Figure 3.8(a))

	Surface Resistance (nm)		
Framework	H_2	CH_4	CO_2
LTA	1.1	-0.3	5.4
CHA	1.1	0.4	10.1
AFI	4.6	18.6	41.5
MFI	4.2	22.4	57.3
AEL	6.9	26.4	189.4
ATO	11.1	105.3	425.8
	Surface Resistance Error (nm)		
LTA	0.4	0.3	0.9
CHA	0.3	0.8	1.5
AFI	1.2	4.4	6.8
MFI	0.8	2.8	8.4
AEL	1.0	3.7	28.5
ATO	1.9	19.9	94.3

Table B.12.24 – CO_2 $D_{0,bulk}$, $D_{0,slab}$, and Q_{ads} in Different Frameworks (Figures 3.8(b) and B.19)

Framework	$D_{0,bulk}$ m^2/s E-10	$D_{0,slab}$ m^2/s E-10	Q_{ads} kJ/mol	$D_{0,slab,estimate}$ m^2/s E-10
MFI	188	7	21.9	4
AEL	474	6	23.3	1
ATO	1015	6	21.7	13
AFI	661	34	17.2	28
LTA	60	19	17.4	22
CHA	39	6	20.1	10
		Errors		
MFI	15	1	0.1	
AEL	36	1	0.3	
ATO	76	1	0.1	
AFI	65	4	0.1	
LTA	4	2	0.1	
CHA	2	1	0.1	

Table B.12.25 – CH_4 $D_{0,bulk}$, $D_{0,slab}$, and Q_{ads} in Different Frameworks (Figures 3.8(c) and B.19)

Framework	$D_{0,bulk}$ m^2/s E-10	$D_{0,slab}$ m^2/s E-10	Q_{ads} kJ/mol	$D_{0,slab,estimate}$ m^2/s E-10
MFI	321	29	17.4	22
AEL	462	37	18.7	15
ATO	2152	54	17.2	87
AFI	1142	123	15.2	72
LTA	5	6	15.2	32
CHA	1	1	16.3	21
		Errors		
MFI	25	2	0.6	
AEL	40	4	0.4	
ATO	167	9	0.3	
AFI	163	19	0.4	
LTA	0.5	0.6	0.3	
CHA	0.1	0.2	0.5	

Table B.12.26 – H_2 $D_{0,bulk}$, $D_{0,slab}$, and Q_{ads} in Different Frameworks (Figures 3.8(d) and B.19)

Framework	$D_{0,bulk}$ m^2/s E-10	$D_{0,slab}$ m^2/s E-10	Q_{ads} kJ/mol	$D_{0,slab,estimate}$ m^2/s E-10
MFI	1796	617	7.6	550
AEL	3397	845	8.0	794
ATO	7068	1390	7.6	1436
AFI	3134	1025	3.8	1001
LTA	534	368	6.3	410
CHA	453	290	7.2	345
		Errors		
MFI	136	58	0.6	
AEL	260	70	0.4	
ATO	436	170	0.3	
AFI	306	146	0.4	
LTA	38	25	0.3	
CHA	31	23	0.5	

Table B.12.27 – Slab Ideal Selectivity (Figure 3.9 of Main Text)

Framework	Simulation CO_2/CH_4	Estimate CO_2/CH_4	Simulation CO_2/H_2	Estimate CO_2/H_2
MFI	1.8	1.0	1.2	1.3
AEL	1.3	2.0	1.0	0.7
ATO	0.8	0.8	0.5	0.8
AFI	1.4	3.5	0.9	0.9
LTA	15.9	13.4	1.7	1.4
CHA	75.9	76.2	1.3	1.5
			Errors	
MFI	0.3		0.2	
AEL	0.2		0.1	
ATO	0.2		0.1	
AFI	0.3		0.2	
LTA	2.1		0.2	
CHA	25.0		0.2	

B.13 Software

-Vienna Ab Initio Simulation Package (VASP 5.4.4):[39] used for generating DFT energies for CO_2 and H_2 force field fitting.

-Large-scale Atomic/Molecular Massively Parallel Simulator (LAMMPS) version 08/22/2018:[40, 41] used for all equilibrium molecular dynamics simulations.

-RASPA 2014 (Version 2.0):[42] used for GCMC simulations to generate isotherms and load unit cells.

-Pymatgen 4.4.0[43] and Atomic Simulation Environment (ASE) 3.11.10:[44] used to read unit cells into our python file that generated the Hill Sauer data file.

-2D nanosheet database:[45] nanosheets used in the study were downloaded from the Knio et al. database.

-Matlab R2016b (9.1.0.441655), September 7, 2016:[46] the fitnlm() function was used to predict diffusivities and ideal selectivities for slabs of six different frameworks.

B.14 Appendix B References

1. Boulfelfel, S.E., P.I. Ravikovitch, L. Koziol, and D.S. Sholl, *Improved Hill–Sauer force field for accurate description of pores in 8-ring zeolites.* The Journal of Physical Chemistry C, 2016. **120**(26): p. 14140-14148.

2. Plimpton, S., P. Crozier, and A. Thompson, *LAMMPS-large-scale atomic/molecular massively parallel simulator.* Sandia National Laboratories, 2007. **18**.

3. Hill, J.-R. and J. Sauer, *Molecular mechanics potential for silica and zeolite catalysts based on ab initio calculations. 2. Aluminosilicates.* The Journal of Physical Chemistry, 1995. **99**(23): p. 9536-9550.

4. Boulfelfel, S.E., P.I. Ravikovitch, and D.S. Sholl, *Modeling diffusion of linear hydrocarbons in silica zeolite LTA using transition path sampling.* The Journal of Physical Chemistry C, 2015. **119**(27): p. 15643-15653.

5. Fang, H., P. Kamakoti, J. Zang, S. Cundy, C. Paur, P.I. Ravikovitch, and D.S. Sholl, *Prediction of CO_2 Adsorption Properties in Zeolites Using Force Fields Derived from Periodic Dispersion-Corrected DFT Calculations.* The Journal of Physical Chemistry C, 2012. **116**(19): p. 10692-10701.

6. Fang, H.J., R. Awati, S.E. Boulfelfel, P.I. Ravikovitch, and D.S. Sholl, *First-Principles-Derived Force Fields for CH_4 Adsorption and Diffusion in Siliceous Zeolites.* Journal of Physical Chemistry C, 2018. **122**(24): p. 12880-12891.

7. Manz, T.A. and D.S. Sholl, *Chemically Meaningful Atomic Charges That Reproduce the Electrostatic Potential in Periodic and Nonperiodic Materials.* Journal of Chemical Theory and Computation, 2010. **6**(8): p. 2455-2468.

8. Watanabe, T., T.A. Manz, and D.S. Sholl, *Accurate Treatment of Electrostatics during Molecular Adsorption in Nanoporous Crystals without Assigning Point Charges to Framework Atoms.* The Journal of Physical Chemistry C, 2011. **115**(11): p. 4824-4836.

9. Manz, T.A. and D.S. Sholl, *Methods for Computing Accurate Atomic Spin Moments for Collinear and Noncollinear Magnetism in Periodic and Nonperiodic Materials.* Journal of Chemical Theory and Computation, 2011. **7**(12): p. 4146-4164.

10. Harris, J.G. and K.H. Yung, *Carbon dioxide's liquid-vapor coexistence curve and critical properties as predicted by a simple molecular model.* The Journal of Physical Chemistry, 1995. **99**(31): p. 12021-12024.

11. Boulfelfel, S.E., P.I. Ravikovitch, L. Koziol, and D.S. Sholl, *Improved Hill-Sauer Force Field for Accurate Description of Pores in 8-Ring Zeolites.* Journal of Physical Chemistry C, 2016. **120**(26): p. 14140-14148.

12. Hill, J.R. and J. Sauer, *Molecular Mechanics Potential for Silica and Zeolite Catalysts Based on Ab-Initio Calculations .2. Aluminosilicates.* Journal of Physical Chemistry, 1995. **99**(23): p. 9536-9550.

13. Yang, Q.Y., Q. Xu, B. Liu, C.L. Zhong, and B. Smit, *Molecular Simulation of CO2/H-2 Mixture Separation in Metal-organic Frameworks: Effect of Catenation and Electrostatic Interactions.* Chinese Journal of Chemical Engineering, 2009. **17**(5): p. 781-790.

14. Fiorin, G., M.L. Klein, and J. Henin, *Using collective variables to drive molecular dynamics simulations.* Molecular Physics, 2013. **111**(22-23): p. 3345-3362.

15. Plimpton, S., *Fast Parallel Algorithms for Short-Range Molecular-Dynamics.* Journal of Computational Physics, 1995. **117**(1): p. 1-19.

16. Grimme, S., *Semiempirical GGA-type density functional constructed with a long-range dispersion correction.* Journal of computational chemistry, 2006. **27**(15): p. 1787-1799.

17. Kresse, G. and J. Hafner, *Abinitio Molecular-Dynamics for Liquid-Metals.* Physical Review B, 1993. **47**(1): p. 558-561.

18. Kresse, G. and J. Hafner, *Ab-Initio Molecular-Dynamics Simulation of the Liquid-Metal Amorphous-Semiconductor Transition in Germanium.* Physical Review B, 1994. **49**(20): p. 14251-14269.

19. Kresse, G. and J. Furthmuller, *Efficiency of ab-initio total energy calculations for metals and semiconductors using a plane-wave basis set.* Computational Materials Science, 1996. **6**(1): p. 15-50.

20. Kresse, G. and J. Furthmuller, *Efficient iterative schemes for ab initio total-energy calculations using a plane-wave basis set.* Physical Review B, 1996. **54**(16): p. 11169-11186.

21. Blochl, P.E., *Projector Augmented-Wave Method.* Physical Review B, 1994. **50**(24): p. 17953-17979.

22. Kresse, G. and D. Joubert, *From ultrasoft pseudopotentials to the projector augmented-wave method.* Physical Review B, 1999. **59**(3): p. 1758-1775.

23. Fang, H.J., P. Kamakoti, P.I. Ravikovitch, M. Aronson, C. Paur, and D.S. Sholl, *First principles derived, transferable force fields for CO_2 adsorption in Na-exchanged cationic zeolites.* Physical Chemistry Chemical Physics, 2013. **15**(31): p. 12882-12894.

24. Pulido, A., M.R. Delgado, O. Bludsky, M. Rubes, P. Nachtigall, and C.O. Arean, *Combined DFT/CC and IR spectroscopic studies on carbon dioxide adsorption on the zeolite H-FER.* Energy & Environmental Science, 2009. **2**(11): p. 1187-1195.

25. Arean, C.O., G.T. Palomino, M.R.L. Carayol, A. Pulido, M. Rubes, O. Bludsky, and P. Nachtigall, *Hydrogen adsorption on the zeolite Ca-A: DFT and FT-IR investigation.* Chemical Physics Letters, 2009. **477**(1-3): p. 139-143.

26. Darkrim, F. and D. Levesque, *Monte Carlo simulations of hydrogen adsorption in single-walled carbon nanotubes.* The Journal of chemical physics, 1998. **109**(12): p. 4981-4984.

27. Pham, T.D. and R.F. Lobo, *Adsorption equilibria of CO_2 and small hydrocarbons in AEI-, CHA-, SIT-, and RRO-type siliceous zeolites.* Microporous and Mesoporous Materials, 2016. **236**: p. 100-108.

28. Bai, P., M. Tsapatsis, and J.I. Siepmann, *TraPPE-zeo: Transferable potentials for phase equilibria force field for all-silica zeolites.* The Journal of Physical Chemistry C, 2013. **117**(46): p. 24375-24387.

29. Martin, M.G. and J.I. Siepmann, *Transferable potentials for phase equilibria. 1. United-atom description of n-alkanes.* The Journal of Physical Chemistry B, 1998. **102**(14): p. 2569-2577.

30. Wick, C.D., M.G. Martin, and J.I. Siepmann, *Transferable potentials for phase equilibria. 4. United-atom description of linear and branched alkenes and alkylbenzenes.* The Journal of Physical Chemistry B, 2000. **104**(33): p. 8008-8016.

31. Hill, J.R. and J. Sauer, *Molecular mechanics potential for silica and zeolite catalysts based on ab initio calculations. 1. Dense and microporous silica.* The Journal of Physical Chemistry, 1994. **98**(4): p. 1238-1244.

32. Granato, M.A., T.J. Vlugt, and A.E. Rodrigues, *Molecular simulation of propane− propylene binary adsorption equilibrium in zeolite 13X.* Industrial & Engineering Chemistry Research, 2007. **46**(22): p. 7239-7245.

33. Fang, H., R. Awati, S.E. Boulfelfel, P.I. Ravikovitch, and D.S. Sholl, *First-principles-derived force fields for CH_4 adsorption and diffusion in siliceous zeolites.* The Journal of Physical Chemistry C, 2018. **122**(24): p. 12880-12891.

34. Newsome, D.A. and D.S. Sholl, *Predictive assessment of surface resistances in zeolite membranes using atomically detailed models.* The Journal of Physical Chemistry B, 2005. **109**(15): p. 7237-7244.

35. Liu, L., D. Nicholson, and S.K. Bhatia, *Interfacial resistance and length-dependent transport diffusivities in carbon nanotubes.* The Journal of Physical Chemistry C, 2016. **120**(46): p. 26363-26373.

36. Sellers, H. and J. Gislason, *Adsorption and desorption rate constants for small molecules on metal surfaces: an example of Trouton's rule.* Surface science, 1999. **426**(2): p. 147-153.

37. Pranami, G. and M.H. Lamm, *Estimating error in diffusion coefficients derived from molecular dynamics simulations.* Journal of chemical theory and computation, 2015. **11**(10): p. 4586-4592.

38. Dutta, R.C. and S.K. Bhatia, *Interfacial barriers to gas transport in zeolites: distinguishing internal and external resistances.* Physical Chemistry Chemical Physics, 2018. **20**(41): p. 26386-26395.

39. Hafner, J. and G. Kresse, *The vienna ab-initio simulation program vasp: An efficient and versatile tool for studying the structural, dynamic, and electronic properties of materials*, in *Properties of Complex Inorganic Solids*. 1997, Springer. p. 69-82.

40. Brown, W.M., P. Wang, S.J. Plimpton, and A.N. Tharrington, *Implementing molecular dynamics on hybrid high performance computers–short range forces.* Computer Physics Communications, 2011. **182**(4): p. 898-911.

41. Kresse, G. and J. Furthmüller, *Efficient iterative schemes for ab initio total-energy calculations using a plane-wave basis set.* Physical review B, 1996. **54**(16): p. 11169.

42. Dubbeldam, D., S. Calero, D.E. Ellis, and R.Q. Snurr, *RASPA: molecular simulation software for adsorption and diffusion in flexible nanoporous materials.* Molecular Simulation, 2016. **42**(2): p. 81-101.

43. Tran, R., Z. Xu, B. Radhakrishnan, D. Winston, W. Sun, K.A. Persson, and S.P. Ong, *Surface energies of elemental crystals.* Scientific data, 2016. **3**: p. 160080.

44. Larsen, A.H., J.J. Mortensen, J. Blomqvist, I.E. Castelli, R. Christensen, M. Dułak, J. Friis, M.N. Groves, B. Hammer, and C. Hargus, *The atomic simulation environment—a Python library for working with atoms.* Journal of Physics: Condensed Matter, 2017. **29**(27): p. 273002.

45. Knio, O., A.J. Medford, S. Nair, and D.S. Sholl, *Database of Computation-Ready 2D Zeolitic Slabs.* Chemistry of Materials, 2018. **31**(2): p. 353-364.

46. *MATLAB*. R2016b (9.1.0.441655), The MathWorks Inc.: Natick, Massachusetts.

APPENDIX C. SUPPORTING INFORMATION FOR CHAPTER 4

C.1 Nanotubes used in XRD Patterns

All unit cells are constructed such that the cell wall is 5 nm away from the nanotube edge. An example for NT-4 is shown in **Figure C.2**.

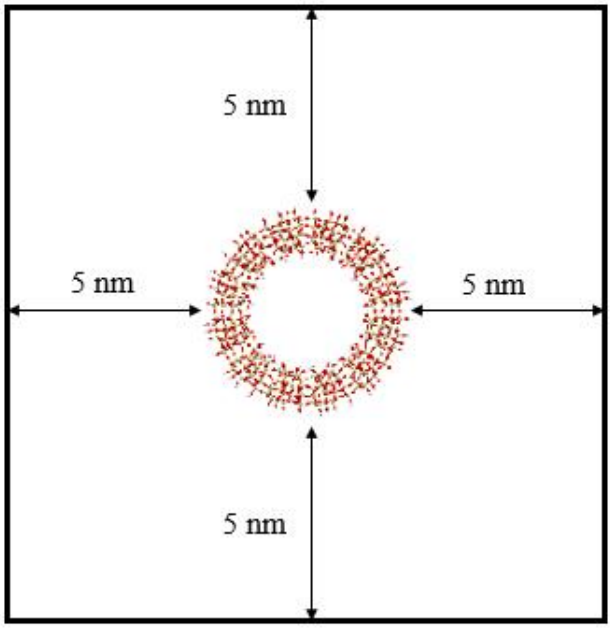

Figure C.1 The walls of NT-4's unit cell are 5 nm away from the nanotube edge.

C.2 Nanotubes from Various Frameworks

Nanotubes from the TON and ITH frameworks are shown in **Figure C.2**. Some of the outer bonds on the ITH nanotube do not appear because the Si-O distance of 2.70 Å is too large.

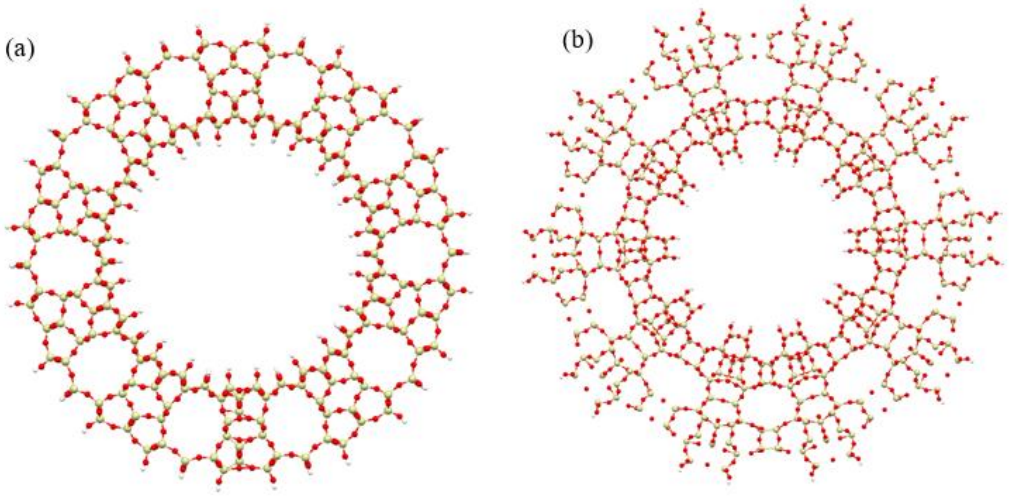

Figure C.2. (a) A TON–(1.5, 13.8, 2.78, b, a, c) nanotube.
(b) An ITH–(2.6, 12.6, 2.8, c, a, b) nanotube.

Two nanotubes made from BEA (100) nanosheets are shown in **Figure C.3**. They have the same orientation, but the nanosheet was extended more prior to curling in **Figure C.3(a)**.

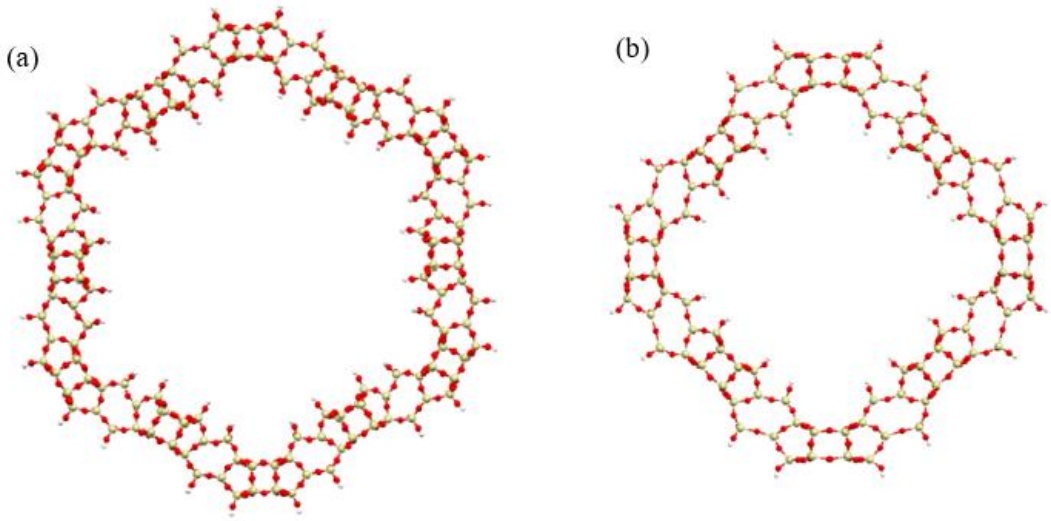

Figure C.3. (a) A BEA–(1.2, 15.6, 4.0, a, c, b) nanotube.
(b) A BEA–(1.2, 10.4, 2.2, a, c, b) nanotube.

C.3 Unit Cells for NT-3 and NT-4

Table - C.1 NT-3 Unit Cell

	a (Å)	b (Å)	c (Å)	alpha (°)	beta (°)	gamma (°)	
	154.647	13.2375	154.579	90	90	90	
Atom	x (Å)	y (Å)	z (Å)	Atom	x (Å)	y (Å)	z (Å)
O	99.97	2.64	78.31	O	54.68	2.64	76.27
O	93.42	0.90	91.90	O	61.22	0.90	62.68
O	91.90	9.12	93.39	O	62.75	9.12	61.19
O	92.65	3.17	92.65	O	62.00	3.17	61.93
O	94.25	11.96	93.09	O	60.40	11.97	61.49
O	91.81	12.74	93.31	O	62.83	12.74	61.27
O	91.65	12.05	95.78	O	63.00	12.05	58.80
O	90.63	1.01	95.05	O	64.01	1.01	59.53
O	91.04	3.45	94.60	O	63.61	3.45	59.98
O	93.15	4.94	94.44	O	61.50	4.95	60.14
O	92.37	9.66	95.84	O	62.28	9.65	58.73
O	93.51	11.36	97.30	O	61.18	11.35	57.23
O	93.26	7.45	94.82	O	61.38	7.46	59.76
O	94.25	9.70	94.15	O	60.40	9.70	60.43
O	94.59	5.89	96.31	O	60.05	5.89	58.28
O	95.26	6.23	93.89	O	59.38	6.23	60.69
O	96.29	11.16	94.38	O	58.34	11.15	60.22
O	91.30	5.29	92.76	O	63.35	5.29	61.82
O	89.57	11.98	94.34	O	65.08	11.98	60.25
O	89.46	9.82	93.05	O	65.19	9.82	61.53
O	87.97	11.75	92.41	O	66.68	11.75	62.17
O	90.45	7.61	92.01	O	64.19	7.62	62.57
O	91.95	2.32	90.39	O	62.69	2.33	64.19
O	91.21	9.84	91.09	O	63.43	9.84	63.49
O	89.80	5.44	90.73	O	64.85	5.44	63.85
O	92.18	6.35	90.63	O	62.47	6.35	63.95
O	95.54	2.46	77.17	O	59.11	2.46	77.41
O	88.88	2.37	93.97	O	65.76	2.37	60.62
O	90.99	11.60	89.27	O	63.66	11.60	65.30
O	90.49	0.84	88.88	O	64.16	0.84	65.70
O	89.69	3.16	89.61	O	64.96	3.16	64.96
O	89.32	12.23	87.52	O	65.32	12.24	67.06

O	88.75	12.54	90.05	O	65.90	12.54	64.53
O	86.32	12.94	90.83	O	68.33	12.94	63.75
O	88.21	0.98	91.90	O	66.44	0.98	62.69
O	88.42	3.53	91.69	O	66.23	3.53	62.89
O	87.64	4.68	89.58	O	67.01	4.68	65.01
O	92.70	11.83	91.11	O	61.95	11.83	63.47
O	96.43	3.99	89.50	O	58.22	3.99	65.08
O	94.37	3.10	90.82	O	60.28	3.10	63.76
O	95.83	5.06	91.68	O	58.82	5.06	62.91
O	98.98	7.80	86.14	O	55.67	7.80	68.43
O	97.73	5.61	86.02	O	56.92	5.61	68.56
O	97.86	3.16	85.43	O	56.79	3.16	69.15
O	95.34	9.11	89.79	O	59.31	9.11	64.80
O	97.63	9.09	90.79	O	57.01	9.09	63.79
O	99.63	10.20	85.83	O	55.01	10.20	68.74
O	101.34	8.50	86.57	O	53.30	8.49	68.01
O	97.66	6.17	92.97	O	56.99	6.15	61.60
O	95.88	7.60	91.78	O	58.76	7.60	62.81
O	95.74	10.09	92.14	O	58.92	10.09	62.44
O	96.45	7.88	85.93	O	58.20	7.88	68.65
O	94.73	9.29	87.26	O	59.92	9.29	67.32
O	95.72	10.03	84.87	O	58.93	10.03	69.71
O	94.11	8.10	85.07	O	60.54	8.10	69.52
O	92.26	5.54	88.23	O	62.39	5.53	66.35
O	93.55	7.66	88.83	O	61.10	7.66	65.75
O	93.06	10.06	89.23	O	61.58	10.06	65.35
O	95.67	4.25	85.95	O	58.98	4.25	68.62
O	93.16	4.16	86.29	O	61.49	4.16	68.30
O	91.49	3.09	87.97	O	63.15	3.09	66.61
O	90.77	5.00	86.27	O	63.87	5.00	68.31
O	91.89	6.93	84.52	O	62.76	6.92	70.06
O	94.05	5.64	84.50	O	60.59	5.64	70.09
O	94.13	3.09	84.22	O	60.51	3.09	70.36
O	94.33	5.36	89.68	O	60.32	5.36	64.91
O	98.85	3.52	80.48	O	55.79	3.51	74.09
O	100.55	1.56	80.49	O	54.10	1.56	74.09
O	97.16	1.33	83.70	O	57.49	1.33	70.87
O	98.57	5.72	81.89	O	56.07	5.72	72.68
O	98.00	10.73	83.95	O	56.65	10.73	70.63
O	98.28	3.45	82.94	O	56.36	3.44	71.64
O	99.88	7.89	82.51	O	54.77	7.89	72.07

O	97.89	7.12	83.92	O	56.76	7.11	70.66
O	101.67	10.77	78.83	O	52.98	10.77	75.75
O	99.17	10.75	79.11	O	55.47	10.75	75.48
O	99.61	1.67	84.23	O	55.04	1.67	70.34
O	99.90	12.40	84.50	O	54.75	12.40	70.08
O	100.41	10.15	83.42	O	54.23	10.15	71.15
O	101.79	0.72	85.12	O	52.86	0.72	69.46
O	101.16	0.40	82.70	O	53.49	0.40	71.88
O	102.78	0.46	80.71	O	51.87	0.46	73.86
O	100.64	12.26	80.56	O	54.00	12.26	74.02
O	100.69	9.77	80.94	O	53.95	9.77	73.63
O	102.30	8.70	82.59	O	52.35	8.70	71.99
O	97.38	10.57	77.22	O	57.27	10.57	77.35
O	96.06	12.24	83.47	O	58.59	12.24	71.11
O	96.55	4.29	81.32	O	58.10	4.29	73.26
O	96.25	10.02	82.30	O	58.40	10.02	72.28
O	94.85	1.18	82.69	O	59.80	1.18	71.89
O	96.86	0.27	81.42	O	57.79	0.27	73.16
O	95.74	1.09	79.30	O	58.91	1.08	75.28
O	97.15	12.20	79.17	O	57.50	12.20	75.41
O	96.93	9.79	79.76	O	57.72	9.79	74.82
O	95.15	8.26	80.84	O	59.50	8.26	73.74
O	94.94	3.53	79.46	O	59.70	3.53	75.12
O	93.47	1.62	78.34	O	61.18	1.62	76.24
O	94.52	5.78	80.75	O	60.12	5.78	73.83
O	94.20	3.46	81.78	O	60.45	3.46	72.80
O	92.83	7.62	80.15	O	61.82	7.62	74.43
O	93.61	7.31	82.63	O	61.04	7.31	71.95
O	92.40	1.94	82.77	O	62.25	1.94	71.81
O	98.25	1.26	79.51	O	56.40	1.26	75.06
O	97.55	8.02	81.57	O	57.10	8.02	73.01
Si	94.07	6.12	94.88	Si	60.57	6.13	59.71
Si	95.15	10.74	93.43	Si	59.49	10.74	61.15
Si	93.13	2.36	91.42	Si	61.52	2.36	63.16
Si	93.06	12.69	92.36	Si	61.59	12.69	62.22
Si	90.91	12.76	94.60	Si	63.74	12.76	59.99
Si	89.98	2.41	95.04	Si	64.67	2.41	59.54
Si	92.02	4.21	93.64	Si	62.63	4.21	60.94
Si	92.11	10.91	96.72	Si	62.57	10.90	57.85
Si	92.94	8.96	94.55	Si	61.71	8.96	60.02
Si	88.87	4.24	90.38	Si	65.78	4.24	64.20

Si	88.57	10.98	93.63	Si	66.07	10.98	60.95
Si	90.70	9.11	92.39	Si	63.94	9.12	62.19
Si	90.91	6.19	91.54	Si	63.73	6.19	63.04
Si	92.02	10.80	90.15	Si	62.63	10.81	64.43
Si	90.93	2.30	89.21	Si	63.72	2.30	65.37
Si	89.87	12.65	88.96	Si	64.78	12.65	65.61
Si	87.84	12.83	91.29	Si	66.81	12.83	63.30
Si	88.05	2.35	92.65	Si	66.59	2.35	61.93
Si	96.14	8.98	91.12	Si	58.51	8.98	63.46
Si	95.25	4.34	90.42	Si	59.40	4.34	64.17
Si	97.75	7.09	85.49	Si	56.90	7.09	69.09
Si	97.16	4.21	86.34	Si	57.49	4.21	68.24
Si	99.83	8.96	86.74	Si	54.82	8.95	67.84
Si	96.11	6.29	92.59	Si	58.53	6.29	61.99
Si	94.30	4.27	85.23	Si	60.35	4.27	69.35
Si	95.24	8.87	85.82	Si	59.41	8.87	68.76
Si	93.09	6.26	89.35	Si	61.56	6.26	65.23
Si	94.18	9.08	88.73	Si	60.46	9.08	65.85
Si	91.91	4.40	87.20	Si	62.73	4.40	67.38
Si	93.43	7.03	84.16	Si	61.22	7.03	70.43
Si	99.41	2.28	79.70	Si	55.23	2.28	74.88
Si	98.08	4.26	81.62	Si	56.57	4.26	72.95
Si	98.49	7.17	82.48	Si	56.16	7.17	72.10
Si	98.23	2.41	84.10	Si	56.42	2.41	70.47
Si	99.48	10.90	84.43	Si	55.17	10.89	70.14
Si	100.62	0.49	84.14	Si	54.03	0.49	70.43
Si	101.25	0.33	81.15	Si	53.40	0.33	73.43
Si	100.53	10.88	79.86	Si	54.11	10.88	74.72
Si	100.84	9.12	82.35	Si	53.81	9.11	72.23
Si	94.03	7.21	81.13	Si	60.62	7.21	73.45
Si	93.87	2.38	82.86	Si	60.78	2.38	71.72
Si	96.46	10.74	83.68	Si	58.18	10.74	70.90
Si	96.22	0.43	82.84	Si	58.43	0.43	71.74
Si	97.01	0.36	79.86	Si	57.63	0.36	74.72
Si	97.65	10.78	78.77	Si	57.00	10.78	75.81
Si	96.48	9.05	81.08	Si	58.17	9.05	73.50
Si	94.92	2.22	78.58	Si	59.72	2.22	76.00
Si	95.07	4.32	80.82	Si	59.58	4.32	73.76
H	94.06	11.95	96.75	H	60.66	12.01	57.73
H	94.89	5.75	97.19	H	59.74	5.76	57.40
H	97.10	11.37	94.81	H	57.53	11.36	59.79

H	89.90	11.60	87.07	H	64.74	11.61	67.51
H	85.84	0.48	91.20	H	68.81	0.48	63.38
H	86.77	4.94	89.31	H	67.87	4.92	65.29
H	101.54	7.87	85.85	H	53.11	7.86	68.73
H	98.07	5.39	92.57	H	56.58	5.36	61.99
H	90.13	5.57	86.74	H	64.52	5.57	67.84
H	91.65	6.15	85.08	H	62.99	6.14	69.50
H	102.49	0.87	85.73	H	52.15	0.85	68.85
H	102.94	1.23	80.15	H	51.70	1.25	74.41
H	103.22	8.49	82.56	H	51.43	8.49	72.02
H	93.14	1.05	79.07	H	61.51	1.05	75.51
H	93.11	8.24	79.47	H	61.54	8.25	75.11
H	91.51	1.68	82.96	H	63.14	1.70	71.61
O	87.76	2.63	97.41	O	66.88	2.63	57.17
O	72.72	0.90	98.53	O	81.93	0.90	56.05
O	70.67	9.12	97.96	O	83.98	9.12	56.62
O	71.68	3.17	98.24	O	82.97	3.17	56.34
O	72.11	11.96	99.84	O	82.54	11.97	54.74
O	70.69	12.74	97.85	O	83.96	12.74	56.73
O	68.47	12.05	98.95	O	86.18	12.06	55.64
O	68.60	1.01	97.70	O	86.05	1.01	56.89
O	69.19	3.46	97.82	O	85.46	3.46	56.76
O	70.39	4.95	99.57	O	84.26	4.95	55.01
O	68.78	9.65	99.59	O	85.87	9.66	54.99
O	68.06	11.36	101.31	O	86.56	11.37	53.27
O	70.11	7.45	99.86	O	84.54	7.46	54.72
O	71.19	9.70	100.37	O	83.46	9.70	54.21
O	69.50	5.89	101.75	O	85.15	5.89	52.83
O	71.92	6.23	101.12	O	82.73	6.23	53.46
O	72.02	11.16	102.26	O	82.64	11.16	52.33
O	70.91	5.29	97.12	O	83.74	5.29	57.46
O	68.68	11.98	96.41	O	85.97	11.98	58.17
O	69.74	9.82	95.68	O	84.90	9.82	58.90
O	69.55	11.75	94.07	O	85.10	11.75	60.52
O	71.14	7.62	96.02	O	83.51	7.61	58.57
O	73.29	2.32	96.50	O	81.35	2.33	58.07
O	72.32	9.84	96.21	O	82.33	9.84	58.37
O	71.92	5.44	94.81	O	82.72	5.44	59.77
O	73.20	6.35	96.82	O	81.45	6.35	57.76
O	86.54	2.46	93.00	O	68.11	2.47	61.58
O	68.66	2.37	95.64	O	85.99	2.37	58.95

O	73.78	11.60	95.11	O	80.87	11.60	59.47
O	73.87	0.84	94.48	O	80.78	0.84	60.10
O	72.83	3.16	94.16	O	81.82	3.16	60.42
O	74.46	12.23	92.79	O	80.19	12.24	61.79
O	71.98	12.54	93.57	O	82.66	12.55	61.02
O	70.09	12.94	91.85	O	84.56	12.94	62.73
O	70.12	0.98	94.02	O	84.53	0.98	60.56
O	70.40	3.53	94.09	O	84.25	3.53	60.48
O	71.84	4.68	92.36	O	82.81	4.68	62.22
O	73.04	11.83	97.51	O	81.60	11.83	57.07
O	76.31	3.99	99.93	O	78.34	3.99	54.65
O	74.13	3.10	98.81	O	80.52	3.10	55.77
O	74.12	5.06	100.50	O	80.53	5.06	54.08
O	80.49	7.80	100.47	O	74.16	7.80	54.11
O	79.97	5.61	99.32	O	74.68	5.61	55.25
O	80.54	3.16	99.14	O	74.11	3.16	55.44
O	75.51	9.11	99.13	O	79.14	9.12	55.45
O	75.79	9.09	101.62	O	78.86	9.09	52.96
O	81.08	10.20	100.87	O	73.57	10.20	53.70
O	81.32	8.50	102.72	O	73.36	8.50	51.85
O	73.91	6.15	102.74	O	80.74	6.16	51.84
O	74.06	7.60	100.60	O	80.59	7.60	53.98
O	73.67	10.09	100.65	O	80.98	10.09	53.93
O	79.40	7.87	98.17	O	75.25	7.88	56.41
O	77.39	9.29	97.34	O	77.26	9.29	57.24
O	79.95	10.03	97.00	O	74.70	10.03	57.57
O	78.98	8.10	95.71	O	75.67	8.10	58.87
O	75.31	5.53	95.69	O	79.33	5.54	58.89
O	75.44	7.66	97.10	O	79.21	7.66	57.47
O	74.85	10.06	96.88	O	79.79	10.07	57.70
O	79.00	4.25	97.51	O	75.65	4.25	57.07
O	77.45	4.15	95.50	O	77.20	4.16	59.08
O	75.15	3.09	94.90	O	79.49	3.09	59.68
O	76.27	5.00	93.42	O	78.38	5.01	61.16
O	78.34	6.92	93.52	O	76.31	6.92	61.06
O	79.45	5.63	95.38	O	75.20	5.63	59.20
O	79.73	3.09	95.30	O	74.92	3.09	59.27
O	75.10	5.36	98.20	O	79.55	5.36	56.38
O	85.32	3.51	97.53	O	69.33	3.51	57.05
O	86.15	1.56	99.00	O	68.49	1.56	55.59
O	81.68	1.33	97.67	O	72.96	1.33	56.91

O	83.96	5.72	97.99	O	70.69	5.72	56.59
O	81.89	10.73	98.52	O	72.75	10.73	56.06
O	82.91	3.44	98.25	O	71.73	3.44	56.32
O	84.08	7.89	99.43	O	70.57	7.89	55.15
O	81.86	7.11	98.41	O	72.79	7.11	56.17
O	88.16	10.77	99.13	O	66.49	10.77	55.45
O	86.67	10.74	97.11	O	67.97	10.74	57.47
O	82.45	1.67	100.05	O	72.20	1.67	54.53
O	82.36	12.40	100.44	O	72.29	12.40	54.14
O	83.55	10.15	100.35	O	71.09	10.15	54.23
O	82.76	0.72	102.38	O	71.87	0.72	52.19
O	84.56	0.39	100.63	O	70.09	0.39	53.95
O	87.09	0.46	101.04	O	67.56	0.45	53.54
O	86.15	12.26	99.11	O	68.50	12.26	55.47
O	85.84	9.76	99.35	O	68.81	9.76	55.23
O	85.21	8.70	101.56	O	69.43	8.70	53.02
O	87.40	10.57	94.62	O	67.24	10.57	59.96
O	81.33	12.24	96.59	O	73.31	12.24	57.98
O	83.45	4.29	95.94	O	71.20	4.29	58.63
O	82.45	10.02	96.18	O	72.20	10.02	58.40
O	81.41	1.18	95.15	O	73.24	1.17	59.42
O	83.51	0.26	96.26	O	71.13	0.26	58.32
O	84.79	1.08	94.23	O	69.86	1.08	60.35
O	85.60	12.20	95.39	O	69.04	12.20	59.19
O	84.98	9.79	95.49	O	69.67	9.79	59.09
O	83.16	8.26	94.50	O	71.49	8.26	60.08
O	84.25	3.53	93.62	O	70.40	3.53	60.95
O	84.48	1.62	91.79	O	70.16	1.62	62.79
O	82.93	5.78	93.90	O	71.72	5.78	60.67
O	81.87	3.46	94.15	O	72.78	3.45	60.43
O	82.59	7.62	92.14	O	72.05	7.62	62.43
O	80.84	7.31	94.05	O	73.81	7.31	60.52
O	80.12	1.95	93.07	O	74.53	1.94	61.50
O	85.85	1.25	96.52	O	68.79	1.26	58.07
O	83.73	8.02	96.94	O	70.92	8.02	57.64
Si	70.47	6.13	100.58	Si	84.18	6.13	54.00
Si	72.26	10.74	100.80	Si	82.39	10.74	53.78
Si	72.99	2.36	98.04	Si	81.66	2.36	56.54
Si	72.14	12.69	98.45	Si	82.51	12.69	56.13
Si	69.13	12.76	97.71	Si	85.52	12.77	56.88
Si	68.28	2.41	97.12	Si	86.37	2.41	57.46

Si	70.51	4.21	98.19	Si	84.14	4.21	56.39
Si	67.88	10.90	99.80	Si	86.76	10.91	54.77
Si	70.18	8.96	99.44	Si	84.47	8.96	55.14
Si	71.76	4.24	93.83	Si	82.89	4.24	60.75
Si	68.79	10.99	95.20	Si	85.85	10.99	59.38
Si	70.94	9.12	96.42	Si	83.71	9.12	58.16
Si	71.78	6.19	96.18	Si	82.87	6.19	58.40
Si	73.53	10.80	96.44	Si	81.11	10.81	58.14
Si	73.80	2.30	95.03	Si	80.85	2.30	59.55
Si	73.48	12.65	93.99	Si	81.16	12.65	60.59
Si	70.46	12.83	93.39	Si	84.19	12.83	61.19
Si	69.38	2.35	94.26	Si	85.26	2.35	60.32
Si	74.76	8.98	100.49	Si	79.89	8.98	54.09
Si	74.92	4.34	99.37	Si	79.73	4.34	55.21
Si	80.43	7.09	99.07	Si	74.21	7.09	55.51
Si	79.41	4.20	98.99	Si	75.24	4.20	55.59
Si	80.40	8.95	101.50	Si	74.25	8.95	53.08
Si	73.47	6.29	101.21	Si	81.18	6.30	53.37
Si	78.94	4.27	95.95	Si	75.71	4.27	58.63
Si	78.89	8.87	97.07	Si	75.75	8.87	57.51
Si	74.76	6.26	96.97	Si	79.89	6.26	57.61
Si	75.84	9.08	97.61	Si	78.81	9.08	56.97
Si	76.03	4.40	94.88	Si	78.61	4.40	59.70
Si	79.43	7.02	94.67	Si	75.22	7.02	59.91
Si	86.28	2.27	97.62	Si	68.36	2.28	56.96
Si	83.95	4.26	97.42	Si	70.70	4.26	57.16
Si	83.41	7.17	98.21	Si	71.23	7.17	56.37
Si	81.87	2.41	98.79	Si	72.77	2.41	55.79
Si	82.21	10.90	100.04	Si	72.43	10.89	54.53
Si	83.03	0.49	100.89	Si	71.61	0.49	53.69
Si	85.94	0.32	99.93	Si	68.70	0.32	54.65
Si	86.70	10.87	98.67	Si	67.95	10.87	55.91
Si	84.69	9.11	100.18	Si	69.95	9.11	54.40
Si	82.35	7.21	93.67	Si	72.30	7.21	60.91
Si	80.77	2.38	94.39	Si	73.88	2.38	60.19
Si	81.36	10.74	97.05	Si	73.29	10.74	57.53
Si	81.96	0.43	96.42	Si	72.68	0.43	58.16
Si	84.94	0.36	95.61	Si	69.70	0.36	58.97
Si	86.20	10.77	95.63	Si	68.45	10.77	58.96
Si	83.62	9.05	95.77	Si	71.03	9.05	58.81
Si	85.00	2.22	93.17	Si	69.64	2.22	61.41

Si	83.14	4.32	94.41	Si	71.51	4.32	60.16
H	68.78	11.98	101.50	H	85.80	11.95	53.08
H	68.89	5.75	102.46	H	85.75	5.75	52.12
H	72.06	11.37	103.18	H	82.60	11.38	51.41
H	75.15	11.61	93.06	H	79.50	11.61	61.52
H	69.53	0.48	91.62	H	85.12	0.48	62.96
H	71.65	4.93	91.47	H	83.00	4.93	63.11
H	82.05	7.89	102.52	H	72.64	7.86	52.03
H	74.44	5.36	102.90	H	80.19	5.38	51.68
H	75.54	5.57	93.10	H	79.10	5.58	61.48
H	77.74	6.14	93.59	H	76.91	6.14	60.99
H	82.58	0.87	103.30	H	72.05	0.86	51.27
H	87.65	1.24	100.90	H	67.00	1.23	53.68
H	85.70	8.48	102.34	H	68.94	8.49	52.24
H	83.69	1.05	91.87	H	70.96	1.06	62.71
H	83.32	8.26	92.04	H	71.32	8.25	62.54
H	79.51	1.71	92.39	H	75.14	1.69	62.18
O	65.12	2.63	96.39	O	89.52	2.63	58.19
O	56.62	0.90	83.92	O	98.03	0.90	70.65
O	56.08	9.11	81.86	O	98.56	9.12	72.72
O	56.35	3.17	82.88	O	98.30	3.17	71.70
O	55.18	11.96	84.04	O	99.47	11.96	70.53
O	56.20	12.74	81.82	O	98.45	12.74	72.75
O	54.14	12.05	80.45	O	100.51	12.05	74.13
O	55.28	1.01	79.93	O	99.37	1.01	74.64
O	55.46	3.45	80.51	O	99.18	3.45	74.07
O	54.55	4.94	82.42	O	100.09	4.94	72.16
O	53.73	9.66	81.04	O	100.92	9.65	73.54
O	51.89	11.36	81.30	O	102.77	11.36	73.31
O	54.16	7.45	82.33	O	100.48	7.45	72.25
O	54.26	9.70	83.52	O	100.39	9.70	71.06
O	52.22	5.89	82.75	O	102.43	5.89	71.83
O	53.97	6.23	84.53	O	100.67	6.22	70.05
O	53.04	11.16	85.18	O	101.60	11.15	69.39
O	56.93	5.29	81.65	O	97.71	5.29	72.93
O	56.43	11.98	79.37	O	98.21	11.98	75.21
O	57.60	9.82	79.92	O	97.05	9.82	74.66
O	58.90	11.75	78.95	O	95.75	11.75	75.63
O	58.01	7.61	81.30	O	96.64	7.61	73.28
O	58.66	2.32	83.41	O	95.99	2.32	71.17
O	58.43	9.83	82.41	O	96.22	9.83	72.16

O	59.45	5.44	81.37	O	95.20	5.44	73.21
O	58.34	6.35	83.48	O	96.31	6.35	71.10
O	68.32	2.46	93.12	O	86.32	2.46	61.46
O	57.10	2.37	78.96	O	97.55	2.37	75.62
O	60.11	11.59	83.12	O	94.54	11.59	71.45
O	60.70	0.84	82.90	O	93.95	0.84	71.69
O	60.46	3.16	81.83	O	94.19	3.16	72.75
O	62.46	12.24	82.56	O	92.19	12.23	72.02
O	60.56	12.55	80.80	O	94.10	12.54	73.78
O	61.09	12.94	78.30	O	93.56	12.94	76.28
O	59.22	0.98	79.42	O	95.42	0.98	75.17
O	59.30	3.53	79.70	O	95.35	3.53	74.89
O	61.53	4.67	80.08	O	93.12	4.68	74.50
O	57.67	11.83	83.69	O	96.98	11.83	70.88
O	57.20	3.98	87.73	O	97.44	3.98	66.85
O	57.08	3.10	85.29	O	97.56	3.10	69.29
O	55.61	5.06	86.12	O	99.03	5.06	68.45
O	58.83	7.80	91.62	O	95.82	7.81	62.96
O	59.56	5.61	90.60	O	95.09	5.61	63.98
O	60.01	3.16	91.00	O	94.64	3.16	63.58
O	57.49	9.11	86.64	O	97.15	9.11	67.94
O	55.47	9.09	88.13	O	99.17	9.09	66.45
O	58.77	10.20	92.33	O	95.88	10.20	62.24
O	57.30	8.49	93.47	O	97.41	8.51	61.17
O	53.57	6.16	87.06	O	101.07	6.17	67.52
O	55.50	7.60	86.12	O	99.15	7.60	68.46
O	55.25	10.09	85.81	O	99.39	10.09	68.77
O	60.27	7.88	89.53	O	94.37	7.87	65.05
O	59.98	9.29	87.37	O	94.66	9.29	67.21
O	61.56	10.04	89.42	O	93.09	10.03	65.15
O	62.19	8.10	87.93	O	92.45	8.10	66.65
O	60.37	5.54	84.75	O	94.27	5.53	69.83
O	59.21	7.66	85.57	O	95.43	7.66	69.01
O	59.11	10.06	84.95	O	95.53	10.06	69.63
O	60.64	4.25	88.84	O	94.00	4.25	65.73
O	61.62	4.15	86.50	O	93.04	4.15	68.08
O	60.98	3.09	84.22	O	93.67	3.09	70.36
O	62.82	5.00	84.44	O	91.83	5.00	70.13
O	63.77	6.92	86.28	O	90.88	6.92	68.30
O	62.71	5.64	88.18	O	91.93	5.63	66.40
O	62.92	3.09	88.38	O	91.73	3.09	66.20

O	58.09	5.36	85.82	O	96.55	5.36	68.76
O	63.79	3.51	94.33	O	90.85	3.51	60.25
O	62.94	1.56	95.79	O	91.70	1.56	58.79
O	61.85	1.33	91.26	O	92.80	1.33	63.32
O	62.71	5.72	93.38	O	91.94	5.72	61.19
O	61.22	10.74	91.86	O	93.43	10.73	62.71
O	61.95	3.45	92.61	O	92.69	3.44	61.96
O	61.53	7.89	94.21	O	93.12	7.89	60.36
O	61.30	7.11	91.78	O	93.35	7.11	62.80
O	63.82	10.77	97.60	O	90.82	10.76	56.98
O	64.83	10.74	95.30	O	89.81	10.75	59.28
O	60.17	1.67	93.11	O	94.48	1.67	61.46
O	59.78	12.40	93.23	O	94.86	12.40	61.34
O	60.47	10.15	94.21	O	94.18	10.15	60.36
O	58.31	0.72	94.56	O	96.33	0.72	60.01
O	60.73	0.39	95.22	O	93.92	0.39	59.35
O	61.63	0.46	97.62	O	93.01	0.46	56.96
O	62.84	12.26	95.85	O	91.80	12.26	58.73
O	62.47	9.76	95.70	O	92.17	9.77	58.89
O	60.24	8.70	96.26	O	94.39	8.70	58.30
O	67.35	10.57	94.69	O	87.29	10.57	59.90
O	62.60	12.24	90.42	O	92.05	12.24	64.16
O	64.22	4.29	91.92	O	90.43	4.29	62.66
O	63.52	10.02	91.17	O	91.13	10.02	63.40
O	63.89	1.18	89.76	O	90.76	1.17	64.82
O	63.98	0.26	92.14	O	90.66	0.26	62.44
O	66.38	1.09	92.22	O	88.27	1.08	62.36
O	65.78	12.20	93.51	O	88.86	12.20	61.07
O	65.39	9.79	93.02	O	89.26	9.79	61.56
O	65.33	8.26	90.95	O	89.31	8.26	63.63
O	66.64	3.53	91.46	O	88.01	3.53	63.12
O	68.34	1.62	90.74	O	86.30	1.62	63.84
O	65.73	5.78	90.45	O	88.92	5.77	64.13
O	64.99	3.46	89.65	O	89.66	3.45	64.93
O	67.09	7.62	89.28	O	87.56	7.62	65.30
O	64.55	7.31	88.71	O	90.09	7.31	65.86
O	65.03	1.95	87.60	O	89.60	1.94	66.98
O	64.94	1.26	94.29	O	89.71	1.25	60.29
O	63.50	8.02	92.66	O	91.14	8.02	61.91
Si	53.71	6.12	83.00	Si	100.93	6.12	71.57
Si	54.43	10.74	84.66	Si	100.22	10.74	69.92

Si	57.18	2.36	83.91	Si	97.46	2.36	70.67
Si	56.40	12.68	83.38	Si	98.25	12.68	71.20
Si	55.54	12.76	80.40	Si	99.11	12.76	74.18
Si	55.62	2.41	79.37	Si	99.03	2.41	75.21
Si	55.81	4.21	81.84	Si	98.84	4.21	72.74
Si	53.10	10.91	80.38	Si	101.54	10.90	74.21
Si	54.56	8.96	82.18	Si	100.09	8.96	72.40
Si	60.21	4.23	80.74	Si	94.44	4.24	73.84
Si	57.54	10.98	78.86	Si	97.11	10.98	75.72
Si	57.55	9.11	81.32	Si	97.09	9.11	73.25
Si	58.19	6.18	81.93	Si	96.46	6.19	72.65
Si	58.84	10.80	83.58	Si	95.81	10.80	71.00
Si	60.19	2.30	83.11	Si	94.46	2.30	71.47
Si	60.94	12.65	82.31	Si	93.71	12.64	72.27
Si	59.94	12.83	79.40	Si	94.71	12.83	75.18
Si	58.65	2.35	78.90	Si	96.00	2.35	75.68
Si	55.94	8.98	86.67	Si	98.71	8.98	67.91
Si	56.99	4.34	86.25	Si	97.65	4.34	68.33
Si	60.01	7.09	90.87	Si	94.63	7.09	63.70
Si	59.57	4.21	89.94	Si	95.07	4.21	64.63
Si	57.89	8.95	92.07	Si	96.76	8.96	62.54
Si	54.68	6.29	85.91	Si	99.97	6.29	68.67
Si	61.96	4.27	88.02	Si	92.68	4.27	66.56
Si	60.97	8.87	88.54	Si	93.67	8.87	66.04
Si	58.99	6.26	84.91	Si	95.66	6.26	69.67
Si	58.98	9.08	86.17	Si	95.66	9.08	68.41
Si	61.44	4.40	84.97	Si	93.21	4.40	69.61
Si	63.32	7.03	87.80	Si	91.32	7.02	66.78
Si	64.19	2.28	95.21	Si	90.45	2.28	59.37
Si	63.19	4.26	93.09	Si	91.45	4.26	61.49
Si	62.25	7.17	93.02	Si	92.40	7.17	61.55
Si	60.97	2.41	91.98	Si	93.67	2.41	62.59
Si	60.06	10.90	92.90	Si	94.59	10.89	61.67
Si	59.74	0.49	94.04	Si	94.90	0.49	60.54
Si	62.02	0.32	96.07	Si	92.62	0.32	58.50
Si	63.49	10.87	96.10	Si	91.15	10.87	58.48
Si	61.18	9.11	95.12	Si	93.46	9.11	59.46
Si	65.64	7.21	89.83	Si	89.00	7.21	64.75
Si	64.23	2.38	88.83	Si	90.42	2.38	65.75
Si	62.22	10.74	90.66	Si	92.43	10.74	63.91
Si	63.07	0.43	90.87	Si	91.58	0.43	63.71

Si	65.26	0.36	93.05	Si	89.39	0.36	61.53
Si	65.88	10.78	94.14	Si	88.76	10.77	60.44
Si	64.46	9.05	91.98	Si	90.18	9.05	62.60
Si	67.41	2.22	91.88	Si	87.24	2.22	62.70
Si	65.40	4.32	90.89	Si	89.25	4.32	63.69
H	52.10	11.96	82.05	H	102.57	11.99	72.59
H	51.30	5.74	82.58	H	103.35	5.76	72.00
H	52.27	11.37	85.67	H	102.39	11.36	68.91
H	62.56	11.61	83.30	H	92.08	11.60	71.29
H	61.01	0.48	77.70	H	93.63	0.48	76.88
H	62.20	4.92	79.47	H	92.44	4.93	75.11
H	57.85	7.89	94.01	H	96.93	7.84	60.65
H	53.72	5.39	87.62	H	100.93	5.39	66.95
H	62.73	5.58	83.65	H	91.91	5.57	70.92
H	63.40	6.14	85.80	H	91.24	6.14	68.78
H	57.43	0.87	94.87	H	97.21	0.85	59.70
H	62.03	1.24	98.03	H	92.62	1.25	56.55
H	59.81	8.48	97.07	H	94.82	8.49	57.49
H	67.87	1.05	90.09	H	86.77	1.05	64.49
H	67.54	8.25	89.86	H	87.10	8.25	64.72
H	65.30	1.70	86.73	H	89.31	1.68	67.84

Table C.2 NT-4 Unit Cell

	a (Å)	b (Å)	c (Å)	alpha (°)	beta (°)	gamma (°)	
	147.84	13.37	147.85	90	90	90	
Atom	x (Å)	y (Å)	z (Å)	Atom	x (Å)	y (Å)	z (Å)
O	93.84	2.63	74.06	O	54.00	2.63	73.79
O	88.57	1.06	87.23	O	59.27	1.06	60.61
O	87.04	9.22	88.48	O	60.80	9.22	59.36
O	87.70	3.31	87.92	O	60.14	3.31	59.92
O	89.48	12.07	87.96	O	58.36	12.07	59.88
O	87.27	12.97	88.96	O	60.57	12.97	58.88
O	86.08	11.96	91.08	O	61.77	11.96	56.77
O	85.56	0.96	90.34	O	62.29	0.96	57.50
O	86.11	3.42	89.97	O	61.73	3.42	57.87
O	88.21	5.17	89.54	O	59.63	5.17	58.31
O	86.98	9.67	90.97	O	60.87	9.68	56.88
O	87.09	10.97	93.09	O	60.75	10.97	54.76
O	88.39	7.71	89.92	O	59.45	7.71	57.93
O	89.23	9.96	89.26	O	58.62	9.96	58.59
O	90.18	6.16	90.74	O	57.67	6.16	57.10
O	90.06	6.60	88.25	O	57.79	6.60	59.59
O	91.40	11.19	89.26	O	56.44	11.19	58.58
O	86.08	5.24	88.23	O	61.76	5.24	59.62
O	84.80	12.31	88.94	O	63.04	12.31	58.91
O	84.68	9.95	88.13	O	63.16	9.95	59.72
O	83.43	11.72	86.83	O	64.42	11.72	61.02
O	85.47	7.66	87.26	O	62.37	7.66	60.58
O	87.11	2.38	85.65	O	60.73	2.38	62.20
O	86.27	10.02	86.25	O	61.57	10.03	61.59
O	84.65	5.47	86.06	O	63.19	5.47	61.78
O	87.08	6.13	86.19	O	60.77	6.13	61.66
O	89.75	1.81	73.83	O	58.10	1.81	74.01
O	84.23	2.25	88.78	O	63.61	2.26	59.07
O	86.28	11.83	84.33	O	61.56	11.83	63.52
O	85.84	0.94	83.84	O	62.00	0.94	64.00
O	84.81	3.18	84.82	O	63.03	3.18	63.03
O	85.17	12.49	82.15	O	62.68	12.49	65.69
O	84.00	12.71	84.45	O	63.84	12.71	63.40
O	81.68	13.08	85.47	O	66.16	13.08	62.37
O	83.74	0.78	86.54	O	64.10	0.78	61.30

O	83.43	3.38	86.60	O	64.41	3.38	61.25
O	82.69	4.67	84.52	O	65.16	4.67	63.33
O	87.45	12.25	86.54	O	60.39	12.25	61.30
O	91.10	4.05	84.00	O	56.74	4.05	63.85
O	89.49	3.25	86.02	O	58.36	3.25	61.83
O	91.06	5.29	86.30	O	56.79	5.29	61.55
O	93.03	8.10	82.70	O	54.82	8.10	65.14
O	92.21	5.73	82.32	O	55.64	5.73	65.52
O	92.50	3.26	81.73	O	55.34	3.26	66.12
O	90.33	8.99	84.95	O	57.51	8.99	62.90
O	92.62	9.66	84.75	O	55.22	9.66	63.10
O	93.75	10.38	82.16	O	54.09	10.38	65.69
O	94.91	9.09	83.94	O	52.93	9.09	63.91
O	92.52	6.06	88.16	O	55.32	6.06	59.68
O	91.73	7.81	86.54	O	56.11	7.81	61.31
O	90.96	10.12	87.05	O	56.88	10.12	60.80
O	90.85	7.75	81.49	O	56.99	7.75	66.36
O	89.08	9.10	82.75	O	58.76	9.10	65.09
O	90.34	10.10	80.84	O	57.50	10.10	67.00
O	88.61	8.34	80.35	O	59.24	8.34	67.50
O	86.85	5.88	83.75	O	61.00	5.88	64.10
O	88.18	7.86	84.71	O	59.66	7.86	63.14
O	88.28	10.44	84.87	O	59.57	10.44	62.98
O	90.28	4.43	81.63	O	57.57	4.43	66.21
O	87.67	4.88	81.76	O	60.17	4.88	66.09
O	86.48	3.38	83.32	O	61.36	3.38	64.53
O	85.19	5.22	81.84	O	62.65	5.22	66.01
O	86.42	6.98	80.04	O	61.43	6.98	67.80
O	88.74	5.91	79.94	O	59.11	5.91	67.90
O	88.50	3.31	80.15	O	59.35	3.31	67.70
O	89.12	5.42	84.82	O	58.72	5.42	63.03
O	93.45	3.44	76.62	O	54.39	3.44	71.23
O	94.95	1.40	76.07	O	52.90	1.40	71.77
O	91.60	1.44	80.23	O	56.24	1.44	67.62
O	93.27	5.63	78.12	O	54.58	5.63	69.72
O	92.56	10.84	79.98	O	55.28	10.84	67.87
O	92.86	3.38	79.16	O	54.99	3.38	68.69
O	94.42	7.99	78.30	O	53.43	7.99	69.54
O	93.00	7.09	80.27	O	54.84	7.09	67.57
O	95.53	10.40	73.95	O	52.31	10.40	73.90
O	93.64	11.07	75.27	O	54.20	11.07	72.58

O	94.10	1.52	80.30	O	53.74	1.52	67.54
O	94.45	12.35	80.54	O	53.40	12.35	67.30
O	94.84	10.10	79.55	O	53.00	10.10	68.29
O	96.41	0.53	80.36	O	51.44	0.53	67.48
O	95.06	0.09	78.27	O	52.78	0.09	69.58
O	97.15	0.62	76.96	O	50.69	0.62	70.89
O	95.65	12.25	75.94	O	52.19	12.25	71.90
O	95.24	9.94	76.77	O	52.60	9.94	71.07
O	96.73	8.87	78.47	O	51.11	8.87	69.38
O	91.47	10.96	73.99	O	56.38	10.96	73.85
O	90.60	12.40	79.70	O	57.25	12.40	68.14
O	91.21	4.30	77.48	O	56.64	4.30	70.36
O	90.78	10.03	78.42	O	57.06	10.03	69.42
O	89.29	1.22	79.07	O	58.56	1.22	68.77
O	91.45	0.55	77.97	O	56.40	0.55	69.88
O	90.03	0.81	75.97	O	57.81	0.81	71.88
O	91.67	12.20	76.13	O	56.18	12.20	71.71
O	91.83	9.62	76.22	O	56.02	9.62	71.62
O	89.83	8.23	76.75	O	58.02	8.23	71.09
O	89.50	3.31	75.78	O	58.35	3.31	72.07
O	87.64	1.47	75.14	O	60.21	1.47	72.70
O	89.20	5.75	76.56	O	58.64	5.75	71.29
O	88.80	3.51	77.91	O	59.04	3.51	69.93
O	87.77	7.57	75.43	O	60.07	7.57	72.42
O	87.92	7.35	78.00	O	59.93	7.35	69.85
O	86.81	2.01	78.72	O	61.03	2.01	69.13
O	92.53	1.27	75.76	O	55.31	1.27	72.09
O	91.95	7.81	78.09	O	55.90	7.81	69.76
Si	89.20	6.40	89.57	Si	58.65	6.40	58.27
Si	90.25	10.74	88.33	Si	57.60	10.74	59.52
Si	88.27	2.51	86.70	Si	59.58	2.51	61.15
Si	88.22	12.97	87.70	Si	59.63	12.97	60.14
Si	85.96	12.90	89.83	Si	61.88	12.90	58.01
Si	84.92	2.39	90.18	Si	62.92	2.39	57.67
Si	87.05	4.26	88.98	Si	60.80	4.26	58.86
Si	86.13	10.65	91.92	Si	61.71	10.65	55.93
Si	87.92	9.20	89.75	Si	59.93	9.20	58.10
Si	83.88	4.27	85.41	Si	63.96	4.27	62.44
Si	83.87	11.26	88.24	Si	63.98	11.26	59.61
Si	85.86	9.17	87.51	Si	61.99	9.17	60.33
Si	85.74	6.13	86.99	Si	62.10	6.13	60.86

Si	87.06	11.17	85.48	Si	60.78	11.17	62.36
Si	86.09	2.36	84.46	Si	61.75	2.36	63.39
Si	85.33	12.85	83.64	Si	62.52	12.85	64.20
Si	83.23	12.84	85.79	Si	64.62	12.85	62.06
Si	83.43	2.06	87.45	Si	64.41	2.06	60.40
Si	91.53	9.22	85.87	Si	56.31	9.22	61.98
Si	90.24	4.42	85.27	Si	57.61	4.42	62.57
Si	92.30	7.16	81.68	Si	55.54	7.16	66.16
Si	91.58	4.30	82.50	Si	56.27	4.30	65.34
Si	93.49	9.41	83.40	Si	54.35	9.41	64.44
Si	91.31	6.48	87.30	Si	56.53	6.48	60.55
Si	88.92	4.63	80.88	Si	58.92	4.63	66.96
Si	89.69	8.80	81.35	Si	58.15	8.80	66.50
Si	87.85	6.33	84.87	Si	59.99	6.33	62.98
Si	88.96	9.17	84.31	Si	58.89	9.17	63.53
Si	86.42	4.82	82.66	Si	61.42	4.82	65.19
Si	87.91	7.21	79.55	Si	59.93	7.21	68.30
Si	93.73	2.26	75.60	Si	54.12	2.26	72.25
Si	92.73	4.17	77.81	Si	55.11	4.17	70.03
Si	93.19	7.09	78.71	Si	54.65	7.09	69.13
Si	92.82	2.43	80.40	Si	55.03	2.43	67.44
Si	93.95	10.86	80.63	Si	53.89	10.86	67.21
Si	94.97	0.29	79.84	Si	52.87	0.29	68.01
Si	95.67	0.21	76.81	Si	52.17	0.21	71.04
Si	95.14	10.84	75.46	Si	52.70	10.84	72.38
Si	95.26	9.32	78.24	Si	52.58	9.32	69.61
Si	88.66	7.21	76.64	Si	59.18	7.21	71.21
Si	88.29	2.41	78.89	Si	59.56	2.41	68.96
Si	91.05	10.89	79.73	Si	56.79	10.89	68.12
Si	90.69	0.56	79.33	Si	57.16	0.56	68.52
Si	91.46	0.35	76.44	Si	56.38	0.35	71.41
Si	92.14	10.89	75.40	Si	55.71	10.89	72.44
Si	91.08	8.89	77.37	Si	56.76	8.89	70.48
Si	89.12	1.86	75.24	Si	58.73	1.86	72.61
Si	89.73	4.33	76.96	Si	58.12	4.33	70.88
H	87.68	11.37	93.71	H	60.17	11.37	54.13
H	90.59	5.97	91.57	H	57.26	5.97	56.27
H	92.04	11.72	89.71	H	55.81	11.72	58.13
H	85.37	12.03	81.35	H	62.48	12.04	66.50
H	81.29	0.44	86.00	H	66.55	0.44	61.84
H	81.84	4.95	84.22	H	66.01	4.95	63.62

H	95.73	8.68	84.18	H	52.11	8.68	63.66
H	93.29	5.68	88.57	H	54.56	5.68	59.28
H	84.40	5.54	81.44	H	63.45	5.54	66.41
H	86.34	6.24	80.70	H	61.50	6.24	67.15
H	97.18	0.71	80.88	H	50.66	0.71	66.97
H	98.01	1.01	76.92	H	49.83	1.01	70.92
H	97.50	8.34	78.54	H	50.34	8.34	69.30
H	86.75	1.15	75.19	H	61.10	1.15	72.65
H	87.54	8.02	74.63	H	60.30	8.02	73.21
H	85.93	1.73	78.89	H	61.92	1.73	68.96
O	83.77	2.63	91.24	O	64.08	2.63	56.61
O	69.72	1.06	93.27	O	78.12	1.06	54.58
O	67.87	9.22	92.56	O	79.98	9.22	55.28
O	68.69	3.31	92.86	O	79.16	3.31	54.99
O	69.54	12.07	94.42	O	78.30	12.07	53.43
O	67.57	12.97	93.00	O	80.27	12.97	54.84
O	65.14	11.96	93.03	O	82.70	11.96	54.82
O	65.52	0.96	92.21	O	82.32	0.96	55.64
O	66.12	3.42	92.50	O	81.73	3.42	55.34
O	67.54	5.17	94.10	O	80.30	5.17	53.74
O	65.69	9.68	93.75	O	82.16	9.68	54.09
O	63.91	10.97	94.91	O	83.94	10.97	52.93
O	67.30	7.71	94.45	O	80.54	7.71	53.40
O	68.29	9.96	94.84	O	79.55	9.96	53.00
O	67.48	6.16	96.41	O	80.36	6.16	51.44
O	69.58	6.60	95.06	O	78.27	6.60	52.78
O	69.38	11.19	96.73	O	78.47	11.19	51.12
O	67.61	5.24	91.60	O	80.23	5.24	56.24
O	66.36	12.31	90.85	O	81.49	12.31	56.99
O	67.00	9.95	90.34	O	80.84	9.95	57.50
O	67.50	11.72	88.61	O	80.35	11.72	59.24
O	68.14	7.66	90.60	O	79.70	7.66	57.25
O	70.36	2.38	91.21	O	77.48	2.38	56.64
O	69.42	10.03	90.78	O	78.42	10.03	57.06
O	68.77	5.47	89.29	O	79.07	5.47	58.56
O	69.88	6.13	91.45	O	77.97	6.13	56.40
O	81.91	1.80	87.58	O	65.93	1.81	60.26
O	66.21	2.26	90.28	O	81.63	2.25	57.57
O	71.09	11.83	89.83	O	76.75	11.83	58.02
O	71.29	0.94	89.20	O	76.55	0.94	58.64
O	69.93	3.18	88.80	O	77.91	3.18	59.04

O	72.42	12.49	87.78	O	75.43	12.49	60.07
O	69.85	12.71	87.92	O	78.00	12.71	59.93
O	67.80	13.08	86.42	O	80.04	13.08	61.43
O	67.90	0.78	88.74	O	79.94	0.78	59.11
O	67.70	3.38	88.50	O	80.14	3.38	59.35
O	69.13	4.67	86.81	O	78.72	4.67	61.03
O	69.76	12.25	91.95	O	78.09	12.25	55.90
O	73.79	4.05	93.84	O	74.06	4.05	54.00
O	71.23	3.25	93.45	O	76.62	3.25	54.39
O	71.77	5.29	94.95	O	76.07	5.29	52.90
O	75.87	8.10	94.86	O	71.97	8.10	52.99
O	75.79	5.73	93.96	O	72.05	5.73	53.88
O	76.46	3.26	93.92	O	71.39	3.26	53.93
O	72.58	8.99	93.64	O	75.27	8.99	54.20
O	73.90	9.66	95.53	O	73.95	9.66	52.31
O	76.71	10.38	95.21	O	71.14	10.38	52.63
O	75.74	9.09	97.11	O	72.10	9.09	50.74
O	70.89	6.06	97.15	O	76.96	6.06	50.69
O	71.90	7.81	95.65	O	75.94	7.81	52.19
O	71.07	10.12	95.24	O	76.77	10.12	52.60
O	75.84	7.75	92.37	O	72.01	7.75	55.48
O	73.85	9.10	91.47	O	73.99	9.10	56.38
O	76.14	10.10	91.60	O	71.71	10.10	56.24
O	75.70	8.34	89.85	O	72.14	8.34	57.99
O	71.87	5.88	90.03	O	75.97	5.88	57.81
O	71.71	7.86	91.67	O	76.13	7.86	56.18
O	71.62	10.44	91.83	O	76.22	10.44	56.02
O	75.42	4.43	91.94	O	72.42	4.43	55.90
O	74.01	4.88	89.75	O	73.83	4.88	58.10
O	72.07	3.38	89.50	O	75.78	3.38	58.35
O	72.70	5.22	87.64	O	75.14	5.21	60.20
O	74.87	6.98	87.80	O	72.98	6.98	60.04
O	76.12	5.91	89.76	O	71.73	5.91	58.08
O	75.82	3.31	89.66	O	72.02	3.31	58.19
O	72.09	5.42	92.53	O	75.76	5.42	55.31
O	81.35	3.44	92.18	O	66.49	3.44	55.66
O	82.57	1.40	93.21	O	65.27	1.40	54.64
O	77.30	1.44	92.39	O	70.54	1.44	55.46
O	79.96	5.63	92.78	O	67.89	5.63	55.07
O	78.00	10.84	93.09	O	69.84	10.84	54.75
O	78.86	3.38	92.94	O	68.99	3.38	54.91

O	80.38	7.99	93.86	O	67.47	7.99	53.98
O	77.96	7.09	93.62	O	69.88	7.09	54.22
O	84.71	10.40	92.65	O	63.14	10.40	55.20
O	82.62	11.07	91.67	O	65.23	11.07	56.17
O	78.49	1.52	94.59	O	69.36	1.52	53.25
O	78.45	12.35	95.01	O	69.39	12.35	52.84
O	79.51	10.10	94.86	O	68.34	10.10	52.99
O	79.59	0.53	96.62	O	68.26	0.53	51.23
O	80.73	0.09	94.40	O	67.11	0.09	53.44
O	82.91	0.62	95.56	O	64.93	0.62	52.29
O	83.04	12.25	93.75	O	64.81	12.25	54.09
O	82.12	9.94	93.81	O	65.73	9.94	54.03
O	81.39	8.87	95.95	O	66.45	8.87	51.90
O	82.63	10.96	89.15	O	65.21	10.96	58.69
O	77.25	12.40	91.25	O	70.59	12.40	56.59
O	79.48	4.30	90.67	O	68.36	4.30	57.17
O	78.45	10.03	90.78	O	69.39	10.03	57.07
O	77.15	1.22	89.80	O	70.70	1.22	58.04
O	79.18	0.55	91.12	O	68.66	0.55	56.72
O	80.20	0.81	88.90	O	67.64	0.81	58.95
O	80.88	12.20	90.39	O	66.97	12.20	57.45
O	80.88	9.62	90.58	O	66.96	9.62	57.26
O	79.42	8.23	89.11	O	68.42	8.23	58.73
O	80.10	3.31	88.34	O	67.74	3.31	59.50
O	79.73	1.47	86.41	O	68.12	1.47	61.43
O	79.28	5.75	88.47	O	68.56	5.75	59.37
O	77.91	3.51	88.80	O	69.94	3.51	59.04
O	79.54	7.57	86.67	O	68.30	7.57	61.17
O	77.39	7.35	88.08	O	70.45	7.35	59.77
O	76.22	2.01	87.48	O	71.63	2.01	60.36
O	81.64	1.27	90.96	O	66.21	1.27	56.89
O	79.33	7.81	91.62	O	68.52	7.81	56.23
Si	68.01	6.40	94.97	Si	79.84	6.40	52.87
Si	69.61	10.74	95.26	Si	78.24	10.74	52.58
Si	70.03	2.51	92.73	Si	77.81	2.51	55.11
Si	69.13	12.97	93.19	Si	78.71	12.97	54.65
Si	66.16	12.90	92.30	Si	81.68	12.90	55.54
Si	65.34	2.39	91.58	Si	82.50	2.39	56.27
Si	67.44	4.26	92.82	Si	80.41	4.26	55.03
Si	64.44	10.65	93.49	Si	83.40	10.65	54.35
Si	67.21	9.20	93.95	Si	80.63	9.20	53.89

Si	68.96	4.27	88.29	Si	78.89	4.27	59.56
Si	66.50	11.26	89.69	Si	81.35	11.26	58.15
Si	68.12	9.17	91.05	Si	79.73	9.17	56.79
Si	68.52	6.13	90.69	Si	79.33	6.13	57.16
Si	70.48	11.17	91.08	Si	77.36	11.17	56.76
Si	70.88	2.36	89.73	Si	76.96	2.36	58.12
Si	71.21	12.85	88.66	Si	76.64	12.85	59.18
Si	68.30	12.85	87.91	Si	79.55	12.84	59.93
Si	66.96	2.06	88.92	Si	80.88	2.06	58.92
Si	72.38	9.22	95.14	Si	75.46	9.22	52.70
Si	72.25	4.42	93.73	Si	75.60	4.42	54.12
Si	76.39	7.16	93.72	Si	71.45	7.16	54.13
Si	75.32	4.30	93.50	Si	72.53	4.30	54.34
Si	75.50	9.41	95.61	Si	72.35	9.41	52.23
Si	71.04	6.48	95.67	Si	76.81	6.48	52.17
Si	75.40	4.63	90.39	Si	72.45	4.63	57.45
Si	75.38	8.80	91.29	Si	72.47	8.80	56.55
Si	71.41	6.33	91.46	Si	76.44	6.33	56.38
Si	72.44	9.17	92.14	Si	75.40	9.17	55.71
Si	72.61	4.82	89.12	Si	75.24	4.82	58.73
Si	76.05	7.21	88.85	Si	71.80	7.21	59.00
Si	82.38	2.26	91.91	Si	65.47	2.26	55.94
Si	79.96	4.17	92.16	Si	67.89	4.17	55.69
Si	79.41	7.09	93.00	Si	68.43	7.09	54.84
Si	77.76	2.43	93.53	Si	70.09	2.43	54.32
Si	78.13	10.86	94.62	Si	69.72	10.86	53.22
Si	79.33	0.29	95.11	Si	68.52	0.29	52.73
Si	82.30	0.21	94.20	Si	65.55	0.21	53.65
Si	83.20	10.84	93.07	Si	64.64	10.84	54.78
Si	80.85	9.32	94.56	Si	66.99	9.32	53.28
Si	78.94	7.21	88.04	Si	68.90	7.21	59.80
Si	76.80	2.41	88.85	Si	71.04	2.41	59.00
Si	77.46	10.89	91.66	Si	70.38	10.89	56.18
Si	77.63	0.56	91.15	Si	70.22	0.56	56.70
Si	80.51	0.35	90.37	Si	67.33	0.35	57.48
Si	81.75	10.89	90.44	Si	66.10	10.89	57.41
Si	79.52	8.89	90.51	Si	68.32	8.89	57.34
Si	80.38	1.86	87.74	Si	67.46	1.86	60.10
Si	79.19	4.33	89.13	Si	68.65	4.33	58.72
H	63.66	11.37	95.73	H	84.19	11.37	52.12
H	66.97	5.97	97.18	H	80.88	5.97	50.67

H	69.30	11.72	97.50	H	78.54	11.72	50.34
H	73.21	12.04	87.55	H	74.63	12.04	60.30
H	67.15	0.44	86.35	H	80.70	0.44	61.50
H	68.96	4.95	85.93	H	78.88	4.95	61.92
H	75.94	8.68	97.94	H	71.91	8.68	49.91
H	70.92	5.68	98.01	H	76.92	5.68	49.83
H	72.65	5.54	86.75	H	75.19	5.54	61.10
H	74.27	6.24	88.07	H	73.58	6.24	59.78
H	79.53	0.71	97.54	H	68.31	0.71	50.30
H	83.37	1.01	96.29	H	64.47	1.01	51.56
H	81.71	8.34	96.65	H	66.13	8.34	51.19
H	79.24	1.15	85.67	H	68.61	1.15	62.18
H	80.12	8.02	86.08	H	67.73	8.02	61.77
H	75.63	1.73	86.80	H	72.22	1.73	61.04
O	63.85	2.63	91.10	O	84.00	2.63	56.74
O	55.07	1.06	79.96	O	92.78	1.06	67.89
O	54.75	9.22	78.00	O	93.09	9.22	69.84
O	54.91	3.31	78.86	O	92.94	3.31	68.99
O	53.98	12.07	80.38	O	93.86	12.07	67.47
O	54.22	12.97	77.96	O	93.62	12.97	69.88
O	52.99	11.96	75.87	O	94.86	11.96	71.97
O	53.88	0.96	75.79	O	93.96	0.96	72.06
O	53.93	3.42	76.46	O	93.92	3.42	71.39
O	53.25	5.17	78.49	O	94.59	5.17	69.36
O	52.63	9.68	76.71	O	95.21	9.68	71.14
O	50.74	10.97	75.74	O	97.11	10.97	72.10
O	52.84	7.71	78.45	O	95.01	7.71	69.39
O	52.99	9.96	79.51	O	94.86	9.96	68.34
O	51.23	6.16	79.59	O	96.62	6.16	68.26
O	53.44	6.60	80.73	O	94.40	6.60	67.12
O	51.90	11.19	81.39	O	95.95	11.19	66.46
O	55.45	5.24	77.30	O	92.39	5.24	70.54
O	55.48	12.31	75.84	O	92.37	12.31	72.01
O	56.24	9.95	76.14	O	91.60	9.95	71.71
O	57.99	11.72	75.70	O	89.85	11.72	72.14
O	56.59	7.66	77.25	O	91.25	7.66	70.59
O	57.17	2.38	79.48	O	90.67	2.38	68.36
O	57.07	10.03	78.45	O	90.78	10.03	69.39
O	58.04	5.47	77.15	O	89.80	5.47	70.70
O	56.72	6.13	79.18	O	91.12	6.13	68.66
O	66.09	1.81	87.67	O	81.76	1.81	60.17

O	55.90	2.25	75.42	O	91.94	2.26	72.42
O	58.73	11.83	79.42	O	89.11	11.83	68.42
O	59.37	0.94	79.28	O	88.47	0.94	68.56
O	59.04	3.18	77.91	O	88.80	3.18	69.94
O	61.17	12.49	79.54	O	86.67	12.49	68.30
O	59.77	12.71	77.39	O	88.08	12.71	70.45
O	60.04	13.08	74.87	O	87.80	13.08	72.98
O	58.08	0.78	76.12	O	89.76	0.78	71.73
O	58.19	3.38	75.82	O	89.66	3.38	72.02
O	60.36	4.67	76.22	O	87.48	4.67	71.63
O	56.23	12.25	79.33	O	91.61	12.25	68.52
O	56.61	4.05	83.77	O	91.24	4.05	64.08
O	55.66	3.25	81.35	O	92.18	3.25	66.49
O	54.64	5.29	82.57	O	93.21	5.29	65.27
O	56.77	8.10	86.08	O	91.08	8.10	61.77
O	57.50	5.73	85.56	O	90.34	5.73	62.29
O	57.87	3.26	86.11	O	89.97	3.26	61.73
O	56.17	8.99	82.62	O	91.67	8.99	65.23
O	55.19	9.66	84.71	O	92.65	9.66	63.14
O	56.88	10.38	86.98	O	90.97	10.38	60.87
O	54.75	9.09	87.09	O	93.09	9.09	60.75
O	52.29	6.06	82.91	O	95.56	6.06	64.94
O	54.09	7.81	83.04	O	93.75	7.81	64.81
O	54.03	10.12	82.12	O	93.81	10.12	65.73
O	58.91	7.75	84.80	O	88.94	7.75	63.04
O	58.69	9.10	82.63	O	89.15	9.10	65.21
O	59.72	10.10	84.68	O	88.13	10.10	63.16
O	61.02	8.34	83.43	O	86.83	8.34	64.42
O	58.95	5.88	80.20	O	88.90	5.88	67.64
O	57.45	7.86	80.88	O	90.39	7.86	66.97
O	57.26	10.44	80.88	O	90.58	10.44	66.96
O	59.07	4.43	84.23	O	88.78	4.43	63.61
O	60.26	4.88	81.91	O	87.58	4.88	65.93
O	59.50	3.38	80.10	O	88.34	3.38	67.74
O	61.43	5.21	79.73	O	86.41	5.21	68.12
O	62.37	6.98	81.68	O	85.47	6.98	66.16
O	61.30	5.91	83.74	O	86.54	5.91	64.10
O	61.25	3.31	83.43	O	86.60	3.31	64.41
O	56.89	5.42	81.64	O	90.96	5.42	66.21
O	61.82	3.44	89.49	O	86.02	3.44	58.36
O	61.55	1.40	91.06	O	86.30	1.40	56.79

O	59.62	1.44	86.08	O	88.23	1.44	61.76
O	60.61	5.63	88.57	O	87.23	5.63	59.27
O	59.36	10.84	87.04	O	88.49	10.84	60.81
O	59.92	3.38	87.70	O	87.92	3.38	60.14
O	59.88	7.99	89.48	O	87.96	7.99	58.36
O	58.88	7.09	87.27	O	88.96	7.09	60.57
O	63.10	10.40	92.62	O	84.75	10.40	55.22
O	62.90	11.07	90.33	O	84.95	11.07	57.52
O	58.30	1.52	88.21	O	89.54	1.52	59.64
O	57.93	12.35	88.39	O	89.92	12.35	59.46
O	58.58	10.10	89.22	O	89.26	10.10	58.62
O	57.10	0.53	90.17	O	90.74	0.53	57.67
O	59.59	0.09	90.06	O	88.26	0.09	57.79
O	59.68	0.62	92.52	O	88.17	0.62	55.32
O	61.31	12.25	91.73	O	86.54	12.25	56.11
O	60.79	9.94	90.96	O	87.05	9.94	56.88
O	58.58	8.87	91.40	O	89.26	8.87	56.44
O	65.09	10.96	89.08	O	82.75	10.96	58.76
O	60.58	12.40	85.47	O	87.26	12.40	62.37
O	62.20	4.30	87.11	O	85.65	4.30	60.73
O	61.59	10.03	86.27	O	86.25	10.03	61.57
O	61.78	1.22	84.65	O	86.06	1.22	63.19
O	61.66	0.55	87.08	O	86.19	0.55	60.77
O	64.09	0.81	86.85	O	83.75	0.81	61.00
O	63.14	12.20	88.18	O	84.71	12.20	59.66
O	62.98	9.62	88.28	O	84.87	9.62	59.57
O	63.52	8.23	86.28	O	84.33	8.23	61.56
O	64.53	3.31	86.48	O	83.32	3.31	61.36
O	66.01	1.47	85.19	O	81.84	1.47	62.65
O	64.00	5.75	85.84	O	83.84	5.75	62.00
O	63.03	3.51	84.81	O	84.82	3.51	63.03
O	65.69	7.57	85.17	O	82.15	7.57	62.68
O	63.40	7.35	84.00	O	84.45	7.35	63.84
O	63.33	2.01	82.69	O	84.52	2.01	65.16
O	63.03	1.27	89.12	O	84.82	1.27	58.73
O	61.30	7.81	87.45	O	86.54	7.81	60.39
Si	52.73	6.40	79.33	Si	95.11	6.40	68.52
Si	53.28	10.74	80.85	Si	94.56	10.74	66.99
Si	55.69	2.51	79.96	Si	92.16	2.51	67.89
Si	54.84	12.97	79.41	Si	93.00	12.97	68.44
Si	54.13	12.90	76.39	Si	93.72	12.90	71.45

Si	54.34	2.39	75.32	Si	93.50	2.39	72.53
Si	54.32	4.26	77.76	Si	93.53	4.26	70.09
Si	52.23	10.65	75.50	Si	95.61	10.65	72.35
Si	53.22	9.20	78.13	Si	94.62	9.20	69.72
Si	59.00	4.27	76.80	Si	88.85	4.27	71.04
Si	56.55	11.26	75.38	Si	91.29	11.26	72.47
Si	56.18	9.17	77.46	Si	91.66	9.17	70.38
Si	56.70	6.13	77.63	Si	91.14	6.13	70.22
Si	57.34	11.17	79.52	Si	90.50	11.17	68.32
Si	58.72	2.36	79.19	Si	89.13	2.36	68.65
Si	59.80	12.85	78.94	Si	88.04	12.85	68.90
Si	59.00	12.85	76.05	Si	88.85	12.85	71.80
Si	57.45	2.06	75.40	Si	90.39	2.06	72.45
Si	54.77	9.22	83.20	Si	93.07	9.22	64.65
Si	55.93	4.42	82.37	Si	91.91	4.42	65.47
Si	58.01	7.16	85.96	Si	89.83	7.16	61.88
Si	57.67	4.30	84.92	Si	90.18	4.30	62.92
Si	55.93	9.41	86.13	Si	91.92	9.41	61.72
Si	53.64	6.48	82.30	Si	94.20	6.48	65.55
Si	60.39	4.63	83.43	Si	87.45	4.63	64.41
Si	59.61	8.80	83.87	Si	88.24	8.80	63.98
Si	57.48	6.33	80.51	Si	90.37	6.33	67.33
Si	57.41	9.17	81.75	Si	90.44	9.17	66.10
Si	60.10	4.82	80.38	Si	87.74	4.82	67.46
Si	62.06	7.21	83.23	Si	85.79	7.21	64.62
Si	62.57	2.26	90.24	Si	85.27	2.26	57.61
Si	61.15	4.17	88.26	Si	86.70	4.17	59.58
Si	60.14	7.09	88.22	Si	87.70	7.09	59.63
Si	58.86	2.43	87.04	Si	88.98	2.42	60.80
Si	58.10	10.86	87.91	Si	89.75	10.86	59.93
Si	58.27	0.29	89.20	Si	89.57	0.29	58.65
Si	60.55	0.21	91.31	Si	87.30	0.21	56.53
Si	61.98	10.84	91.53	Si	85.87	10.84	56.31
Si	59.51	9.32	90.24	Si	88.33	9.32	57.60
Si	64.20	7.21	85.33	Si	83.64	7.21	62.52
Si	62.44	2.41	83.88	Si	85.41	2.41	63.96
Si	60.33	10.89	85.86	Si	87.51	10.89	61.99
Si	60.86	0.56	85.74	Si	86.99	0.56	62.10
Si	62.98	0.35	87.85	Si	84.87	0.35	59.99
Si	63.53	10.89	88.96	Si	84.31	10.89	58.89
Si	62.36	8.89	87.06	Si	85.48	8.89	60.78

Si	65.19	1.86	86.43	Si	82.66	1.86	61.42
Si	63.39	4.33	86.09	Si	84.46	4.33	61.75
H	49.90	11.37	75.94	H	97.94	11.37	71.91
H	50.30	5.97	79.53	H	97.54	5.97	68.32
H	51.19	11.72	81.71	H	96.65	11.72	66.13
H	61.77	12.04	80.12	H	86.08	12.04	67.73
H	59.78	0.44	74.27	H	88.07	0.44	73.58
H	61.04	4.95	75.63	H	86.80	4.95	72.22
H	54.13	8.68	87.68	H	93.71	8.68	60.17
H	51.56	5.68	83.37	H	96.29	5.68	64.48
H	62.18	5.54	79.24	H	85.66	5.54	68.61
H	61.84	6.24	81.29	H	86.00	6.24	66.55
H	56.27	0.71	90.59	H	91.57	0.71	57.26
H	59.28	1.01	93.28	H	88.57	1.01	54.56
H	58.13	8.34	92.03	H	89.71	8.34	55.81
H	66.41	1.15	84.40	H	81.43	1.15	63.45
H	66.50	8.02	85.37	H	81.35	8.02	62.48
H	63.62	1.73	81.84	H	84.22	1.73	66.00